Exploiting DNA Surfaces for Sensing and Nanomaterial Applications

Samantha M. L. Lunn

A thesis submitted for the degree of

Doctor of Philosophy in Chemistry

School of Chemistry

Newcastle University

July 2018

Abstract

The synthetic methodology for the on-column specific conversion of guanosine to thioguanosine is described, without the use of expensive thioguanosine phosphoramidites. The thiolated oligomer, once self-annealed, exhibits destabilisation compared to the fully complementary duplex as observed in a reduced Tm. Subsequent Cd^{2+} addition to the disrupted thioG central region indicates a binding ratio of 4:1 thiobase:metal resulting in increased base stacking and overall duplex stability. Equilibrium molecular dynamic calculations reinforce the hypothesis of metal induced restoration of the damaged duplex by the ten-fold reduction in base flexibility upon the addition of the metal stimuli. Hence, the healing of an unstable modified duplex in response to a chemical stimulus has been demonstrated.

The electronic behaviour ferrocene modified DNA silicon junctions was investigated by JV curves obtained by using a top eutectic gallium-indium electrode (EGaIn). The charge transport mechanism in single stranded DNA was found to be tunneling with little rectification. However, in double stranded DNA, charge hopping was observed in addition to electron tunneling, with increased rectification. The difference in charge transport between single and double stranded DNA shows promise for the electronic detection of complementary DNA strands in sensing applications and a better understanding of the electronic properties of DNA.

Finally, an enhancement in surface immobilised repeat sequences was explored using an enzymatic extension protocol. The oligo seed immobilised on the surface is multiplexed in the z direction increasing the number of repeat sequences per probe molecule. An increase in fluorescence intensity is observed from the oligo seed to the extended DNA following the addition of the fluorescent intercalator PicoGreen. The technique was applied to the BAT-25 micro satellite sequence in which a single base mismatch was distinguished from the fully complementary target. This approach allows increased sensitivity to DNA targets whilst maintaining high selectivity.

Acknowledgements

Table of Contents

Abbreviations

α	alpha
ε	extinction coefficient
λ	Lambda
μL	microliter
μm	micrometer
nm	nanometer
π	pi
1BM	1 base mismatch
1D	one dimensional
2D	two dimensional
3D	three dimensional
3-HPA	3-hydroxypicolinic acid
A	deoxyriboadenine
AFM	atomic force microscopy
APEGDMES	acetalpolyethyleneglycoldimethylethoxysilane
bp	base pair
BSA	bovine serum albumin
C	deoxyribocytosine
cAFM	conductive atomic force microscopy
CCDC	Cambridge Crystallographic Data Centre
CD	circular dichroism
CFTR	cystic fibrosis transmembrane conductance regulator
CPG	controlled pore glass
CV	cyclic voltammetry
DAPI	4',6-diamidino-2-phenylindole
DNA	deoxyribose nucleic acid
dN	deoxynucleotide
dNTP	deoxynuleotide triphosphate
dsDNA	double stranded DNA
E.Coli	Escherichia coli

EDTA	ethylene diaminetetraacetic acid
EGaIn	eutectic gallium-indium
Exo-	exonuclease minus
extDNA	extended double stranded DNA
Fc	ferrocene
FEL	X-ray free electron laser
FET	field effect transistor
G	deoxyriboguanosine
HATU	[dimethylamino(triazolo[4,5-b]pyridin-3-yloxy)methylidene]-dimethylazanium;hexafluorophosphate
HPLC	high-performance liquid chromatography
hr	hour
HRMS	high resolution mass spectrometry
IR	infra-red spectroscopy
J	current density
MALDI-TOF MS	matrix assisted laser desorption time-of-flight spectroscopy
MBJ	molecular break junction
MD	equilibrium molecular dynamics
mM	millimolar
MSI	microsatellite instabilities
NMR	nuclear magnetic resonance
Oligo	oligomer
PCR	polymerase chain reaction
PEG	polyethylene glycol
PG	PicoGreen
RCA	rolling circle amplification
RMSF	root-mean square fluctuations
s	second
SAM	self-assembled monolayer
SiO_2	silicon dioxide
SiH	silicon hydride
ssDNA	single stranded DNA

ssextDNA	extended single stranded DNA
STM	scanning tunneling microscopy
T	deoxyribothymine
TBE	tris boric acid EDTA
TE	tris-EDTA
TEAA	triethylammonium acetate
tG	6-thio-2-deoxyguanosine
Tgo	*Thermococcus gorgonarius*
TIRF	total internal reflection fluorescence
Tm	melting temperature
TP	triphosphate
UV-Vis	ultraviolet-visible spectrometry
XPS	x-ray photoelectron spectroscopy

Chapter 1.

Introduction: Exploitation of DNA Surfaces for Sensing and Nanomaterial Applications

# Table of Contents

Introduction

The role of DNA has shifted outside the limits of its biological function into the field of nanomaterials. The discovery of the DNA structure by Watson and Crick in 1962[1] initiated extensive research into alternative applications of DNA rather than the biological function in the body. DNA has since been studied for utilization in a variety of fields such as drug delivery,[2] conductive materials[3] and sensors.[4]

The discovery of the bonding interactions between the DNA bases allows for major advancements in nanotechnology due to the programmability of the sequence. Complementary base pairing exists via hydrogen bonding between adenine (A) and thymine (T), and guanine (G) and cytosine (C), Figure 1. The hydrogen bonds coupled with the $\pi-\pi$ interactions developed between stacked bases and the increase in entropy by the dispersion of water molecules produces a double helix architecture. The small dimension of the height and width of DNA, *ca* 2 nm, and the possibility for the length to reach many microns couple with the controllable nature, make DNA an attractive molecule for the use in nanomaterials.[5,6]
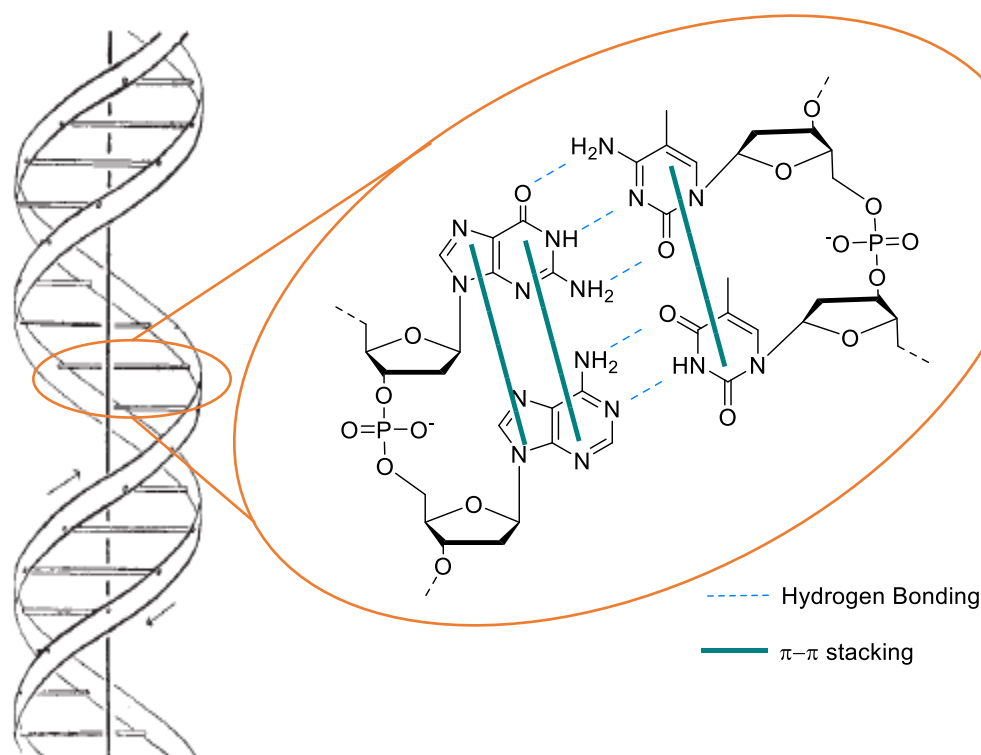
**Figure 1.** *The DNA double helix structure.[1] The deoxyribose nucleotides are connected via a phosphodiester bond in the 3'-5' direction. Hydrogen bonds form between complementary base pairs: A forms two hydrogen bonds with T, and G forms three hydrogen bonds with C. The alignment of the bases allows $\pi-\pi$ stacking which is stronger in GC base pairs therefore they are more thermostable.[7]*

The design of the DNA sequence, relying upon the complementary base pairs, has introduced an abundance of potential applications into 1D,[5,6] 2D[8-11] and 3D[12,13] nanomaterials pioneered by the work of Ned Seeman in 1982.[14] DNA origami, created as the result of folding the DNA strand in a controlled and designed manner, constructs remarkably ordered structures manipulated simply by the programmability of the complementary DNA base pairs, Figure 2. Many highly organised structures have been possible such as the Holliday junction,[15] 4-armed junction,[14] DNA tiles,[14] and even 3D boxes.[13]
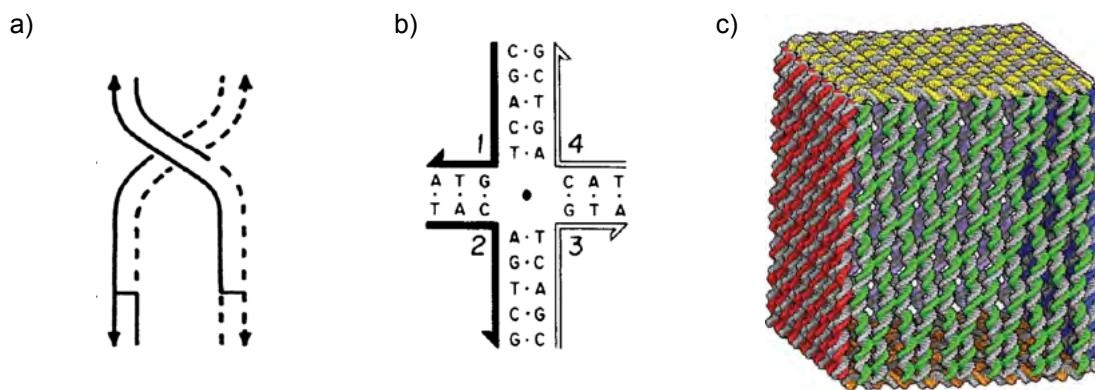
Figure 2. DNA ordered structures formed through sequence design relying on complementary base pariing. a) the Holliday junction,[15] b) the 4-armed junction[14] and c) a DNA 3D box with a closable lid.[13]

The manipulation of DNA has led to the formation of nanorobots,[16] nanocomputers,[17] and nanocapsules,[18] highlighting the versatility of the DNA structure to be used in a wide range of nanomaterials. DNA can also act as a template to form conductive wires by the deposition of metal ions and electrostatic attraction to the negatively charged backbone, Figure 3a.[19-21] DNA can be used as a scaffold to afford increased control over the site of metal ions, by the modification of specific bases in the duplex to attract desired groups for the distinct anchoring of groups along the DNA strand, Figure 3b.[22-24] This can be used for the directed assembly of nanomaterials at user defined regions in the DNA strand.
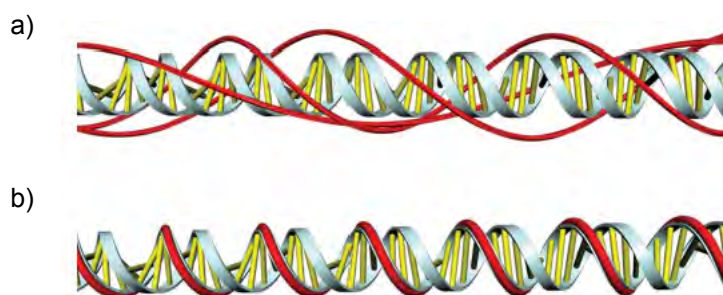
Figure 3. DNA acting as a) a template and b) a scaffold.[23]

Many interesting shapes and devices can be made through the solution-based control of DNA, however, the scope of this thesis is directed towards the synthetic methods for DNA modification and the integration of DNA with surfaces for nanomaterial and sensing applications.

1.1 Sources and synthesis of DNA

In order to achieve the high specificity of sequence design for the creation of functional nano-architectures, two methods of DNA synthesis are employed; automated DNA synthesis and enzymatic synthesis.

1.2.1 Automated synthesis for standard bases

Automated solid phase synthesis using conventional phosphoramidite chemistry, developed by Beaucage and Carruthers in 1982,[25] can be used to site specifically incorporate nucleosides into DNA oligonucleotides up to 100 bases in length. A major advancement in the development of the automated synthesiser was the immobilisation of the phosphoramidite on a controlled pore glass (CPG) solid support via a ICAA linkage allowing for easy purification. The general process is the step-by-step addition of each base in the direction of 3'-5'. 3' and 5' refer to the carbon atoms on the deoxyribose sugar. The 5' carbon is attached to a phosphate whilst the 3' carbon has a hydroxyl group. This labelling of the carbon atoms gives the DNA strand a direction.

In this method of DNA synthesis, the first base is already attached to the CPG bead at the 3'-terminus and deprotected to expose a free 5'-hydroxyl for the coupling with the next nucleoside in the sequence, Scheme 1. After the reaction between the two bases, it is essential to carry out a capping step to block the 5'-OH of any nucleosides which have not been successfully added onto the oligomer to avoid this base being able to react in the next cycle, disrupting the desired sequence. Following the oxidation of phosphorus (III) to phosphorus (V) to give the phosphate group, the cycle is repeated to afford the desired oligonucleotide. Since the automation of the system, the desired sequence is simply keyed into the synthesiser and the specific DNA oligomer is produced.
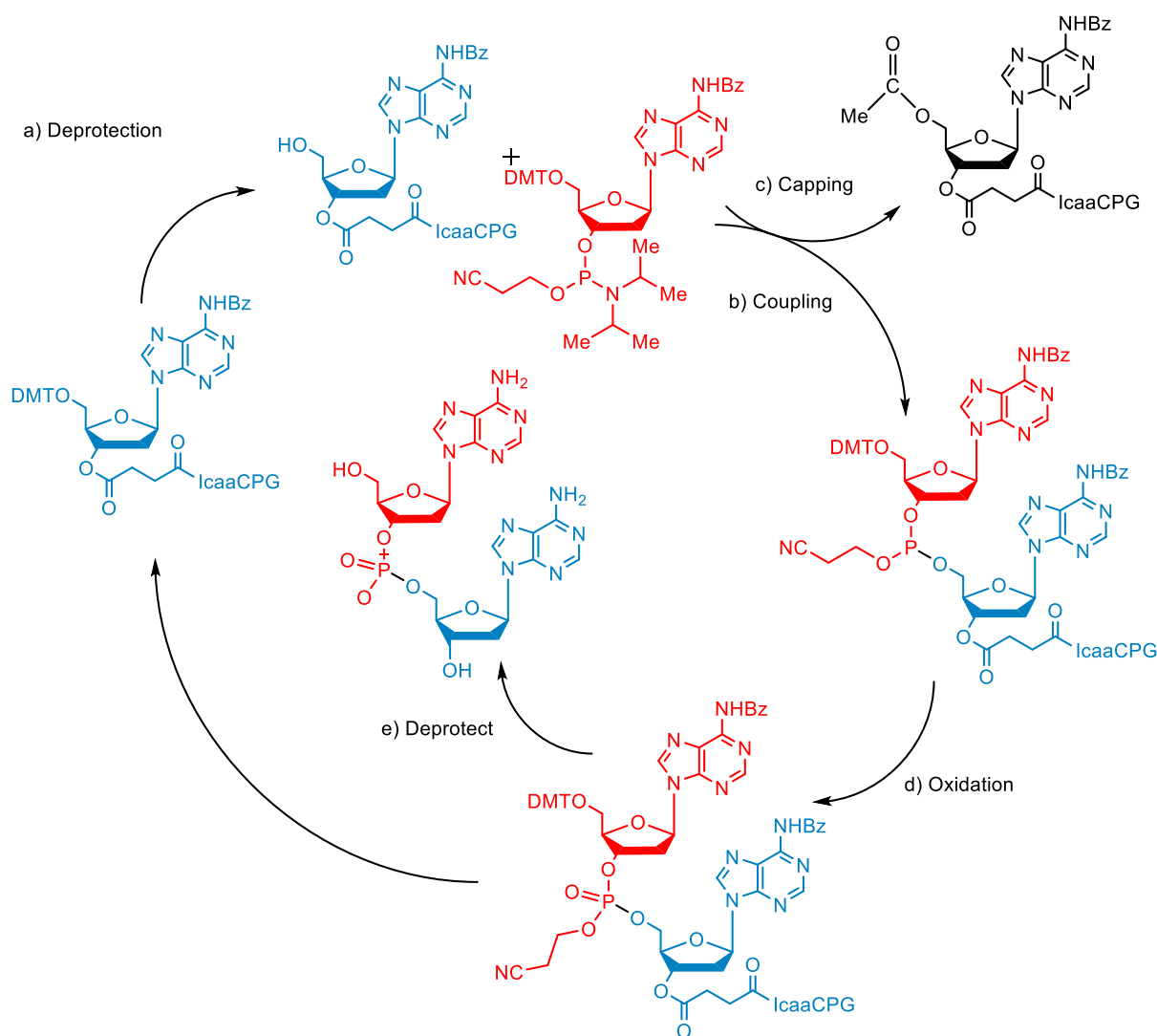
Scheme 1. *The chemical reactions used in the synthesis of DNA via automated phosphoramidite chemistry. a) $Cl_3C.COOH$ in CH_2Cl_2, b) tetrazole in CH_3CN, c) n-methylimidazole in $(CH_3CO)_2O$, d) I_2, H_2O in THF and e) concentrated NH_3.*

The oligomer is cleaved from the solid support following synthesis by treatment in 3% trichloroacetic acid in DCM to remove the DMT protecting group, followed by submersion in concentrated aqueous ammonia for 5 hours at 55 °C to remove the remaining protecting groups and cleave the oligomer from the CPG bead. To separate the oligomer from the beads, it is dissolved in nanopure water, filtered and subsequently purified via reverse phase HPLC. Although the automated DNA method allows complete control over the sequence, the process is limited by length as each step has a yield of 99.5%, Figure 4. Therefore, the maximum DNA length obtainable is approximately 120 bases if bought commercially (Eurofins), with lower lengths achievable in standard research laboratories.
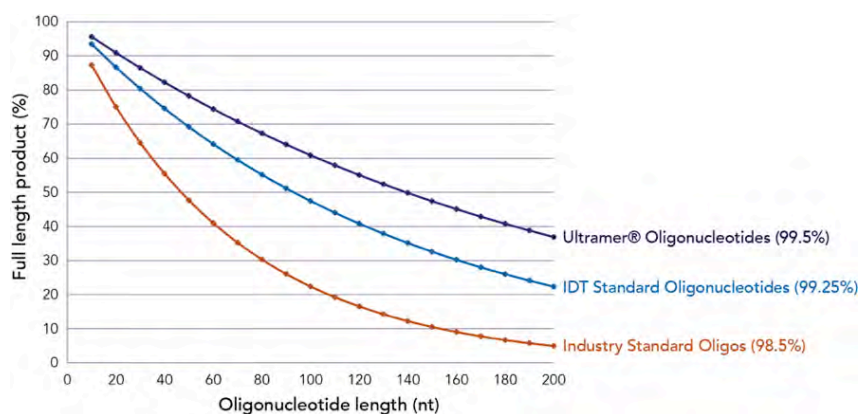
Figure 4. A graph highlighting the decrease in yield of oligomers with increasing length by phosphoramidite synthesis. (www.itdDNA.com)

1.1.1.2 Incorporation of modified bases

Several methods to increase the properties and hence applications of DNA as a nanomaterial have been attempted via the incorporation of modified DNA bases. The nucleoside can be modified with additional functional groups in the phosphate backbone,[26] the sugar[27] or the base itself,[28] Figure 5. One particular area of phosphate backbone modification involves the replacement of the phosphate with a phosphorothioate group for increased strand stability as this backbone linkage is resistant to degradation.[29] Sugar modifications have been used for gene silencing.[30] The most common form of nucleoside modification is to the nucleobase itself. Base modifications are employed for added functionality in the hydrogen bonding region such as redox groups adding electrochemical properties on the DNA strand.[31] Others use completely artificial nucleobases, like the Shionoya group who incorporate modified bases, such as hydroxypyridone, for the assembly of metal ions to form metallised DNA.[32-36] The design of the nucleobase is crucial as to not affect the structural integrity of the DNA strand, causing destabilisations in the base pairing region and hence overall duplex structure. Artificial bases are designed to be planar and aromatic so as fit in with the other bases for base stacking to retain the duplex structure.[37-39]
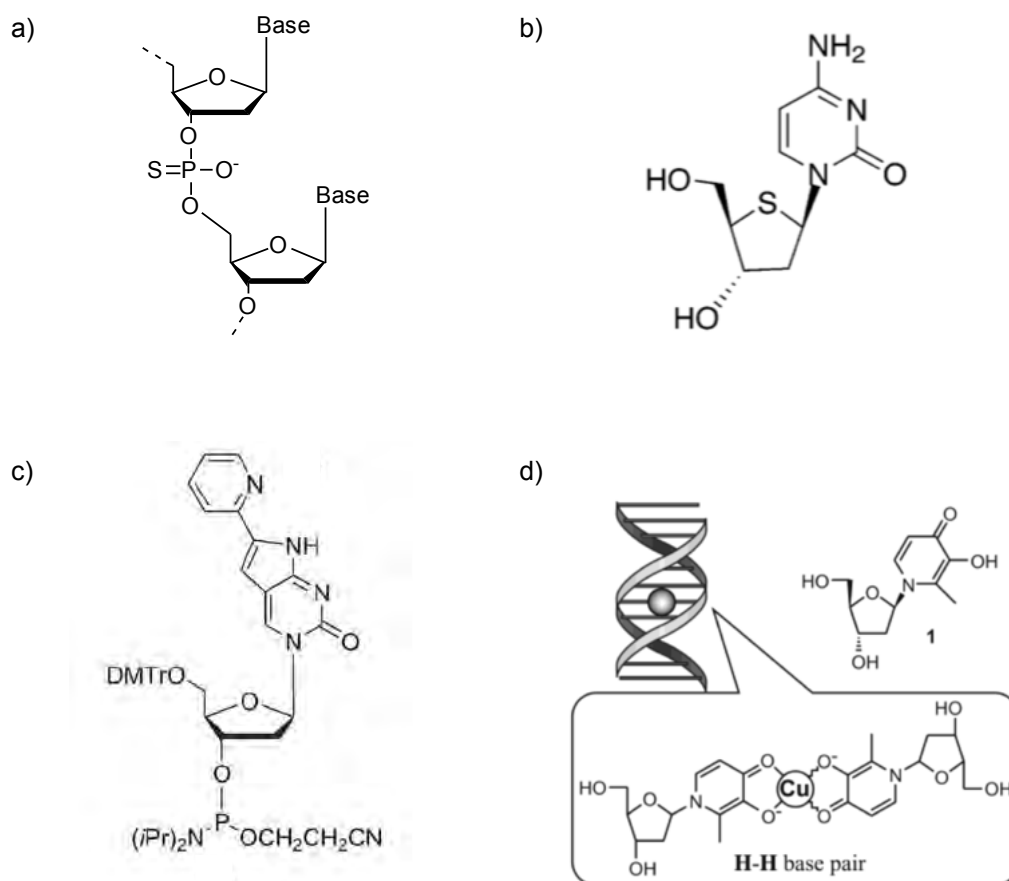
Figure 5. Examples of nucleoside modifications possible to afford new properties on the DNA. a) phosphorothioate backbone modification b) deoxyribose sugar modification[27] c) nucleobase modification[28] d) artificial nucleoside.[33]

In order to incorporate non-canonical bases into the DNA sequence, a phosphoramidite monomer bearing the desired modification is utilised. Commercially available protected modified phosphoramidites are available however they are extremely expensive. For this reason, several groups have synthesised their own modified phosphoramidites to produce phosphoramidites bearing a multitude of different functional groups. Nevertheless, there are complications associated with this approach as the modified phosphoramidite monomer must be protected and stable to the repetitive reaction conditions in the synthesiser and the deprotection steps. Ultra-mild reagents can be used in the synthesiser to reduce the potential conversion of the modification.[40,41] The modified phosphoramidite can then simply be inserted into the oligonucleotide at predetermined sites. Zheng *et el.* used commercially available 6-deoxy-guanosine to form the protected phosphoramidite involving the protection of the thione and amine groups on the nucleobase and the subsequent attachment of the phosphoramidite.[42]
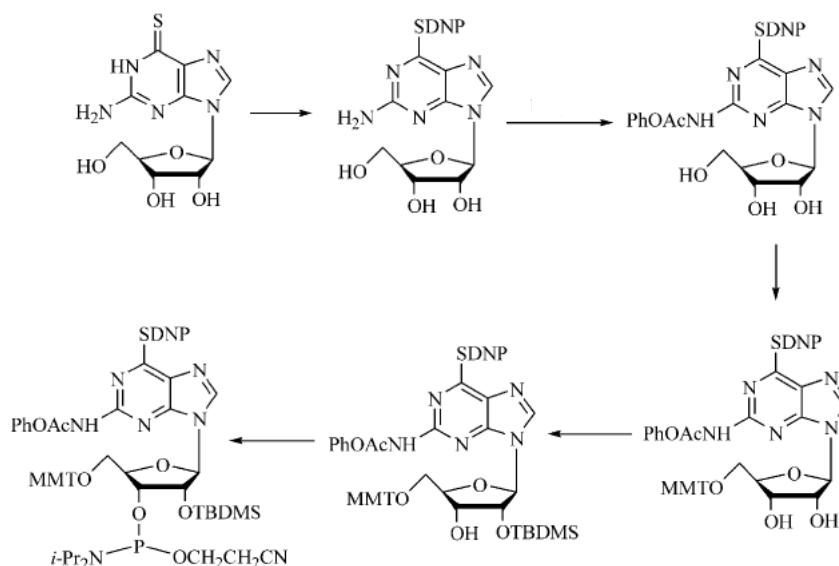
Figure 6. The synthesis of the modified 6-deoxy-guanosine phosphoramidite by the protection of the labile groups, the thione and the amine group, followed by the addition of the phosphoramidite moiety.[42]

The synthesis of modified phosphoramidites is lengthy and complicated and the modification needs to be protected from the conditions in the synthesiser. A cost-effective, simple method for the incorporation of modified bases into DNA would be beneficial.

1.1.2 Enzymatic synthesis

The synthesis of DNA via the phosphoramidite method is limited in respect of length. Longer DNA sequences are needed for applications such as nanomaterials. Genomic DNA is readily available in a variety of lengths, however, the sequence is limited by those available. In order to achieve sequence specificity, enzymatic extension methods are employed.

Several enzymatic methods to achieve more control over the sequence are routinely used such as primer extensions, the polymerase chain reaction (PCR), rolling circle amplification (RCA) and the slippage reaction. Each extension method requires a DNA template, a primer, dNTPs and a DNA polymerase. Primer extensions involve the isothermal extension of a short oligomer known as the primer which bonds to a template and produces one copy of DNA, complementary to the template strand.[43] PCR also extends a primer sequence, via thermal cycling, on both ends of the duplex primer, resulting in exact copies of the primer strand. [44] PCR allows some control over the concentration which increases with each cycle; this method is routinely employed for DNA amplification.

The DNA slippage reaction has been employed to produce long repeat sequence DNA, much like the slippage reaction which occurs in vivo.[45-47] Tandem repeat sequences are unstable in the genome and consequently, a slip during DNA replication can occur, Scheme 2. This method has been utilised in research laboratories to produce long repeat sequence DNA, capable of DNA extension up to 2,000 bp.[46] Although the slippage reaction is good to produce long tandem repeat sequences, the range of sequences able to slip is limited.
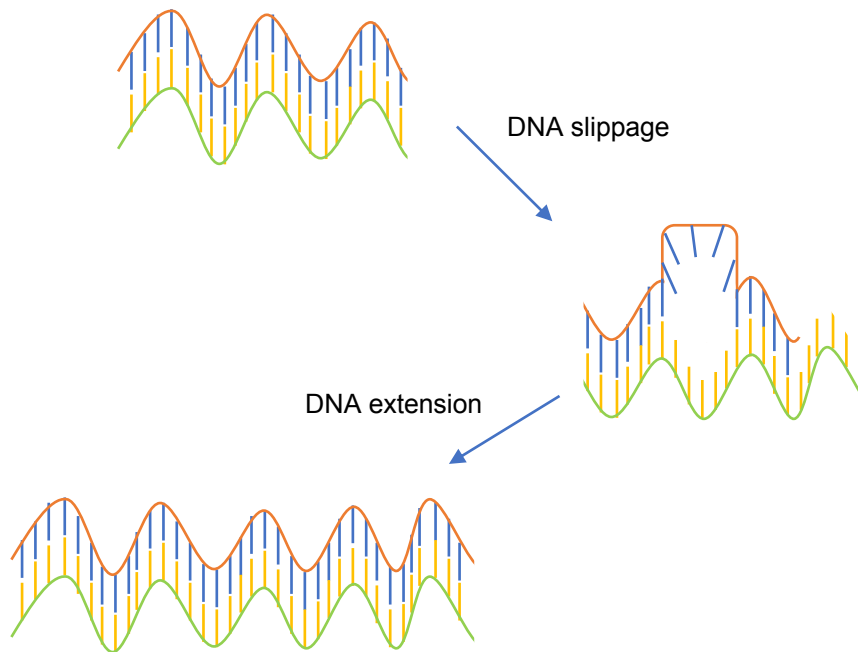
Scheme 2. Enzymatic extension of DNA via the slippage reaction. A stable loop forms resulting in a shift in the DNA strand. Once the loop flattens, two sticky ends are formed which can be extended by the DNA polymerase.

RCA enables the synthesis of long DNA by the replication of circular or plasmid DNA.[48] Once extended, the single strand is displaced to allow for further extension of the plasmid, Scheme 3. The ssDNA is converted into dsDNA. RCA is extremely effective for the production of long repeat sequence DNA however; the sequence is limited by the commercially available template strands and the repeat sequence size is restricted to the length of the plasmid.
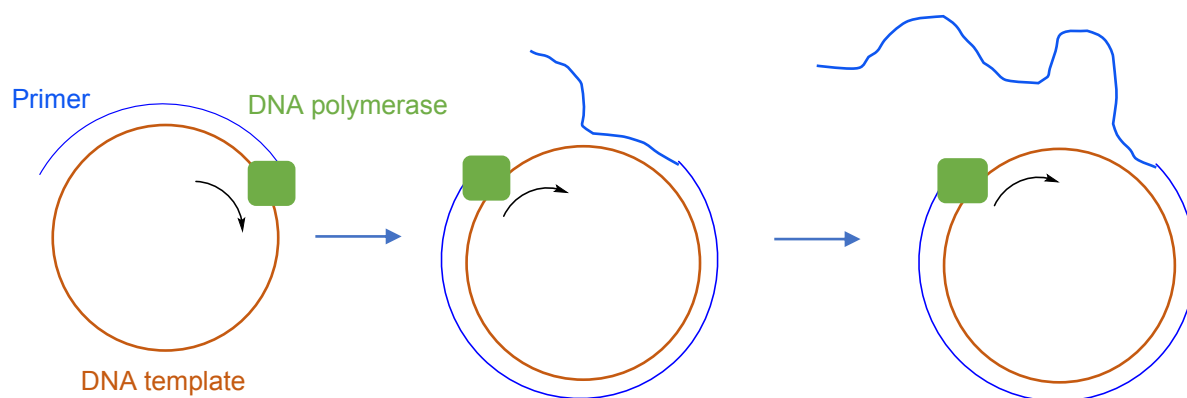
Scheme 3. Enzymatic extension by rolling circle amplification. The primer is extended by the DNA polymerase. The strand is displaced to allow for continual extension.

There are several ways to incorporate modified bases into DNA by enzymatic approaches affording long DNA with additional properties.[49,50] Modified triphosphates can be enzymatically incorporated during PCR and further functionalised via post synthetic modification. This method relies upon the ability of modified DNA polymerase enzymes, which are disabled in the exonuclease domain, to incorporate modified bases. The Kool group investigated the ability of the DNA polymerase to incorporate modified bases with both oxygen atoms on thymidine replaced with hydrogen or halogens.[51] In most cases, a DNA base bearing a moiety which is able to undergo further conversions is of use, as one modified triphosphate can lead to multiple functionalities on the DNA. The Carell group used 5-alkyne modified deoxyuridine triphosphate instead of a natural base in the PCR reaction, producing highly modified DNA strands.[52] The alkyne moiety can then undergo a Cu^I catalysed azide-alkyne cycloaddition, known as the click reaction, which allows the directed Ag staining of the DNA strand. This method can prove problematic as the polymerases have certain limits on the modifications, which can reduce the number of modifications suitable.

Each of the enzymatic methods described can produce long DNA however the sequence design is limited by currently available sequences and also restricted by the necessity of templates.

Depending on synthetic route, DNA can be short (<148 bp) or long (>148 bp), modified or natural and has a range of potential applications, including nanomaterials,[53] drug delivery,[2] and bio-sensing.[54] One key approach to develop DNA based systems, is to integrate the DNA strands with a surface.[55] There are two ways this can be achieved: either by building the DNA up from surface or by the synthesis of DNA followed by immobilisation to the surface. In both instances, the DNA is ideally orientated

9

perpendicular to the surface. For the post-synthetic attachment of DNA, it is mandatory for the DNA to contain a connecter molecule at one end to covalently attach to the surface to avoid the physisorption.

1.2 DNA immobilised surfaces

Many biomolecular recognition events of interest for various applications such as drug discovery,[56] bio-sensing,[57] and diagnostics[58] rely upon the immobilisation of a probe biomolecule on a surface and interactions with a target molecule in solution. The most common type of bio-device remains to be a DNA-based device with a huge market in DNA chips and microarrays. The ordering of the DNA molecules via self-assembly allows the characterisation of DNA strands end-to-end in a more ordered manner. In solution the organisation of DNA can take up many forms however, with surface immobilised DNA, each strand is organised uniformly in one direction making it easier for characterisation and manipulation. DNA can be immobilised on a variety of surfaces for specific applications. The following section discusses the surfaces, linkers and methods for DNA immobilisation.

1.2.1 Methods of DNA integration with the surfaces

A range of surfaces are exploited depending on their attributes whether it be for optical,[59,60] conductors[61] or semi-conductors.[62] Planar substrates such as silicon, glass, mica or plastic are compatible with the direct attachment of DNA, Figure 7a, or they can be used as a template for the deposition of metal films, endorsing the surface with new properties such as conductivity with gold films, Figure 7b. These planar substrates are advantageous as they are atomically flat if prepared correctly which allows for a good starting point for the self-assembly of the molecules. Silicon is the surface of choice in field-effect transistors (FET). [63,64]

Porous silicon (pSi) has also attracted interest for DNA attachment due to the large surface to volume ratio, and the ability to form stable monolayers through the formation of the covalent Si-C bond. [65] pSi has been integrated with probe DNA strands in sensing devices.[66]
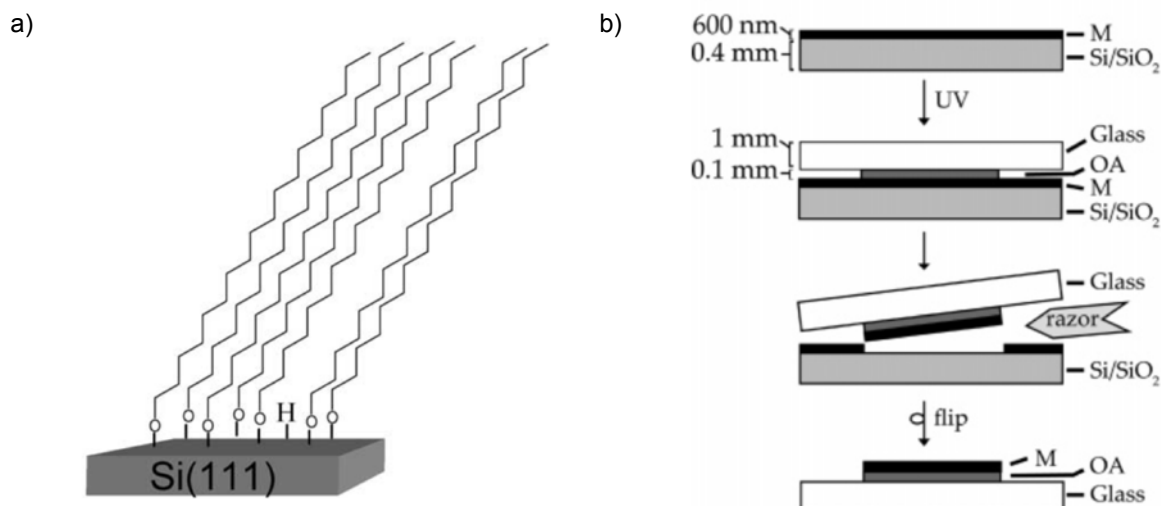
Figure 7. *Example of a silicon surface used in a) the direct attachment of molecules for monolayer formation[67] and b) the use of the silicon surface as a template for the formation of ultra-flat metal surfaces.[68] Metal (M) was evaporated onto the silicon substrate and the metal layer attached to a glass slide with an optical adhesive (OA). The metal-modified glass substrate is cleaved from the silicon by a razor to expose the flat metal surface available for monolayer immobilisation.*

The surface of choice for many applications is gold due to its conducting properties and the well-known formation of well-ordered SAMs.[69] To prepare the gold surface, template stripped methods are employed or lithography providing flat surfaces, ideal for monolayer formation.[68] DNA can subsequently attach to the gold surface with the addition of a 5'-thiol modification, taking advantage of the strong covalent Au-S interaction.[70] The thiol functionality can be added to the oligomer via conventional phosphoramidite DNA synthesis using a thiol-terminated spacer at either the 3' or 5' end. Gold surfaces are easy to pattern, inert and do not form oxides.
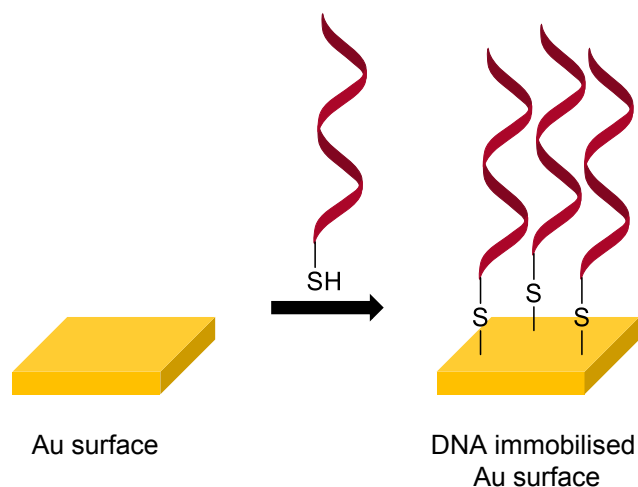
Figure 8. *The attachment of thiol-modified DNA to the gold surface.*

Nanoparticle surfaces are also an area of interest due to their high volume to surface ratio.[71] Nanoparticle usually refers to particles smaller than 200 nm, although as the monolayers self-assemble, the size is not a big issue. The curvature and defect in the nanoparticle must be controlled for a uniform monolayer to form. The gold thiol interaction is also routinely exploited for DNA attachment to nanoparticles for use as a DNA bio-sensor, Figure 9.[72,73]

number of dA increasing
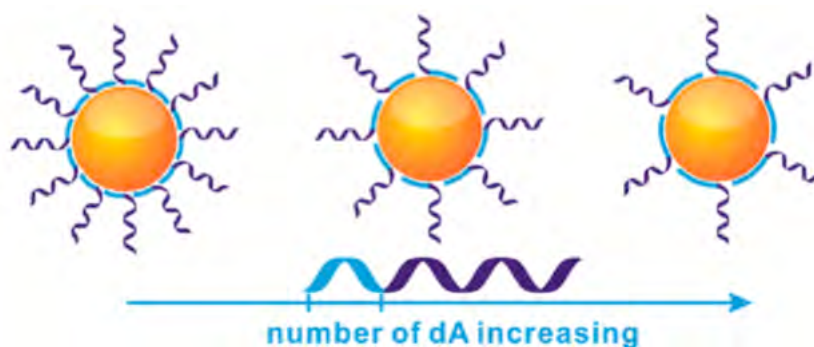
Figure 9. The immobilisation of DNA probe strands on a gold nanoparticle surface forming a monolayer capable of DNA sensing.[72] The strands are anchored by a poly(A) region at one end of the strand which can determine the loading of the monolayer by changing the length of the poly(A) section.

Once the substrate is chosen for the desired application, the connector which acts as the interface between the surface and the SAM is selected. The physical adsorption of DNA to the surface does not require modified DNA as the attraction between the negatively charged backbone and the positively charged surface is sufficient to hold the DNA, Figure 10a. In spite of the advantage that the DNA does not require a modification for surface attachment, the physisorption is not preferred as the DNA assembles in a random orientation and is easily affected by a change in ionic strength.[57]

For greater control over monolayer uniformity, the desired alignment, perpendicular to the surface can be achieved by the addition of a connecter functional group to the DNA strand. This connector is capable of covalent bonding to the surface and is necessary for successful immobilisation, Figure 10b. The thiol functionality is frequently employed for covalent attachment to gold surfaces.[74-76] The surface is simply immersed in the DNA-connector solution for self-assembly and covalent attachment to the surface.[70] The time and temperature can be altered to create the best possible conditions for uniform SAM formation.

Linker molecules are also utilised for DNA attachment. A linker is defined as a molecule attached to the surface at one end which the probe molecule can then subsequently

be attached to, at the opposite end, Figure 10c.[77] Linker molecules weaken the probe surface interactions, making the hybridisation event more like the situation in bulk solution compared to oligomers located close to the surface. Various linker molecules have been employed to attach the DNA such as aldehydes,[78,79] epoxy,[80] and isothiocyanates,[81] all requiring the DNA to be modified with an amine. The DNA strand must be modified at one end with a functional group capable of reacting with the exposed group at the terminus of the linker molecule. A well-studied example is the surface modification of biotin-streptavidin.[82] Streptavidin (or avidin) contains 4 binding sites which have a high affinity for biotin molecules, one of the strongest biomolecular attractions. Biotin-labelled DNA can specifically bind to the streptavidin molecules attached to a surface. This method also allows the selective spacing of the probe as the immobilisation can be localised in known regions on the surface resulting in its high use in DNA microarrays.[83]

Silanisation reactions are often employed for monolayer formation to glass and silicon surfaces for optical sensing.[84,85] The silane can be alkyne terminated for hydrosilylation chemistry or alkoxy terminated for silanisation covalent attachment.[84,86,87] Silane monolayers possess higher thermal stability compared to gold-thiol interaction, making them an attractive option for devices requiring higher temperatures.[88]

a)

b)

c)

Physical
adsorption

Covalent
Immobilisation

Streptavidin-Biotin
Immobilisation
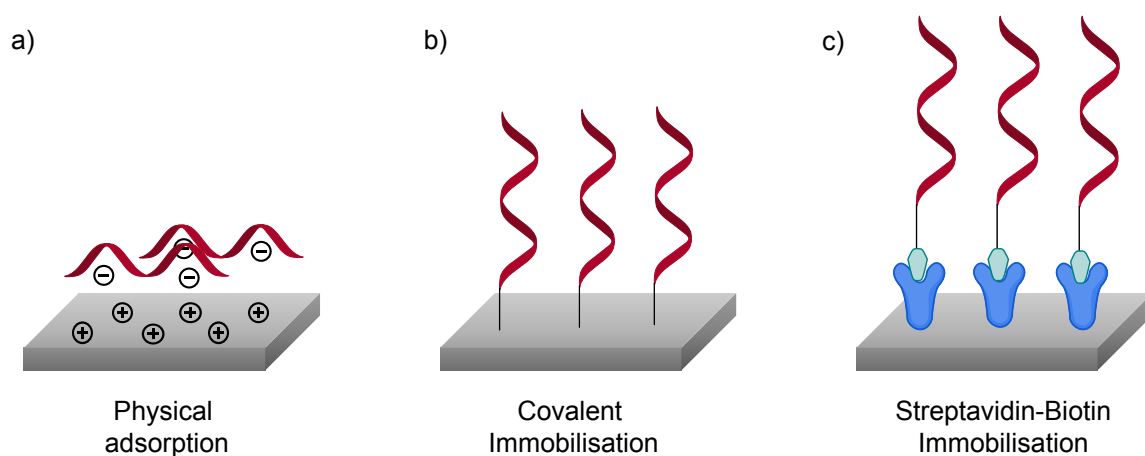
Figure 10. a) The unmodified DNA physical adsorption to a surface. b) The covalent immobilisation of DNA to the surface. c) Attachment of biotin-labelled DNA to a streptavidin modified surface.

A method to avoid the over-crowding of the surface with the monolayer, resulting in disordered SAMs, can be avoided by the utilisation of mixed monolayers. Mercaptohexanol is routinely used as a spacer which is attached to the surface at the same time as the linker for the DNA probe resulting in more control over the probe DNA density.[89,90]

The growth of DNA off the surface rather than post-synthetic attachment has also been explored. The synthesis of DNA by conventional phosphoramidite chemistry is a great example of the construction of DNA base by base off the surface. The process has also been demonstrated using a silicon wafer as the surface by a modified procedure in the synthesiser.[91] The growth of long DNA off the surface is less studied due to the complications associated with the control of the immobilisation of the longer strands. Several groups have attempted the fabrication of long DNA surfaces by the assembly of concatemers from an immobilised short strand in the z-direction to the surface[92] or by the enzymatic extension by RCA of a surface bound oligomer.[93] There are much fewer examples of long DNA off surfaces compared to the post-synthetic attachment therefore this thesis investigates an alternative method for the growth of DNA off a surface.

A variety of DNA-immobilised surfaces can be established and are exploited for assembly of nanomaterials and sensing. The complementary nature of the DNA strand can be taken advantage of to detect the presence of a known disease target strand[94-96] or can be used in the directed assembly of materials.[3,97,98] Depending on the application, these DNA surfaces are often characterised electronically or optically. The following sections discuss both the electronic and optical characterisation of DNA surfaces.

1.2.2 Electronic characterisation of DNA monolayers

There are conflicting reports stating that DNA is an insulator[19] and also a semi-conductor.[99] A great deal of research has been undertaken to investigate the potential electron transfer in DNA due to the obvious conceivable use in molecular electronics as a result of the small dimensions and programmability.[100] It has previously been suggested that bare DNA permits electron transfer by the $\pi-\pi$ stacking of the nucleobases which conflicts with others who state that it is an insulator.[101] The electron transport through DNA is now thought to depend upon the specific constituents and hence can express different electrical characteristics in different situations.[102]

The conductivity of DNA monolayers has been studied by a variety of methods such as molecular break junctions (MBJ)[103]: scanning tunneling microscopy (STM)[104] and conductive atomic force microscopy (cAFM).[105] Each method relies upon the formation of good electrical contacts, reliably and reproducibly, at both ends of the DNA molecules. Scanning probe techniques such as STM and cAFM introduced a convenient method for the electrical characterisation of single DNA molecules,

Figure 11. STM involves the contact of the STM metallic tip with the DNA to form the metal-DNA-metal junction. The tip is controlled by a sensitive transducer and is moved in and out of contact with the DNA whilst recording the conductance. cAFM similarly involves the contact of a metal coated AFM tip with the DNA monolayer and has the added advantage of simultaneously recording the force and image of the surface.
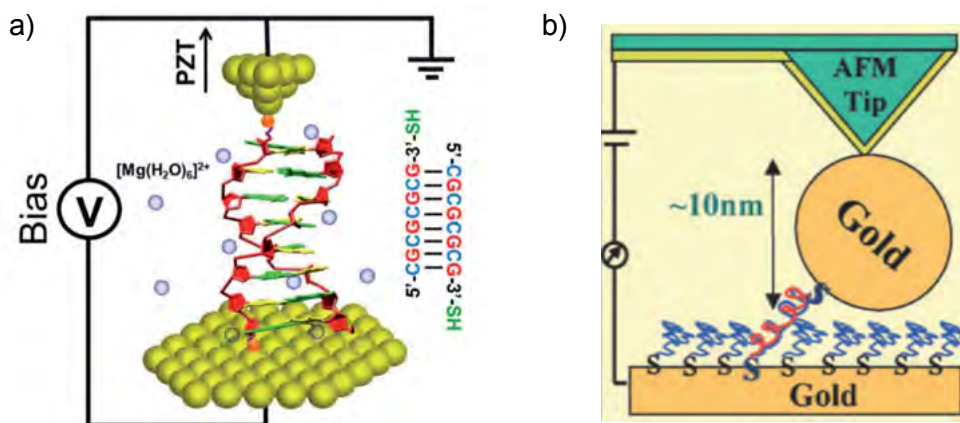
Figure 11. *Charge transport through single DNA molecules by a) STM [104] and b) cAFM .[105]*

Each method for electrical characterisation described so far has been developed for the charge transport measurements through individual DNA strands rather than the DNA monolayer as a whole. Large-area molecular junctions are frequently employed for the study of organic alkanethiol monolayers however the study of DNA using these large area junctions are less common. Katsouras *et al.*[106] formed large area molecular junctions with a DNA monolayer, however, the DNA molecules were lying flat across the surface therefore the charge transport is studied through the diameter of the duplex rather than through the length of the duplex. Investigations into the charge transport through perpendicular DNA monolayers, and hence through the length of the DNA strand, using a large-area molecular junction would be beneficial.

1.2.2.1 DNA monolayers for sensing applications

One of the main uses of DNA immobilised surfaces is for bio-sensing applications. DNA biosensors consist of short single stranded probe oligomers immobilised onto a surface.[4] The probe strand is designed to be complementary to a target strand of interest. If a solution containing the target strand is placed in contact with the probe-immobilised surface, the strands will hybridise and produce a readout signal, Figure 12. Several readout methods are frequently employed such as electrical,[107] electrochemical,[108] mass[109] or optical.[110] For electrical determination, the addition of a molecular label capable of transmitting an electrical signal is often required to increase

the conductive properties of the DNA.[111] This can be achieved via the attachment of DNA to conductive nanowires able to recognise a hybridisation event and transmit the electrical transport signal. Other groups use multi-walled carbon nanotubes (MWCNT) as a conductive film which can efficiently distinguish changes which occur after hybridisation events.[112,113] In spite of considerable advances in electrical DNA bio-sensors, the currently accessible electrical devices are expensive, challenging to use and complicated.
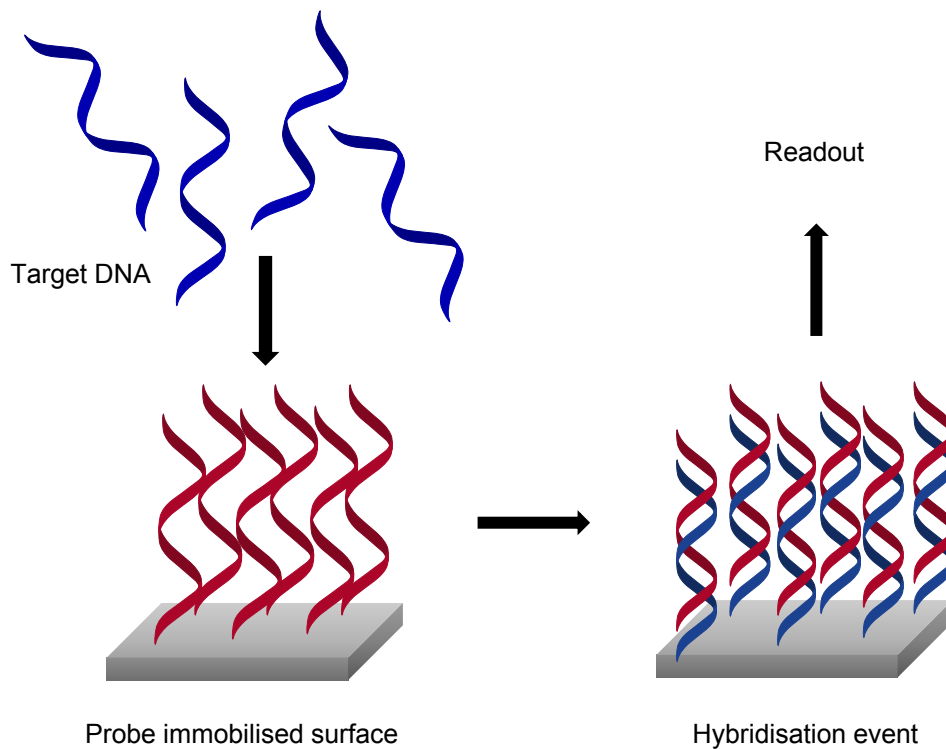
Figure 12. A representation of the hybridisation between surface-immobilised probe DNA and target DNA producing a readout.

Optical recognition of hybridisation events in biosensors are the most frequently employed methods due to the simplicity and sensitivity of the process.[4] Fluorescence based sensors rely upon the emission of fluorescent light upon a change in their energy level when excited by light. However, in order to observe the readout, the complementary target needs to be labelled with expensive fluorophores before coming into contact with the DNA-probe surface, Figure 13.
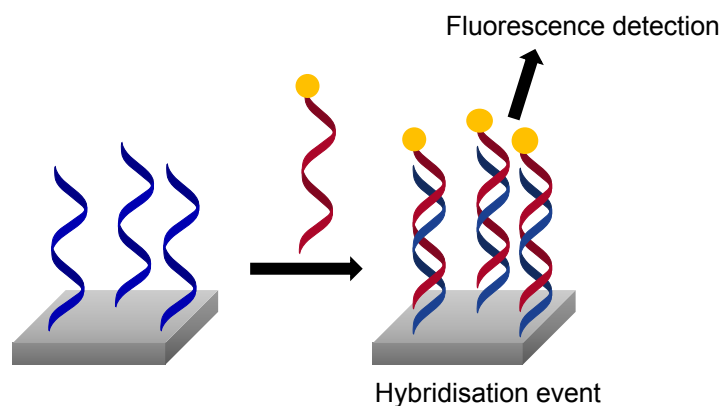
Figure 13. *The fluorescence readout of a labelled target strand hybridising with a surface immobilised probe.*

To avoid using the expensive labelled strands, several groups have turned their attention to using morpholino functionalised probe strands.[114,115] Morpholino is an artificial nucleic acid comprising of morpholine ring, in place of the sugar moiety, phosphorodiamidates, as an alternative to the phosphate backbone, and natural nucleic acid bases. Although morpholino is unnatural DNA, the hybridisation with target DNA strands retain high efficiency and specificity making it an attractive alternative to natural DNA bases. Hu *et al.*[114] utilise morpholino probes for label-free sequence specific detection of target strands. To allow for label-free detection zirconium ions are added, which bind to the DNA backbone and are supplemented with the fluorescent dye Rhodamine B, Figure 14. This combination results in a complex formed from the conjugation of the terminal carboxylic group on Rhodamine B with the zirconium-phosphate coordination. Fluorescence is then observed upon hybridisation with natural DNA bases containing the phosphate group resulting in a specific binding to dsDNA. Although the costly labelled target strands are not required, the morpholino oligomer is expensive therefore the overall cost saving is reduced. An optimised method of DNA detection which does not require either labelled target strands or expensive probe strands would be advantageous.
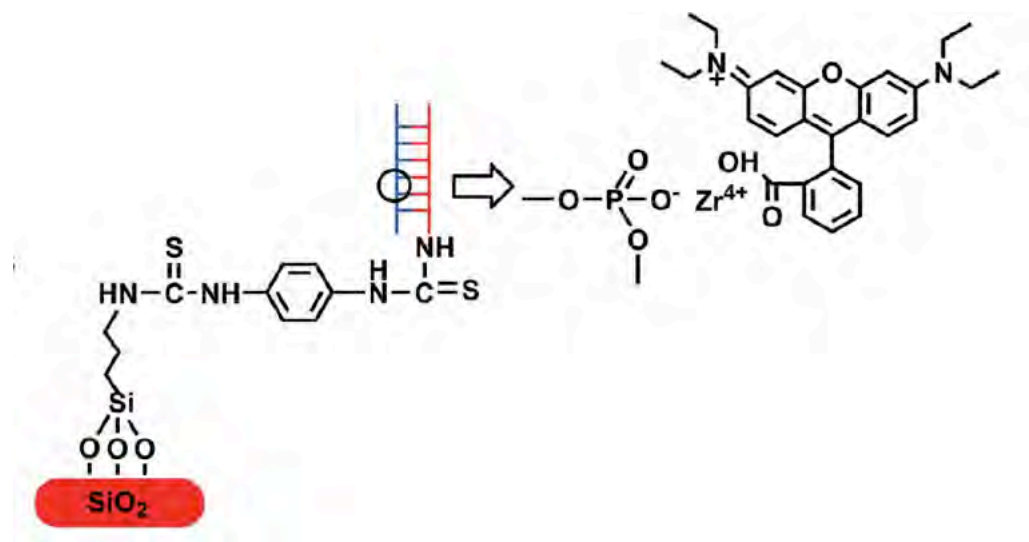
Figure 14. *The surface modification with morpholino probe DNA. Hybridisation with complementary DNA produces a fluorescent readout, amplified by the interaction of the phosphate backbone with Zr^{4+} ions and Rhodamine B.*[114]

DNA arrays are also popular as they are able to screen for multiple diseases on one chip using only one DNA sample.[116] Each DNA probe strand, coding for different diseases, is localised on the surface separate from the other strands. A DNA sample in contact with the patterned surface will hybridise to each probe in which the specific target is present. Voicu *et al.*[117] obtain a patterned silicon surface by the selective photo-oxidation of the silicon through a mask, Figure 15. This creates oxide squares flanked by H-terminated regions which are modified with linker molecules, unreactive at the terminus preventing the immobilisation of DNA probe strands in the next step of the surface modification. Other methods for surface patterning include spotted arrays achieved by the spotting of DNA sequences using a robotic spotter to confine DNA probes to selected areas.[118] Alternatively, in-situ patterning, employed in the Affymetrix array, uses a patterned surface obtained by the photolithography, and the subsequent ink-jet printing of nucleobases in the order of the sequence desired.[119,120] Genechip technology, operated by Illumina,[121] synthesise probe DNA strands on polystyrene beads which are subsequently deposited into pitted glass surfaces.
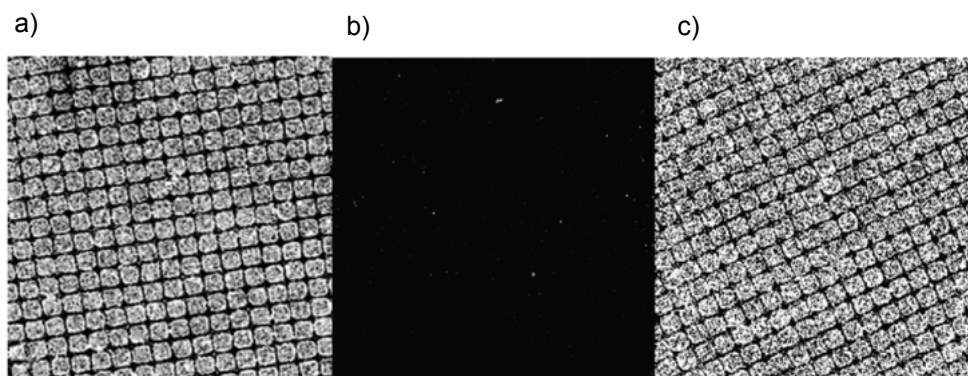
Figure 15. *Fluorescence images of a patterned silicon surface a) of hybridised DNA, b) after dehybridisation and c) following three denature/rehybridise cycles.* [122]

A major limitation of DNA microarrays is the ability to only detect gene sequences present in the particular array design. For this reason, sequencing methods, on a surface, which provide a direct measurement of the nucleobase sequence, base by base, in a DNA strand are employed for determination of target sequences, Figure 16.[123] Each base is labelled with a different fluorescent tag which allows the sequence to be calculated. Sequencing approaches combine surface-immobilised DNA with modified bases for sequence recognition to provide an exact determination of the DNA sequence.
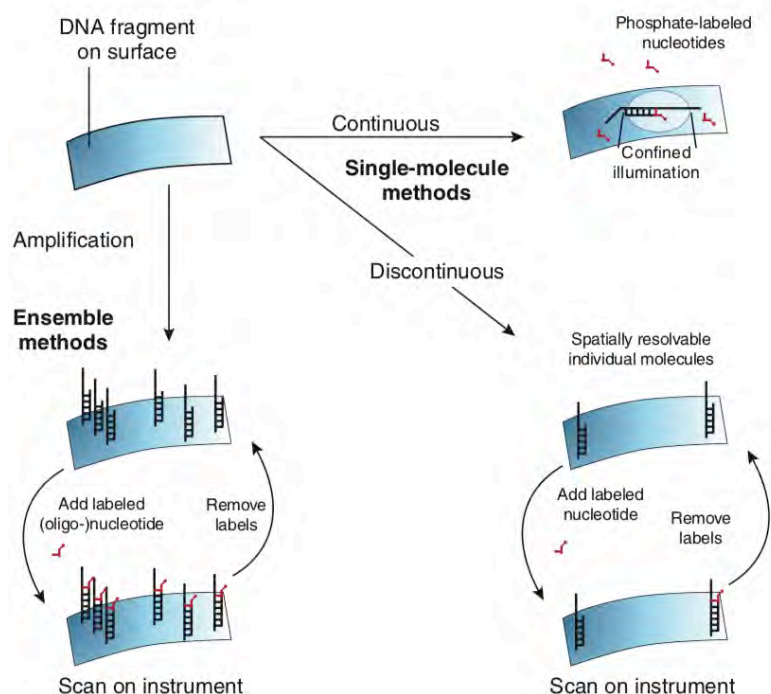
Figure 16. *Methods for sequencing by synthesis utilising a surface for nucleotide immobilisation.*[123]

Although there are a wide range of DNA-based biosensors, a label-free, cost-effective and sensitive method would be advantageous.

Aims of the project

DNA immobilised surfaces are frequently employed for nanomaterial and sensing applications. The modification of DNA bases places new properties onto the DNA, expanding the range of functions possible however, the incorporation is limited by complicated synthetic methods or costly commercially available modified nucleobases. A method for the simple, cost-effective synthesis of modified bases in oligomers would therefore be beneficial.

Chapter 2 will discuss the utilization of the solid silica surface (CPG) in conventional phosphoramidite DNA synthesis as a means to simplify the purification in modified DNA synthesis. The subsequent stability of the modified oligomer is investigated to discern the effect of the modified base on the duplex.

The electrical characterisation of DNA-surfaces is an ongoing area of research for the potential use of DNA in molecular electronic systems. Chapter 3 will involve the synthesis of a DNA monolayer on semi-conductor silicon surfaces and the study into the charge transport mechanism using the large area contact method, the EGaIn technique, for the possible utilisation as a sensing platform.

The immobilisation of DNA on surfaces is most often associated with DNA-based sensing devices. Chapter 4 will explore the growth of short immobilised probe DNA strands from a surface, increasing the number of target binding sites per probe molecule.

References

1   Watson, J. D. & Crick, F. H. C. THE STRUCTURE OF DNA. *Cold Spring Harbor Symposia on Quantitative Biology* **18**, 123-131 (1953).

2   Alemdaroglu, F. E., Alemdaroglu, N. C., Langguth, P. & Herrmann, A. DNA Block Copolymer Micelles – A Combinatorial Tool for Cancer Nanotechnology. *Advanced Materials* **20**, 899-902 (2008).

3   Al-Mahamad, L. L. G., El-Zubir, O., Smith, D. G., Horrocks, B. R. & Houlton, A. A coordination polymer for the site-specific integration of semiconducting sequences into DNA-based materials. *Nature Communications* **8**, 720 (2017).

4   Drummond, T. G., Hill, M. G. & Barton, J. K. Electrochemical DNA sensors. *Nature Biotechnology* **21**, 1192 (2003).

5   Stoltenberg, R. M. & Woolley, A. T. DNA-Templated Nanowire Fabrication. *Biomedical Microdevices* **6**, 105-111 (2004).

6   Watson, S. M. D., Wright, N. G., Horrocks, B. R. & Houlton, A. Preparation, Characterization and Scanned Conductance Microscopy Studies of DNA-Templated One-Dimensional Copper Nanostructures. *Langmuir* **26**, 2068-2075 (2010).

7   Cooper, V. R. *et al.* Stacking Interactions and the Twist of DNA. *Journal of the American Chemical Society* **130**, 1304-1308 (2008).

8   Seeman, N. C. & Kallenbach, N. R. Design of immobile nucleic acid junctions. *Biophysical Journal* **44**, 201-209 (1983).

9   Rothemund, P. W. K. Folding DNA to create nanoscale shapes and patterns. *Nature* **440**, 297 (2006).

10   Liu, W., Zhong, H., Wang, R. & Seeman, N. C. Crystalline Two-Dimensional DNA-Origami Arrays. *Angewandte Chemie* **123**, 278-281 (2011).

11   Wei, B., Dai, M. & Yin, P. Complex shapes self-assembled from single-stranded DNA tiles. *Nature* **485**, 623 (2012).

12   Goodman, R. P., Berry, R. M. & Turberfield, A. J. The single-step synthesis of a DNA tetrahedron. *Chemical Communications*, 1372-1373 (2004).

13   Andersen, E. S. *et al.* Self-assembly of a nanoscale DNA box with a controllable lid. *Nature* **459**, 73 (2009).

14   Seeman, N. C. Nucleic acid junctions and lattices. *Journal of Theoretical Biology* **99**, 237-247 (1982).

15   Holliday, R. A mechanism for gene conversion in fungi. *Genetics Research* **89**, 285-307 (2008).

16   Green, S. J., Bath, J. & Turberfield, A. J. Coordinated Chemomechanical Cycles: A Mechanism for Autonomous Molecular Motion. *Physical Review Letters* **101**, 238101 (2008).

17   Tabor, J. J. & Ellington, A. D. Playing to win at DNA computation. *Nature Biotechnology* **21**, 1013 (2003).

18   Lee, H. *et al.* Molecularly Self-Assembled Nucleic Acid Nanoparticles for Targeted In Vivo siRNA Delivery. *Nature nanotechnology* **7**, 389-393 (2012).

19   Braun, E., Eichen, Y., Sivan, U. & Ben-Yoseph, G. DNA-templated assembly and electrode attachment of a conducting silver wire. *Nature* **391**, 775 (1998).

20   Jan, R., Michael, M., Wolfgang, P., Ingolf, M. & Hans, K. S. Construction of highly conductive nanowires on a DNA template. *Applied Physics Letters* **78**, 536-538 (2001).

21   Monson, C. F. & Woolley, A. T. DNA-Templated Construction of Copper Nanowires. *Nano Letters* **3**, 359-363 (2003).

22   Pasternack, R. F., Goldsmith, J. I., Szép, S. & Gibbs, E. J. A spectroscopic and thermodynamic study of porphyrin/DNA supramolecular assemblies. *Biophysical Journal* **75**, 1024-1031 (1998).

23   Galindo, M. A. *et al.* Pyrrolyl-, 2-(2-thienyl)pyrrolyl- and 2,5-bis(2-thienyl)pyrrolyl-nucleosides: synthesis, molecular and electronic structure, and redox behaviour of C5-thymidine derivatives. *Organic & Biomolecular Chemistry* **9**, 1555-1564 (2011).

24   Haug, R. & Richert, C. A porphycene-DNA hybrid and its DNA-templated interactions with a porphyrin. *Journal of Porphyrins and Phthalocyanines* **16**, 545-555 (2012).

25   Beaucage, S. L. & Caruthers, M. H. Deoxynucleotide phosphoramidites - a NEw Class of Key Intermediates for Deoxypolynucleotide Synthesis. *Tetrahedron Lett.* **22**, 1859-1862 (1981).

26   Gan, R. *et al.* DNA phosphorothioate modifications influence the global transcriptional response and protect DNA from double-stranded breaks. *Scientific Reports* **4**, 6642 (2014).

27   Haraguchi, K. *et al.* Novel Stereoselective Entry to 2'-β-Carbon-Substituted 2'-Deoxy-4'-thionucleosides from 4-Thiofuranoid Glycals. *Organic Letters* **6**, 2645-2648 (2004).

28   Zhao, H., Leonard, P., Guo, X., Yang, H. & Seela, F. Silver-Mediated Base Pairs in DNA Incorporating Purines, 7-Deazapurines, and 8-Aza-7-deazapurines: Impact of Reduced Nucleobase Binding Sites and an Altered Glycosylation Position. *Chemistry – A European Journal* **23**, 5529-5540 (2017).

29   Agrawal, S. & Iyer, R. P. Modified oligonucleotides as therapeutic and diagnostic agents. *Current Opinion in Biotechnology* **6**, 12-19 (1995).

30   Deleavey, Glen F. & Damha, Masad J. Designing Chemically Modified Oligonucleotides for Targeted Gene Silencing. *Chemistry & Biology* **19**, 937-954 (2012).

31   Beilstein, A. E. & W. Grinstaff, M. On-column derivatization of oligodeoxynucleotides with ferrocene. *Chemical Communications*, 509-510 (2000).

32   Takezawa, Y. & Shionoya, M. Metal-Mediated DNA Base Pairing: Alternatives to Hydrogen-Bonded Watson–Crick Base Pairs. *Accounts of Chemical Research* **45**, 2066-2076 (2012).

33   Tanaka, K. *et al.* Efficient Incorporation of a Copper Hydroxypyridone Base Pair in DNA. *Journal of the American Chemical Society* **124**, 12494-12498 (2002).

34   Tanaka, K., Yamada, Y. & Shionoya, M. Formation of Silver(I)-Mediated DNA Duplex and Triplex through an Alternative Base Pair of Pyridine Nucleobases. *Journal of the American Chemical Society* **124**, 8802-8803 (2002).

35   Tanaka, K., Tengeiji, A., Kato, T., Toyama, N. & Shionoya, M. A Discrete Self-Assembled Metal Array in Artificial DNA. *Science* **299**, 1212-1213 (2003).

36   Clever, G. H. & Shionoya, M. in *Interplay between Metal Ions and Nucleic Acids* (eds Astrid Sigel, Helmut Sigel, & Roland K. O. Sigel) 269-294 (Springer Netherlands, 2012).

37   Godde, F., Toulmé, J.-J. & Moreau, S. Benzoquinazoline Derivatives as Substitutes for Thymine in Nucleic Acid Complexes. Use of Fluorescence Emission of Benzo[g]quinazoline-2,4-(1H,3H)-dione in Probing Duplex and Triplex Formation. *Biochemistry* **37**, 13765-13775 (1998).

38   Brotschi, C., Häberli, A. & Leumann, C. J. A Stable DNA Duplex Containing a Non-Hydrogen-Bonding and Non-Shape-Complementary Base Couple: Interstrand Stacking as the Stability Determining Factor. *Angewandte Chemie International Edition* **40**, 3012-3014 (2001).

39   Wilhelmsson, L. M., Holmén, A., Lincoln, P., Nielsen, P. E. & Nordén, B. A Highly Fluorescent DNA Base Analogue that Forms Watson−Crick Base Pairs

with Guanine. *Journal of the American Chemical Society* **123**, 2434-2435 (2001).

40   Zhang, W. & Huang, Z. in *Current Protocols in Nucleic Acid Chemistry*   (John Wiley & Sons, Inc., 2001).

41   Gillet, L. C. J. & Schärer, O. D. Preparation of C8-Amine and Acetylamine Adducts of 2'-Deoxyguanosine Suitably Protected for DNA Synthesis. *Organic Letters* **4**, 4205-4208 (2002).

42   Zheng, Q., Wang, Y. & Lattmann, E. Synthesis of S6-(2,4-dinitrophenyl)-6-thioguanosine phosphoramidite and its incorporation into oligoribonucleotides. *Bioorganic & Medicinal Chemistry Letters* **13**, 3141-3144 (2003).

43   Carey, M. F., Peterson, C. L. & Smale, S. T. The Primer Extension Assay. *Cold Spring Harb. Protoc.* **2013**, 164-173 (2013).

44   Mullis, K. *et al.* Specific Enzymatic Amplification of DNA In Vitro: The Polymerase Chain Reaction. *Cold Spring Harb. Symp. Quant. Biol.* **51**, 263-273 (1986).

45   Petruska, J., Hartenstine, M. J. & Goodman, M. F. Analysis of Strand Slippage in DNA Polymerase Expansions of CAG/CTG Triplet Repeats Associated with Neurodegenerative Disease. *J. Biol. Chem.* **273**, 5204-5210 (1998).

46   Kotlyar, A. *et al.* Synthesis of novel poly(dG)–poly(dG)–poly(dC) triplex structure by Klenow exo(−) fragment of DNA polymerase I. *Nucleic Acids Research* **33**, 6515-6521 (2005).

47   Wells, R. D., Dere, R., Hebert, M. L., Napierala, M. & Son, L. S. Advances in mechanisms of genetic instability related to hereditary neurological diseases. *Nucleic Acids Research* **33**, 3785-3798 (2005).

48   Ali, M. M. *et al.* Rolling circle amplification: a versatile tool for chemical biology, materials science and medicine. *Chemical Society Reviews* **43**, 3324-3341 (2014).

49   Marx, A. & Summerer, D. Molecular Insights into Error-Prone DNA Replication and Error-Free Lesion Bypass. *ChemBioChem* **3**, 405-407 (2002).

50   Kuwahara, M. *et al.* Systematic characterization of 2'-deoxynucleoside- 5'-triphosphate analogs as substrates for DNA polymerases by polymerase chain reaction and kinetic studies on enzymatic production of modified DNA. *Nucleic Acids Research* **34**, 5383-5394 (2006).

51   Kim, T. W., Delaney, J. C., Essigmann, J. M. & Kool, E. T. Probing the active site tightness of DNA polymerase in subangstrom increments. *Proceedings of the National Academy of Sciences of the United States of America* **102**, 15803-15808 (2005).

52   Gierlich, J. *et al.* Synthesis of Highly Modified DNA by a Combination of PCR with Alkyne-Bearing Triphosphates and Click Chemistry. *Chemistry – A European Journal* **13**, 9486-9494 (2007).

53   Nadrian, C. S. Nanomaterials Based on DNA. *Annual Review of Biochemistry* **79**, 65-87 (2010).

54   Wang, J. From DNA biosensors to gene chips. *Nucleic Acids Research* **28**, 3011-3016 (2000).

55   Zhang, X. & Hu, H. DNA molecules site-specific immobilization and their applications. *Central European Journal of Chemistry* **12**, 977-993 (2014).

56   Yan, Z. & Wang, J. Specificity quantification of biomolecular recognition and its implication for drug discovery. *Scientific Reports* **2**, 309 (2012).

57   Nimse, S., Song, K., Sonawane, M., Sayyed, D. & Kim, T. Immobilization Techniques for Microarray: Challenges and Applications. *Sensors* **14**, 22208 (2014).

58   Pei, H., Zuo, X., Zhu, D., Huang, Q. & Fan, C. Functional DNA Nanostructures for Theranostic Applications. *Accounts of Chemical Research* **47**, 550-559 (2014).

59   Li, Y. *et al.* Biomimetic Surfaces for High-Performance Optics. *Advanced Materials* **21**, 4731-4734 (2009).

60   Damborský, P., Švitel, J. & Katrlík, J. Optical biosensors. *Essays in Biochemistry* **60**, 91-100 (2016).

61   Love, J. C., Estroff, L. A., Kriebel, J. K., Nuzzo, R. G. & Whitesides, G. M. Self-Assembled Monolayers of Thiolates on Metals as a Form of Nanotechnology. *Chemical Reviews* **105**, 1103-1170 (2005).

62   Vilan, A. & Cahen, D. Chemical Modification of Semiconductor Surfaces for Molecular Electronics. *Chemical Reviews* **117**, 4624-4666 (2017).

63   Wong, H. S. P. Beyond the conventional transistor. *IBM Journal of Research and Development* **46**, 133-168 (2002).

64   Pouthas, F., Gentil, C., Côte, D. & Bockelmann, U. DNA detection on transistor arrays following mutation-specific enzymatic amplification. *Applied Physics Letters* **84**, 1594-1596 (2004).

65   Bateman, J. E., Eagling, R. D., Worrall, D. R., Horrocks, B. R. & Houlton, A. Alkylation of Porous Silicon by Direct Reaction with Alkenes and Alkynes. *Angewandte Chemie International Edition* **37**, 2683-2685 (1998).

66   Francia, G. D., Ferrara, V. L., Manzo, S. & Chiavarini, S. Towards a label-free optical porous silicon DNA sensor. *Biosensors and Bioelectronics* **21**, 661-665 (2005).

67   Richter, C. A., Hacker, C. A., Richter, L. J. & Vogel, E. M. Molecular devices formed by direct monolayer attachment to silicon. *Solid-State Electronics* **48**, 1747-1752 (2004).

68   Weiss, E. A. *et al.* Si/SiO2-Templated Formation of Ultraflat Metal Surfaces on Glass, Polymer, and Solder Supports: Their Use as Substrates for Self-Assembled Monolayers. *Langmuir* **23**, 9686-9694 (2007).

69   Bain, C. D. & Whitesides, G. M. Molecular-Level Control over Surface Order in Self-Assembled Monolayer Films of Thiols on Gold. *Science* **240**, 62-63, doi:

 (1988).

70   Nuzzo, R. G. & Allara, D. L. Adsorption of bifunctional organic disulfides on gold surfaces. *Journal of the American Chemical Society* **105**, 4481-4483 (1983).

71   Bigioni, T. P. *et al.* Kinetically driven self assembly of highly ordered nanoparticle monolayers. *Nature Materials* **5**, 265 (2006).

72   Pei, H. *et al.* Designed Diblock Oligonucleotide for the Synthesis of Spatially Isolated and Highly Hybridizable Functionalization of DNA–Gold Nanoparticle Nanoconjugates. *Journal of the American Chemical Society* **134**, 11876-11879 (2012).

73   Saha, K., Agasti, S. S., Kim, C., Li, X. & Rotello, V. M. Gold Nanoparticles in Chemical and Biological Sensing. *Chemical Reviews* **112**, 2739-2779 (2012).

74   Mirkin, C. A., Letsinger, R. L., Mucic, R. C. & Storhoff, J. J. A DNA-based method for rationally assembling nanoparticles into macroscopic materials. *Nature* **382**, 607 (1996).

75   Herne, T. M. & Tarlov, M. J. Characterization of DNA Probes Immobilized on Gold Surfaces. *Journal of the American Chemical Society* **119**, 8916-8920 (1997).

76   Peterson, A. W., Heaton, R. J. & Georgiadis, R. M. The effect of surface probe density on DNA hybridization. *Nucleic Acids Research* **29**, 5163-5168 (2001).

77   Rao, A. N. & Grainger, D. W. Biophysical properties of nucleic acids at surfaces relevant to microarray performance. *Biomaterials Science* **2**, 436-471 (2014).

78   Le Berre, V. *et al.* Dendrimeric coating of glass slides for sensitive DNA microarrays analysis. *Nucleic Acids Research* **31**, e88-e88 (2003).

79   Fixe, F., Dufva, M., Telleman, P. & Christensen, C. B. V. Functionalization of poly(methyl methacrylate) (PMMA) as a substrate for DNA microarrays. *Nucleic Acids Research* **32**, e9-e9 (2004).

80   Beier, M. & Hoheisel, J. D. Versatile derivatisation of solid support media for covalent bonding on DNA-microchips. *Nucleic Acids Research* **27**, 1970-1977 (1999).

81   Benters, R., Niemeyer, C. M., Drutschmann, D., Blohm, D. & Wöhrle, D. DNA microarrays with PAMAM dendritic linker systems. *Nucleic Acids Research* **30**, e10-e10 (2002).

82   Korwin-Edson, M. L., Clare, A. G., Hall, M. M. & Goldstein, A. Biospecificity of glass surfaces: streptavidin attachment to silica. *Journal of Non-Crystalline Solids* **349**, 260-266 (2004).

83   Tan, W.-H. & Takeuchi, S. A trap-and-release integrated microfluidic system for dynamic microarray applications. *Proceedings of the National Academy of Sciences* **104**, 1146-1151 (2007).

84   Chrisey, L. A., Lee, G. U. & O'Ferrall, C. E. Covalent Attachment of Synthetic DNA to Self-Assembled Monolayer Films. *Nucleic Acids Research* **24**, 3031-3039 (1996).

85   Lowe, R. D., Pellow, M. A., Stack, T. D. P. & Chidsey, C. E. D. Deposition of Dense Siloxane Monolayers from Water and Trimethoxyorganosilane Vapor. *Langmuir* **27**, 9928-9935 (2011).

86   Henke, L., Piunno, P. A. E., McClure, A. C. & Krull, U. J. Covalent immobilization of single-stranded DNA onto optical fibers using various linkers. *Analytica Chimica Acta* **344**, 201-213 (1997).

87   Shircliff, R. A. *et al.* High-Resolution X-ray Photoelectron Spectroscopy of Mixed Silane Monolayers for DNA Attachment. *ACS Applied Materials & Interfaces* **3**, 3285-3292 (2011).

88   Chandekar, A., Sengupta, S. K. & Whitten, J. E. Thermal stability of thiol and silane monolayers: A comparative study. *Applied Surface Science* **256**, 2742-2749 (2010).

89   Levicky, R., Herne, T. M., Tarlov, M. J. & Satija, S. K. Using Self-Assembly To Control the Structure of DNA Monolayers on Gold: A Neutron Reflectivity Study. *Journal of the American Chemical Society* **120**, 9787-9792 (1998).

90   Devaraj, N. K. *et al.* Chemoselective Covalent Coupling of Oligonucleotide Probes to Self-Assembled Monolayers. *Journal of the American Chemical Society* **127**, 8600-8601 (2005).

91   Pike, A. R. *et al.* DNA On Silicon Devices: On-Chip Synthesis, Hybridization, and Charge Transfer. *Angewandte Chemie International Edition* **41**, 615-617 (2002).

92   Sun, L., Svedhem, S. & Åkerman, B. Construction and Modeling of Concatemeric DNA Multilayers on a Planar Surface as Monitored by QCM-D and SPR. *Langmuir* **30**, 8432-8441 (2014).

93   Wang, C. *et al.* DNA microarray fabricated on poly(acrylic acid) brushes-coated porous silicon by in situ rolling circle amplification. *Analyst* **137**, 4539-4545 (2012).

94   Park, J.-Y. & Park, S.-M. DNA Hybridization Sensors Based on Electrochemical Impedance Spectroscopy as a Detection Tool. *Sensors (Basel, Switzerland)* **9**, 9513-9532 (2009).

95   Rahman, M. M., Li, X.-B., Lopa, N. S., Ahn, S. J. & Lee, J.-J. Electrochemical DNA Hybridization Sensors Based on Conducting Polymers. *Sensors (Basel, Switzerland)* **15**, 3801-3829 (2015).

96   Kim, J. *et al.* Precise and selective sensing of DNA-DNA hybridization by graphene/Si-nanowires diode-type biosensors. *Scientific Reports* **6**, 31984 (2016).

97   Mbindyo, J. K. N. *et al.* DNA-Directed Assembly of Gold Nanowires on Complementary Surfaces. *Advanced Materials* **13**, 249-254 (2001).

98   Chung, S.-W. *et al.* Top-Down Meets Bottom-Up: Dip-Pen Nanolithography and DNA-Directed Assembly of Nanoscale Electrical Circuits. *Small* **1**, 64-69 (2005).

99   Porath, D., Bezryadin, A., de Vries, S. & Dekker, C. Direct measurement of electrical transport through DNA molecules. *Nature* **403**, 635 (2000).

100 Wang, K. DNA-Based Single-Molecule Electronics: From Concept to Function. *Journal of Functional Biomaterials* **9**, 8 (2018).

101 Murphy, C. J. *et al.* Long-range photoinduced electron transfer through a DNA helix. *Science* **262**, 1025-1029 (1993).

102 Cohen, H., Nogues, C., Naaman, R. & Porath, D. Direct measurement of electrical transport through single DNA molecules of complex sequence. *Proceedings of the National Academy of Sciences of the United States of America* **102**, 11589-11593 (2005).

103 Wang, K. *et al.* Structure determined charge transport in single DNA molecule break junctions. *Chemical Science* **5**, 3425-3431 (2014).

104 Jun, Q., Sicheng, L., Song, X., Michael, A. S. & Mitra, D. Direct measurement of electrical transport through single DNA molecules. *Journal of Applied Physics* **106**, 033702 (2009).

105 H. Cohen *et al.* Electrical characterization of self-assembled single- and double-stranded DNA monolayers using conductive AFM. *Faraday Discuss.* **131**, 367-376 (2005).

106 Katsouras, I., Piliego, C., Blom, P. W. M. & de Leeuw, D. M. Transverse charge transport through DNA oligomers in large-area molecular junctions. *Nanoscale* **5**, 9882-9887 (2013).

107 Ji-Min, C. *et al.* An electrostatic micromechanical biosensor for electrical detection of label-free DNA. *Applied Physics Letters* **100**, 163701 (2012).

108 Gooding, J. J. Electrochemical DNA Hybridization Biosensors. *Electroanalysis* **14**, 1149-1156 (2002).

109 Lazerges, M., Perrot, H., Zeghib, N., Antoine, E. & Compere, C. In situ QCM DNA-biosensor probe modification. *Sensors and Actuators B: Chemical* **120**, 329-337 (2006).

110 Ferguson, J. A., Boles, T. C., Adams, C. P. & Walt, D. R. A fiber-optic DNA biosensor microarray for the analysis of gene expression. *Nature Biotechnology* **14**, 1681 (1996).

111 Hahm, J.-i. & Lieber, C. M. Direct Ultrasensitive Electrical Detection of DNA and DNA Sequence Variations Using Nanowire Nanosensors. *Nano Letters* **4**, 51-54 (2004).

112 Cai, H., Cao, X., Jiang, Y., He, P. & Fang, Y. Carbon nanotube-enhanced electrochemical DNA biosensor for DNA hybridization detection. *Analytical and Bioanalytical Chemistry* **375**, 287-293 (2003).

113 Tam, P. D., Hong, H. S. & Hieu, N. V. Novel portable electrical detection system for DNA SENSOR application. *Journal of Experimental Nanoscience* **9**, 652-660 (2014).

114   Hu, W., Hu, Q., Li, L., Kong, J. & Zhang, X. Detection of sequence-specific DNA with a morpholino-functionalized silicon chip. *Analytical Methods* **7**, 2406-2412 (2015).

115   Tercero, N., Wang, K., Gong, P. & Levicky, R. Morpholino Monolayers: Preparation and Label-free DNA Analysis by Surface Hybridization. *Journal of the American Chemical Society* **131**, 4953-4961 (2009).

116   Schena, M., Shalon, D., Davis, R. W. & Brown, P. O. Quantitative Monitoring of Gene Expression Patterns with a Complementary DNA Microarray. *Science* **270**, 467-470 (1995).

117   Voicu, R. *et al.* Formation, Characterization, and Chemistry of Undecanoic Acid-Terminated Silicon Surfaces: Patterning and Immobilization of DNA. *Langmuir* **20**, 11713-11720 (2004).

118   Derisi, J. *et al.* Use of a cDNA microarray to analyse gene expression patterns in human cancer. *Nature Genetics* **14**, 457, doi:10.1038/ng1296-457 (1996).

119   Chee, M. *et al.* Accessing Genetic Information with High-Density DNA Arrays. *Science* **274**, 610-614 (1996).

120   Hacia, J. G., Brody, L. C., Chee, M. S., Fodor, S. P. A. & Collins, F. S. Detection of heterozygous mutations in BRCA1 using high density oligonucleotide arrays and two–colour fluorescence analysis. *Nature Genetics* **14**, 441 (1996).

121   Barbosa-Morais, N. L. *et al.* A re-annotation pipeline for Illumina BeadArrays: improving the interpretation of gene expression data. *Nucleic Acids Research* **38**, e17-e17 (2010).

122   D Conzone, S. & Pantano, C. *Glass slides to DNA microarrays*. Vol. 7 (2004).

123   Fuller, C. W. *et al.* The challenges of sequencing by synthesis. *Nature Biotechnology* **27**, 1013 (2009).

Chapter 2.

Modification of On-Column DNA for Duplex Healing

This chapter is based upon the following article:

Table of Contents

2.1 Introduction

DNA has moved beyond its biological function into the arena of nanotechnology where it has been re-purposed as a building material for the construction of functional nano-architectures.[1] Artificial oligonucleotides incorporating modified nucleosides at predetermined sites are of increasing interest due to their potential applications in conducting nanowires,[2] functional DNA origami structures[3] and drug delivery systems.[4] Of particular interest is the modified purine, 6-thio-2-deoxyguanosine (tG) due to the utilisation in therapeutics[5] and the ability to coordinate metal ions forming coordination polymers.[6,7] tG is a modified guanosine (G) base with the ketone group replaced with a thione functionality, Scheme 1.

2-deoxyguanosine   6-thio-2-deoxyguanosine
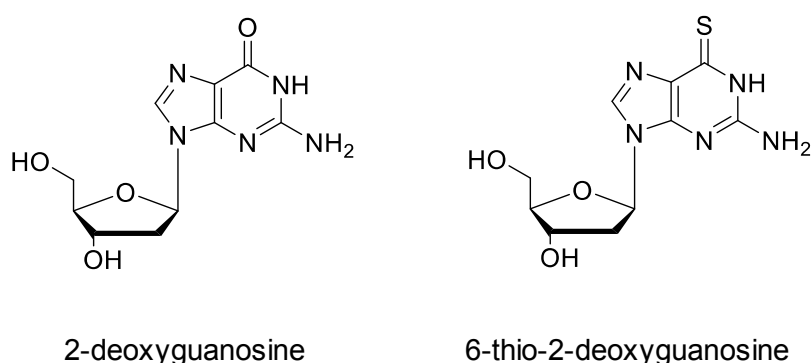
Scheme 1: A schematic representation of 2-deoxyguanosine and 6-thio-2-deoxyguanosine.

Thiol-bearing artificial nucleobases are typically exploited as soft ligands to bind soft transition metals, for example, gold nanoparticles[8] and silver ions.[9] Takezawa *et al.* reported an artificial mercaptopyridone-bearing nucleoside which, when incorporated into oligonucleotides was able to direct the soft transition metal (Pd^{2+} and Pt^{2+}) alignment via metal-mediated base pairing, figure 1.[9] In the therapeutics field, specific tG incorporation is used to destabilise telomere DNA sequences[10] and thus reduce the growth rate of cancerous tumours.[11]
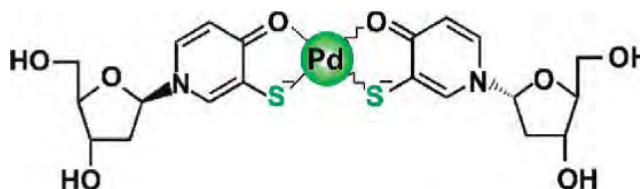

Figure 1: Artificial ligandoside mercaptopyridone forming metal mediated base pairs with Pd^{2+}.

Despite the multitude of uses of tG, the cost of the tG phosphoramidite for synthesis is prohibitively high, likewise premade tG containing oligos. For this reason, an abundance of routes for the synthesis of this modified nucleobase have been explored. Reported syntheses of DNA containing tG include incorporation by chemical[12] or enzymatic[11] approaches. Enzymatic synthesis can prove problematic due to the polymerases limit on structure toleration.[13,14] Incorporation of protected tG bases can be achieved through chemical synthesis,[15-17] however, it is time consuming and can involve complex organic chemistry with low yields. The synthesis of protecting the tG phosphoramidite has been investigated in which the nucleoside must be stable to the reaction conditions in the DNA synthesiser to prevent hydrolysis and oxidation of the thione group.[15]

As the synthesis of the modified phosphoramidite bases can be a lengthy and difficult process, a method to convert G to tG in an oligomer that is still covalently bound to the CPG solid support would be advantageous. This removes the need for complex protecting group chemistry, and purification is performed simply by washing the CPG beads.

Previously reported on-column oligomer modification methods have focussed on employing the Sonogashira reaction at 5-iodouridine sites, inserted into a growing oligomer through phosphoramidite chemistry. In one example alkynyl-ferrocene is coupled to the oligomer to give redox active tagged nucleobases, Figure 2.[18] Other functional groups added to DNA through this method include fluorescent ruthenium tags, alkynyl-derivatised amines and biotin.[19,20] In all instances, a non-canonical DNA base must be inserted during automated oligomer synthesis before further functionalisation can take place.
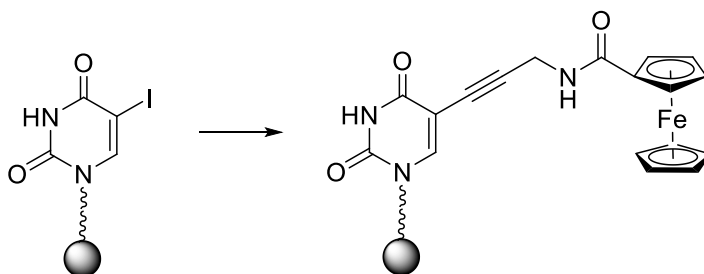

Figure 2. *The on-column modification of iodouridine to the redox tagged 3'5'-dibenzoyl-5-(ferrocenoyl proparglamide) uridine artificial nucleobase.*

Although a redox group is successfully added into the oligomer sequence in the iodouridine example, the bulky ferrocene group remains on the outside of the duplex, therefore the stability of the system is hardly affected as the hydrogen bonding region remains intact and uncompromised. Hence, it would be beneficial to explore the stability of a duplex containing a modified base in the hydrogen bonding region, synthesised via the on-column conversion method.

Other on-column functionalisation approaches have included the conversion of the 5'-OH to a 5'-I through phosphorous chemistry which can then lead to the addition of multiple functional groups such as azides, thioethers and thiols.[21] This is purely a demonstration of the power of further organic modifications that can then become possible by the introduction of a functional moiety at the 5'-site. However, by nature, there is only one 5'-site per oligo and therefore multiply modified oligonucleotides are not feasible. In attempts to associate new material all along a DNA duplex, templating approaches which do not rely on organic synthesis have been an area of focussed research by several groups.[22-24]

DNA, an anionic polymer, is able to act as a template for the electrostatic binding of metal ions resulting in conductive nanowires upon reduction to the metal.[25] This method of metal depositing is convenient and versatile however, there is a lack of control over the growth of the metal so it is therefore not site specific. The metal mainly binds to the negatively charged phosphate backbone and as a result is not involved in the hydrogen bonding. Another method used to metallise DNA in a more specific approach involves the replacement of the hydrogen bond base pairing with metal-mediated base pairs. This can be achieved either by replacing the whole base with specially designed ligand nucleosides which can bind to metal ions or modifying the DNA bases to induce metal coordination. By using metal-base pairs, the structure and the assembly/disassembly process of the DNA is altered whilst also affecting the electron transfer properties of the DNA duplex. Shionoya and coworkers synthesised the artificial oligonucleotide hydroxypyridone, which, when incorporated into a DNA strand was able to form metal-mediated base pairing through Cu^{2+} ions, Figure 3.[26] The Cu^{2+} ions formed magnetic chains through ferromagnetic coupling. The stability of the whole duplex is affected by the inclusion of the artificial base however, as the full base is unnatural, it is therefore not 100 % comparable to the stability of the natural bases.
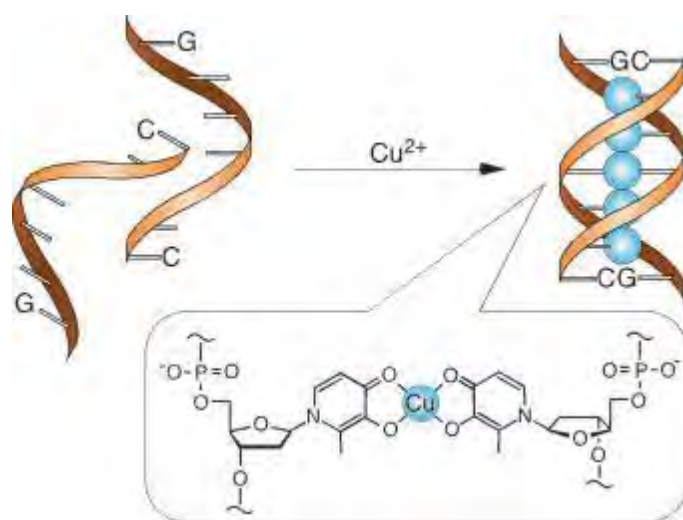
Figure 3: *A schematic representation of the Cu²⁺ metal mediated base pairing between artificial hydroxypyridone bases.*[26]

An alternative approach, would be to assemble modified nucleobases into coordination polymers by using metals as the bridging groups between adjacent nucleobases. In this way, oligomer-like materials can be achieved in a simple one pot reaction. The Zamora group have exploited thiol-bearing nucleobases to create several coordination complexes with various metals highlighting the versatility regarding the incorporation of the thiol modification into DNA bases.[27] The crystal structures obtained from work by Zamora provide insight into the specific metal binding of thiopurine derivatives however, as the structures involve single nucleobase binding, the stability of the thiobases in a duplex strand has not been explored experimentally. More recently, tG nucleoside metal binding has moved from crystal-based studies to investigations of the nucleoside in solution. Al-Mahamad *et al.* discovered the spontaneous formation of a coordination polymer by the addition of gold ions to tG which results in a structural arrangement analogous to DNA.[28] The protocol was transferred to an oligomer bearing a 5' overhang of 4 consecutive tG bases resulting in the formation of long wire-like Au-thiolate-DNA concatemers upon the addition of Au ions. The tG bases in this example are overhangs and not involved in duplex formation therefore the stability of the system is not affected.

Although many methods for the incorporation of thioguanosine into DNA have been explored, site specific incorporation of tG bases into duplexes, in an uncomplicated approach would allow for stability studies to be undertaken and controlled coordination within a duplex. A study into the stability of a tG modified duplex strand would be advantageous to increase understanding of the effects of this modified base on the

duplex structure. Here, the successful conversion of guanosine to thioguanosine on-column is reported with studies into the stability of the resulting modified duplex.

2.2 Results and Discussion

This work in this chapter focusses on the synthesis of the tG monomer within a surface bound oligomer and its subsequent binding of metal ions. Previously in the Pike group an on-column synthetic method for conversion of G to tG was developed.[29] Here, the protocol has been exploited to non-mono basic oligonucleotides and its specificity and versatility in making oligos for locating binding metal sites at predetermined sites via stability, ratio, titrations and metal coordination is explored. The overall process of this chapter is outlined in Scheme 2 depicting the on-column conversion of G to tG, cleavage from the controlled pore glass (CPG) bead, formation of the duplex and subsequent binding of cadmium ions. The oligo sequences used are described in Table 1.

Scheme 2. *Schematic representation of the synthesis of (dA)₆(dtG)₄(dT)₆ and the subsequent binding of metal ions.*

Table 1. *The base sequences of the oligomers synthesised.*

Name	Sequence
oligo-1	5'- TTT TTT GGGG AAA AAA-3'
oligo-2	5'- TTT TTT CCCC AAA AAA-3'
oligo-3	5'- TTT TTT tGtGtGtG AAA AAA-3'

2.2.1 On column synthesis

The oligonucleotides shown in Table 1 were synthesised using a DNA synthesiser following conventional phosphoramidite chemistry. During the synthesis of **oligo-3**, the oligonucleotide remains bound to the CPG solid support during the full reaction before

33

removal upon completion of the synthesis, allowing for easy isolation and purification. The stepwise cyclic phosphoramidite protocol, described in Chapter 1, was then repeated to afford a 16-mer (d-T)$_6$(d-G)$_4$(d-A)$_6$. The protected oligonucleotide was then removed from the synthesiser and subjected to a thiolation reaction following the Jones procedure as shown in Scheme 3.[30]
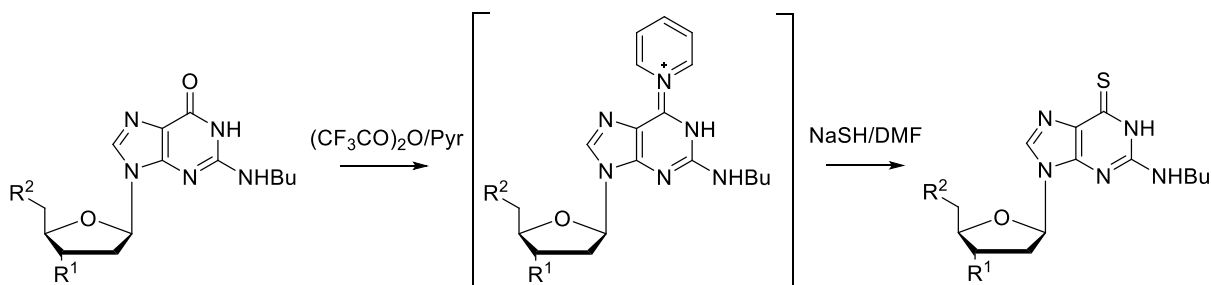
Scheme 3. *Scheme showing the synthetic route to d-tG following the Jones procedure.*

The CPG bead was added to trifluoroacetic anhydride in anhydrous DMF to afford a pyridinium intermediate. Upon addition of sodium sulphide, the intermediate was then converted to the desired thiol. The synthesis has been carried out using both sodium sulphide and sodium hydrasulfide in which both reactions occurred successfully regardless of the sulfur derivative. After 24 hours, the beads were washed several times with water and ethanol and dried under vacuum. Previously in practice, concentrated aqueous ammonia is used to cleave and deprotect the oligomer from the CPG bead, however, here we used anhydrous gaseous methylamine.[31] The cleaved oligomer was then dissolved in water for analysis. Reverse-phase high performance liquid chromatography (HPLC) is routinely used to purify short DNA oligomers based on the difference in hydrophobicity between strands causing the oligomers to elute at different times. The DNA products were analysed on a C18 HPLC reverse phase column. The mobile phase was buffer A: 5 % acetonitrile in 0.1 M triethylammonium acetate (TEAA) at pH 6.5 and buffer B: 65 % acetonitrile in 0.1 M triethylammonium acetate (TEAA) at pH 6.5 (0-25 % over 25 mins).
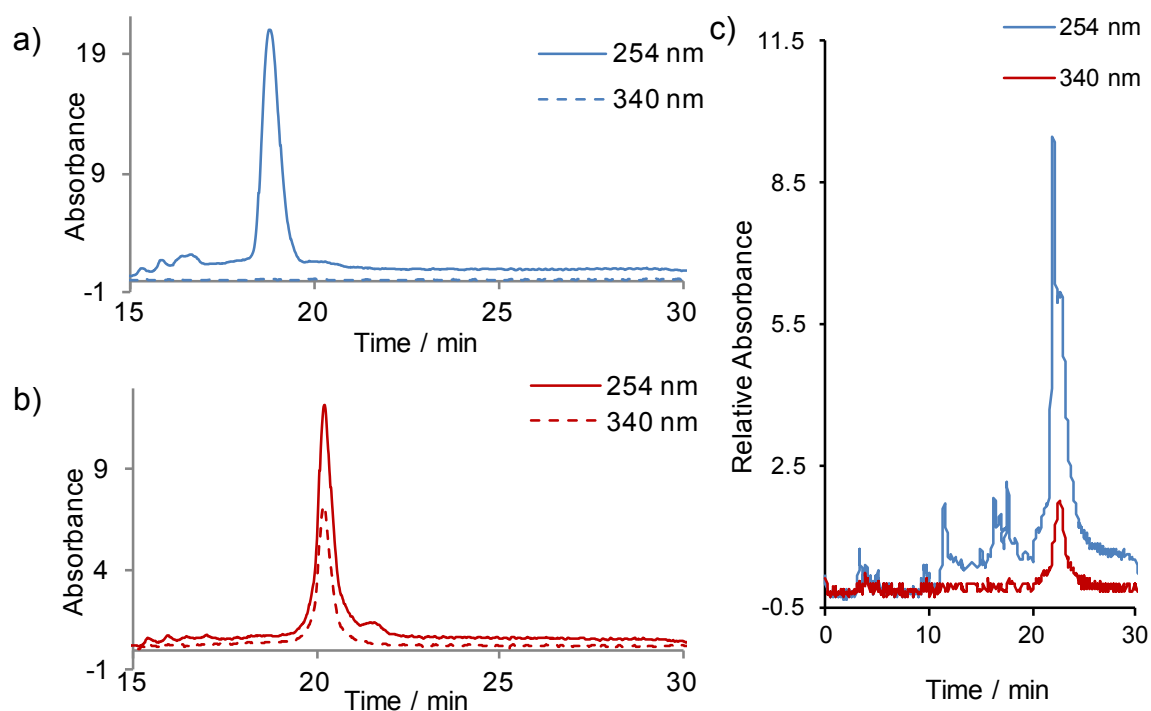
Figure 4. Reverse phase HPLC chromatogram of a) **oligo-1** *and b)* **oligo-3**. *c) coinjection of* **oligo-1** *and* **oligo-3**.

The spectra were monitored at 2 wavelengths: 260 nm and 340 nm. Figure 4 highlights the difference in HPLC spectra between **oligo-1**(a) and **oligo-3** (b). **Oligo-3** exhibits a longer retention time of 20.22 min compared 18.72 min for **oligo-1**, and absorbs in the 340 nm region attributed to the thiol group of the oligonucleotide.[32] A co-injection of both **oligo-1** and **oligo-3** confirms the conversion as two peaks are observed indicating the presence of two different oligomers.

2.2.2 Characterisation: UV, IR and DNA digestion

Ultraviolet-visible spectroscopy (UV-Vis) is a useful instrument for determining the presence of certain functional groups due to the difference in absorption band. An additional peak at 340 nm is present in the UV spectrum for **oligo-3,** compared to that for **oligo-1**, which is attributed to the C=S group of the tG base, Figure 5a. The appearance of the peak at 1200 cm^{-1} in the infrared (IR) spectra is also used to confirm the presence of the thiol group, Figure 5b.
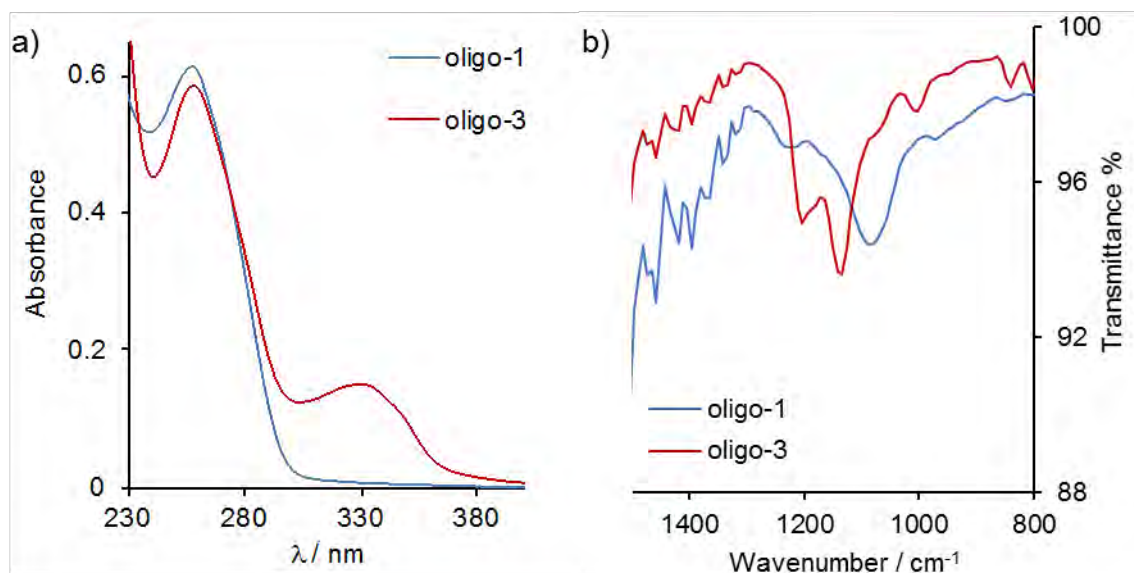
Figure 5. *a) UV-Vis spectrum highlighting the different in absorption bands between **oligo-1** and **oligo-3**. b) The IR spectra displaying the additional 1200 cm^{-1} peak associated with the thiol group.*

In order to fully confirm the successful specific conversion of the guanosine base, DNA digestions were performed in which the DNA strand is broken into the individual oligonucleotides which make up the oligo. The DNA was incubated at 37 °C with snake venom phosphodiesterase and bacterial alkaline phosphatase which breaks the phosphodiester bond between the bases and removes the phosphate group. Analysis of the digested products was carried out by HPLC and compared to dN standards displayed in Figure 6. HPLC chromatograms confirm the selectivity of the synthesis as there is no peak representing the **G** base present in **oligo-3** and there is the appearance of a peak corresponding to the **tG** which is also absorbing at 340 nm. The selectivity of the reaction is confirmed as the retention time of the peaks corresponding to the A and T bases remain unchanged and hence indicate the bases are untouched by the reaction conditions.
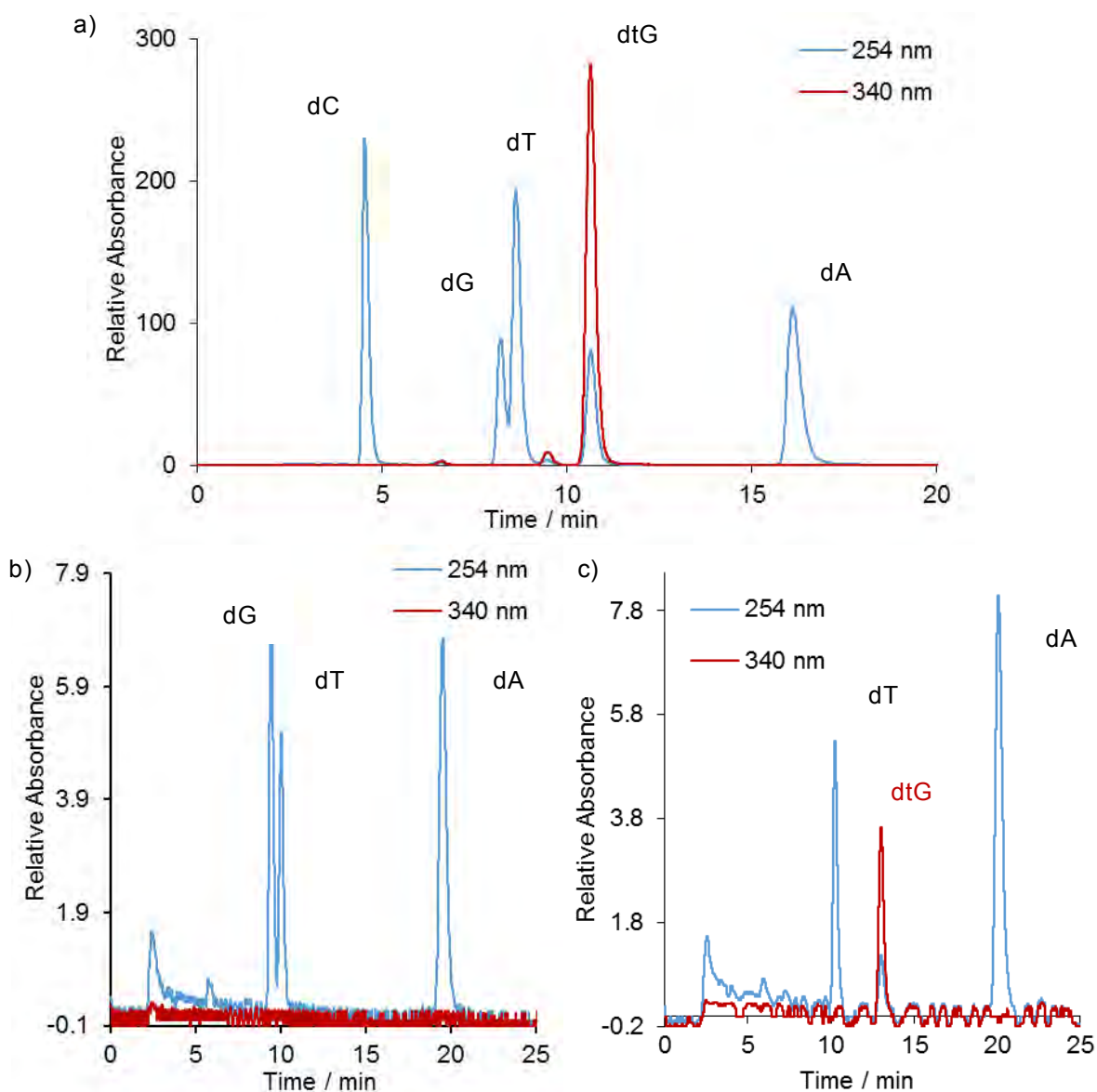
Figure 6. *HPLC traces for the digestion products from a) standard deoxynucleotides for dA, dG, dC, dT and dtG b)* ***duplex-1*** *and c)* ***duplex-3***.

### 2.2.3 Confirmation A, T and C do not convert

For further confirmation of the selectivity of the reaction for guanosine, the thiolation reaction was attempted on penta-adenine, penta-cytosine and penta-thymine oligomers whilst bound to the CPG. The cleaved products were characterised by UV-Vis, IR, matrix assisted laser desorption ionisation-time of flight mass spectrometry (MALDI-TOF), HPLC co-injections and DNA digestions, Figure 7-10. There was no change in spectroscopic data for any of the oligomers either before or after the thiolation reaction, affirming the selectivity of the reaction for guanosine over the other 3 native nucleobases.
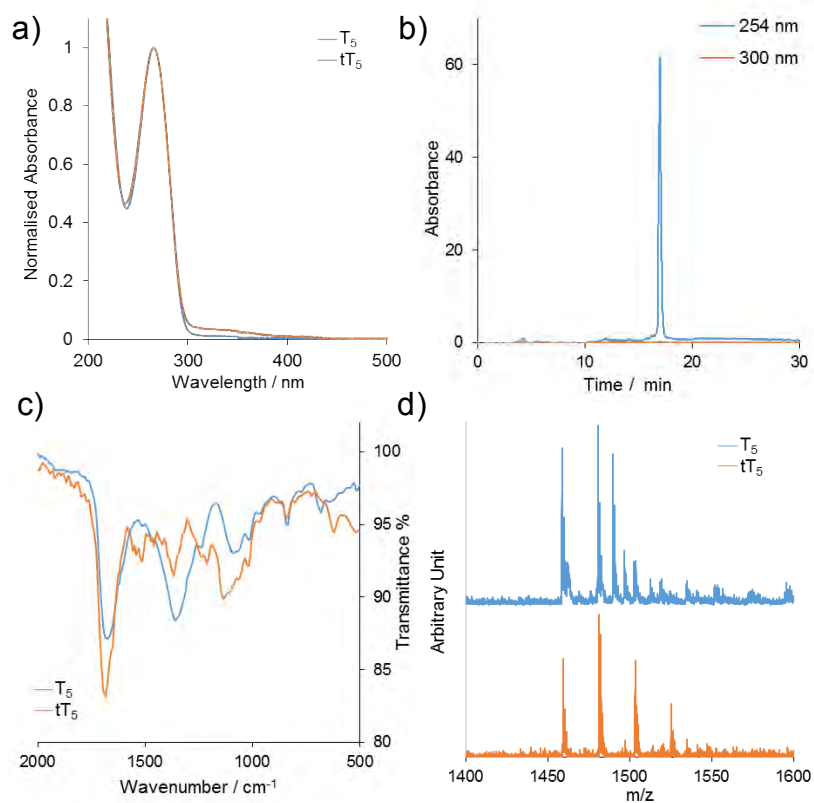
Figure 7. a) UV-Vis comparison between T_5 and tT_5. b) HPLC chromatogram of co-injection of T_5 and tT_5. c) IR spectra comparing A_5 and tA_5. d) Comparison of tT_5 MALDI-TOF: m/z (positive mode) 1459.57 (theoretical value for $C_{50}H_{62}N_{10}O_{33}P_4S_5$ (M+) 1614.80).
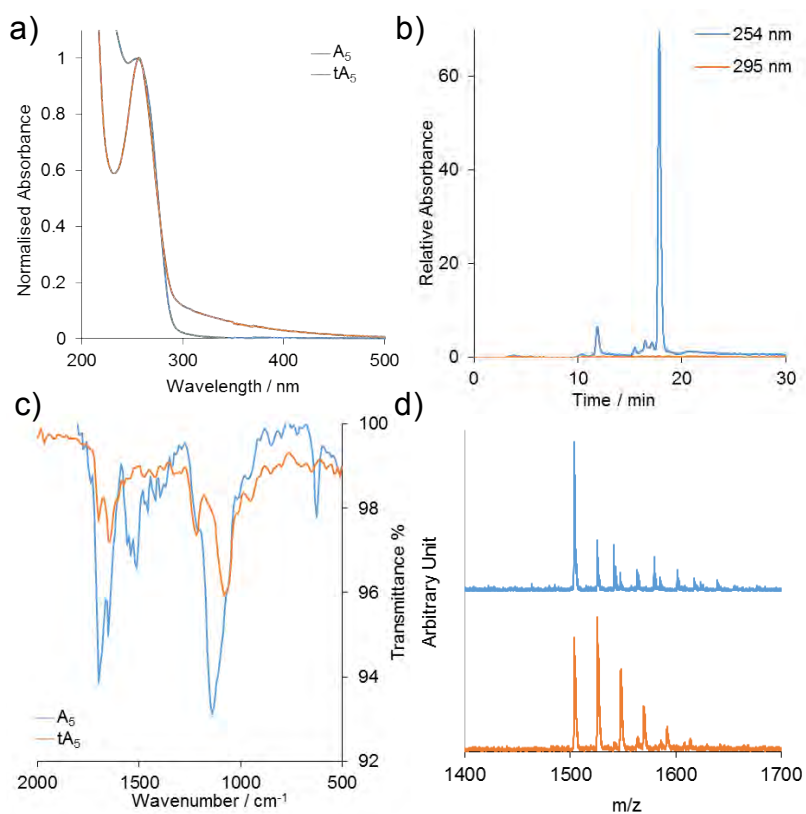
Figure 8. *a) UV-Vis comparison between A_5 and tA_5. b) HPLC chromatogram of co-injection of A_5 and tA_5.ci) IR spectra comparing A_5 and tA_5. d) Comparison of tA_5 MALDI-TOF: m/z (positive mode) 1503.93 (theoretical value for $C_{50}H_{57}N_{25}O_{23}P_4S_5$ (M+) 1659.75).*
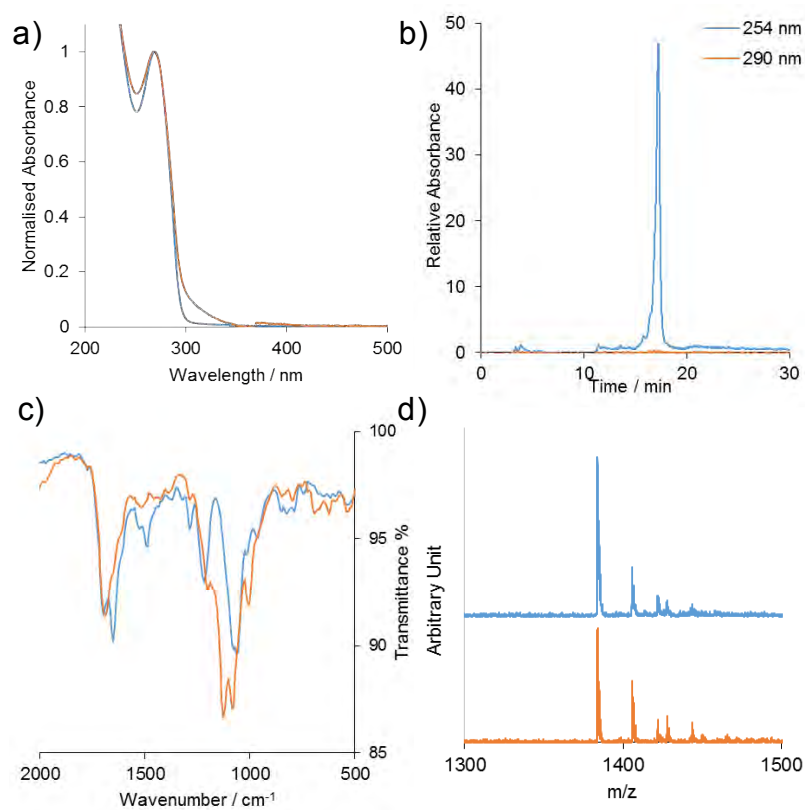
Figure 9. *a) UV-Vis comparison between C_5 and tC_5. b) HPLC chromatogram of co-injection of C_5 and tC_5. c) IR spectra comparing C_5 and tA_5. d) Comparison of tC_5 MALDI-TOF: m/z (positive mode) 1383.84 (theoretical value for $C_{45}H_{57}N_{15}O_{28}P_4S_5$ (M+) 1464.20)*
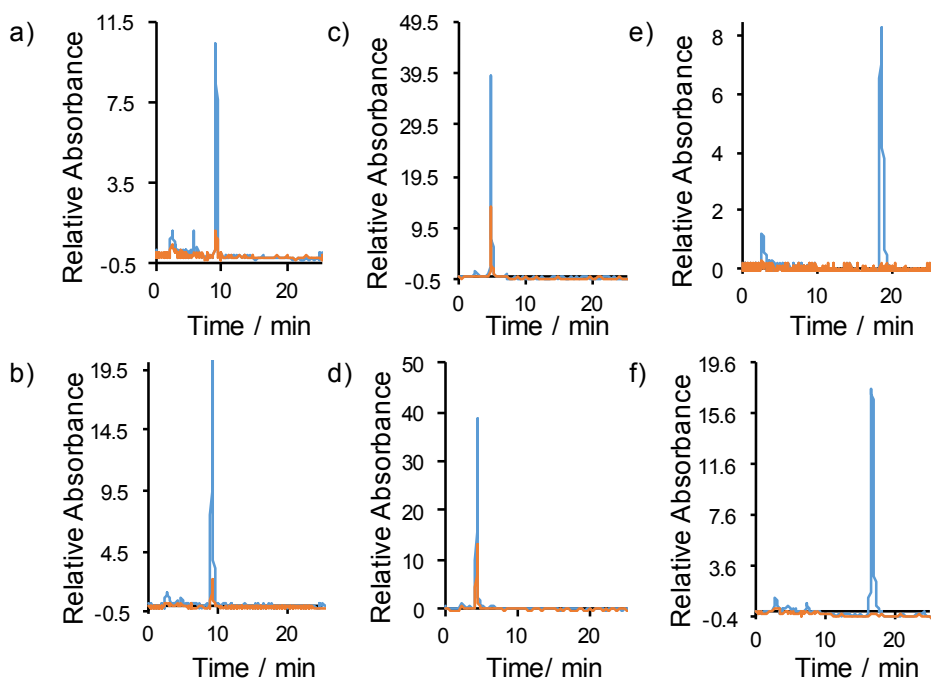
**Figure 10.** *HPLC traces of the digestion products for a) T b) tT c) C d) tC e) A f) tA*

2.2.4 UV titration of duplex-3 with Cd^{2+}

With a view to study the effect of the replacement of G with tG on the stability of the duplex, several duplexes were formed, see Table 2. The G bearing **oligo-1** forms a fully complementary duplex with **oligo-2**, **duplex-1**, and a G:G mismatched **duplex-2** is formed from the self-annealing of **oligo-1**. Similarly, **oligo-3** can self-hybridize to form **duplex-3** forming a mismatched tG central portion held together by the terminal A_6:T_6 sections. **Duplex-4** is formed via the hybridisation of **oligo-2** and **oligo-3.**

Table 2. The base sequences of the duplexes formed.

Name	Sequence
duplex-1	5'-TTT TTT GGGG AAA AAA-3' 3'- AAA AAA CCCC TTT TTT-5'
duplex-2	5'-TTT TTT GGGG AAA AAA-3' 3'-AAA AAA GGGG TTT TTT-5'
duplex-3	5'-TTT TTT tGtGtGtG AAA AAA<3' 3'-AAA AAA tGtGtGtG TTT TTT<5'
duplex-4	5'-TTT TTT tGtGtGtG AAA AAA-3' 3'-AAA AAA C C C C TTT TTT-5'

It is known that the thiol group has a binding affinity for Cd^{2+} [7] therefore it is expected that the **duplex-3** will direct metal assembly towards the central tG region, comparable to the metal-mediated base pairs employed by Shionoya.[26] In order to establish if this is the case, metal ions were added to **duplex-3** and monitored by UV-Vis absorbance. Upon addition of increasing concentrations of Cd^{2+} to a fixed concentration of **duplex-3**, the absorbance at 341 nm for **duplex-3** exhibits a blue shift down to 319 nm and a decrease in absorbance, Figure 11. The change in absorbance is associated with the deprotonation of the N(1) group and the switch from the thione to the metal coordinating thiol group,[32] Scheme 3.
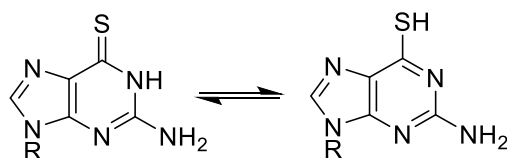

*Scheme 3. Scheme highlighting the structural change from the thione form of **tG** to the thiol.*
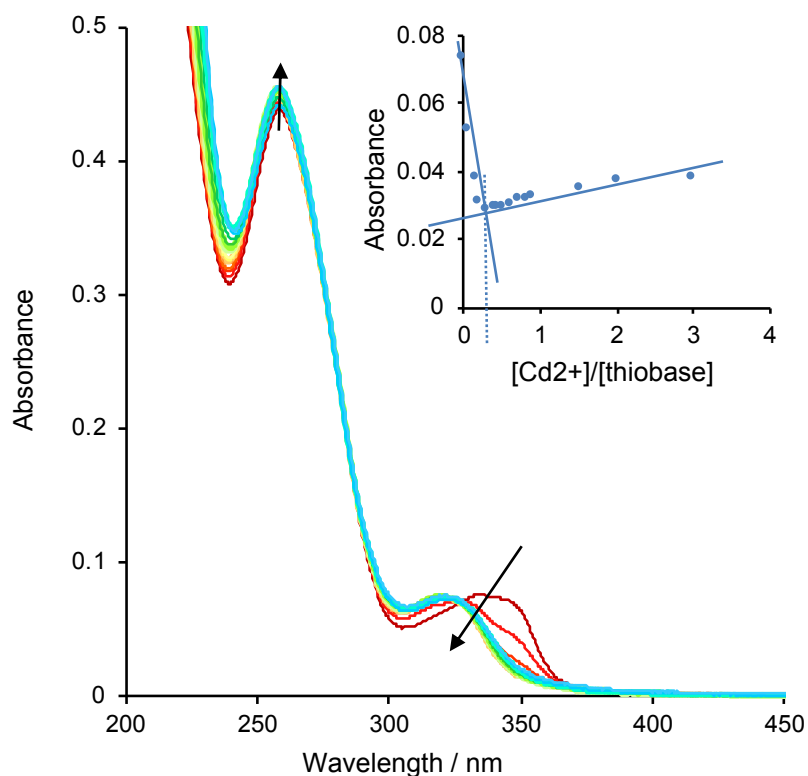
Figure 11. *UV-Vis absorption titration spectrum of duplex-3 with Cd²⁺. Inset: Binding curve of the complex formed between duplex-3 and Cd²⁺.*

The isosbestic points in the DNA titration plot at 257 nm and 325 nm confirm that there are two species in solution, free DNA and DNA bound to the metal ions. The plot of the absorbance at 341 nm against the ratio of Cd^{2+} to thiobase, Figure 11 inset, displays a binding ratio of 1:4 metal:thiobase representing two metal ions to 8 thiobases in **duplex-3**. The 1:4 metal:thiobase ratio was further confirmed by a Job plot where upon increasing concentrations of cadmium in a fixed volume of solution, the 341 nm peak again exhibits a blue shift to 319 nm and a decrease in absorbance, Figure 12. A plot of mole fraction times by the absorbance against the mole fraction of thiobase, gives a mole fraction of 0.8 corresponding to 1:4 metal:thiobase ratio in agreement with the fixed concentration titration.
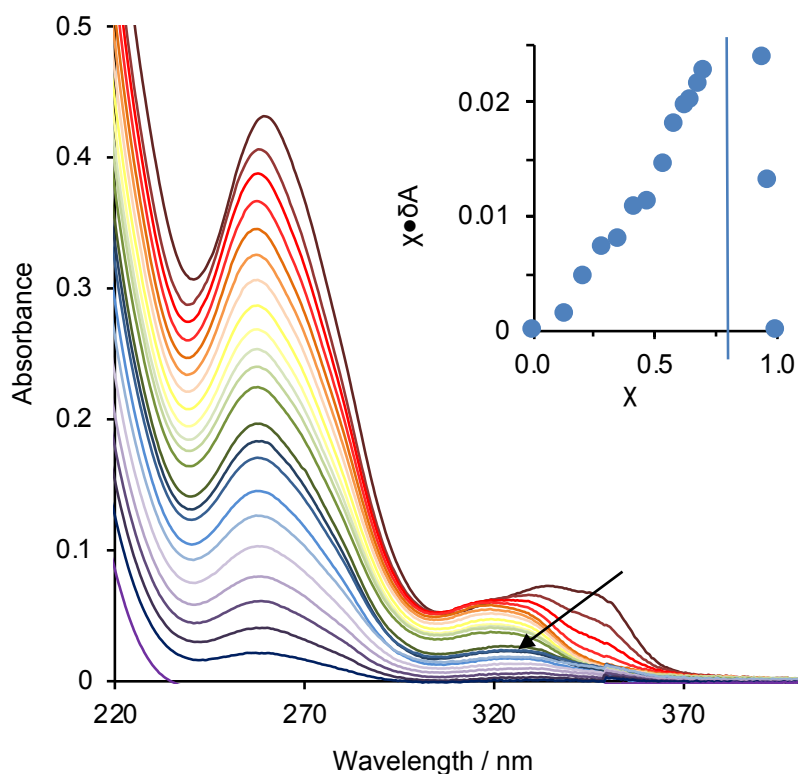
Figure 12. *UV-Vis plot showing the change in absorbance of duplex-3 with increasing concentrations of Cd2+ (from red to purple). Inset: Job plot of the mole fraction (X) of duplex-3 multiplied by the absorbance at 341 nm against the mole fraction.*

2.2.5 Comparison of tG and mercaptopurine metal binding

Although we presume the Cd^{2+} ions bind through the S(6) and N(7) positions, the binding of Cd^{2+} has not been documented. On the other hand, the binding to mercaptopurine has been previously investigated by Zamora's group.[24,27,33] Low temperature NMR studies carried out at 218 K were used to compare the binding of mercaptopurine and tG with Cd^{2+} ions. In both NMR spectra the bases exhibit the same shift of the N1 proton attributed to the binding of the metal at these positions, see Figure 13. This observation implies that the cadmium is also binding through the N7 on the tG as well as the S(6) as confirmed by the earlier UV titrations.
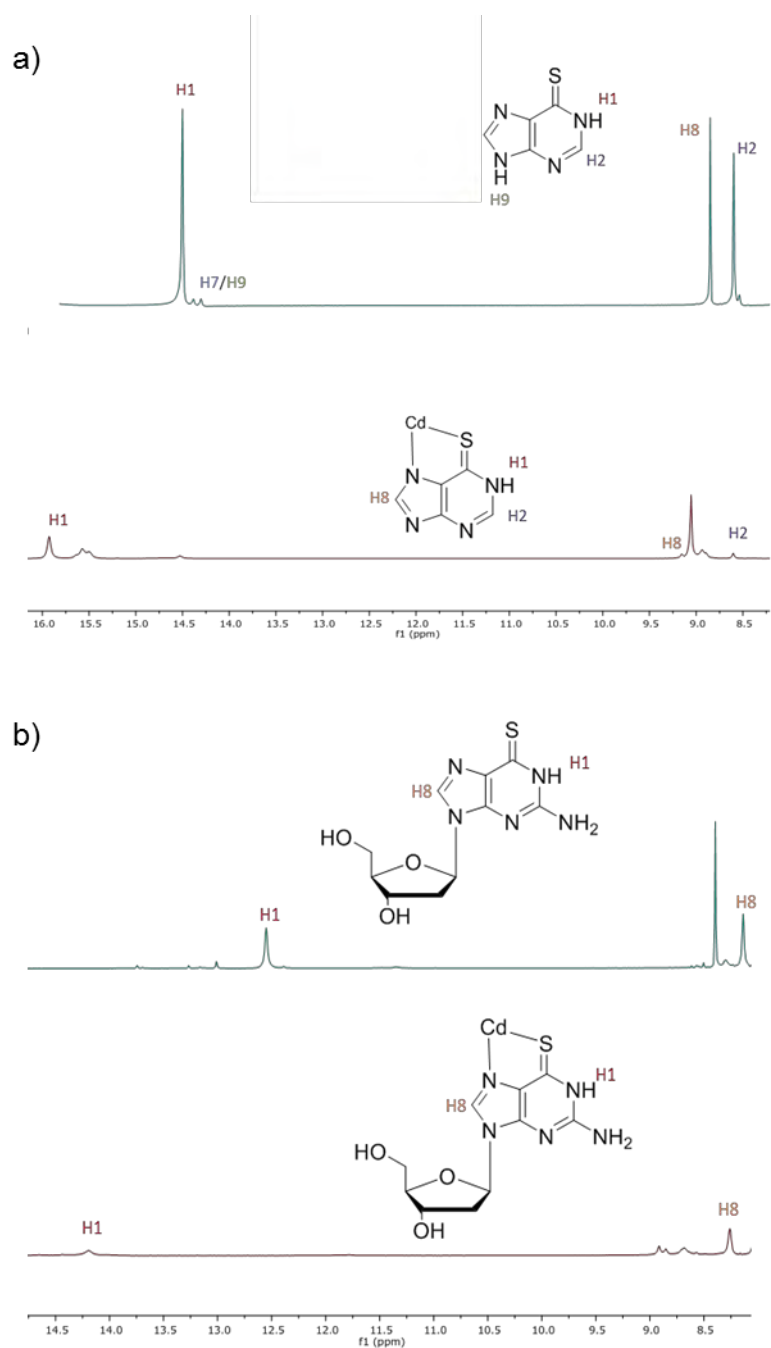
Figure 13. *NMR comparison at 218 K in DMF-d7 of a) mercaptopurine and b) thioguanosine in the absence and presence of Cd^{2+}.*

A search of the CCDC for sulphur and nitrogen containing ligands coordinated to cadmium ions is displayed in Table 3. The most common structure reported is with 4 sulphur ligands and 2 nitrogen ligands which indicates that the 1:4 cadmium:thiobase ratio is plausible.

Table 3. *Table representing the number of structures acquired from the CSD search of cadmium complexes bearing ligands with nitrogen and sulphur atoms.*

Number of structures		Nitrogen donors							
		1	2	3	4	5	6	7	8
Sulfur Donors	1	0	0	0	6	12	3	0	0
	2	0	37	10	60	0	0	0	
	3	4	16	4	0	0	0		
	4	28	80	0	0	0			
	5	1	0	0	0				
	6	0	0	0					
	7	0	0						
	8	0							

2.2.6 Melting temperatures

In order to assess the stability of the thiolated oligomers the melting temperatures, Tm, were calculated using variable temperature UV-Vis. **Duplex-3** is compared to the fully complementary **duplex-1** and **duplex-2** with the G:G mismatched central section. **Duplex-1** displays the expected 'S-shaped' sigmoidal denaturation curve with a Tm of 32.2 °C whereas **duplex-2** displays a slightly distorted shape with a Tm of 28.1 °C however still resembles a denaturation curve, Figure 14. Due to the now bulky mismatched region, it is expected that the duplex has unwound slightly however G:G mismatch hydrogen bonds are possible. However, in **duplex-3** with the central tG mismatch, the curve does not resemble a denaturation curve and is more like a steady increase in absorbance. This observation is attributed to the unwinding of the duplex in the bulky tG central region which will only be held together by the hydrogen bonding in the terminal A_6:T_6 regions rather than any hydrogen bonding present in the central tGtG region. It is proposed that the tG bases are pushed outward from the duplex. An estimation of the Tm is 22.5 °C which is a 10 °C decrease in stabilisation compared to **duplex-1,** analogous to the previously reported value by Somerville *et al.*[34]
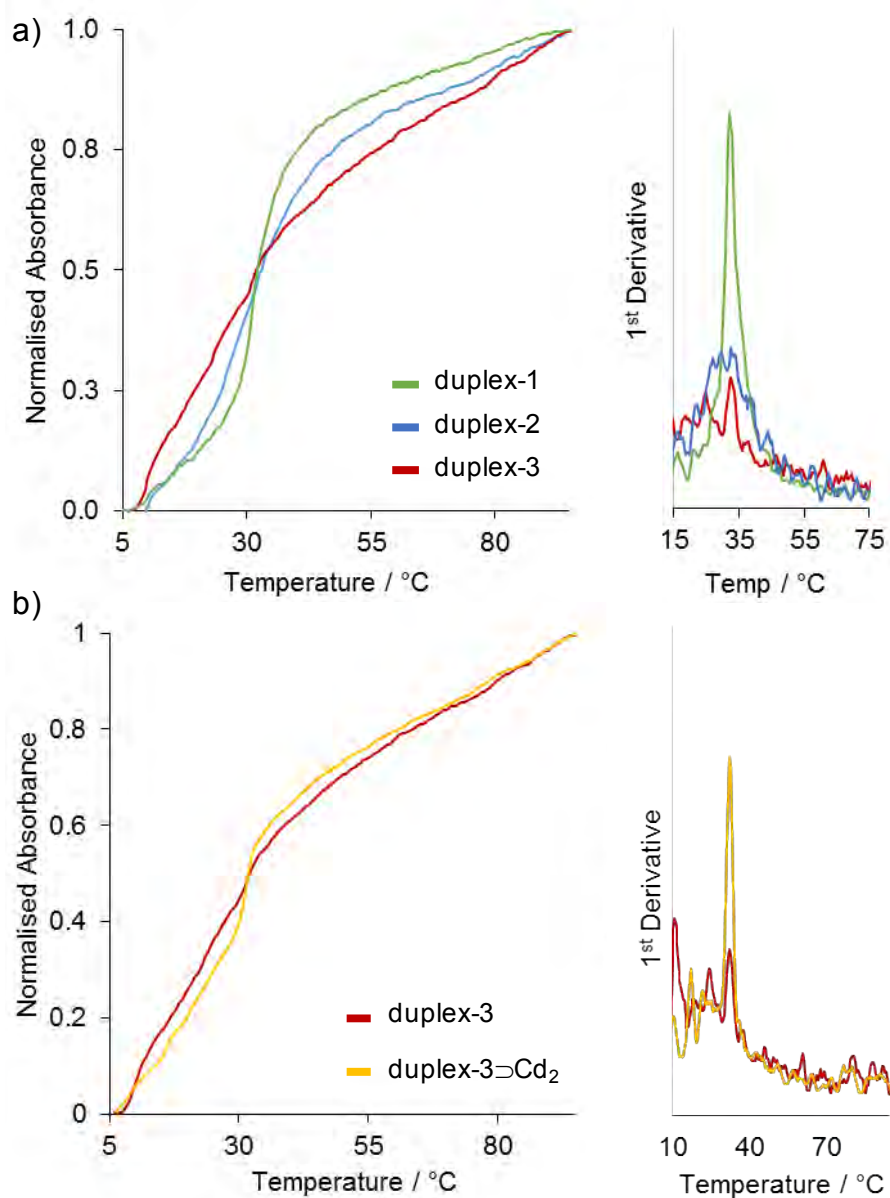
Figure 14. *Melting temperature profiles and the Tm calculated from the first derivative for a)* ***duplex-1***, ***duplex-2*** *and* ***duplex-3***. *b)* ***duplex-3⊃Cd₂***.

However, when cadmium ions are added to **duplex-3**, **duplex-3⊃Cd₂**, a more expected denaturation curve is observed with a sharp increase in hyperchromicity corresponding to a Tm of 30.0 °C which is c.a 7.5 °C stabilisation compared to **duplex-3**. This observation indicates that the metal ions bring the tG bases back into the duplex formation healing the strand and resulting in an increased Tm.

2.2.7 Investigation into hairpin formation

It is conceivable that **oligo-3** could form a hairpin structure rather than the desired **duplex-3**, which would also account for the 1:4 metal binding ratio obtained from the metal titrations. In order to dispel this theory, the Tm values at a ten-fold difference in concentration for **duplex-3⊃Cd₂** were obtained. If a hairpin was formed, no change in Tm would be expected as the Tm for hairpin structures is independent of concentration. On the other hand, duplexes exhibit a change in Tm upon varying concentrations. The Tm for **duplex-3** and **duplex-3⊃Cd₂** at a concentration of 5.5 μM and 0.55 μM are displayed in Figure 15. In both the case of the hairpin and duplex conformations, the thermodynamics rely upon the AT complementary section; 12 bases for the duplex and 6 bases for the hairpin. For hairpin formation, the predicted Tm for the AT section is 12 °C whereas for duplex formation the predicted Tm is 24 °C. As both systems are relatively unstable, the Tm data relies upon the observation of small changes in the overall system stability. There is a concentration dependent difference in the absence of Cd^{2+} ions, although an exact Tm value is unobtainable due to the instability of the system. By comparing the low concentration melting temperature profiles from both situations, there is an indication that the cadmium dissociation constant is probably greater than 1 μM therefore is only weakly associated at the low concentration. The difference in Tm of **duplex-3⊃Cd₂** is marked indicating that the duplex is stabilised by the cadmium and the 7.5 °C increased stability is most likely due to the stabilisation of a duplex than from the more unstable hairpin.
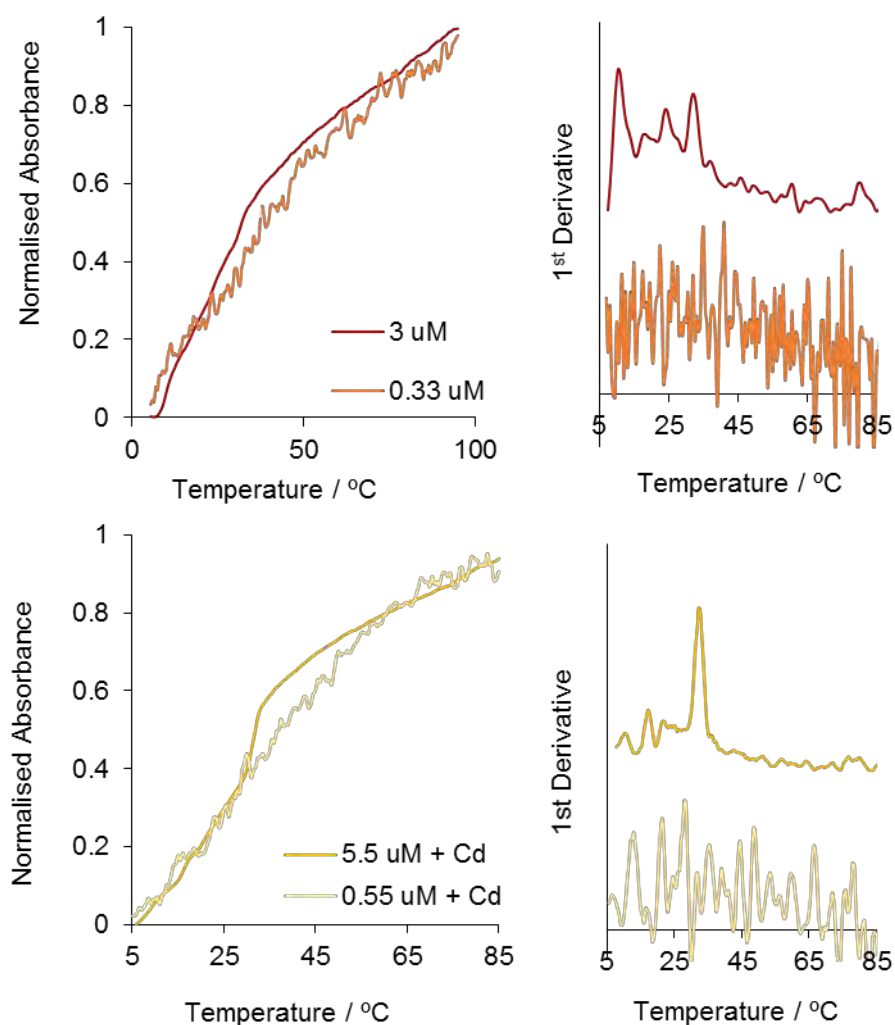
Figure 15. *Comparison of **duplex-3** in the absence and presence of cadmium ions at two different concentrations.*

Duplex-3⊃Cd₂ was also compared to a control duplex, **duplex-4**, to further confirm the formation of a duplex rather than a hairpin. **Duplex-4** was created from annealing **oligo-2** and **oligo-3** which results in tG bases paired against C bases in the central section, Scheme 4. If hairpin formation was the predominant structure, a binding titration of **duplex-4** with cadmium ions would also be expected to give a ratio of 1:4, however a binding ratio of 1:2 Cd:thiobase is obtained, Figure 16. This observation indicates the duplex is forming and the Cd^{2+} are bound only to the tG bases.
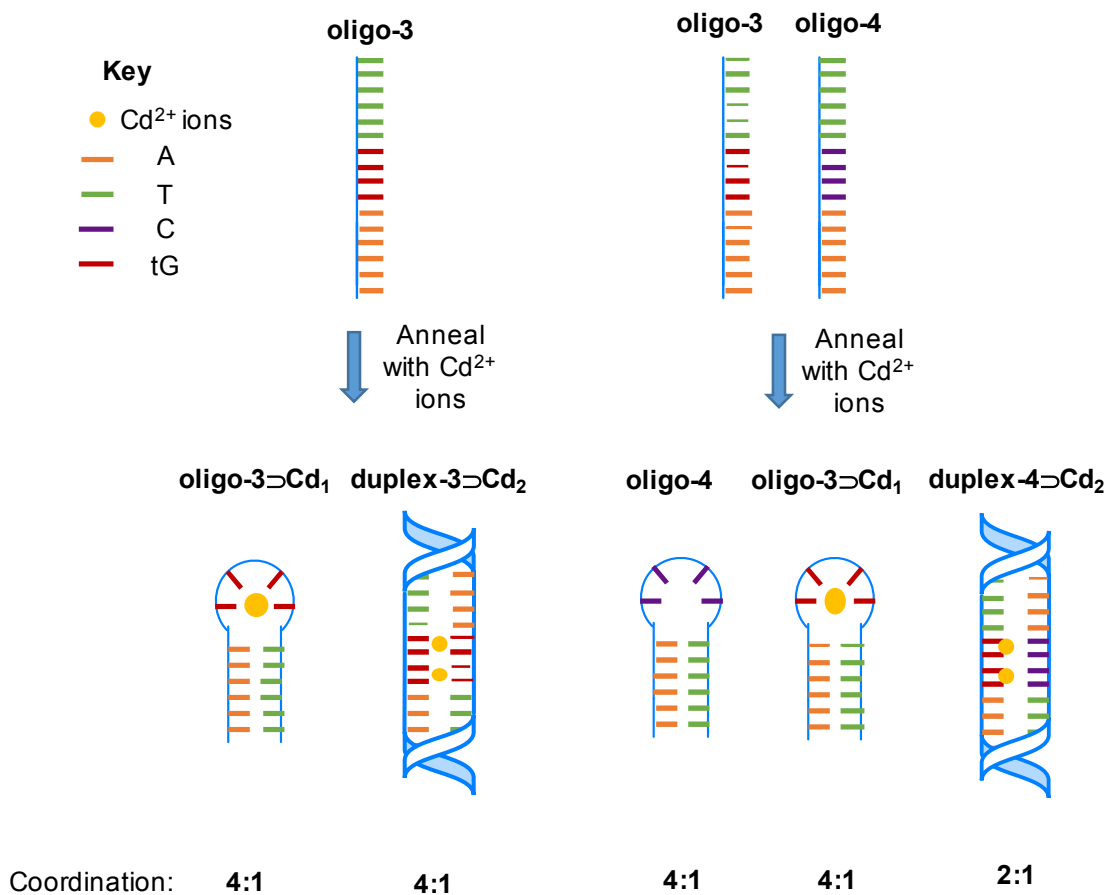
Scheme 4. Illustration of the potential metal coordination complexes with **duplex-3** and **duplex-4**
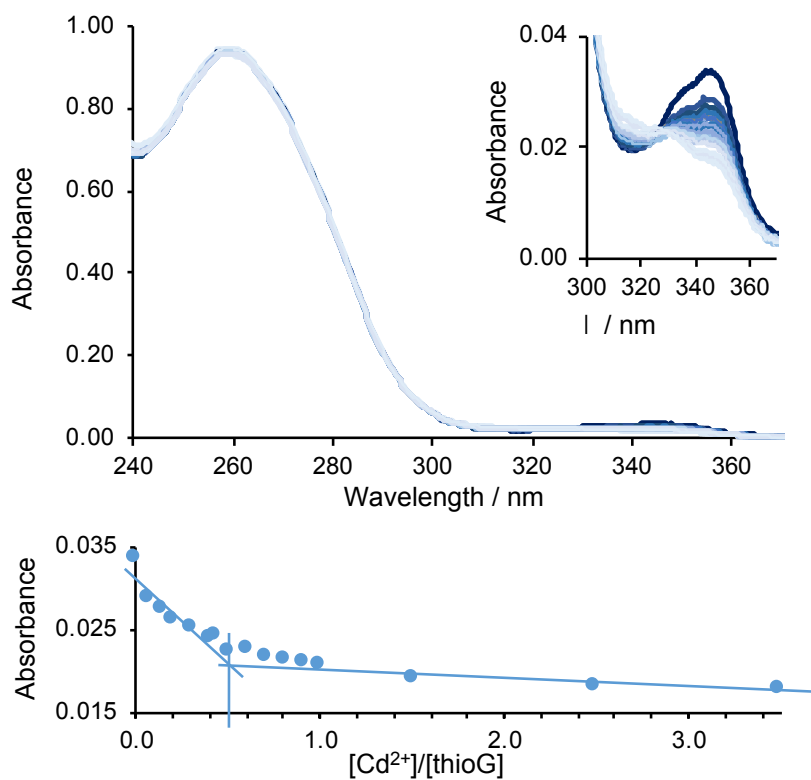

Figure 16. a) UV-Vis binding titration of **duplex-4** with increasing concentrations of Cd^{2+}. b) Binding curve of the complex between Cd^{2+} and tG.

The Tm of **duplex-4** was investigated in the absence and presence of cadmium ions, Figure 17. No change in Tm was observed between **duplex-4** and **duplex-4⊃Cd₂**, 24.5 °C, therefore it is hypothesised that the cadmium ions are bound to the tG on one strand but do not take part in strengthening the duplex. The binding of metal ions in **duplex-4** should not have an effect on the melting temperature as they are not involved in the bonding between the two strands. As no change in the Tm is observed it is assumed that the cadmium is not taking part in the bonding for the **duplex-4** however as the melting temp increases for the cadmium addition to **duplex-3** we can hypothesise that the ions are forming inter-strand metal mediated base pairs and restabilising the duplex. We conclude that the duplex is formed, and that hairpin formation is not taking place.
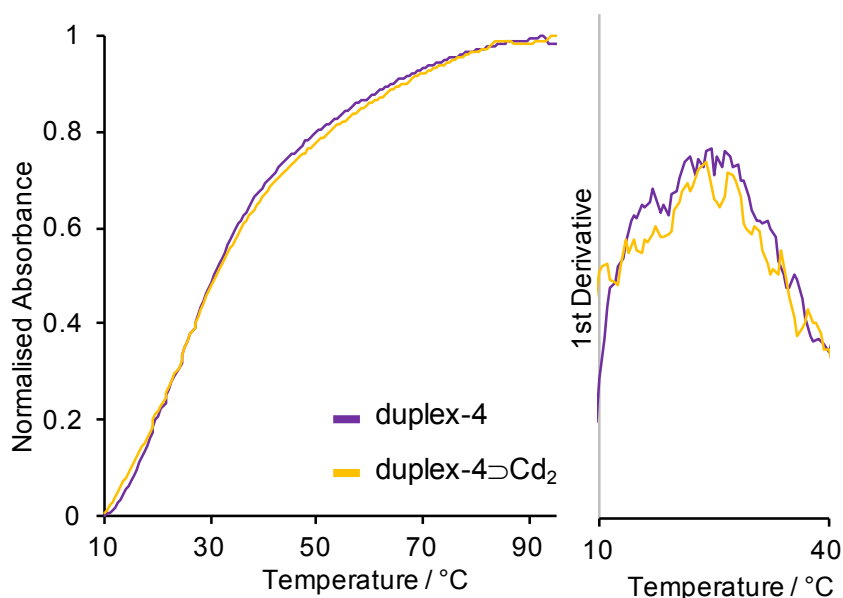
Figure 17. *Melting temperature profiles and the Tm calculated from the first derivative for **duplex-4**, and* ***duplex-3⊃Cd₂***

2.2.8 CD

The circular dichroism (CD) spectra was used to compare the conformational structure of **duplex-3** compared with **duplex-1**, **duplex-2** and **duplex-3⊃Cd₂**, Figure 18. Exciton splitting is observed for all duplexes at 264.5 nm consistent with B-form DNA indicating structural order from the stacking of the DNA bases in the system.[35] For the mismatched duplexes, **duplex-2** and **duplex-3**, the peak splitting shifted to 266.5 nm indicating a change in the conformation as expected due to the destabilisation of the mismatched central regions. The order in these duplexes is associated with the terminal AT regions in which base stacking is still present, only arranged differently. In

duplex-3, an extra absorption band at 340 nm is observed due to the presence of the tG group however no peak splitting is observed indicating that the tG bases are not stacked in a chiral manner. This supports the theory that the tG bases are pushed outwards from the duplex and not involved in hydrogen bonding. Upon addition of Cd^{2+} bases, the peak at 340 nm now displays exciton splitting, crossing the x axis at 320 nm which corresponds to the wavelength of the tG once converted to a thiol for metal bonding. The exciton splitting signifies the increase of order in this area demonstrating that the bases are now stacked in a more ordered manner. The splitting at 260 nm is again shifted for **duplex-3⊃Cd₂**, once more signifying a change in the stacked conformation compared to the other duplexes. The CD spectra for **duplex-4** and **duplex-4⊃Cd₂** also exhibits exciton splitting at 321 nm upon cadmium addition, illustrating the increased stacking in the tG area of the duplex.
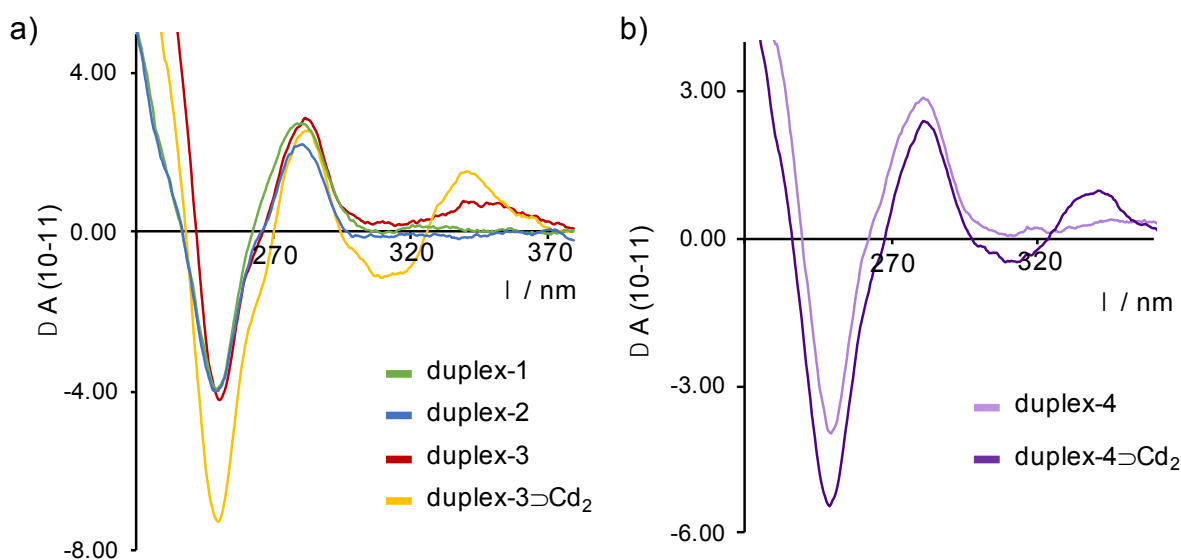
Figure 18. CD spectra of a) **duplex-1**, **duplex-2**, **duplex-3** and **duplex-3⊃Cd₂** b) **duplex-4** and **duplex-3⊃Cd₂**.

2.2.9 Molecular modelling

Equilibrium molecular dynamics (MD) simulations were carried out, in collaboration with Dr. Agnieszka Bronowska, to assess the stability and flexibility of the DNA strands down to the atomistic detail. Each duplex was induced with 50 ns of unrestrained MD simulations and by monitoring the system energetics, trajectories were obtained and analysed in terms of the stability of deviations from **duplex-1**, the native DNA geometry.
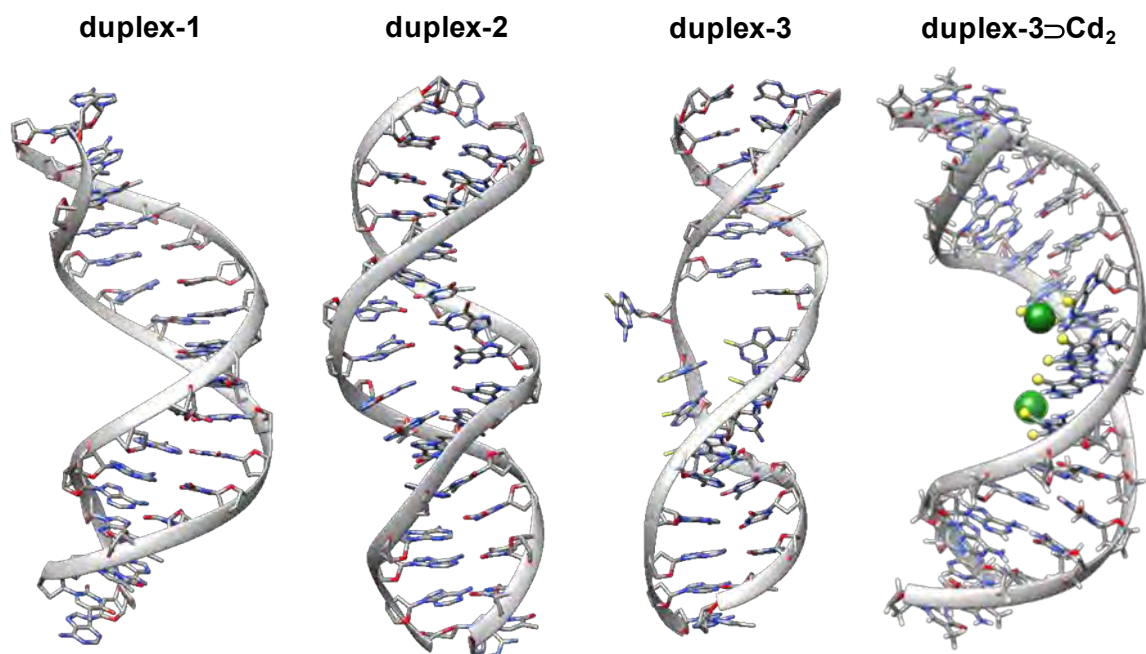
Figure 19. *Snapshots representing the highest populated clusters in conformational ensembles of the DNA duplexes. Cadmium ions (green spheres) are found interacting with the sulphur atoms of the central tG bases inducing stabilisation on the whole duplex.*
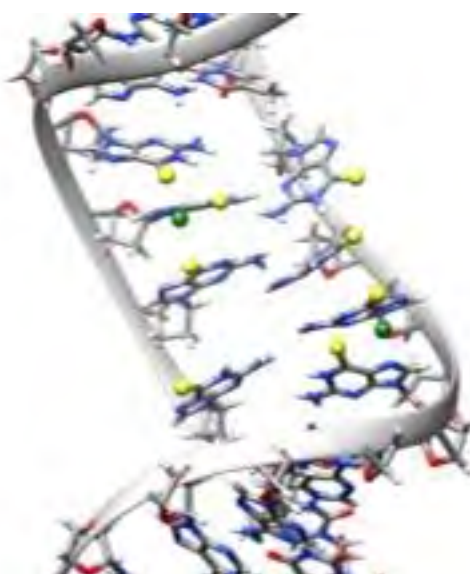
Figure 20. *A zoomed in snapshot of the Cd²⁺ binding to the sulphur in **duplex-3**. This is a representation of the binding which could potentially occur as developed in the modelling programme and is not limited to that shown.*

Duplex-1 displays the expected DNA structure with major and minor grooves and clear base stacking throughout the whole DNA duplex, see Figure 19. **Duplex-2** shows slight distortion in the central GG mismatched region which supports the lower Tm observed previously. However, the bases are still stacked in an ordered manner indicating the presence of some mismatched hydrogen bonding between the G bases also previously hypothesised. **Duplex-3** reveals a noticeably distorted duplex structure with the tG bases pushed outward from the framework and not taking part in base stacking,[34] however the structure maintains a right-handed helical conformation as seen in the CD spectra and as previously reported.[36] The hydrogen bonding is also clearly broken in the central region consistent with Tm destabilisation. The flexibility of the system was determined in terms of per-residue root-mean square fluctuations (RMSF), Figure 21. In **duplex-3**, all 16 bases exhibit a tenfold increase in flexibility to 2 nm from 0.2 nm observed in **duplex-1** accounted for by the partial unwinding of the duplex. In **duplex-2**, only the central G mismatched area displays a slight increase in base fluctuations, the A:T regions remain at approximately 0.2 nm. Upon addition of cadmium ions to **duplex-3**, the duplex is stabilised through interactions between the sulphur atoms of the tG bases and the Cd²⁺ ions (Cd-S distances of 2.60 – 2.75 Å) which results in increased base stacking of the formerly protruding tG bases. A representation of the possible binding is displayed in Figure 20. The considerable stabilising effect of the Cd²⁺ ions is clearly observed in the RMSF values as the flexibility of each base returns to that of the fully complementary **duplex-1** at 0.2 nm.
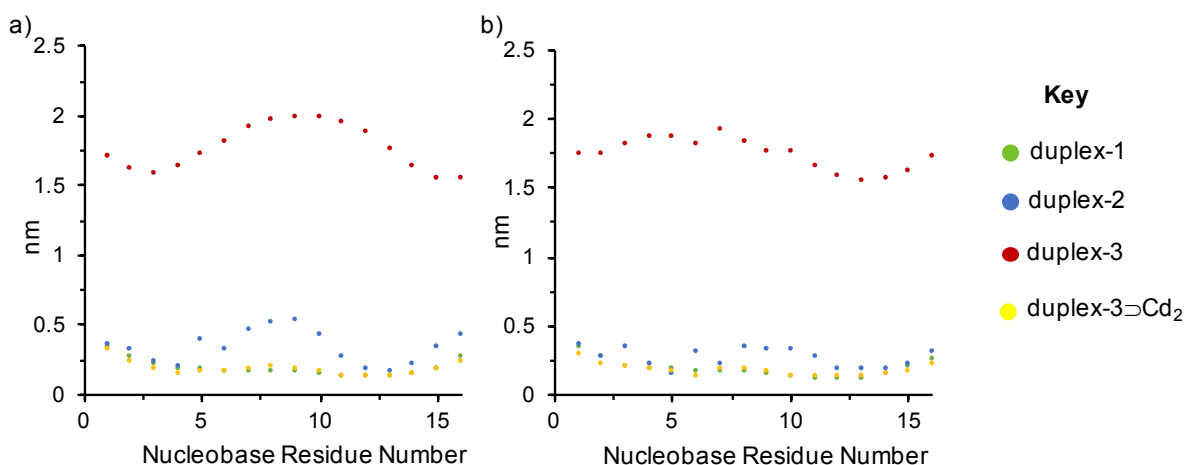
Figure 21. *RMSF values for the fluctuations in a) strand 1 and b) strand 2 of **duplex-1**, **-2**, **-3** and **duplex-3⊃Cd₂**.*

Duplex-4 was modelled in the absence and presence of Cd^{2+} ions, Figure 22. The duplex structure is not affected by the interaction with metal ions. Increased base stacking is observed between the tG bases however there is no change in the bonding or overall duplex structure between the 2 strands. This reaffirms the Tm data that the metal ions do not affect the strand stability.

duplex-4   **duplex-4⊃Cd₂**
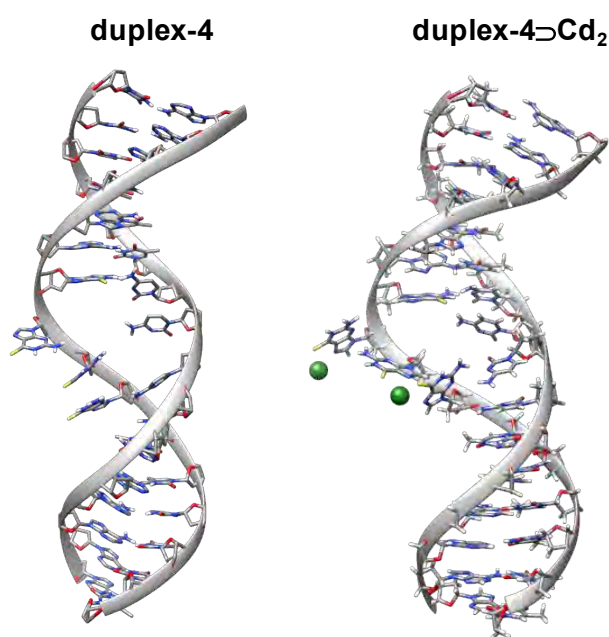
Figure 22. *Snapshots representing the highest populated clusters in conformational ensembles of **duplex-4** and **duplex-4⊃Cd₂**. Cadmium ions (green spheres) form interactions with the sulphur atoms of the central tG bases however unlike the case of **duplex-3**, the metal addition does not induce duplex stabilisation.*

The plausible hairpin structures were also modelled, see Figure 23, in the absence and presence of cadmium ions, and the overall energies of each system were calculated and compared to the energies for the duplex derivatives, Figure 24. It is clear that the hairpin structure is not able to direct the cadmium ions into a coordinated role, and hence the instability and overall energy of the system remains high.
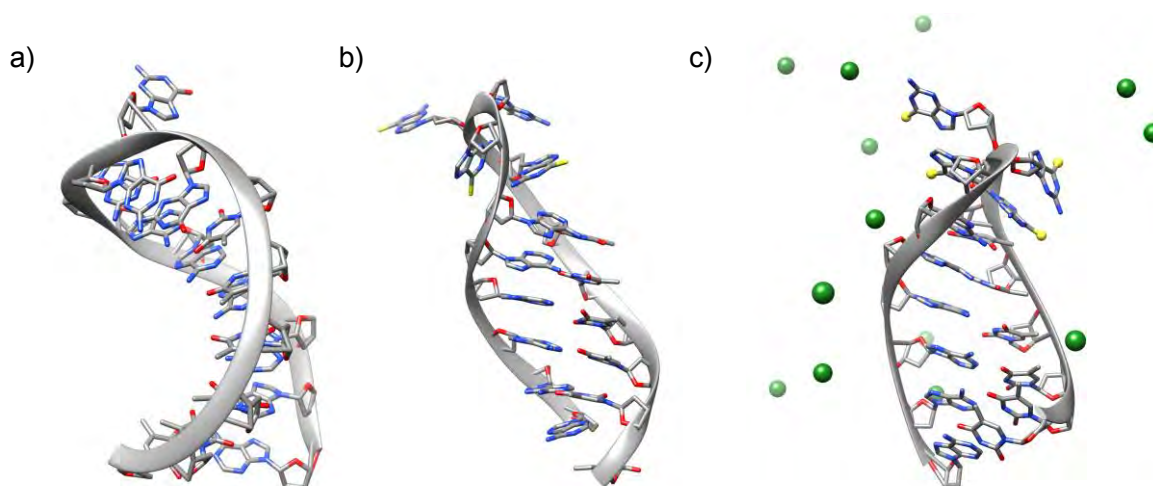
Figure 23. *Model snapshots representing the highest populated clusters in the conformational ensembles of a)* **hairpin-1**, *b)* **hairpin-2** *and c)* **hairpin-2⊃Cd**. *Cd2+ (green spheres) are not forming significant interactions with the sulphur atoms on the tG.*
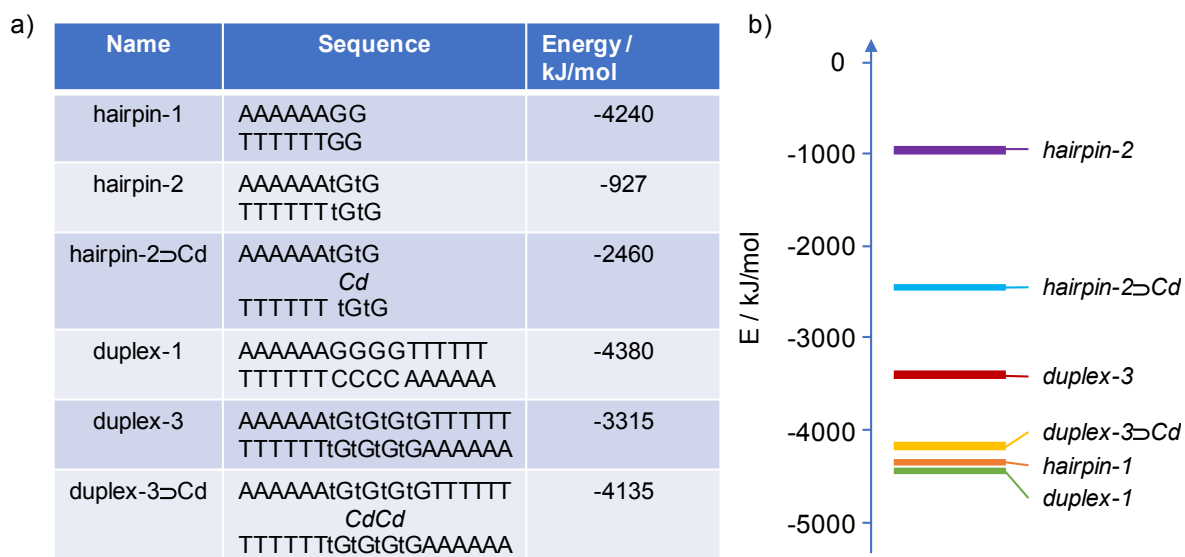
The lowest energy conformation obtained for **duplex-1** and **hairpin-1** (-4380 kJ/mol and -4240 kJ/mol) are comparable, however after the conversion of G to tG, a noticeable difference between the energies is observed. **Hairpin-2** containing the tG base, increases to -927 kJ/mol indicating a substantial decrease in stability. The energy of **duplex-3** is also destabilised however only to -3315 kJ/mol which is then stabilised to -4135 kJ/mol upon cadmium binding. **Hairpin-2** is also stabilised in the presence of cadmium, however the energy calculated is -2460 kJ/mol which indicates that this structure is less stable compared to the destabilised **duplex-3**, even without cadmium ions. This suggests that although the natural hairpin containing G has a comparable energy to the fully complementary **duplex-1**, the hairpin conformation containing tG is profoundly destabilised with slight stabilisation upon cadmium addition however not as efficiently re-stabilised as when in duplex configuration.

a)

| Name	Sequence	Energy / kJ/mol
hairpin-1	AAAAAAGG TTTTTTGG	-4240
hairpin-2	AAAAAAtGtG TTTTTTtGtG	-927
hairpin-2⊃Cd	AAAAAAtGtG Cd TTTTTT tGtG	-2460
duplex-1	AAAAAAGGGGTTTTTT TTTTTT CCCC AAAAAA	-4380
duplex-3	AAAAAAtGtGtGtGTTTTTT TTTTTTtGtGtGtGAAAAAA	-3315
duplex-3⊃Cd	AAAAAAtGtGtGtGTTTTTT CdCd TTTTTTtGtGtGtGAAAAAA	-4135

b)

Figure 24. *a) Table displaying the sequences for potential hairpin conformations and duplex structures, and the calculated energy of the systems. b) A graphical representation of the differences in energy for the oligomer conformations.*

2.2.10 Crystallisation of oligomers

Crystallisation of DNA duplexes is an excellent way of elucidating the structure, the orientation of each base and any interaction with metal ions.[37] Attempts were made to crystallise fully complementary **duplex-1** using several crystal screens such as the MPD, PACT JSCG-plus and HELIX to gain optimum conditions to form crystals for a 16-mer. Sitting drop vapour diffusion 96 well plates were set up using the mosquito crystallisation robot which automates the crystal set up and allows small volumes down to 25 nL to be used. **Duplex-1** was added to the various reservoir solutions and left at 4 °C for crystallisation. Crystals were harvested using the cryoprotectant polyethylene gycol (PEG) 400 20 % and stored in liquid nitrogen. The Helix screen produced the largest amount and best quality crystals in several of the conditions, however they were unstable and experiments performed to try and interpret the structure failed (carried out in collaboration with Dr Arnaud Basle). The crystals were too unstable and were easily damaged either during the freezing of the crystals or in transit to the diffractometer.

In order to increase the stability of the crystals to withstand the harvesting process, a hanging drop vapour diffusion 24-well plate was set up with the cryoprotectant, PEG 400 20 %, in the reservoir solution. The optimised conditions used for the 24-well plate were adjusted from one of the conditions from the original 96 well plate which produced good quality crystals. Single crystals obtained from the pre-cryoprotected solutions were sufficiently stable to run in the diffractometer, Figure 22.
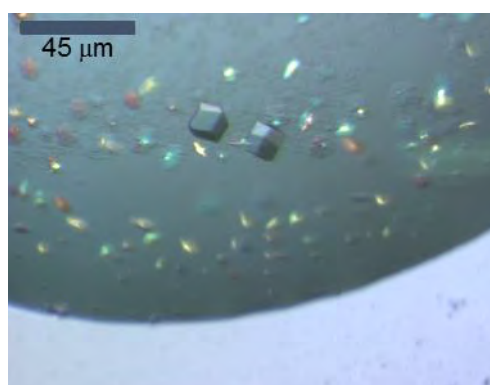
Figure 22. *Crystals of* *duplex-1* *obtained from the hanging drop vapour diffusion method using the following reservoir solution: 50 mM bis-tris pH7, 20 % w/v PEG 2000 mme, 100 mM NaCl, 20 % PEG 400.*

Unfortunately, the resolution of the crystals could only be resolved down to 1.5 Å and the reflections did not match the predictions, therefore a unit cell could not be fully

obtained. Although the structure could not be fully resolved, an estimation of the unit cell was 37x47x54 which confirmed that **duplex-1** had crystallised as this is too large to correspond to salt crystals and is of a similar size to previously reported duplex crystals.[37] The crystals obtained were fibrous which is a common habit for oligonucleotide crystals.

In order to gain an exact unit cell and determine the structure the next step would be to try an X-ray free electron laser (FEL). The X-Ray free electron laser passes exceptionally high-speed electrons, at a tuneable frequency, through a magnetic system in short pulses. This allows images of proteins/DNA crystals to be obtained which do not stack in a manner allowing conventional imaging techniques. The short pulse duration captures the image of the structure before the crystal is destroyed. These studies are ongoing and will be extended to the tG bearing duplex once optimum conditions have been achieved.

2.3 Conclusion

tG bearing oligos were synthesised via an on-column conversion of G bases within a mixed-base short oligonucleotide. The specific thiolation of guanosine within a short oligomer bound to the CPG support to thioguanosine is described here. The oligomer remains bound to the solid support throughout the synthesis for ease of isolation and purification. The thiolation reaction is found to be specific to the guanosine base and leaves the other three native bases unaltered. **Duplex-3** was formed through the self-hybridisation of the thiolated **oligo-3,** allowing for investigations into the effect of the tG base on the stability of the duplex. **Duplex-3** was found to be destabilised due to the bulky tG central region as observed by a lower Tm compared to the native fully complementary **duplex-1** and the lack of base stacking in the tG region as observed in CD spectra. Subsequent addition of Cd^{2+} to the distorted duplex heals the helix resulting in an increased Tm and exciton splitting in the CD spectra at 320 nm attributed to the increased base stacking in the tG area. A metal titration and Job plot monitored by UV-Vis indicated a Cd^{2+}:thiobase binding ratio of 1:4 with metal binding through S and the N(7) positions on the tG. MD simulations illustrated the destabilisation of the duplex and a tenfold increase in base fluctuations to 2 nm for **duplex-3** which returned to 0.2 nm upon Cd^{2+} addition, comparable to fully complementary **duplex-1**. Continuation of crystallisation experiments would unveil further detail into the structure of the duplex and reveal the exact nature of the binding interaction of the metal ions. The cadmium induced stabilisation of multiple base mismatches within a DNA duplex emphasises the promise for the metal mediated healing of DNA damage. Further investigations into this approach could aid in the development and design of functional DNA hybrid nanomaterials containing remarkably artificial and unstable bases which are subsequently healed in response to chemical stimuli.

2.4 Experimental

DNA Synthesis

DNA synthesis was performed using an EXPEDITE™ Nucleic Acid System. All reagents used to synthesise DNA oligonucleotides were purchased from Glen Research or Sigma Aldrich, and used as received unless stated otherwise. Oligomers were purchased from Eurofins (Ebersburg, Germany) whilst still bound to the CPG solid support.

High-Performance Liquid Chromatography (HPLC)

HPLC was performed on a Waters 2487 machine using Picolog software, using an APEX ODS C18 5 um 250 mm reverse phase column. Buffer A was 0.1 M triethyl ammonium acetate at pH 6.5 with 5 % acetonitrile, and buffer B was 0.1 M triethyl ammonium acetate at pH 6.5 with 65 % acetonitrile at the gradient 0-30 % B over a period of 25 minutes (increasing 10 % buffer B at 5 minute intervals. The gradient was returned to 0% B after 25 minutes) at a rate of 1 ml/min. Absorbance was monitored at two wavelengths: 254 nm and 340 nm.

Ultraviolet-Visible Spectroscopy (UV-Vis) and Titrations

UV-Vis spectra were recorded on a Varian Cary100 Bio UV-visible spectrophotometer with a Varian Temperature controller within the range of 200 nm to 600 nm. The spectrometer was blanked with nanopure water. The DNA concentrations were calculated using the absorbance at 260 nm and the Beer-Lambert law; A = cle.

Extinction Coefficient calculation:

Using **oligo-3**:

At 21°C, A260 = 0.479, A340 = 0.140

At 95°C, A260 = 0.597, A340 = 0.148

εoligo = 0.9 x ((6 x 15400) + (4 x 8800) + (6 x 8700))   *Values from Sigma Aldrich and Jena Biosciences*

$\qquad$ = 161820 $M^{-1}cm^{-1}$

Concentration of oligo = ss A260 / εoligo

$\qquad\qquad$ = 3.69 μM

Therefore, concentration of dtG = 4 x 3.69 = 14.76 μM

ss tdG ε = 0.148 / 14.76 x10^{-6}

   = 10027 M^{-1}cm^{-1}

ds tdG ε = 0.140 / 14.76 x10^{-6}

   = 9485 M^{-1}cm^{-1}

Compared to free tdGTP ε = **24800 M^{-1}cm^{-1}**

Environment	ε M^{-1}cm^{-1}
tdGTP	**24800**
ss tdG	**10027**
ds tdG	**9485**

The thiobase concentration for the binding titration was 12 μM and the Cd^{2+}concentration was 200 μM. For the Job plot, the thiobase concentration was 12 μM and the Cd^{2+}concentration was 12 μM.

Matrix-Assisted Laser Desorption/Ionisation Time-Of-Flight Mass Spectrometry (MALDI-TOF MS)

MALDI-TOF MS measurements were recorded on a Microflex MALDI-TOF MS instrument using a MSP Anchorchip 600-96. All reagents used for MALDI-TOF MS were purchased from Bruker Daltonics or Sigma Aldrich.

Preparation of the MALDI anchorchip target:

3- Hydroxypicolinic acid (3-HPA) (50 mg) and diammonium hydrogen citrate (5 mg) were dissolved in nanopure water (5 ml). 1 μL of the 3-HPA matrix solution was deposited onto the target position and allowed to dry. 1 μL of the sample solution was deposited onto the matrix spot and allowed to dry.

^{1}H NMR

NMR spectra were recorded on a Bruker Avance 111 300 spectrometer using Topspin software (version 3.2). The spectra acquired was then processed using MestReNova. For low temperature NMR, the temperature was cooled to 218 K using liquid nitrogen and the solvent was DMF-d7.

Infrared Spectroscopy (IR)

FTIR analysis was performed on a Varian 800 FTIR Scimitar series AC 300 spectrometer and a Shimadzu IRAffinity-1S using Labsolutions IR software. For the analysis of oligomers, 1.5 µL of sample was dried directly onto the diamond plate and the spectra recorded at a resolution of 16 for 32 scans.

DNA Digestion

Snake venom phosphodiesterase (0.2 mg), bacterial alkaline phosphatase (100 units) in potassium phosphate buffer (10 mM), magnesium chloride (10 mM, pH 7) was added to dsDNA (2 absorbance units at 260 nm) and incubated at 37 °C for 16-18 hours. 50 µL of digestion product was then analysed by reverse phase HPLC on an APEX ODS C18 5um 250 mm column with 0.1 M triethylammonium acetate, pH 6.5 with 5 % acetonitrile.

Melting Temperatures

Melting curves were obtained on a Varian Cary100 Bio UV-visible spectrophotometer with a Varian Temperature controller. The DNA solutions (3 uM) were preannealed in 0.1M sodium phosphate buffer. The temperature increased from 5 °C to 95 °C at a rate of 1 °C/min and a data interval of 0.5 °C and the absorbance monitored at 260 nm.

CD

CD spectra were recorded on a JASCO J-18 spectropolarimeter with 4 time accumulation and a path length of 1 cm at 20 °C. The raw data from the CD spectra is recorded as ellipticity in millidegrees. In order to take into account concentration effects, the data was converted to change in absorbance:

$\Delta\varepsilon = \theta\ /\ 32982$

$\Delta A = \Delta\varepsilon\ x\ c\ x\ l$

Molecular Modelling

All simulations for 4 studied duplexes (duplex1-4) were carried out using GROMACS 5.1.2,[1] with Amber99SB-ILDN[2] force field for the duplexes and the TIP3P water model. Parameters for thioguanine were obtained by analogy to the native guanine and assigned using ACPYPE.[3] Partial atomic charges on the thioguanine molecule were assigned using the RESP methodology[4] and obtained with the Gaussian09 programme,[5] using HF/6-31G∗ basis set.

The temperature was kept constant at T = 298 K by using velocity rescaling with a coupling time of 0.1 ps. The pressure was kept constant at 1 bar using an isotropic coupling to Parrinello-Rahman barostat with a coupling time of 0.1 ps.[6] A cutoff of 1 nm was used for all nonbonded interactions. Long-range electrostatic interactions were treated with the particle-mesh Ewald[7] method using a grid spacing of 0.1 nm with cubic interpolation. All bonds between hydrogens and heavy atoms were constrained using the LINCS algorithm.[8]

Each of the duplexes were immersed in a cubic TIP3P water box containing ~50,000 atoms. Simulation units were maintained neutral by adding calcium and chloride counterions (0.1 M concentration). In the simulations with cadmium, cadmium cations replaced calcium counterions. Initial conformations of all three systems were assumed to be helical.

Prior to MD simulations, the systems underwent 25000 steps of molecular mechanical energy minimization. This was followed by 100 ps MD simulations, during which position constraints were used on all duplex atoms. After the following unrestrained equilibration phase (1 ns) the production runs were carried for 50 ns, with an integration time step of 2 fs. The cutoff for non-bonded interactions was 0.1 nm. The coordinates were saved every 10 ps.

For the visual inspection of the results we used xmgrace and UCSF Chimera packages.[9,10]

Synthesis of d(A_6t$G_4$$T_6$)

d($A_6$$G_4$$T_6$) (1 µmol) was synthesised on a DNA synthesiser (EXPEDITE™ Nucleic Acid System) applying phosphoramidite bases and standard reagents following standard phosphoramidite procedures. The column was then removed from the device and dried under a high stream of N_2, before the guanosine bases were converted to thio-guanosine bases using the Jones procedure.[30] d($A_6$$G_4$$T_6$) (1 µmol) CPG beads from inside the column were added to dry pyridine (10 ml). Trifluoroacetic anhydride

(1 ml) was added dropwise and the resulting orange solution stirred for 40 min. A suspension of sodium sulphide (1 g) in anhydrous DMF (30 ml) was added in portions. The resulting cloudy dark blue solution was stirred for 24 hours. The clear orange solution was filtered to obtain the CPG beads which were then washed several times with water and ethanol. Anhydrous CH_3NH_2 was passed through the column to deprotect and cleave the oligomer $A_6tG_4T_6$ from the CPG bead. The oligomer was dissolved in water and purified by HPLC. The purified sample was desalted using an Illustra NAP-25 column following manufacturer's protocol.

Crystallisation set up

Crystallisations were performed at 277 K by either the sitting drop or hanging drop vapour diffusion method. For sitting drop, the plates were set up using a Mosquito liquid handling robot (TTP Labtech) by mixing 100 nl of DNA (1.5 mM) with 100 nl crystallisation solution for one drop and 200 nl of DNA (1.5 mM) with 100 nl crystallisation solution for another drop. The crystallisation solution was dependent on the screen used. The optimised conditions which produced crystals in the hanging drop method are shown in Table 4.

Table 4. *Crystallisation conditions used in the hanging drop diffusion method which produced good quality single crystals.*

50 mM bis-tris pH7	20 % w/v PEG 2000 mme	100 mM NaCl	20 % w/v PEG 200
50 mM bis-tris pH7	18 % w/v PEG 2000 mme	200 mM NaCl	20 % w/v PEG 200
50 mM bis-tris pH7	22 % w/v PEG 2000 mme	100 mM NaCl	20 % w/v PEG 200

2.5 References

1   Pinheiro, A. V., Han, D., Shih, W. M. & Yan, H. Challenges and opportunities for structural DNA nanotechnology. *Nat Nanotechnol* **6**, 763-772 (2011).

2   Morrow, T. J., Li, M., Kim, J., Mayer, T. S. & Keating, C. D. Programmed assembly of DNA-coated nanowire devices. *Science* **323**, 352 (2009).

3   Choi, J. S. *et al.* Synthesis of DNA Triangles with Vertexes of Bis(terpyridine)iron(II) Complexes. *J. Am. Chem. Soc* **126**, 8606-8607 (2004).

4   Douglas, S. M., Bachelet, I. & Church, G. M. A Logic-Gated Nanorobot for Targeted Transpost of Molecular Payloads. *Science* **335**, 831-834 (2012).

5   Mender, I., Gryaznov, S., Dikmen, Z. G., Wright, W. E. & Shay, J. W. Induction of telomere dysfunction mediated by the telomerase substrate precursor 6-thio-2'-deoxyguanosine. *Cancer Discov* **5**, 82-95 (2015).

6   Mirkin, C. A., Letsinger, R. L., Mucic, R. C. & Storhoff, J. J. A DNA-based method for rationally assembling nanoparticles ino macroscopic materials. *Nature* **382**, 607-609 (1996).

7   Amo-Ochoa, P. *et al.* Assembling of dimeric entities of Cd(II) with 6-mercaptopurine to afford one-dimensional coordination polymers: synthesis and scanning probe microscopy characterization. *Inorg. Chem.* **48**, 7931-7936 (2006).

8   Zimmermann, N., Meggers, E. & Schultz, P. G. A Novel Silver(I)-Mediated DNA Base Pair. *J. Am. Chem. Soc* **124**, 13684-13685 (2002).

9   Takezawa, Y. *et al.* Soft Metal-Mediated Base Pairing with Novel Synthetic Nucleosides Possessing an O,S-Donor Ligand. *J. Org. Chem.* **73**, 6092-6098 (2008).

10   Spackova, N., Cubero, E., Sponer, J. & Orozco, M. Theoretical Study of the Guanine - 6-Thioguanine Substitution in Duplexes, Triplexes, and Tetraplexes. *J. Am. Chem. Soc* **126**, 14642-14650 (2004).

11   Ling, Y. H., Nelson, J. A., Cheng, Y. C., Anderson, R. S. & Beattie, K. L. 2'-Deoxy-6-thioguanosine 5'-triphosphate as a substrate for purified human DNA polymerases and calf thymus terminal deoxynucleotidyltransferase in vitro. *Mol. Pharmacol.* **40**, 508-514 (1991).

12   Yoshida, S., Yamada, M., Masaki, S. & Saneyoshi, M. Utilization of 2′-Deoxy-6-thioguanosine 5′-Triphosphate in DNA Synthesis in vitro by DNA Polymerase α from Calf Thymus. *Cancer Res.* **39**, 3955-3958 (1979).

13   Ling, Y. H., Chan, J. Y., Beattie, K. L. & Nelson, J. A. Consequences of 6-thioguanine incorporation into DNA on polymerase, ligase, and endonuclease reactions. *Mol. Pharmacol.* **42**, 802-807 (1992).

14   Kuwahara, M. *et al.* Systematic characterization of 2'-deoxynucleoside- 5'-triphosphate analogs as substrates for DNA polymerases by polymerase chain reaction and kinetic studies on enzymatic production of modified DNA. *Nucleic Acids Res* **34**, 5383-5394 (2006).

15   Christopherson, M. S. & Broom, A. D. Synthesis of oligonucleotides containing 2'-deoxy-6-thioguanosine at a predetermined site. *Nucleic Acids Res* **19**, 5719-5724 (1991).

16   Xu, Y. Z., Zheng, Q. & Swann, P. F. Synthesis by Post-Synthetic Substitution of Oligomers Containing Guanine Modified at the 6-poisiton with S-, N-, O-derivatives. *Tetrahedron* **48**, 1729-1740 (1992).

17   Zheng, Q., Wang, Y. & Lattmann, E. Introduction of structural diversity into oligonucleotides containing 6-thioguanine via on-column conjugation. *Tetrahedron* **59**, 1925-1932 (2003).

18 Beilstein, A. E. & Grinstaff, M. W. On-column derivatization of oligodeoxynucleotides with ferrocene. *Chem. Comm.*, 509-510 (2000).

19 Khan, S. I., Beilstein, A. E., Tierney, M. T., Sykora, M. & Grinstaff, M. W. Solid-Phase Synthesis and Photophysical Properties of DNA Labeled at the Nucleobase with Ru(bpy)2(4-m-4'-pa-bpy)2+. *Inorganic Chemistry* **38**, 5999-6002 (1999).

20 Khan, S. I. & Grinstaff, M. W. Palladium(0)-Catalyzed Modification of Oligonucleotides during Automated Solid-Phase Synthesis. *Journal of the American Chemical Society* **121**, 4704-4705 (1999).

21 Miller, G. P. & Kool, E. T. Versatile 5'-Functionalization of Oligonucleotides on Solid Support: Amines, Azides, Thiols, and Thioethers via Phosphorus Chemistry. *J. Org. Chem.* **69**, 2404-2410 (2004).

22 Monson, C. F. & Woolley, A. T. DNA-Templated Construction of Copper Nanowires. *Nano Letters* **3**, 359-363 (2003).

23 Watson, S. M. D., Mohamed, H. D. A., Horrocks, B. R. & Houlton, A. Electrically conductive magnetic nanowires using an electrochemical DNA-templating route. *Nanoscale* **5**, 5349-5359 (2013).

24 Pate, J. *et al.* Solution-based DNA-templating of sub-10 nm conductive copper nanowires. *J. Mater. Chem. C* **2**, 9265-9273 (2014).

25 Braun, E., Eichen, Y., Sivan, U. & Ben-Yoseph, G. DNA-templated assembly and electrode attachment of a conducting silver wire. *Nature* **391**, 775 (1998).

26 Tanaka, K., Tengeiji, A., Kato, T., Toyama, N. & Shionoya, M. A discrete self-assembled metal array in artificial DNA. *Science* **299**, 1212-1213 (2003).

27 Amo-Ochoa, P., Castillo, O., Guijarro, A., Sanz Miguel, P. J. & Zamora, F. Supramolecular architectures based on 6-purinethione complexes. *Inorgan. Chim. Acta.* **417**, 142-147 (2014).

28 Al-Mahamad, L. L. G., El-Zubir, O., Smith, D. G., Horrocks, B. R. & Houlton, A. A coordination polymer for the site-specific integration of semiconducting sequences into DNA-based materials. *Nature Communications* **8**, 720 (2017).

29 Hribesh, S. 2'-deoxy-6-thioguanosine: synthesis of monomer, oligomers and long DNA, and their binding with metal ions. (2013).

30 Kung, P. P. & Jones, R. A. One-Flask Syntheses of 6-Thioguanosine and 2'-Deoxy-6-Thioguanosine. *Tetrahedron Lett.* **32**, 3919-3917 (1991).

31 Reddy, M. P., Hanna, N. B. & Farooqui, F. Ultrafast Cleavage and Deprotection of Oligonucleotides Synthesis and Use of CAcDerivatives. *Nucleosides and Nucleotides* **16**, 1589-1598 (1997).

32 Santosh, C. & Mishra, P. C. Electronic Structures and spectra of 6-mercaptopurine and 6-thioguanine. *Spectrochim. Acta* **49a**, 985-993 (1993).

33 Amo-Ochoa, P. *et al.* Coordination chemistry of 6-thioguanine derivatives with cobalt: toward formation of electrical conductive one-dimensional coordination polymers. *Inorg Chem* **52**, 5290-5299 (2013).

34 Somerville, L. *et al.* Structure and dynamics of thioguanine-modified duplex DNA. *J Biol Chem* **278**, 1005-1011 (2003).

35 Nielsen, L. M., Hoffmann, S. V. & Nielsen, S. B. Electronic coupling between photo-excited stacked bases in DNA and RNA strands with emphasis on the bright states initially populated. *Photochem Photobiol Sci* **12**, 1273-1285, doi:10.1039/c3pp25438k (2013).

36 Johannsen, S., Megger, N., Bohme, D., Sigel, R. K. & Muller, J. Solution structure of a DNA double helix with consecutive metal-mediated base pairs. *Nat Chem* **2**, 229-234 (2010).

37   Kondo, J. *et al.* Crystal Structure of Metallo DNA Duplex Containing Consecutive Watson–Crick-like T–HgII–T Base Pairs. *Angew. Chem. Int. Ed.* **53**, 2385-2388 (2014).

Chapter 3.

Charge transport measurements through DNA-SAMs on semi-conductor silicon

Table of Contents

3.1 Introduction

DNA surfaces are used in a variety of applications on account of the benefits of having it localised for study. The solid support silica surface, used routinely in automated DNA synthesis, was utilised in Chapter 2 to facilitate the specific thiolation of guanosine with simple purification. The immobilisation of DNA, short (SAMs) or long (brushes), has been investigated using a wide range of substrate materials including silicon, silica, gold and silver.[1-4] There are pros and cons for each substrate i.e; ease of preparation, flatness and stability of immobilisation. The choice of surface for a desired application is influenced by the substrate properties e.g. for electronic surfaces, gold-thiol interactions are employed as gold is an excellent flat conductor. Silicon is still the material of choice for electronic components and is effective for use in sensors, *e.g.* field effect transistors (FET) devices[5,6] so it is still worth pursuing despite some synthetic challenges such as oxidation.

The subject of using DNA in molecular electronics is of current interest,[7] in particular, the study of localising DNA by surface attachment. There are many possible methods to study the electron transport such as cAFM,[8] STM,[9] MBJ[10] for single molecule study, or for large area contacts the Hg drop,[11] carbon based electrodes[12] and large area junctions.[13] The determination of the electron transport through the DNA monolayer relies upon on the reproducible contact between two electrodes to produce a molecular sized circuit. The construction of a well-formed DNA monolayer in principle provides one good contact to the DNA molecules for electrical characterisation provided a top contact can be made. Of these techniques, EGaIn has several benefits as it is non-toxic, non-invasive and is stable to high temperatures, therefore allows for further investigations into the charge transport mechanism via temperature dependent measurements.

The materials fabricated in Chapter 2 would be interesting for investigations into the electrical characterisation of a DNA-SAM. However, it would be essential to establish some fundamental behaviour of ssDNA and dsDNA beforehand, which is the focus of this chapter.

In a typical DNA-SAM, the oligos are tethered perpendicular to the surface, and are thus in the ideal position to investigate the electrical transport through the DNA monolayer. The difference in electrical readout between ssDNA and dsDNA has potential in DNA-based bio-sensing applications. Although several methods of

measuring charge transport through SAMs are available and frequently employed, the non-invasive EGaIn technique was chosen for this study.

3.1.1 EGaIn Technique

EGaIn is a eutectic alloy of gallium and indium (75% Ga and 25% In by weight) which exists as a fluid metal capable of forming an electrode which can be useful in the physical organic studies of self-assembled monolayers, SAMs. EGaIn is an ideal candidate for electrode formation due to its following properties; i) high electrical conductivity (3.4×10^4 S cm^{-1})[14] ii) a liquid at room temperature (melting temperature = 15.5 °C) however, does not immediately free flow into different shapes until it reaches the critical surface stress (0.5 N m^{-1})[15] therefore can be sculpted into different shapes in order to form electrical contacts and iii) forms a low resistance contact with many materials.[16] EGaIn has many benefits compared to other well-known top electrodes such as mercury which is toxic and amalgamates with the metals.[17]

To form the cone shaped tip of the EGaIn electrode in order to make the junctions with the surface, a sacrificial film of Ag is required. The EGaIn is placed in a syringe held above the Ag film and a drop is contacted to the surface, see Figure 1.[18] The needle is retracted slowly allowing the EGaIn drop to attach to both the needle and the film eventually forming an hour glass shape which breaks into two cone shaped structures; one attached to the surface, the other protruding from the needle. A layer of Ga_2O_3 forms (approximately 0.7 nm thick)[19] on the outer surface of the EGaIn cone which acts as a protective layer and inhibits alloy formation with the SAMs.[15,20] The protective Ga_2O_3 layer does not affect the electronic characteristics of the SAM tunneling junctions as it is sufficiently conductive. The Ga_2O_3 layer acts as an ohmic contact with a thermally activated charge transport mechanism allowing the SAM to dominate the electrical charge transport.[21] The cone-shaped tip made up of Ga_2O_3/EGaIn is then brought into contact with the SAM and the electrical junction is formed. Each tip remains stable throughout the formation and the duration of the electrical measurement of 5-6 junctions, after which a new tip must be produced, again from an Ag film.[19] The Whitesides group investigated the effect of the size of contact area between the bottom electrode monolayers and the top electrode Ga_2O_3/EGaIn.[22] It was found that the current density obtained for small contact areas (< 1000 μm^2) was irreproducible due to the formation of rough, area-dependent junctions. However, with a larger contact area (1000-4000 μm^2) the charge transport occurs on the peripheral of the cone tip

resulting in smoother junctions generating more reproducible data between and within laboratories.

Figure 1. *A series of photographs showing the formation of a cone-shaped tip of EGaIn using an Ag film.*[18]

Once contact is made between the EGaIn and the sample, a current is passed through the system and J (current density, A/cm^2) values are recorded as a function of V at both negative and positive bias values, Figure 2. This method provides a very stable method for measuring the JV curves where 90% of junctions are stable up to 30 scans. This allows statistically large numbers of data to be acquired (N = 300-800) and are also stable to a range of temperatures enabling temperature-dependent measurements to be obtained.[18]
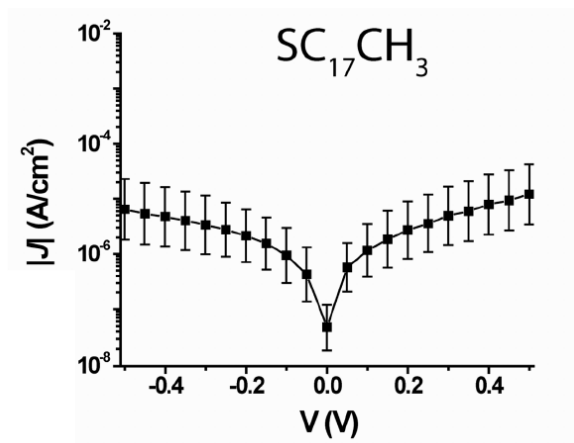
Figure 2. *A typical JV curve obtained from the EGaIn method.*[23]

This method has been extensively utilised to study the charge transport through a variety of *n*-alkanethiolates on template stripped, ultra-flat Au[24-26] or Ag.[27-29] The SAM constituents range from simple thiol-terminated alkyl chains[18] to SAMs with terminal modifications such as aromatic groups,[30] redox active tags[31,32] and SAMs formed on graphene templated surfaces.[33] Several charge transport parameters using EGaIn

have been identified in these SAMs such as rectification capabilities for redox active groups e.g. ferrocene which exhibit high rectification ratios and can act as molecular diodes.[34] Temperature-dependent studies are able to distinguish between the types of charge-transport mechanism and enable the tunneling decay coefficient (β) to be calculated.[21] Although this is a well-known technique with increasing interest, SAMs made from DNA have not yet been investigated.

The synthesis of uniform monolayers relies upon the molecules arranging in the optimum position, perpendicular to the surface, and well-packed with each other. In reality, several defects in the monolayers exist, whether due to the surface flatness, impurities or the packing of the molecules, see Figure 3.[35,36] If the surface is not ultra-flat, step edges and grain boundaries can occur which results in the formation of uneven layers of SAMs. These are known as thin-area defects as they reduce the distance between the electrodes, and thus the tunneling barrier, which can consequently influence the current density obtained. Thick-area defects occur when contaminants exist on the surface, buried in the metal or trapped between molecules, which extends the tunneling barrier. It is therefore crucial to form monolayers on a clean atomically flat surface to minimise potential defect areas which can drastically affect current density measurements. Barber et al. studied the effect of the air environment on the current density measurements for alkyl thiol monolayers with various terminal groups.[37] It was found that regardless of the relative humidity, the current density remained stable indicating that the monolayer was not affected by any water vapour. This study solely investigates functional groups positioned at the terminus of the monolayer however, the current density could be altered with increasing humidity for monolayers containing embedded functional groups or monolayers consisting of molecules known to behave differently with water such as DNA. The change in humidity could conceivably modify the height of the monolayer and hence directly change the current density measurement obtained.
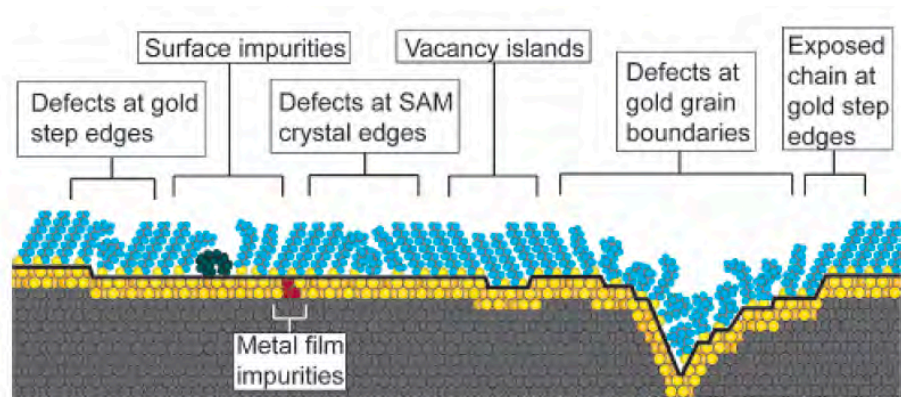
Figure 3. *A diagram highlighting the possible defects which can occur when forming SAMs.*[35]

This chapter describes the synthesis of a DNA monolayer on a semiconductor silicon surface and the subsequent electrical conductivity measurements using the EGaIn technique.

3.2 Results and Discussion

Here the synthesis of a DNA monolayer on a semiconductor silicon surface and the subsequent electrical conductivity measurements using the EGaIn technique are outlined. A siloxane linker is used to tether amino-modified DNA to a silicon hydride surface forming a DNA-SAM suitable for charge transport measurements via the EGaIn technique. Initial *JV* curves obtained indicate a difference in the charge transport mechanism between ssDNA and dsDNA.

3.2.1 Synthesis of the monolayers

In order to form a monolayer of DNA, a linker was used to tether the DNA strand onto the silicon surface, Scheme 1. Polyethylene glycol (PEG) groups have been routinely used to reduce fouling of surfaces with biological material and so here the peg$_4$ linker acetalpolyethyleneglycoldimethylethoxysilane (APEGDMES) was chosen to prevent the non-specific adsorption of DNA onto the surface during SAM formation.[38,39]
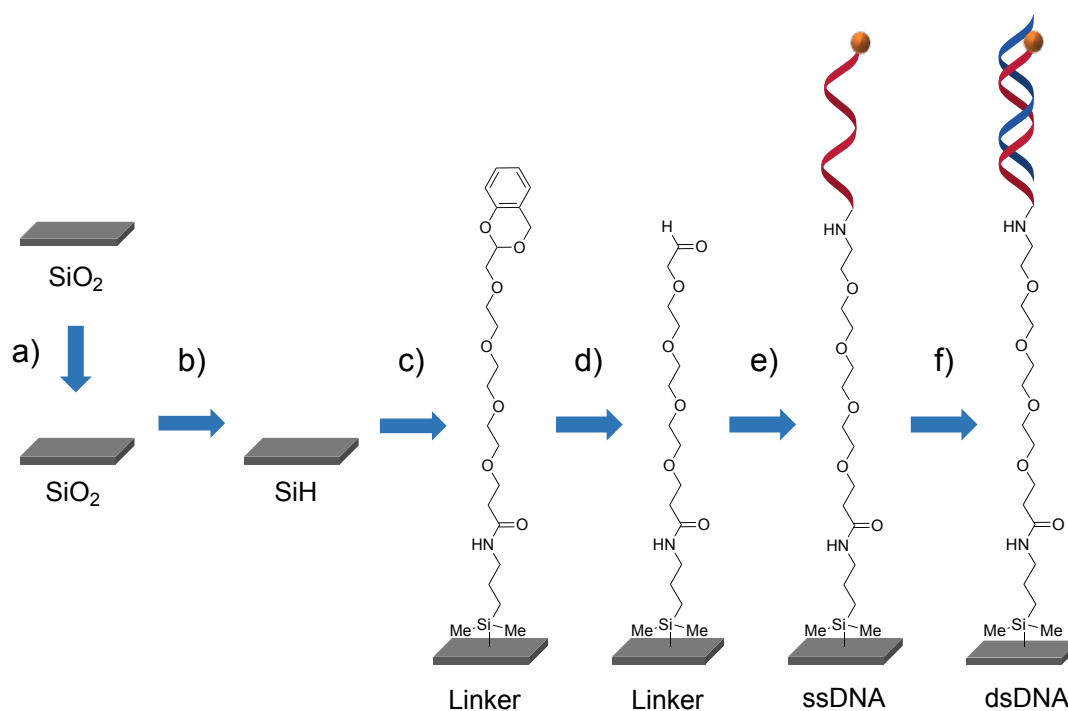
Scheme 1. *Chemical modifications on the surface to afford the DNA monolayer. a) 40 % NH$_4$F b) peg$_4$ linker molecule, toluene c) acetic acid d) probe-1 DNA, NaBH$_3$CN e) target-1 DNA.*

The semiconductor silicon, SiO$_2$, surface in Scheme 1, was a Boron-doped p(100) wafer cut to 1 cm^2 and rigorously cleaned with acetone, IPA and water, in step a. In step b, Piranha solution (4:1 H$_2$SO$_4$:H$_2$O$_2$) was used to remove any remaining organic contaminants from the surface before the chips were etched with oxygen-free ammonium fluoride (NH$_4$F) to remove the oxide layer and reveal Si-H groups.[40] The

chips were immediately placed in peg₄/toluene linker solution overnight, step c, for the silanisation reaction to occur between the free H groups and the siloxane end of the linker.[41] The other end of the linker was protected with an acetal, otherwise the aldehyde could react with the surface and would result in the uneven distribution of upright and inverted linker molecules.

Table 1. *The oligomer sequences used to form the DNA monolayer.*

Oligo Name	DNA sequence (X = Fc, Y= AminoC6)
Probe-1	5'-X-AGA TGT AGT TAG CAA TCG GTC CTT GTT GTA-Y-3'
Target-1	3'- TCT ACA TCA ATC GTT AGC CAG GAA CAA CAT -5'

The probe DNA strand is amino-modified at the 3' end for the attachment to the linker molecule and includes a ferrocene (Fc) group at the 5' end. The Fc is incorporated for later electrical measurements and was chosen as a result of its stability and redox properties.[42] The amino-modified probe DNA, **probe-1**, was added to the surface in the presence of 10% acetic acid solution for one hour to remove the acetal protecting group, step d. Sodium cyanoborohydride was then deposited onto the surface to aid the reductive amination reaction between the 3'-terminal amine on the DNA and the now free aldehyde of the peg-based SAM, step e. The complementary strand, **target-1**, was placed on the surface for hybridisation to form the dsDNA surface, step f.

3.2.2 Characterisation of the monolayers

The characterisation of the monolayers was carried out in collaboration with Dr Bee-Min Goh and Dr Kumar Senthil (NUS). In order to characterise the surfaces, contact angle measurements were used to determine the difference in hydrophobicity, Figure 4. From the bare SiO₂ the contact angle is 64.5° which increases to 58.4° when the surface is etched. As expected, once the DNA was attached to the surface the contact angle decreases to 48.5° due to the affinity of DNA for water and increased hydrophilicity.[43]
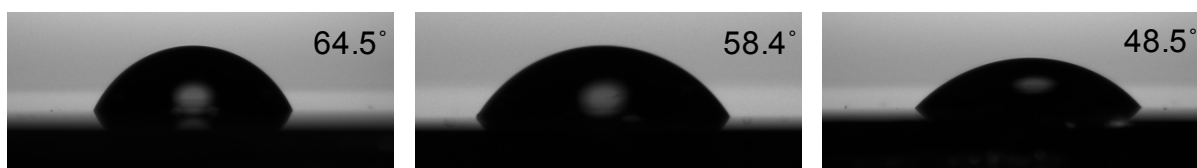
Figure 4. *Contact angle images and corresponding angle for a) SiO₂ b) SiH c) DNA-modified surface (Si-H).*

X-Ray photoelectron spectroscopy (XPS) characterisation of SiO_2 compared to SiH indicated the increase of the SiH binding energy peak compared to the SiO_2 energy peak, confirming the successful removal of the oxide layer from the surface, Figure 5 a) and b). The XPS plots for the APEGDMES linker and the APEGDMES-DNAFc surface are displayed in Figure 5 c) and d). Although there is a slight difference between the two plots, the iron (Fe) peaks from the Fc are not easily discernible suggesting extremely low amounts of ferrocene are attached to the surface.
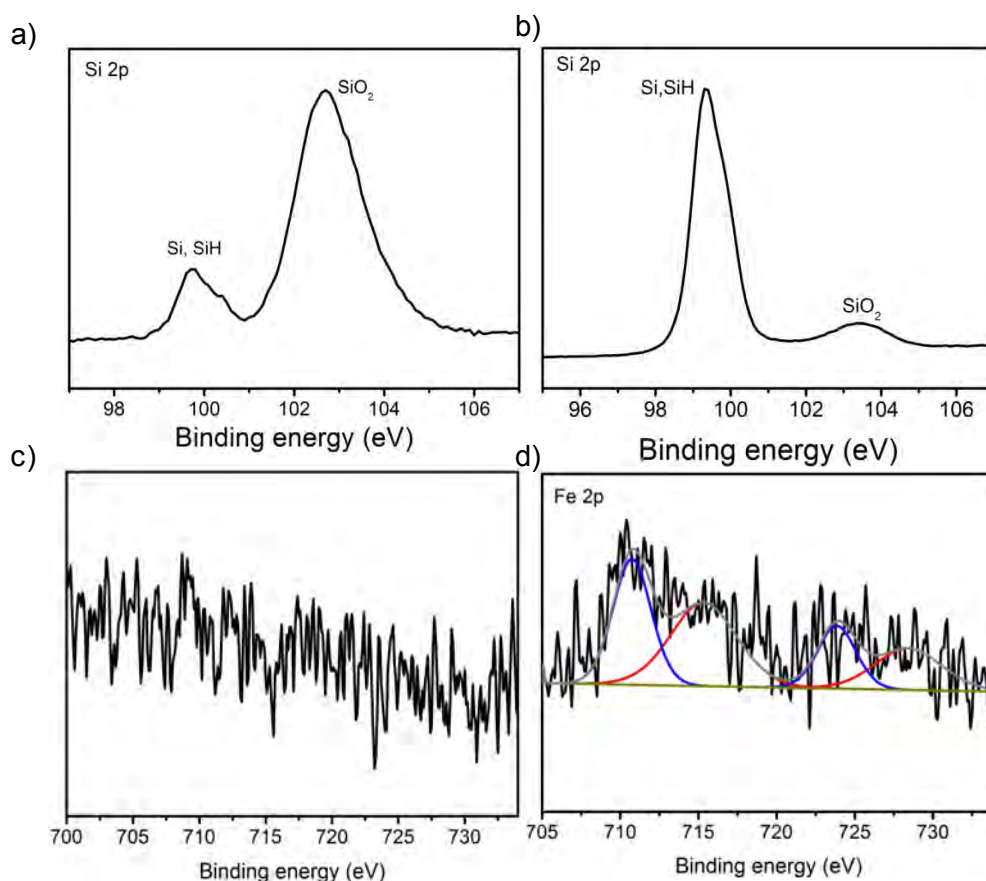
Figure 5. *XPS binding energy profiles highlighting the difference between a) SiO_2 b) SiH c) APEGDMES and d) APEGDMES-DNAFc.*

Ellipsometry is an optical technique which measures the change in polarisation as light transmits or reflects off a material's surface which allows the thickness of a monolayer to be estimated. This technique is sensitive enough to measure nanoscale lengths. The theoretical and measured thickness of the linker monolayers are shown in Table 2. The measured values are very similar to the theoretical values, indicating that the silane linkers are in fact perpendicular to the Si surface. The slight reduction in measured thickness could be due to the packing and defects present in the monolayer.[44] Ellipsometry was unsuccessful for DNA monolayers as they exist in

various conformations which can be explained by the complex interactions possible within DNA monolayers.[43]

Table 2. Table of the theoretical and the actual thickness of the peg$_4$-silane monolayer

| Monolayer	Theoretical Thickness	Actual Thickness
peg$_4$-silane	3.0 nm	2.4 nm ± 0.4 nm

Cyclic voltammetry (CV) measurements are commonly used to electrically characterise surfaces modified with redox active groups.[45,46] The oxidation/reduction peaks at ± 0.4 V are usually observable in the voltammograms and account for the presence of the ferrocene in the monolayer. The CV plot profiles for the ssDNA and the dsDNA surfaces are displayed in Figure 6. The expected oxidation peak is significantly shifted to the right, at > 1 V, therefore the Fc redox potential of ± 0.4 V is not immediately visible in the voltammograms of both ssDNA and dsDNA monolayers. As no ferrocenyl peaks are apparent in this area, the current observed may be due to the DNA bases themselves, which have irreversible oxidation redox potentials ranging from +0.7 V to 1.2 V.[47,48]
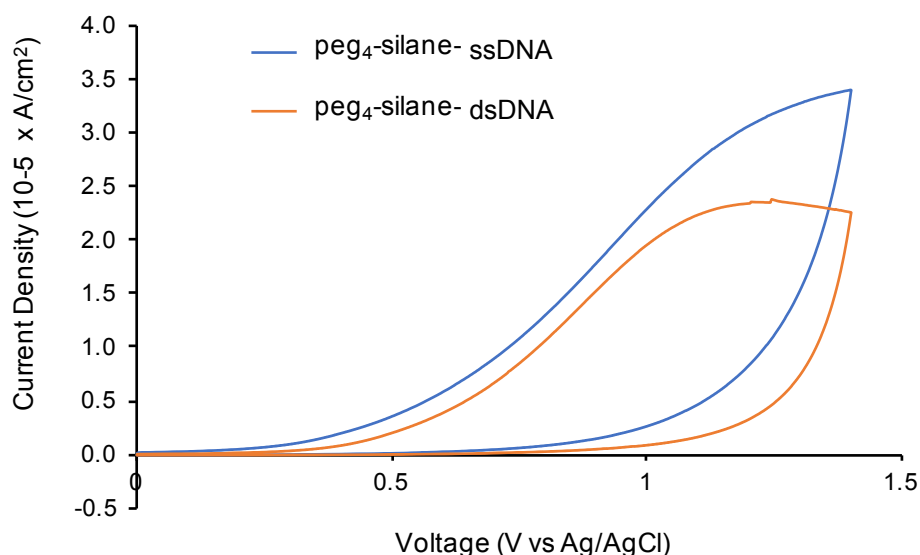
Figure 6. CV chromatogram of the DNA monolayer on silicon surface.

Nijhuis *et al*. have published a plethora of papers investigating Fc terminated monolayers on template stripped gold.[21,28,31,32] They are able to obtain excellent CV data for their monolayers, Figure 7, and can observe slight changes in the monolayer composition based upon the shape of the voltammogram.[45]
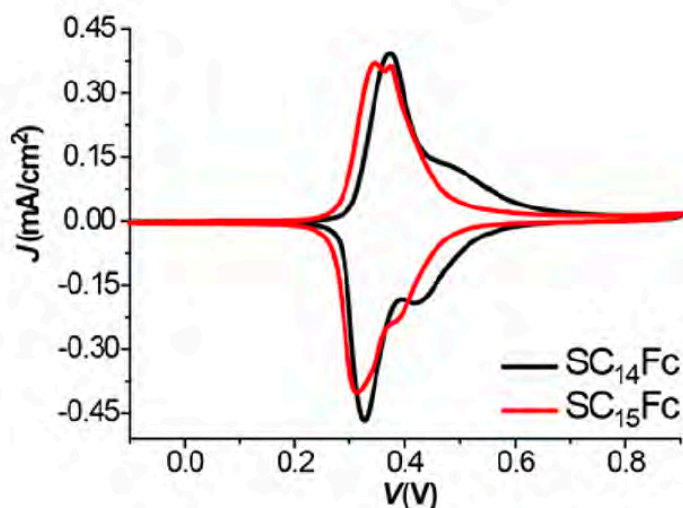
Figure 7. CV showing the characteristic oxidation and reduction peaks associated with Fc groups obtained on a template stripped gold surface.[45]

Due to the nature of monolayers on silicon surfaces, DNA /oxide islands can form in the monolayer, due to incomplete functionalisation,[49] resulting in a rough surface which is known to cause variations in the voltammogram.[45] Therefore, an increased understanding of the monolayer composition is required to better interpret any redox behaviour of the Fc-probe DNA strands.

XPS and CV data suggested that the amount of immobilised Fc-DNA was very low, therefore the sensitive technique of EGaIn, developed by Whitesides *et al.*,[18] was employed to observe the behaviour of the Fc group and investigate the charge transport mechanism through both ssDNA and dsDNA. Certain electronic characteristics associated with surface immobilised Fc in EGaIn plots can be used to understand the composition of the monolayer,[21] and therefore may shed some light on our DNA-based monolayers. The following section describes the use of the EGaIn technique and was carried out in the Nijhuis group, NUS, Singapore.

3.2.3 EGaIn measurements of SiO₂ and SiH

The EGaIn technique was employed to study the charge transport of the DNA monolayers.[18] The molecular junction was formed from an EGaIn tip which was brought into contact with the surface. A current was passed through the monolayer at a positive and negative bias in order to obtain the current density, J. Figure 8 displays the idealised representation of the monolayer, in reality there will likely be defects due to step edges, grain boundaries, impurities, pin holes, oxide islands and etch pits.[27,35,36,50]

The measurements are performed in the solid state in the absence of solvent, therefore the monolayer drives the electrical properties. Statistically large numbers of JV data (N = 300-400) are collected to calculate the yields of working devices and to elucidate any defects in the monolayer. Histograms for each J value at a measured potential are constructed and the data is then fitted to single Gaussian functions which use a nonlinear least-squares fitting method to acquire a log-mean value of J at each potential and the log-standard deviation.
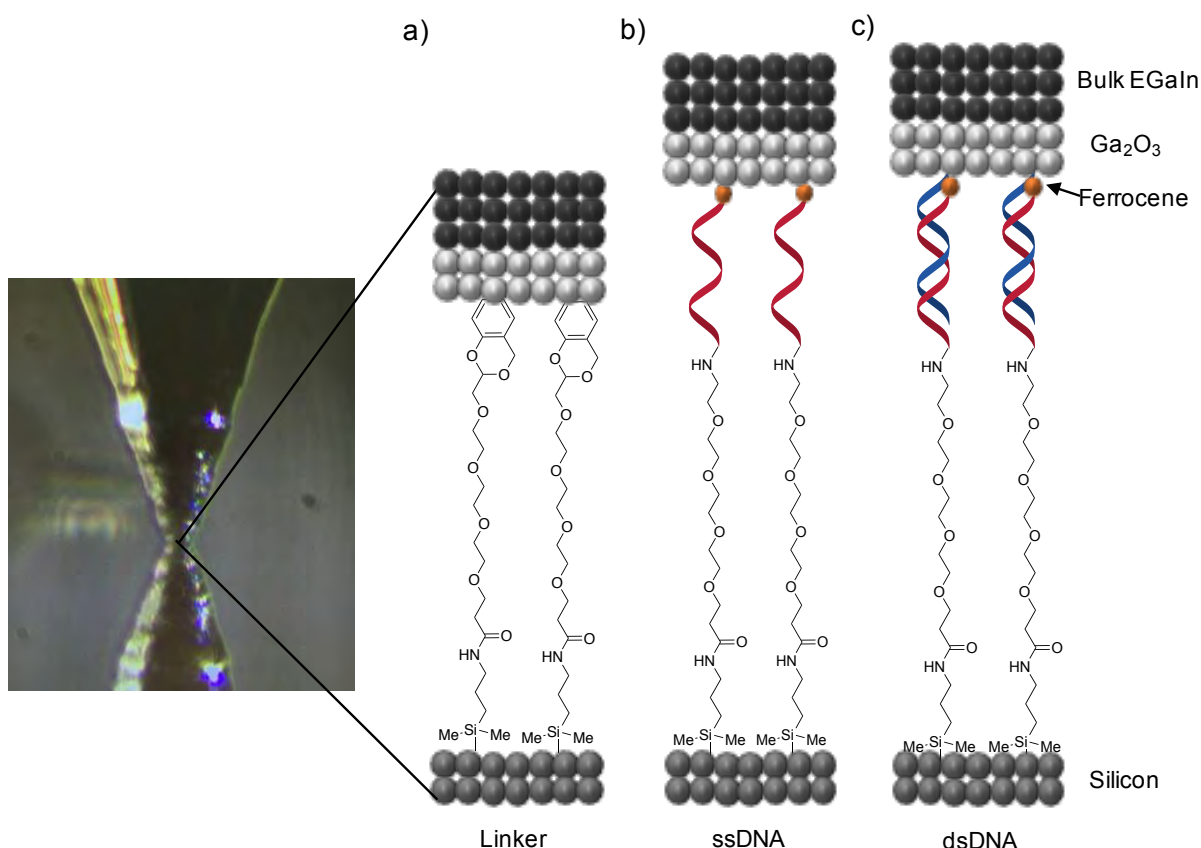
Figure 8. The ideal junctions formed by contact with EGaIn, a) linker b) ssDNa and c) dsDNA.

As the EGaIn technique has not been well documented for monolayers on silicon surfaces,[51] the current density was acquired for bare silicon before and after the etching process. Due to the thick oxide layer present in SiO₂, the current density curve

is expected to display diode type behaviour as the oxide layer acts a Schottky barrier by blocking the current at a negative bias.[52,53] The JV curve for SiO$_2$, displayed in Figure 9a, resembles a Schottky barrier with lower current observed at a negative bias compared to a positive bias. On the other hand, after etching with ammonium fluoride, the oxide layer is removed therefore the diode characteristics should vanish and ohmic contact should be evident. The junctions weren't stable past ±0.5 V. The JV curve for SiH, Figure 9b, displays ohmic contact at low voltages with a shift in curve profile at ±0.1 V indicating a change in transport mechanism. Above ±0.1 V, the curves are again symmetrical illustrating ohmic contact. The charge applied to the silicon surface induces the formation of an oxide layer hence only five junctions were scanned before the curve profile started to change. The JV plots are different for SiO$_2$ and SiH, confirming the removal of oxide and so the charge transport of the linker and DNA molecules were then investigated.
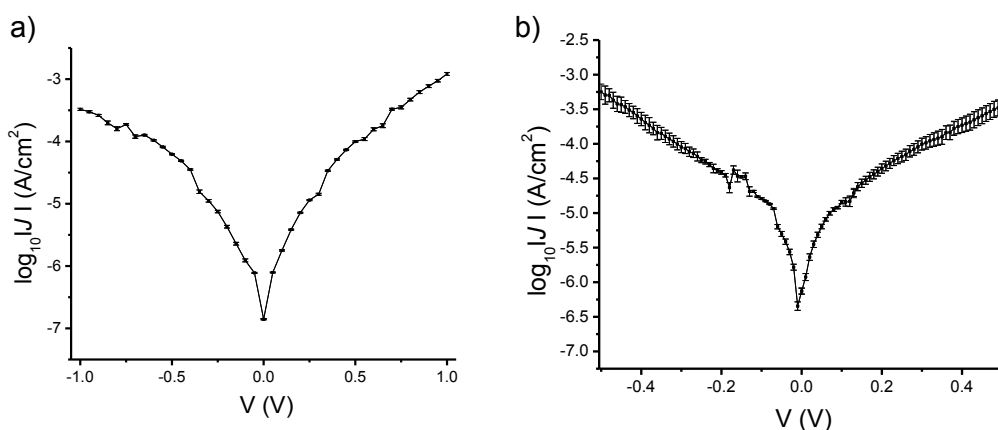
Sample	N of total Junctions	No. of working junctions	Yield	N of trace	Std	Current Density at -0.5 V
SiO$_2$	10	8	80 %	160	0.32	-4.4
SiH	6	5	83. 3%	100	0.49	-3.25

Figure 9. Plot of log/J/ vs V with a bias range of a) -1.0V to +1.0V for SiO$_2$//Ga$_2$0$_3$/EGaIn and b) -0.5 V to +0.5 V for SiH//Ga$_2$0$_3$/EGaIn. The error bars represent the relative standard deviation of the Gaussian function.
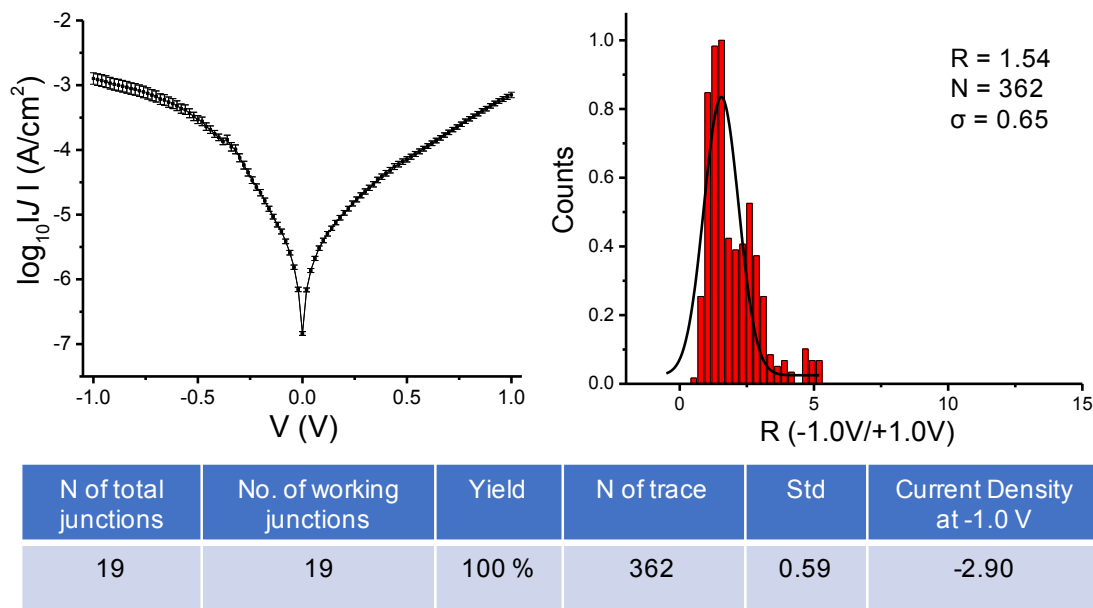
3.2.4 EGaIn junction measurements of peg silane monolayers

The charge transport of Si(100)-OSi(CH$_2$)NHCO(peg)$_4$//Ga$_2$O$_3$/EGaIn monolayers was investigated. It is expected that the linker will exhibit electron tunneling comparable to the alkyl chain monolayers employed by Nijhuis *et al*.[54] The *JV* curve, Figure 10a, exhibits almost symmetrical current density at a positive and negative bias indicating that the current is able to pass through the monolayer in the same manner in both directions. This is highlighted by the low rectification value obtained from the histogram, 1.54, Figure 10b. The rectification is the ratio between the current density at a negative bias compared to the current density at a positive bias, equation 1, providing an internal standard as the values are taken from the same *JV* curve.

$$R = |J(-1.0\ V)|/|J(+1.0\ V)|$$

Equation 1. *The rectification calculation.*

This minimises the ambiguity between comparing the measurements between different junctions. The rectification is calculated by taking current density values of -1.0 V and dividing them by values at +1.0 V; a histogram is then plotted of the determined values to estimate the rectification value. Low rectification is defined as ratios <5, with high rectification known as any value above 5.[21] For example, unmodified alkanethiolate monolayers typically exhibit rectification ratios below 5 whereas molecular diodes can reach rectification ratios of up to 10^5.[34] Here the rectification for the linker monolayer is calculated as 1.54 which is remarkably small, signifying that the charge transport mechanism is most likely electron tunneling occurring in both directions.
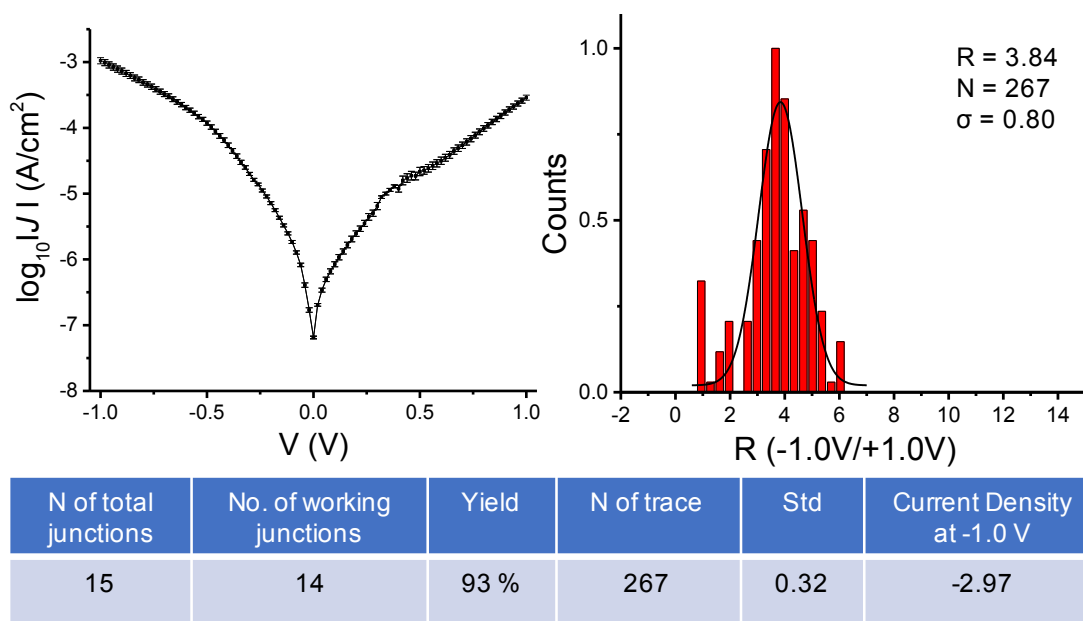
N of total junctions	No. of working junctions	Yield	N of trace	Std	Current Density at -1.0 V
19	19	100 %	362	0.59	-2.90

Figure 10. Plot of log/J/ vs V with a bias range of -1.0V to +1.0V, for Si(100)-0Si(CH₂)NHCO(peg)₄//Ga₂O₃/EGaIn. The error bars represent the relative standard deviation of the Gaussian function. The histogram with a Gaussian fit indicates the value of R. N represents the number of values of R measured for this junction.

3.2.5 EGaIn junction measurements of ssDNA monolayers

The charge transport of Si(100)-OSi(CH₂)NHCO(peg)₄NHssDNAFc//Ga₂O₃/EGaIn monolayers was investigated. With the single stranded DNA attached to the linker molecule, the current density value at -1.0 V is expected to decrease from the -2.90 A/cm² of the linker alone, as the monolayer height should have increased. This is based on the assumption that addition of the ssDNA increases the monolayer thickness, as described in the simplified Simmons equation, equation 2. Simmons determined that the measured current density values have an exponential dependence on the height of the monolayer, *d*. Therefore, as the height increases with the added ssDNA, the current density is expected to decrease exponentially.

$$J = J_0 e^{-\beta d}$$

Equation 2. The Simmons equation.[55]

N of total junctions	No. of working junctions	Yield	N of trace	Std	Current Density at -1.0 V
15	14	93 %	267	0.32	-2.97

Figure 11. Plot of log/J/ vs V with a bias range of -1.0V to +1.0V, for Si(100)-0Si(CH₂)NHCO(peg)₄NHssDNAFc//Ga₂0₃/EGaIn. The error bars represent the relative standard deviation of the Gaussian function. The histogram with a Gaussian fit indicating the value of R.

The *JV* curve and rectification histogram for linker-ssDNA-Fc monolayer is shown in Figure 11. The current density at -1.0V is -2.97 A/cm^2 which is analogous to the value obtained for the linker monolayer (-2.90 A/cm^2). This observation indicates that the DNA portion of the monolayer is not fully stretched and does not make a significant contribution to the height of the monolayer. This is not entirely unexpected and can be explained by the flexibility of single stranded DNA to fold back on itself, as shown in scheme 2. ssDNA in a densely packed SAM should be upright due to the electrostatic repulsion between the negatively charged DNA backbones, however in a less closely packed SAM the repulsion is weaker and therefore a more disordered conformation is expected.[56,57] This folded DNA structure would also account for the inability to obtain ellipsometry for this sample as the DNA would be less ordered and therefore not significantly thicker compared to the linker monolayer. The ferrocene moiety attached to the DNA is also expected to increase the rectification observed, as this is characteristic for Fc monolayers.[21] The rectification for the ssDNA surface is 3.84 which is slightly higher than for the linker (1.54) however, is not significantly different or classed as high rectification. As no significant increase in rectification ratio is observed, this again supports the hypothesis that the ssDNA is coiled and the Fc group is most likely buried in the DNA and not able to contact the EGaIn top electrode which is known to result in a lower rectification ratios.[58] Although no change in the rectification is

observed, the slight hump in the curve at around +0.4 V indicates that the Fc molecule is present somewhere within the monolayer, it simply isn't interfacing with the EGaIn electrode.
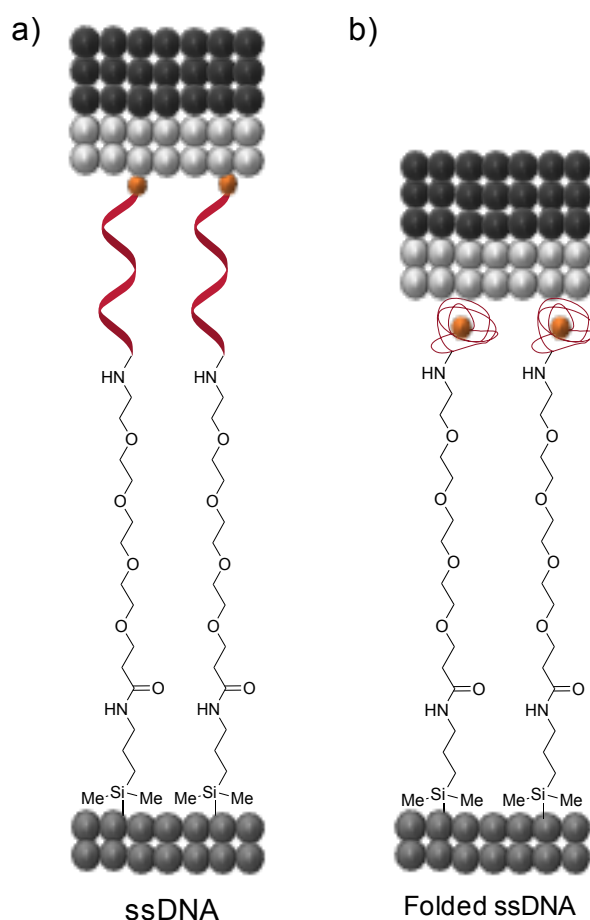
Scheme 2. *Scheme displaying a) a representation of the ideal junction formed for the linker and ssDNA monolayer and b) a portrayal of the most plausible ssDNA conformation in the monolayer.*

3.2.6 EGaIn junction measurements of dsDNA monolayers

The charge transport of Si(100)-OSi(CH$_2$)NHCO(peg)$_4$NHdsDNAFc//Ga$_2$O$_3$/EGaIn monolayers was investigated. When going from ssDNA to dsDNA the height of the monolayer is not expected to increase, rather the thickness of the monolayer increases. However, given the slight reduction in ssDNA monolayer height resulting in an increase in J, and the known rigidity of dsDNA over ssDNA[43] it could be expected that we would see a significant difference in the current density value at -1.0 V. The JV curve and rectification histogram for linker-dsDNA-Fc surface is displayed in Figure 12. Unfortunately, only 5 junctions could be formed and analysed during the time spent in NUS, resulting in the highly variable data within the JV curve presented, which is smoothed upon statistical analysis of larger numbers of data.
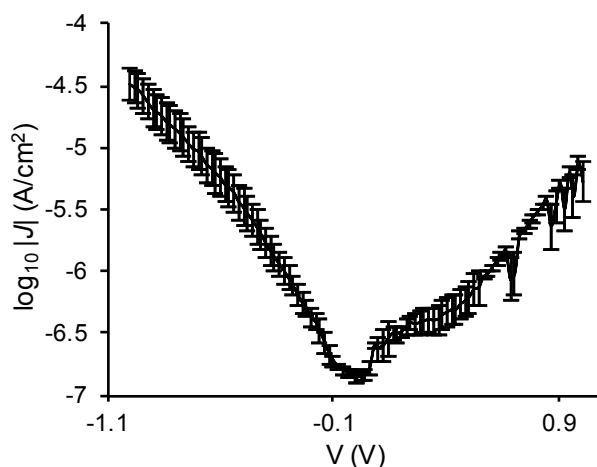
N of total junctions	No. of working junctions	Yield	N of trace	Std	Current Density at -1.0 V
5	5	100 %	100	0.5	-4.48

Figure 12. *Plot of log/J/ vs V with a bias range of -1.0V to +1.0V, for Si(100)-0Si(CH$_2$)NHCO(peg)$_4$NHdsDNAFc//Ga$_2$0$_3$/EGaIn. The error bars represent the relative standard deviation of the Gaussian function.*

However, a considerable decrease in current density is observed at -1.0 V, from -2.97 A/cm^2 to -4.48 A/cm^2 suggesting an increase in monolayer height. It is proposed that the dsDNA is now perpendicular to the monolayer due to the increased rigidity of dsDNA compared to ssDNA as depicted in Figure 9.[59] With the dsDNA in the upright position, the Fc is now located at the exposed surface of the monolayer and is able to contact with the EGaIn to take part in charge transport. This is also evident by the increased rectification of 12.58 observed for this monolayer compared to the linker (1.54) and the linker/ssDNA monolayers (3.84). This observation is a typical feature for monolayers comprising of a terminal Fc group[32] and can be explained by the energy level diagram presented in Scheme 3.
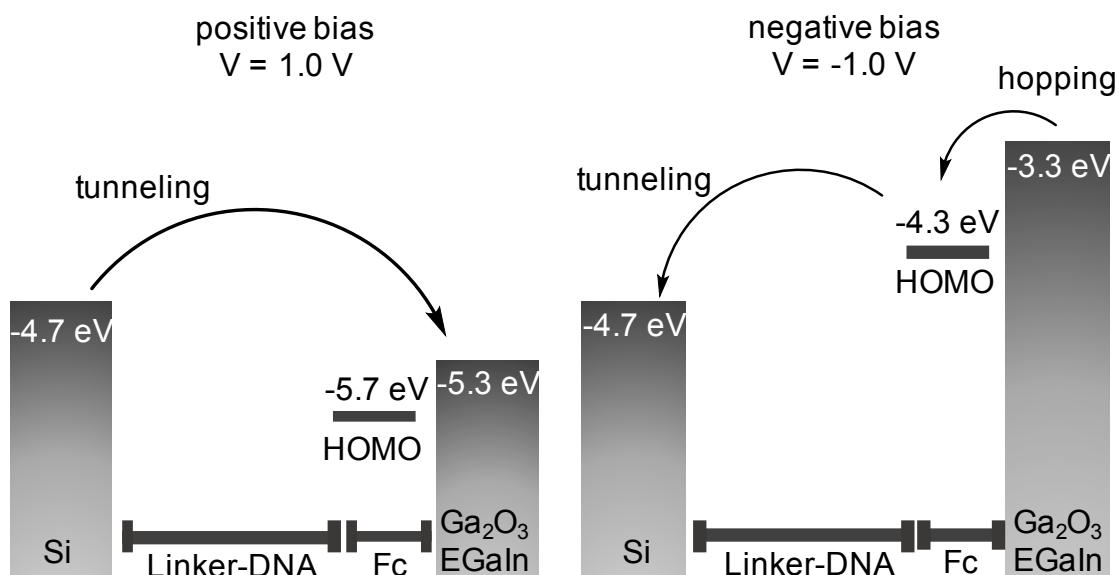
Scheme 3. Energy level diagrams of the dsDNA junctions at both +1.0 V bias and -1.0 V. At a negative bias the Fc moiety is able to take part in the charge transport as the HOMO level is situated inbetween the fermi level of both electrodes.

At a positive bias the HOMO level of the Fc group falls below the fermi levels of both the silicon and the EGaIn electrode and therefore is unable to take part in the charge transport mechanism. This finding signifies that the main mechanism of transport is tunneling which is slow and unfavourable as the current has to pass through the full length of the monolayer with a tunneling barrier equal to $d_{linker-DNA}$ + d_{Fc}.[60-62] In an ideal diode, the current at a positive bias would be negligible however in typical diodes a small amount of current is able to pass through the barrier and is known as leakage current which is known to increase in more defective SAMs.[32,63] Although rectification is observed for this sample, it is still very low compared to other previously studied molecular rectifiers indicating there is a large amount of leakage current in this system. On the other hand, at a negative bias, the HOMO level of the Fc unit now falls in between the fermi levels of both electrodes and so is able to take part in the charge transport. Charge hopping occurs from the EGaIn top electrode to the Fc, followed by tunneling through the rest of the monolayer which is much more favourable and therefore results in a higher current density. The change in charge transport mechanism reduces the width of the tunneling barrier from $d_{linker-DNA}$ + d_{Fc} to $d_{linker-DNA}$. The difference in the charge transport mechanisms observed by the JV curves has the potential to differentiate between ssDNA and dsDNA in sensing applications.

### 3.2.5 EGaIn junctions of different length DNA monolayers

With a view to observe the exponential dependence of current density on the length for these particular linker/DNA monolayers, new surfaces were prepared with DNA of 3 different lengths, all with a terminal ferrocene, shown in Table 3. As the length of the DNA strand increases, the current density value should decrease based upon the Simmons equation as described earlier. Once the JV curves from different DNA length monolayers are acquired, the tunneling decay coefficient, β, can then be calculated from the Simmons equation, which is known to differ between monolayer composition and height.[23,29,64,65] Previously reported beta values for DNA oligomers vary depending on the sequence: He *et al.* report beta values ranging from 0.44 Å^{-1} to 0.61 Å^{-1} for single nucleobase monolayers,[66] whereas the Barton group report values from 0.05 Å^{-1} to 1.00 Å^{-1} depending on the length of the oligomer and the effect of a linker molecule.[67,68] The difference in current density and rectification ratio between the ssDNA and the dsDNA monolayers should also be evident for each of the DNA lengths.

Table 3. DNA sequences of the ssDNA and dsDNA strands used for the length comparison.

Name	DNA sequence (X=amino-C6 Y=Fc)
12-mer ssDNA	5'-Y-AGATGTAGTTAG-X-3'
24-mer ssDNA	5'-Y-AGATGTAGTTAGCAATCGGTCCTT-X-3'
36-mer ssDNA	5'-Y-AGATGTAGTTAGCAATCGGTCCTTGTTGTAAGATGT-X-3'
12-mer dsDNA	5'-Y-AGATGTAGTTAG-X-3' 3'- TCTACATCAATC -5'
24-mer dsDNA	5'-Y-AGATGTAGTTAGCAATCGGTCCTT-X-3' 3'- TCTACATCAATCGTTAGCCAGGAA -5'
36-mer dsDNA	5'-Y-AGATGTAGTTAGCAATCGGTCCTTGTTGTAAGATGT-X-3' 3'- TCTACATCAATCGTTAGCCAGGAACAACATTCTACA -5'

The JV plots and rectification ratio histograms for each of the different surfaces are shown in Figure 13-15. Unfortunately, no difference in current density is observed between the various lengths of DNA and the difference between ssDNA and dsDNA previously detected is not visible. Each of the curves resembles the JV plot obtained for the bare silicon oxide. This observation is attributed to a build-up of oxide layer which is masking any variations between samples caused by the length of time between synthesis of the monolayers and the electrical measurements on the EGaIn

setup.[69] This highlights the importance of the removal of the oxide layer and the preparation of fresh samples for the EGaIn measurements and suggests these surfaces decompose rapidly with exposure to oxygen and moisture. The JV curve is dominated by the oxide layer, therefore the expected decrease in current density is not observed and determination of a beta value is not possible. There is no difference in rectification upon hybridisation of the single stranded surface, the JV curve resembles the typical features of the SiO$_2$ monolayer. Figures 13-15 display the JV plots of ssDNA and dsDNA monolayer for the three different length DNA strands. In each case the current density change and rectification differences are masked by the oxide layer.
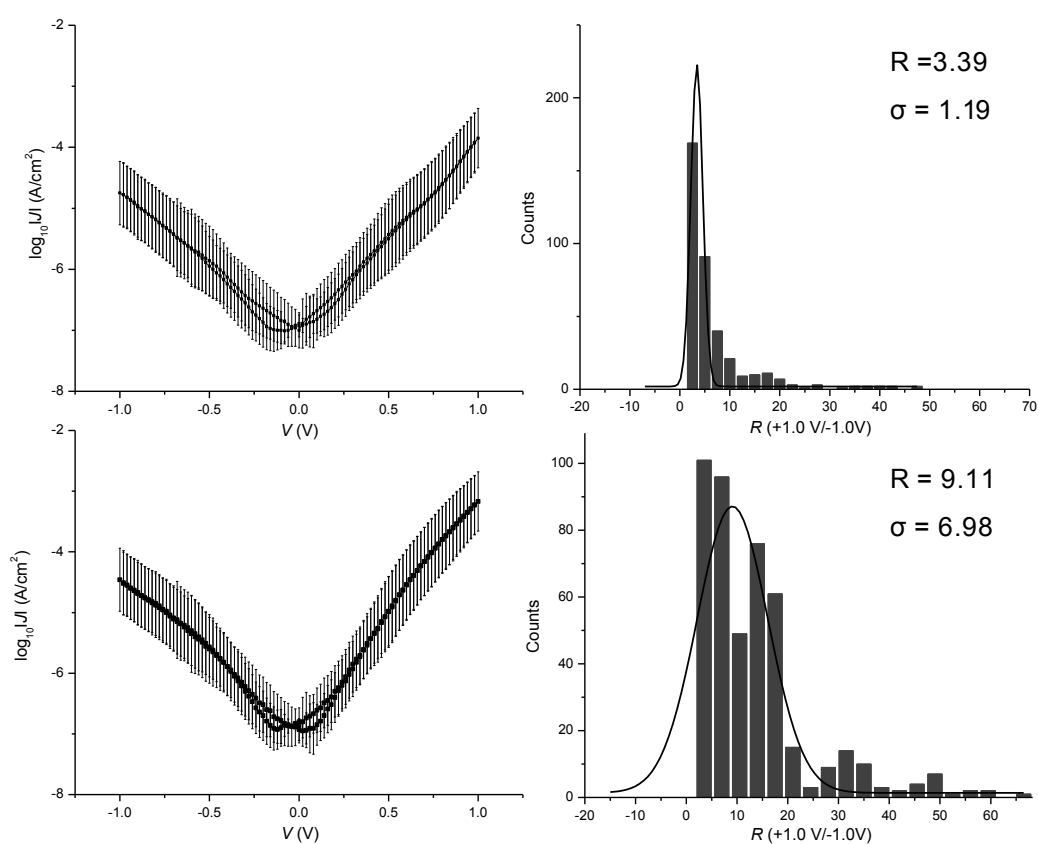
Sample	N of total Junctions	No. of working junctions	Yield	N of trace	Std	Current Density at -0.5 V
ssDNA	20	18	90 %	360	0.62	-4.4
dsDNA	20	19	95 %	380	0.57	-3.25

Figure 13. Plot of log/J/ vs V with a bias range of -1.0V to +1.0V, for a) Si(100)-0Si(CH$_2$)NHCO(peg)$_4$NH12merssDNAFc//Ga$_2$0$_3$/EGaIn and b) Si(100)-0Si(CH$_2$)NHCO(peg)$_4$NH12merdsDNAFc//Ga$_2$0$_3$/EGaIn. The error bars represent the relative standard deviation of the Gaussian function. The histogram with a Gaussian fit indicates the value of R.
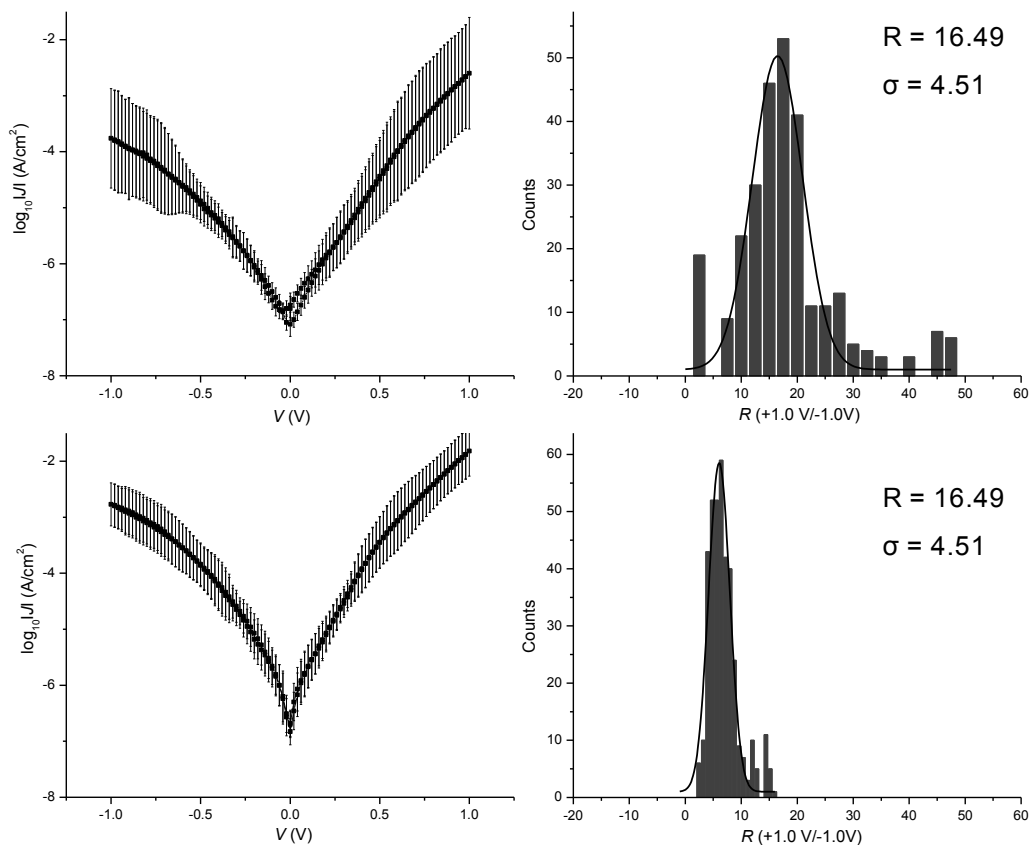
Sample	N of total Junctions	No. of working junctions	Yield	N of trace	Std	Current Density at -1.0 V
ssDNA	20	19	95 %	380	0.73	-3.80
dsDNA	20	20	100 %	400	0.41	-2.86

Figure 14. *Plot of log/J/ vs V with a bias range of -1.0V to +1.0V, for a) Si(100)-0Si(CH₂)NHCO(peg)₄NH24merssDNAFc//Ga₂0₃/EGaIn and b) Si(100)-0Si(CH₂)NHCO(peg)₄NH24merdsDNAFc//Ga₂0₃/EGaIn. The error bars represent the relative standard deviation of the Gaussian function. The histogram with a Gaussian fit indicates the value of R.*

R = 8.91
σ = 3.14

R = 12.46
σ = 3.38
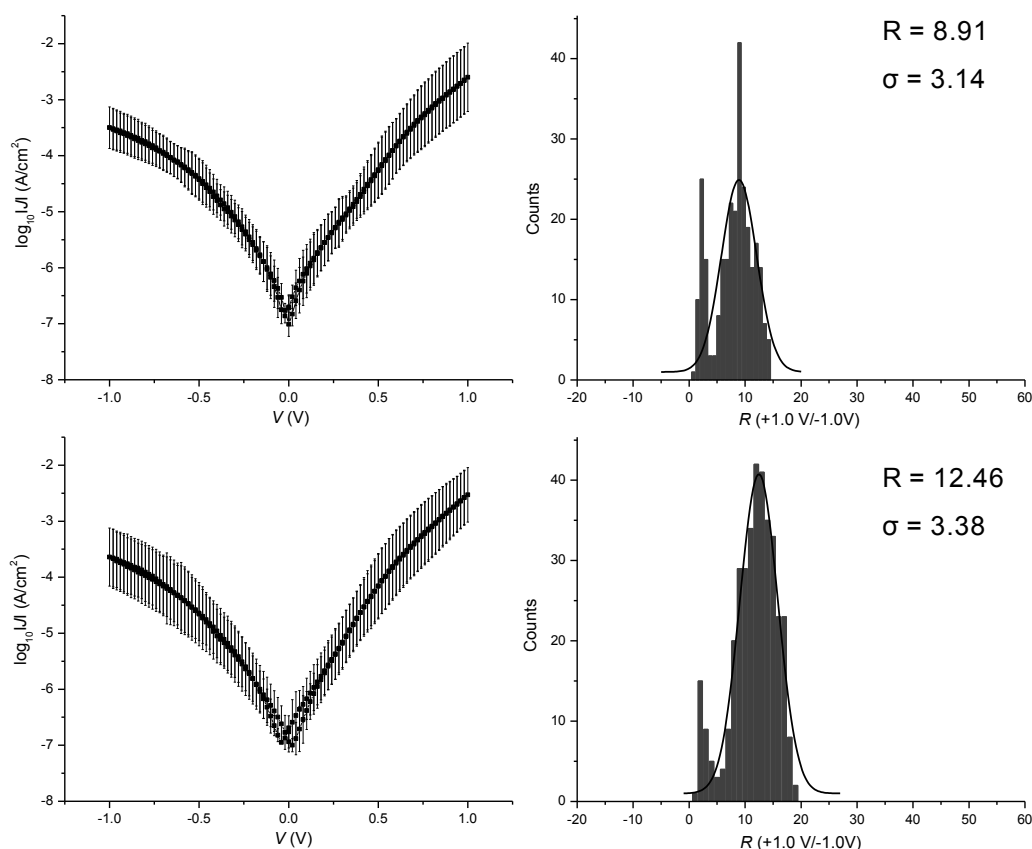
Sample	N of total Junctions	No. of working junctions	Yield	N of trace	Std	Current Density at -1.0 V
ssDNA	20	20	100 %	400	0.53	-3.52
dsDNA	20	20	100 %	400	0.57	-3.62

Figure 15. *Plot of log/J/ vs V with a bias range of -1.0V to +1.0V, for a) Si(100)-0Si(CH₂)NHCO(peg)₄NH36merssDNAFc//Ga₂0₃/EGaIn and b) Si(100)-0Si(CH₂)NHCO(peg)₄NH36merdsDNAFc//Ga₂0₃/EGaIn. The error bars represent the relative standard deviation of the Gaussian function. The histogram with a Gaussian fit indicates the value of R.*

Although a considerable amount of the detail usually observed in the JV curves is unattainable, there are still several characteristics in the JV curves that reveal information concerning the composition of the monolayer. The Fc constituent is detectable in all JV curves by the ridge in the curve profile at approximately +0.6 V representing a change in charge transport at this bias value. This is a well-known characteristic of Fc-terminated monolayers and is once more explained by the fermi level diagram and signifies the switch between charge hopping and electron tunneling.[21] The hysteresis observed in each of the graphs again is evidence of the presence of the Fc group, and the non-zero current observed at low bias values is

thought to be due to the oxidation-reduction mechanism of the Fc.[21] These features are difficult to resolve in the average Gaussian *J*V curves, however upon examination of a single *J*V curve produced from one junction, see Figure 16, the attributes are more easily observable.
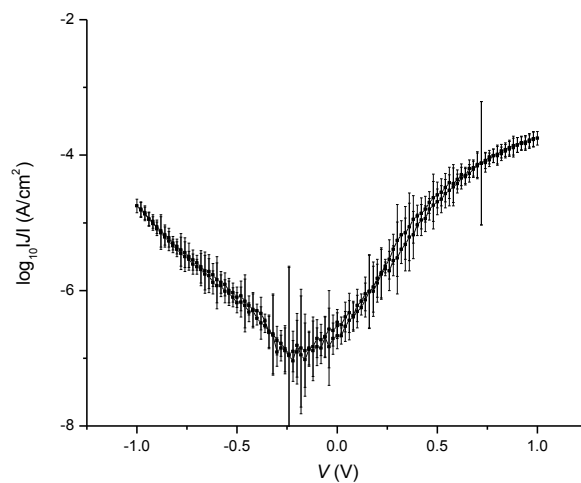
Figure 16. *A single current density curve for 12mer dsDNA highlighting the Fc characteristics.*
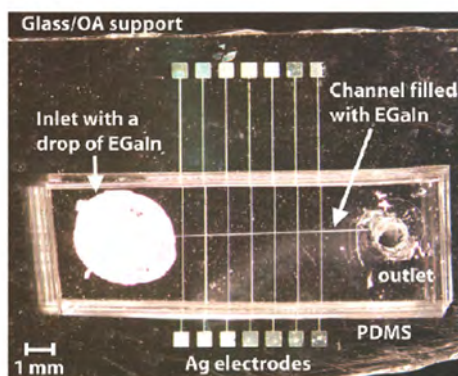
3.2.6 Temperature dependent measurements

Temperature dependent measurements of the current density curves would further confirm the difference in charge transport mechanism between ssDNA and dsDNA. Electron tunneling occurs when an electron burrows through the energy gap regardless of the barrier height and is therefore temperature independent.[70] Whereas charge hopping is temperature dependent as the electron requires an activation energy to hop and overcome the energy barrier.[21] Temperature dependence measurements were carried out on the 12-mer ssDNA and dsDNA surfaces used in the 3.2.5, Figure 17 and 18.
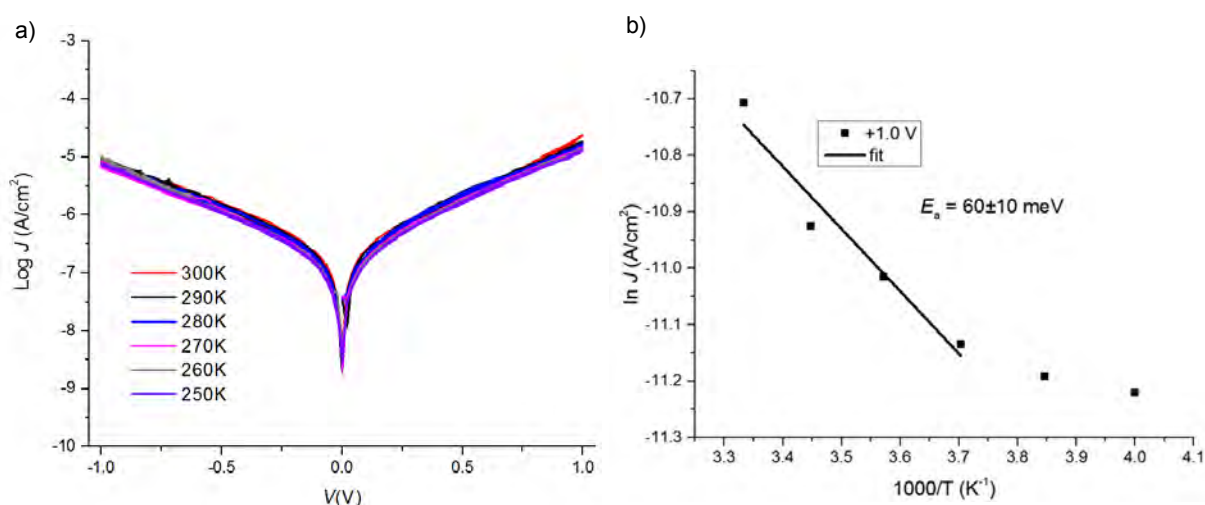
Figure 17. *Temperature-dependent measurements of the junctions formed from the ssDNA samples. a) J(V) curves of Si(100)-0Si(CH₂)NHCO(peg)₄NH12merssDNAFc//Ga₂0₃/EGaIn junctions measured at 250-300 K at 10 K intervals. b) Corresponding Arrhenius plot for J at +1.0 V.*

The temperature was varied from 250 K to 300 K for ssDNA samples and from 220 K to 350 K for dsDNA samples and a current density curve is taken at each temperature. A polydimethylsiloxane (PDMS) device is placed over the sample with a hole containing the EGaIn top electrode allowing contact with the surface as described by Nijhuis *et al*.[21]

Figure 18. PDMS device used to carry out the temperature dependent measurements.[21]

The ssDNA surface was not stable enough to record data above 300 K. This instability could be due to the thickness of the monolayer as it is known to be difficult to obtain temperature dependence measurements for thin monolayers.[71] The natural log of J is plotted against 1000/T (T^{-1}) in order to calculate an activation energy and graphically observe any temperature dependence, Figure 17b. As seen in the *JV* curve, Figure 17a, the change in temperature has no marked effect on the current density *JV* curve which in the correlated Arrhenius plot provides a calculated activation energy of only 60 meV. Therefore, the suggested mechanism of charge transport in the ssDNA monolayer is electron tunneling which is in agreement with the prediction from the room temperature *JV* analysis.
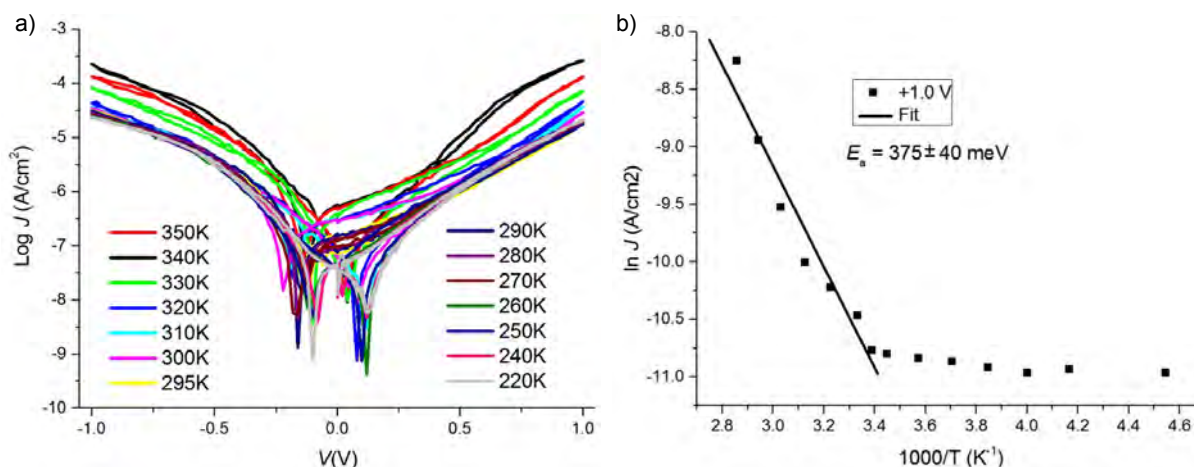

Figure 18. Temperature-dependent measurements of the junctions formed from the dsDNA samples. A) J(V) curves of Si(100)-0Si(CH₂)NHCO(peg)₄NH12merdsDNAFc//Ga₂0₃/EGaIn junctions measured at 250-300 K at 10 K intervals. B) Corresponding Arrhenius plot for J at +1.0 V.

In the dsDNA temperature profile, Figure 18, the samples are stable over the full range of temperatures from 220 K to 350 K. The dsDNA monolayer shows temperature independence up until 295 K, after which temperature dependence is then observed,

see Figure 18b, which clearly indicates a marked change in gradient at 3.4 K^{-1}. The calculated activation energy of 375 meV is much higher compared to the ssDNA value of 60 meV noted earlier.

Nijhuis *et al*. conducted an investigation into the rectification dependence on the thickness of the monolayer.[71] It was found that in general for their monolayers, no rectification is observed for monolayers with a thickness of <20 nm however a sharp increase in rectification value in monolayers with a thickness of >20 nm. The thickness at which the switch in rectification is observed changes with different monolayer compositions, for example the polyferrocenylbutyl methacrylate (PFBMA) brush exhibits the shift at around 14 nm thickness, whereas the polyferrocenylmethyl methacrylate (PFMMA) brush displays the change at 20 nm. The temperature dependence plot for PFMMA demonstrates a temperature independence up to 300 K followed by temperature dependence above 300 K, Figure 19, much like the plots obtained for the dsDNA monolayer sample in this project. It is therefore conceivable that the temperature dependence change at 295 K observed in the dsDNA sample, Figure 18, is due to the thickness of the monolayer rather than any DNA denaturation.
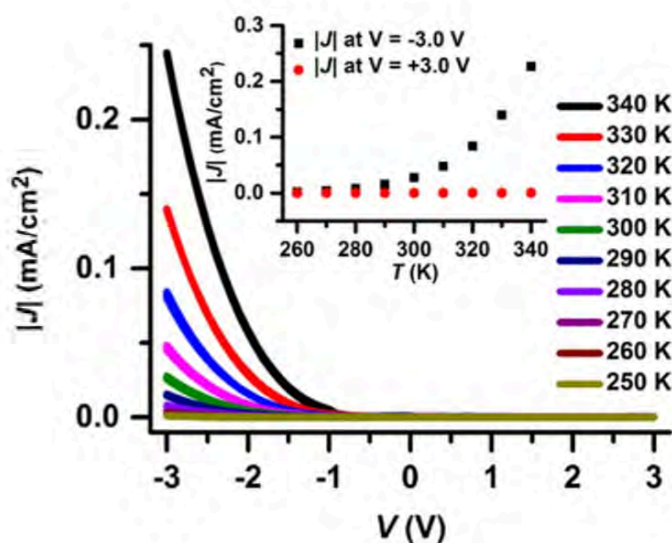
Figure 19. The values of |J| at -3.0V for PFMMA brushes exhibiting temperature dependence above 300 K[71]

The predicted melting temperature of the 12-mer duplex is 305 K,[72] so it is thought that the DNA is starting to denature at this temperature causing the differences in current density above 300 K (3.35 K^{-1} on the graph in Figure 18b). This disagrees with the room temperature current density analysis as the dsDNA was expected to show temperature dependence due to the hypothesis that the mechanism in this type of

monolayer is charge hopping. The non-zero current at low bias values is however visible in the dsDNA temperature profiles and not in the ssDNA supporting the theory that the Fc is in contact with the EGaIn in the dsDNA samples but most likely buried in the ssDNA sample.

In order to acquire a more accurate set of temperature dependence measurements, the experiments should be carried out on the longer 36-mer DNA surfaces where the predicted melting temperature is 344.4 K. Since this temperature is higher than those used in the temperature-dependent studies, DNA denaturation should not occur and therefore not affect the results obtained.

3.2.7 AFM characterisation of the silicon surface after etching

It is imperative to start with a flat surface before modification to gain monolayer uniformity and acquire the best possible JV curves from the EGaIn technique. Further investigation into the roughness of the silicon surface used in this project is required. As discussed previously, an uneven surface results in several defects in the monolayer composition. To clarify if the initial removal of the oxide layer was successful and resulted in surfaces similar to those reported,[40] AFM images were taken of the silicon surface before and after the etching process with ammonium fluoride, Figure 19.
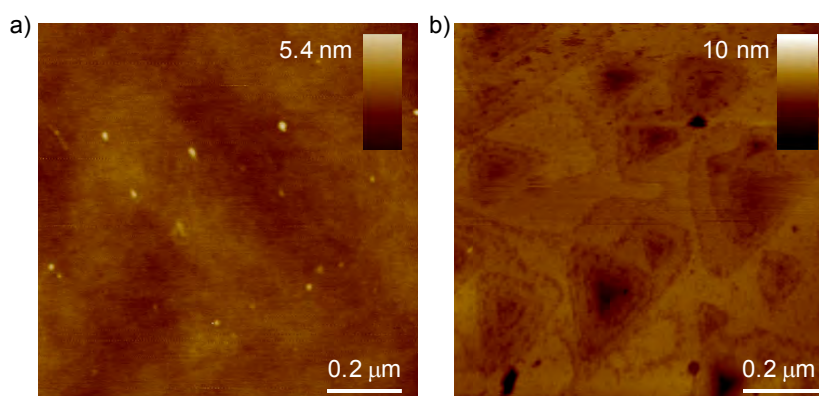
Figure 19. AFM images of a) SiO_2 and b) SiH after the etching process.

There is a clear difference observable in the AFM images between the SiO_2 and the SiH surface indicating the surface has been etched by the ammonium fluoride. However, the SiH image is similar to that for one for the surfaces reported by Allongue *et al.* exhibiting comparable triangular type grooves in the surface after the etching process.[40] The triangular patterns are a result of incomplete degassing of the ammonium fluoride solution, so the oxygen remains in the solution affecting the etching mechanism. Inverted pyramid-like holes are then created which produces an imperfect, rough surface and hence increases the quantity of defects in the monolayer, particularly grain boundaries resulting in thin-area defects.[64] In order to minimise these defects, an improved system for degassing the ammonium fluoride is required to eliminate as many monolayer defects as possible. Another possibility would be to switch to a template-stripped surface, e.g. silver or gold, which are recognised to have remarkably flat surfaces. Using a metallic surface would also increase the conductivity observed in both the JV curves from room temperature and temperature-dependent studies enabling clearer distinctions to be made between samples.

3.3 Conclusion

A ferrocene terminated DNA monolayer was successfully synthesised on p-type (100) silicon surfaces using a peg4 siloxane linker molecule to tether the DNA to the surface. The modified surface was characterised by XPS, AFM, CV and contact angle measurements. With a view to study the charge transport mechanism through the DNA monolayers, the EGaIn technique was employed where current density measurements were obtained at various bias values to obtain JV curves. No change in current density value was observed between the bare linker and the ssDNA surface indicating that the ssDNA is most likely coiled rather than fully stretched and so not contributing to the height of the monolayer. A considerable difference in JV curve profile is observed between ssDNA and dsDNA. The current density at -1.0 V decreases and an increase in rectification is observed signifying the change in charge transport mechanism. The difference in charge transport mechanism has the potential to discriminate between ssDNA (electron tunneling) and dsDNA (charge hopping and tunneling) offering an application in sensing devices.

In order to obtain a beta value and observe the height dependence on the current density, the experiments would need to be repeated with freshly prepared samples. The temperature measurements should be repeated with a longer DNA sequence to confirm that any changes observed are not due to duplex denaturation. Furthermore these experiments would clarify the charge transport mechanisms observed.

Moving to a template-stripped gold surface would drastically improve issues with surface flatness identified in working with silicon. The results obtained would also be more comparable to the extensively studied alkylthiolate monolayers and result in improved CV plots by using a conducting surface.

3.4 Experimental

Chemical reagents

All chemical reagents were purchased from Sigma Aldrich and used as received without further purification. p-Si(100) B-doped wafers, 525 micron thickness, 1-10 Ohm cm, 100 mm diameter, single-side polished, miscut angle <0.5°) were purchased from Compart Technology (Cambridge, UK). APEGDMES was purchased from NewChem Technologies Limited. DNA was purchased from ATDBio (Southampton, U.K.). EGaIn was purchased from Sigma Aldrich.

Pretreatment of silicon surface

Highly doped Si (100) wafers were diced into 1 cm^2 chips. The chips were wiped with acetone, IPA and NP-H$_2$O and sonicated in acetone, IPA and NP-H$_2$O for 15 mins sequentially and dried with N$_2$. The chips were chemically oxidised in freshly-prepared piranha solution (4:1 H$_2$SO$_4$:H$_2$O$_2$) for 10 min at 50 °C, rinsed thoroughly in NP-H$_2$O and dried with N$_2$. The chips were etched in 40% aqueous NH$_4$F for 15 min under an Ar atmosphere. The etching procedure was carried out in a locally-constructed gas tight PTFE cell which allows the removal of all dissolved oxygen by Ar purging for 1 hr. The H-terminated chips were rinsed with NP-H$_2$O, dried with N$_2$ and used immediately for monolayer preparation.

Linker attachment to silicon surface

The pre-cleaned silicon chips were immersed in APEGDMES (233 µM), dissolved in toluene, at 65 °C for 16 h. The chips were washed with toluene, ethanol and NP-H$_2$O 3 times sequentially before being placed in a vacuum oven at 120 °C for 40 min.

DNA attachment to linker

DNA probe solution (40 µL, 100µM) in 10% acetic acid solution was drop cast onto the silicon chips for 1 h in a humid environment. NaCNBH$_3$ (40 µL, 16 µM) in 50 % MeOH solution was deposited on top of the probe solution for a further 2 h in a humid environment. The chips were rinsed with phosphate buffered saline (0.5 x) and excess water to remove any physisorbed DNA molecules. Chips were dried with N$_2$.

DNA hybridisation

DNA target solution (40 μL, 200 nM) in PBS buffer (0.5 x) was drop cast onto the silicon chips for 15 min in a humid environment. Chips were washed with PBS buffer (0.5 x) 3 times and dried with N_2.

Contact angle

Contact angle measurements were performed on a KSV Cam 101 (KSV Instruments Ltd., Finland) using built-in CAM 2008 software. A 1 μL drop of NP-H_2O was dropped onto the surface. The software was used to estimate the angle of the water droplet on the surface. 10 measurements for each sample were obtained. Measurements collected where there was more than a 2° difference in the left and right angle of the droplet were discarded. Measurements which were more than 2 standard deviations away from the average value were also discarded.

AFM

AFM images were obtained using a Dimension V with a nanoscope controller (Veeco Instruments Inc., Metrology Group, Santa Barbara, CA). Nanoscope 8 software was used to collect the data.

XPS

Spectra were acquired on a Thermo-Fisher Scientific K-Alpha instrument using monochromated Al X-rays (1486.6 eV) and the spot size was 400 μm. A pass energy of 200 eV was used for survey scans and 20 eV for narrow scans. Cu, Ag and Au samples were used to calibrate the instrument for energy and intensity. Spectra were fitted with a combination of components represented by Gaussian-Lorentzian convolutions and a Shirley background using the CasaXPS software (Casa Software Ltd, UK).

Cyclic voltammetry

Cyclic voltammograms were recorded using an Ivium CompactStat potentiostat. All potentials in aqueous 0.1 M KCl electrolyte were recorded against an Ag/AgCl wire reference electrode and a platinum wire was used as the counter electrode. An Ivium ModuLight LED light source was used to provide white light to the silicon surface during cyclic voltammetry.

Ellipsometry

Ellipsometry was performed on a Variable Angle Spectroscopic Ellipsometer, V.A.S.E, M190-1700, Digipol. The model for fitting was based upon a 3-layer model to elucidate the monolayer thickness:

EGaIn Junction Formation

A home-built 'EGaIn set up', was used which formed the top-contact using the eutectic metal alloy EGaIn (75.5% Ga and 24.5% In by weight). The EGaIn is moulded into a cone shape tip in order to form large area junctions (~300 uM^2) with the samples. Statistically large numbers of data are collected (approximately 300 scans recorded for each sample: 20 J(V) scans each from 15-20 junctions). The J(V) traces are recorded by sweeping between the following bias values; 0 V → +1.0 V → 0 V → -1.0 V → 0 V, with a 0.1s delay and in steps of 40 mV. The average $\log_{10}|J|$ values are calculated for each bias value resulting in log-average *J*(V) curves and the determination of the values for $\log_{10}|J|$.

Temperature dependence measurements

Temperature dependence measurements were performed in DC by the application of the bias voltage and the current measured by a Keithley 6430 sub-femtoamp remote source meter. A Keithley 2400 was used to gate the transistor. The sample was placed in a sample holder with a temperature control immersed in a dewar of liquid nitrogen.

3.5 References

1   Zhang, H., Tan, H., Wang, R., Wei, W. & Yao, S. Immobilization of DNA on silver surface of bulk acoustic wave sensor and its application to the study of UV-C damage. *Analytica Chimica Acta* **374**, 31-38 (1998).

2   Strother, T., Cai, W., Zhao, X., Hamers, R. J. & Smith, L. M. Synthesis and Characterization of DNA-Modified Silicon (111) Surfaces. *Journal of the American Chemical Society* **122**, 1205-1209 (2000).

3   Hilliard, L. R., Zhao, X. & Tan, W. Immobilization of oligonucleotides onto silica nanoparticles for DNA hybridization studies. *Analytica Chimica Acta* **470**, 51-56 (2002).

4   Petrovykh, D. Y., Kimura-Suda, H., Whitman, L. J. & Tarlov, M. J. Quantitative Analysis and Characterization of DNA Immobilized on Gold. *Journal of the American Chemical Society* **125**, 5219-5226 (2003).

5   Philip Wong, H. S. Beyond the conventional transistor. *Solid-State Electronics* **49**, 755-762 (2005).

6   Yan, F., Mok, S. M., Yu, J., Chan, H. L. W. & Yang, M. Label-free DNA sensor based on organic thin film transistors. *Biosensors and Bioelectronics* **24**, 1241-1245 (2009).

7   Scheer, E. A DNA that conducts. *Nature Nanotechnology* **9**, 960 (2014).

8   Beebe, J. M., Engelkes, V. B., Miller, L. L. & Frisbie, C. D. Contact Resistance in Metal−Molecule−Metal Junctions Based on Aliphatic SAMs: Effects of Surface Linker and Metal Work Function. *Journal of the American Chemical Society* **124**, 11268-11269 (2002).

9   Chen, F., Li, X., Hihath, J., Huang, Z. & Tao, N. Effect of Anchoring Groups on Single-Molecule Conductance: Comparative Study of Thiol-, Amine-, and Carboxylic-Acid-Terminated Molecules. *Journal of the American Chemical Society* **128**, 15874-15881 (2006).

10   Xu, B. & Tao, N. J. Measurement of Single-Molecule Resistance by Repeated Formation of Molecular Junctions. *Science* **301**, 1221-1223 (2003).

11   Slowinski, K., Chamberlain, R. V., Miller, C. J. & Majda, M. Through-Bond and Chain-to-Chain Coupling. Two Pathways in Electron Tunneling through Liquid Alkanethiol Monolayers on Mercury Electrodes. *Journal of the American Chemical Society* **119**, 11910-11919 (1997).

12   McCreery, R. L., Wu, J. & Prasad Kalakodimi, R. Electron transport and redox reactions in carbon-based molecular electronic junctions. *Physical Chemistry Chemical Physics* **8**, 2572-2590 (2006).

13   Kronemeijer, A. J. *et al.* Reversible Conductance Switching in Molecular Devices. *Advanced Materials* **20**, 1467-1473 (2008).

14   Zrnic, D. & Swatik, D. S. On the resistivity and surface tension of the eutectic alloy of gallium and indium. *Journal of the Less Common Metals* **18**, 67-68 (1969).

15   Dickey, M. D. *et al.* Eutectic Gallium-Indium (EGaIn): A Liquid Metal Alloy for the Formation of Stable Structures in Microchannels at Room Temperature. *Advanced Functional Materials* **18**, 1097-1104 (2008).

16   S.J. French, D.J. Saunders & Ingle, G. W. The System Gallium-Indium. *J. Phs. Chem* **42**, 265-274 (1938).

17   Seitz, O. *et al.* Effect of Doping on Electronic Transport through Molecular Monolayer Junctions. *Journal of the American Chemical Society* **129**, 7494-7495 (2007).

18   Chiechi, R. C., Weiss, E. A., Dickey, M. D. & Whitesides, G. M. Eutectic Gallium–Indium (EGaIn): A Moldable Liquid Metal for Electrical Characterization of Self-Assembled Monolayers. *Angewandte Chemie* **120**, 148-150 (2008).

19   Cademartiri, L. *et al.* Electrical Resistance of AgTS–S(CH2)n−1CH3//Ga2O3/EGaln Tunneling Junctions. *The Journal of Physical Chemistry C* **116**, 10848-10860 (2012).

20   Ryan, J. L., Michael, D. D., George, M. W. & David, A. W. Viscoelastic properties of oxide-coated liquid metals. *Journal of Rheology* **53**, 1305-1326 (2009).

21   Nijhuis, C. A., Reus, W. F., Barber, J. R., Dickey, M. D. & Whitesides, G. M. Charge Transport and Rectification in Arrays of SAM-Based Tunneling Junctions. *Nano Letters* **10**, 3611-3619 (2010).

22   Rothemund, P., Morris Bowers, C., Suo, Z. & Whitesides, G. M. Influence of the Contact Area on the Current Density across Molecular Tunneling Junctions Measured with EGaln Top-Electrodes. *Chemistry of Materials* **30**, 129-137 (2018).

23   Nijhuis, C. A., Reus, W. F., Barber, J. R. & Whitesides, G. M. Comparison of SAM-Based Junctions with Ga2O3/EGaln Top Electrodes to Other Large-Area Tunneling Junctions. *The Journal of Physical Chemistry C* **116**, 14139-14150 (2012).

24   Wimbush, K. S. *et al.* Control over Rectification in Supramolecular Tunneling Junctions. *Angewandte Chemie International Edition* **49**, 10176-10180 (2010).

25   Pourhossein, P. & Chiechi, R. C. Directly Addressable Sub-3 nm Gold Nanogaps Fabricated by Nanoskiving Using Self-Assembled Monolayers as Templates. *ACS Nano* **6**, 5566-5573 (2012).

26   Nerngchamnong, N. *et al.* Supramolecular Structure of Self-Assembled Monolayers of Ferrocenyl Terminated n-Alkanethiolates on Gold Surfaces. *Langmuir* **30**, 13447-13455 (2014).

27   Nijhuis, C. A., Reus, W. F. & Whitesides, G. M. Molecular Rectification in Metal−SAM−Metal Oxide−Metal Junctions. *Journal of the American Chemical Society* **131**, 17814-17827 (2009).

28   Nijhuis, C. A., Reus, W. F., Siegel, A. C. & Whitesides, G. M. A Molecular Half-Wave Rectifier. *Journal of the American Chemical Society* **133**, 15397-15411 (2011).

29   Thuo, M. M. *et al.* Odd−Even Effects in Charge Transport across Self-Assembled Monolayers. *Journal of the American Chemical Society* **133**, 2962-2975 (2011).

30   Fracasso, D., Valkenier, H., Hummelen, J. C., Solomon, G. C. & Chiechi, R. C. Evidence for Quantum Interference in SAMs of Arylethynylene Thiolates in Tunneling Junctions with Eutectic Ga–In (EGaln) Top-Contacts. *Journal of the American Chemical Society* **133**, 9556-9563 (2011).

31   Reus, W. F., Thuo, M. M., Shapiro, N. D., Nijhuis, C. A. & Whitesides, G. M. The SAM, Not the Electrodes, Dominates Charge Transport in Metal-Monolayer//Ga2O3/Gallium–Indium Eutectic Junctions. *ACS Nano* **6**, 4806-4822 (2012).

32   Nerngchamnong, N. *et al.* The role of van der Waals forces in the performance of molecular diodes. *Nature Nanotechnology* **8**, 113 (2013).

33   Song, P. *et al.* Noncovalent Self-Assembled Monolayers on Graphene as a Highly Stable Platform for Molecular Tunnel Junctions. *Advanced Materials* **28**, 631-639 (2016).

34   Chen, X. *et al.* Molecular diodes with rectification ratios exceeding 105 driven by electrostatic interactions. *Nature Nanotechnology* **12**, 797 (2017).

35   Love, J. C., Estroff, L. A., Kriebel, J. K., Nuzzo, R. G. & Whitesides, G. M. Self-Assembled Monolayers of Thiolates on Metals as a Form of Nanotechnology. *Chemical Reviews* **105**, 1103-1170 (2005).

36   Weiss, E. A. *et al.* Influence of Defects on the Electrical Characteristics of Mercury-Drop Junctions: Self-Assembled Monolayers of n-Alkanethiolates on Rough and Smooth Silver. *Journal of the American Chemical Society* **129**, 4336-4349 (2007).

37   Barber, J. R. *et al.* Influence of Environment on the Measurement of Rates of Charge Transport across AgTS/SAM//Ga2O3/EGaIn Junctions. *Chemistry of Materials* **26**, 3938-3947 (2014).

38   Glass, N. R., Tjeung, R., Chan, P., Yeo, L. Y. & Friend, J. R. Organosilane deposition for microfluidic applications. *Biomicrofluidics* **5**, 036501-036501-036507 (2011).

39   Mehne, J. *et al.* Characterisation of morphology of self-assembled PEG monolayers: a comparison of mixed and pure coatings optimised for biosensor applications. *Analytical and Bioanalytical Chemistry* **391**, 1783-1791 (2008).

40   Allongue, P., Henry de Villeneuve, C., Morin, S., Boukherroub, R. & Wayner, D. D. M. The preparation of flat H–Si(111) surfaces in 40% NH4F revisited. *Electrochimica Acta* **45**, 4591-4598 (2000).

41   Li, Y.-H. & Buriak, J. M. Dehydrogenative Silane Coupling on Silicon Surfaces via Early Transition Metal Catalysis. *Inorganic Chemistry* **45**, 1096-1102 (2006).

42   M. E. N. P. R. A. Silva, A. J. L. P., J. J. R. Fraustio da Silva, R. Herrmann, N. Deus, T. J. Castilho, M. F. C. G. Silva. Redox potential and substituent effects at ferrocene derivatives. Estimates of Hammett σp and Teft Polar σ substituent constants. *J. Organomet. Chem* **421**, 75-90 (1991).

43   Chrisey, L. A., Lee, G. U. & O'Ferrall, C. E. Covalent Attachment of Synthetic DNA to Self-Assembled Monolayer Films. *Nucleic Acids Research* **24**, 3031-3039 (1996).

44   Rodenhausen, K. B. *et al.* In-situ monitoring of alkanethiol self-assembled monolayer chemisorption with combined spectroscopic ellipsometry and quartz crystal microbalance techniques. *Thin Solid Films* **519**, 2817-2820 (2011).

45   Nerngchamnong, N. *et al.* Nonideal Electrochemical Behavior of Ferrocenyl–Alkanethiolate SAMs Maps the Microenvironment of the Redox Unit. *The Journal of Physical Chemistry C* **119**, 21978-21991 (2015).

46   Vogel, Y. B. *et al.* Reproducible flaws unveil electrostatic aspects of semiconductor electrochemistry. *Nature Communications* **8**, 2066 (2017).

47   Steenken, S., Telo, J. P., Novais, H. M. & Candeias, L. P. One-electron-reduction potentials of pyrimidine bases, nucleosides, and nucleotides in aqueous solution. Consequences for DNA redox chemistry. *Journal of the American Chemical Society* **114**, 4701-4709 (1992).

48   Brooks, S. C. & Richter, M. M. Determination of DNA Bases Using Electrochemistry: A Discovery-Based Experiment. *The Chemical Educator* **7**, 284-287 (2002).

49   Ono, Y., Tabe, M. & Kageshima, H. Scanning-tunneling-microscopy observation of thermal oxide growth on Si(111)7\ifmmode\times\else\texttimes\fi{}7 surfaces. *Physical Review B* **48**, 14291-14300 (1993).

50   Ulman, A. Formation and Structure of Self-Assembled Monolayers. *Chemical Reviews* **96**, 1533-1554 (1996).

51   Ricœur, G., Lenfant, S., Guérin, D. & Vuillaume, D. Molecule/Electrode Interface Energetics in Molecular Junction: A "Transition Voltage Spectroscopy" Study. *The Journal of Physical Chemistry C* **116**, 20722-20730 (2012).

52   Smith, B. L. & Rhoderick, E. H. Schottky barriers on p-type silicon. *Solid-State Electronics* **14**, 71-75 (1971).

53   Salomon, A., Böcking, T., Gooding, J. J. & Cahen, D. How Important Is the Interfacial Chemical Bond for Electron Transport through Alkyl Chain Monolayers? *Nano Letters* **6**, 2873-2876 (2006).

54   Baghbanzadeh, M. *et al.* Odd–Even Effects in Charge Transport across n-Alkanethiolate-Based SAMs. *Journal of the American Chemical Society* **136**, 16919-16925 (2014).

55   Simmons, J. G. Generalized Formula for the Electric Tunnel Effect between Similar Electrodes Separated by a Thin Insulating Film. *J. Appl. Phys.* **34**, 1793-1803 (1963).

56   Chi-Ying, L., Lara, J. G., David, W. G. & David, G. C. Mixed DNA/oligo (ethylene glycol) functionalized gold surfaces improve DNA hybridization in complex media. *Biointerphases* **1**, 82-92 (2006).

57   Lee, C.-Y. *et al.* Surface Coverage and Structure of Mixed DNA/Alkylthiol Monolayers on Gold: Characterization by XPS, NEXAFS, and Fluorescence Intensity Measurements. *Analytical Chemistry* **78**, 3316-3325 (2006).

58   Garrigues, A. R. *et al.* Temperature dependent charge transport across tunnel junctions of single-molecules and self-assembled monolayers: a comparative study. *Dalton Transactions* **45**, 17153-17159 (2016).

59   Kelley, S. O., Barton, J. K., Jackson, N. M. & Hill, M. G. Electrochemistry of Methylene Blue Bound to a DNA-Modified Electrode. *Bioconjugate Chemistry* **8**, 31-37 (1997).

60   Engelkes, V. B., Beebe, J. M. & Frisbie, C. D. Length-Dependent Transport in Molecular Junctions Based on SAMs of Alkanethiols and Alkanedithiols: Effect of Metal Work Function and Applied Bias on Tunneling Efficiency and Contact Resistance. *Journal of the American Chemical Society* **126**, 14287-14296 (2004).

61   McCreery, R. L. Molecular Electronic Junctions. *Chemistry of Materials* **16**, 4477-4496 (2004).

62   Lindsay, S. M. & Ratner, M. A. Molecular Transport Junctions: Clearing Mists. *Advanced Materials* **19**, 23-31 (2007).

63   Yuan, L., Jiang, L., Thompson, D. & Nijhuis, C. A. On the Remarkable Role of Surface Topography of the Bottom Electrodes in Blocking Leakage Currents in Molecular Diodes. *Journal of the American Chemical Society* **136**, 6554-6557 (2014).

64   Yuan, L., Jiang, L., Zhang, B. & Nijhuis, C. A. Dependency of the Tunneling Decay Coefficient in Molecular Tunneling Junctions on the Topography of the Bottom Electrodes. *Angewandte Chemie International Edition* **53**, 3377-3381 (2014).

65   Jiang, L., Sangeeth, C. S. S. & Nijhuis, C. A. The Origin of the Odd–Even Effect in the Tunneling Rates across EGaIn Junctions with Self-Assembled Monolayers (SAMs) of n-Alkanethiolates. *Journal of the American Chemical Society* **137**, 10659-10667 (2015).

66   He, J., Lin, L., Zhang, P. & Lindsay, S. Identification of DNA Basepairing via Tunnel-Current Decay. *Nano Letters* **7**, 3854-3858 (2007).

67   Drummond, T. G., Hill, M. G. & Barton, J. K. Electron Transfer Rates in DNA Films as a Function of Tether Length. *Journal of the American Chemical Society* **126**, 15010-15011 (2004).

68   Slinker, J. D., Muren, N. B., Renfrew, S. E. & Barton, J. K. DNA charge transport over 34 nm. *Nature Chemistry* **3**, 228 (2011).

69   Morita, M., Ohmi, T., Hasegawa, E., Kawakami, M. & Ohwada, M. Growth of native oxide on a silicon surface. *Journal of Applied Physics* **68**, 1272-1281 (1990).

70   Wang, W., Lee, T. & Reed, M. A. Mechanism of electron conduction in self-assembled alkanethiol monolayer devices. *Physical Review B* **68**, 035416 (2003).

71   Gan, L. *et al.* Tuning charge transport across junctions of ferrocene-containing polymer brushes on ITO by controlling the brush thickness and the tether lengths. *European Polymer Journal* **97**, 282-291 (2017).

72   Sugimoto, N., Nakano, S.-i., Yoneyama, M. & Honda, K.-i. Improved Thermodynamic Parameters and Helix Initiation Factor to Predict Stability of DNA Duplexes. *Nucleic Acids Research* **24**, 4501-4505 (1996).

Chapter 4.

Enzymatic Extension of Surface Immobilised Oligo-seeds to Yield Repeat-sequence DNA brushes for Sensing Applications

Table of Contents

4.1 Introduction

Both Chapters 2 and 3 were focussed upon the study of short DNA surfaces. Chapter 2 considered the solid phase synthesis of a 16 bp oligomer, modified whilst immobilised on a CPG silica surface. The investigation into the synthesis of a short DNA monolayer, ranging from 12 bp to 32 bp, via attachment to a silane linker molecule for electron transport studies was investigated in Chapter 3. Most literature for DNA surfaces is based upon short DNA immobilised oligomers below the persistence length of DNA, which is 148 bp, 50 nm.[1] The attachment of short DNA oligomers to a surface is well established and enabled via various functionalities attached to the DNA strand such as amino, thiol or biotin which permit the immobilisation of the DNA.[2] However, the attachment of longer DNA strands to the surface, greater than the persistence length of DNA, is less studied due to the more complex addition of the required terminal connecting groups. The packing density of long DNA monolayers is also problematic, as above the persistence length the DNA is much more flexible and can therefore form many different conformations not possible with surface bound rigid short oligomers.

The straightforward synthesis of long DNA brushes on a surface with good packing density would be advantageous and has many applications, one of which is alluded to in Chapter 3. The detection of the hybridisation between an immobilised probe strand and a solution based complementary target strand is the basis for many DNA bio-sensors currently on the market.[3] As indicated in Chapter 3, the difference in charge transport between ssDNA and dsDNA, determined via the EGaIn technique, has potential in bio-sensing applications. However, in order to collect the statistically large number of data required, the time is excessive for the rapid detection necessary for quick diagnosis. The focus was thus directed towards a device utilising the fluorescence detection of DNA hybridisation. This chapter describes an improved method for the synthesis of long DNA brushes and the fluorescence detection to create a fast, sensitive device.

4.1.1 DNA brushes on surfaces

The popularity of DNA brushes has increased in hybridisation arrays,[4] next-generation sequencing,[5] and coated particle assemblies.[6]. DNA brushes are defined as DNA, which is longer than the persistence length of DNA, tethered to a surface. Once immobilised, the DNA can adopt several conformations dependent on salt concentration, osmotic pressure, charge and packing density.[7] A slight change in the conditions described, results in the elongation or compression of the DNA monolayer.

Bracha *et al.*[7] studied a surface bearing a DNA gradient of brush heights and altered several parameters to observe changes in the brush height. They determined four brush regimes which are adopted depending on the salt concentration, osmotic pressure and packing density of the DNA, Figure 1. The osmotic regime is the result of increased entropy of counter cations within the brush which cause the elongation of the DNA strand, increasing monolayer height. The salted system results in an ionic imbalance and entropy loss causing a reduction in brush height. The mushroom regime is caused by a high salt and low density system which reduces chain interactions, increasing flexibility and folding. The neutral arrangement is a result of salt and density independence, due to high salt concentrations.
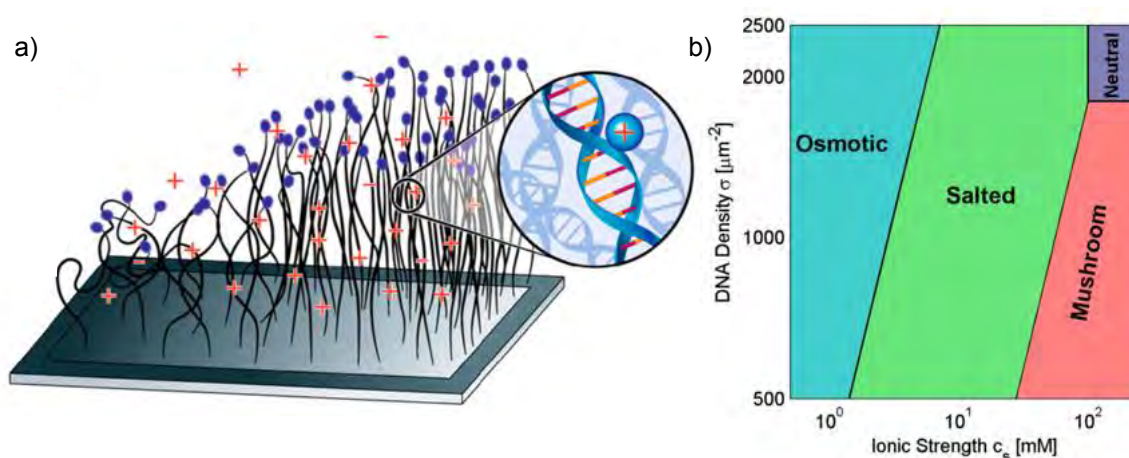

Figure 1. *a) The DNA brush along a density gradient which causes compression or elongation of the DNA height from left to right. b) a plot showing the DNA brush regimes adopted based upon differing DNA densities and ionic strengths.[7]*

The immobilisation of the long DNA on a surface relies upon the post-synthetic attachment of the strands to the surface. As mentioned previously an amino, thiol or biotin functionality is required for surface immobilisation. Therefore, automated DNA synthesis is the obvious choice as the terminal functional group can be simply added during the phosphoramidite process, where high control over the sequence can be achieved. However, the oligomers produced by phosphoramidite synthesis are limited by length, as described in the introduction. Therefore, in order to achieve a DNA monolayer longer than the persistence length, the long DNA must be synthesised in solution, and connecting functionality added after DNA synthesis in order to covalently attach to the surface. Current methods for doing this include the PCR amplification of a short 22 bp dsDNA primer labelled with a biotin moiety at one end. The long dsDNA,

once the desired length is obtained, is then connected to the surface via the biotin/streptavidin linker system.[8]

A procedure for the growth of immobilised short DNA oligomers off a surface would be advantageous to overcome the issues associated with attaching a connecter to the end of the DNA for post synthetic surface immobilisation. The packing of the DNA brush would therefore be determined by the density of the short immobilised probe DNA which should afford well packed long DNA brushes. The Akermann group have explored this possibility by the growth of DNA layers via concatemers, Figure 2.[9] An initial probe strand of 59 bp is immobilised on the surface via a biotin/streptavidin linker system and hybridised with a shorter complementary strand, 34 bp, creating an overhang at the terminus of the layer. Subsequent addition of oligomers containing a complementary sequence to the overhang result in the build-up of dsDNA brushes up to 534 bp. This method allows the formation of long dsDNA brushes from the surface, however; for sensing applications, the dehybridisation to ssDNA for subsequent hybridisation with target molecules is necessary. The whole system would denature as each short oligomer is only held together via complementary hydrogen bonding rather than a complete phosphate backbone from end to end.
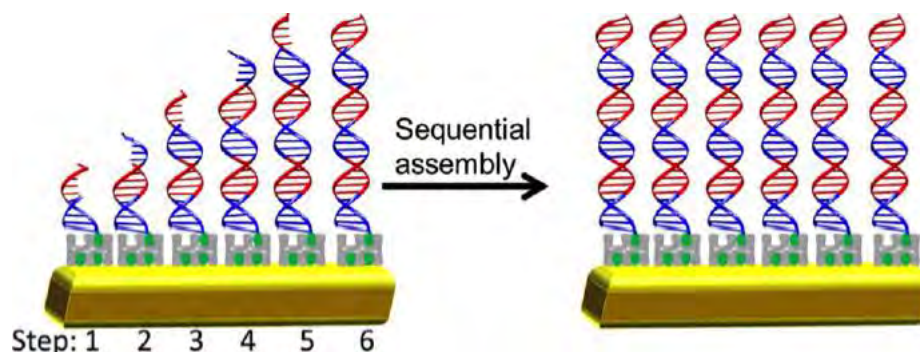

Figure 2. The construction of DNA brushes via the sequential addition of oligomers forming concatemers.[9]

A different method for the growth of short DNA probes off a surface has been demonstrated by Wang *et al.*[10] where RCA is used to generate long DNA brushes for sensing applications. Short DNA probes are immobilised on a poly(acrylic acid) (PAA) modified surface. Circular templates were then used to extend the DNA probe off the surface. This method produces long ssDNA brushes available for hybridisation with target strands, however, it requires a circular template which is limited by the choice of those commercially available. The method is also still reliant on the fluorescent labelling of the target DNA strand which is costly and inconvenient.

The main use of DNA immobilised surfaces is for sensing applications and the utilisation of long DNA brushes would be beneficial to increase the target loading of the probe strand, improving detection sensitivity. For optical detection, many surfaces require the target DNA strand to be labelled with an expensive fluorophore before coming into contact with the probe strand which is costly and unreliable. Therefore, a simple cost effective and sensitive device addressing the issues associated with fluorescent readout devices would be advantageous.

4.2 Results and Discussion

This chapter describes the enzymatic extension protocol of short repeat sequence oligo seeds, covalently attached to a surface, to long extended DNA strands demonstrating the capability of the PCR heat-cool extension off a surface. The extension method provides increased binding sites per probe molecule, multiplexed in the z-direction from the surface. A fluorescent dye is added to the surface where the readout is amplified compared to short oligo strands due to the increased number of binding sites. The sensing properties of the surface are explored by the dehybridisation of the long strands and subsequent rehybridisation with short target strands. The method is versatile in relation to the surface, linker molecule and DNA sequence allowing for a variety of applications. The overall process of surface modification and steps into investigating the sensing abilities are displayed in Scheme 1.
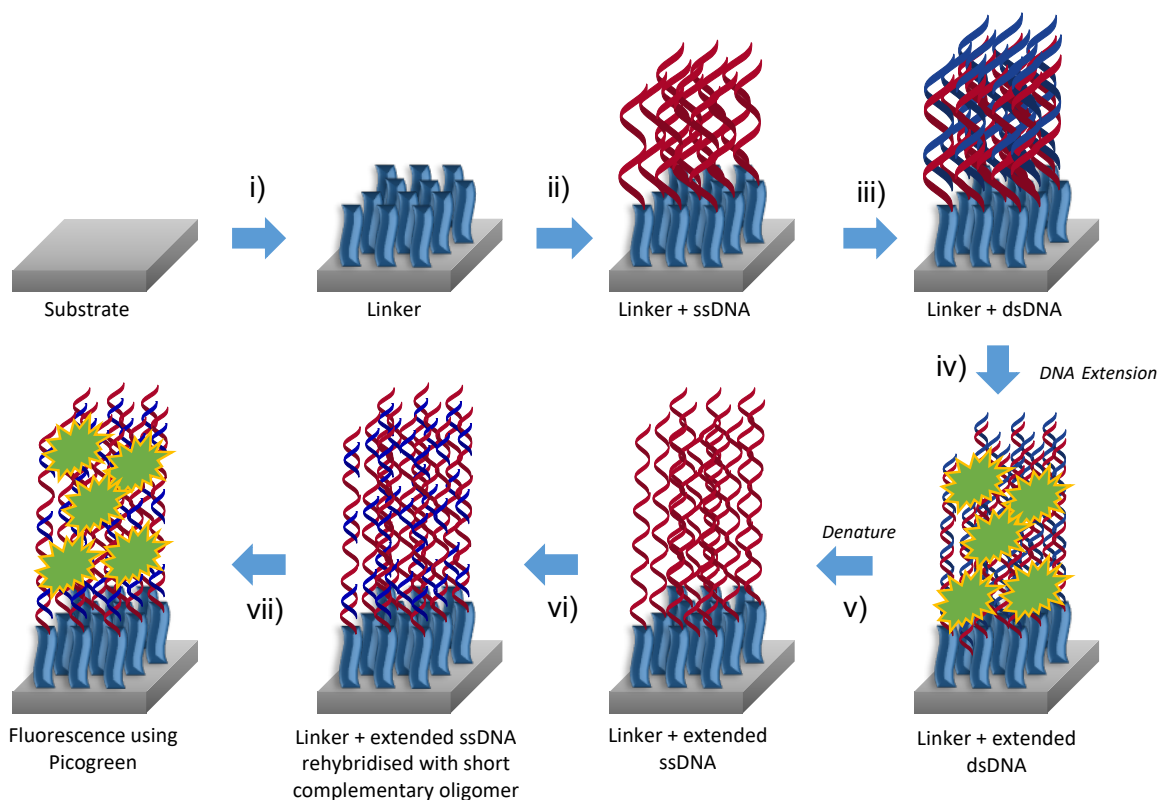
Scheme 1. Schematic overview illustrating the surface functionalisation steps involved to produce multiple repeat-sequence DNA via a surface confined PCR based reaction. i) immobilisation of bifunctional linker, ii) attachment of 5'-amino modified oligo seed, iii) hybridisation of oligoseed complement, iv) PCR based extension of the immobilised ds DNA to yield long DNA brushes and visualisation by PG, v) denaturation to long ssDNA off the surface, vi) re-addition of short target strands and vii) visualisation of bound target strands by PG.

4.2.1 Extension of [GATC]$_5$/[CTAG]$_5$ in solution

In order to ensure maximum DNA extension off the surface, the heat-cool extension of the oligo seed sequence was initially tested in solution, as shown in Scheme 2. In solution, the extension starts with a short dsDNA primer, known as the oligo seed, containing a repeat sequence, step 1. The dsDNA is denatured at 95 °C before reannealing at 55 °C. The oligo seed used must contain a minimum of two repeat units of at least four base pairs to allow for sufficient base overlap to form sticky ends during the annealing process, step 2. The switch in temperature from 95 °C to 55 °C is rapid and therefore, the duplex cannot reanneal in the lowest energy structure as it would simply reform the completely complementary oligo seed. Due to the repeat sequence in the oligo seed, imperfect alignment, in several possible overlap conformations, step 3, will occur resulting in the formation of sticky ends which are able to be extended by DNA polymerase. A thermostable polymerase is required for the heat-cool cycles, and for that reason the *Thermococcus gorgonarius* family B DNA polymerase (Tgo-Pol) mutant, Z3 was chosen.[11] Due to the multiple number of conformations possible in the reannealing step, which increases with each cycle, the DNA strands will be extended to a different number of bases for each duplex and so, a range of DNA lengths is expected in the product. After extension by DNA polymerase at 72 °C, the process is repeated for the desired number of cycles to obtain long dsDNA products. The heat-cool extension method is able to produce sequence specific extended DNA (extDNA), longer than the persistence length of DNA and beyond the limits of automated DNA synthesis. The heat-cool protocol is ideal to trial as an extension method off the surface as the oligo-seed can be covalently attached to the surface using well-known immobilisation techniques for short oligomers.
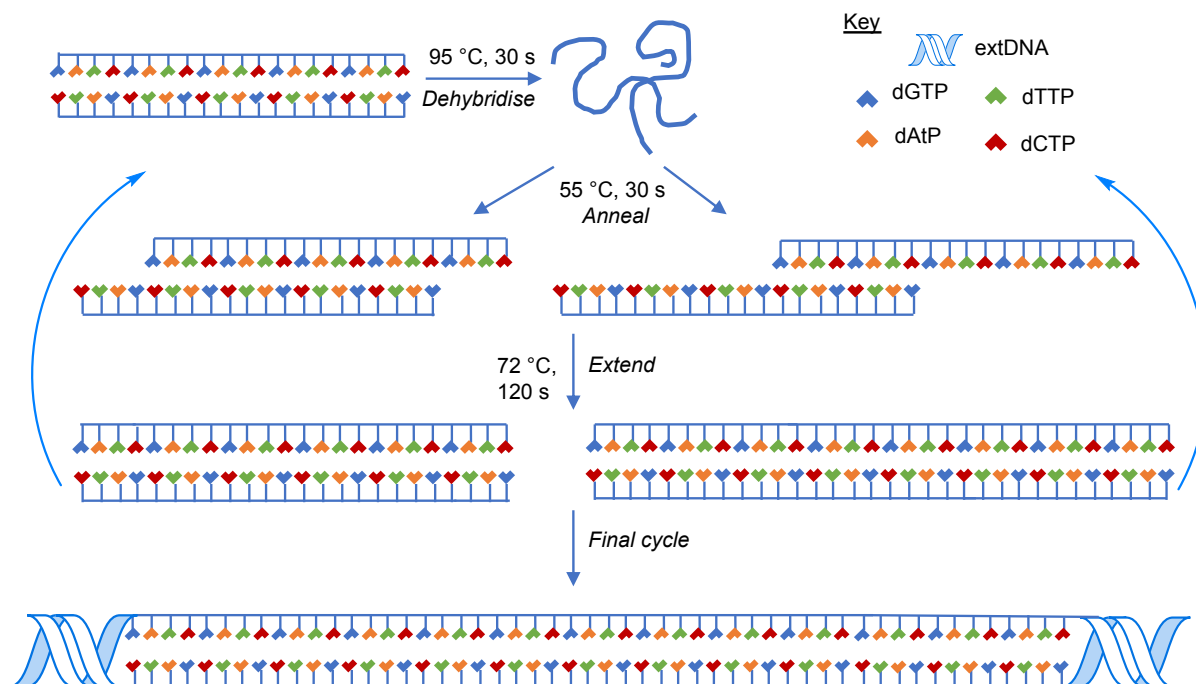
Scheme 2. *The PCR-based heat-cool cycle extension method. Initially the DNA oligo seed is dehybridised at 95 °C to form single strands. The strands are annealed at 55 °C at complementary regions with differing overlap; minimum overlap on the left and maximum overlap on the right. The DNA polymerase binds complementary nucleotides to the sticky ends of the DNA strands at 72 °C. The heat-cool steps are repeated for a desired number of cycles.*

Initially, the sequence [GATC]$_5$/[CTAG]$_5$, see Table 1, was chosen as this sequence was previously successfully extended by this enzymatic extension method.[12] The probe strand is amino-modified at the 5'-end for eventual attachment to the surface. The oligo seed was extended for 20 cycles to acquire the longest possible length attainable for this sequence. Above 20 cycles, the DNA extension rate is known to reduce indicating a reduction in DNA polymerase activity.[12]

Table 1. *DNA sequences used for solution DNA extension.*

Name	Sequence (X = amino-c6)
GATC-probe	5'- X –CTAGCTAGCTAGCTAGCTAG -3'
GATC-target	5' - CTAGCTAGCTAGCTAGCTAG -3'

The DNA product was analysed by gel electrophoresis, Figure 2a, displaying a range of DNA lengths. UV-Vis absorbance indicates that a respectable concentration is achieved, and the modal DNA length is 1000 bp as determined by lane absorbance intensity in ImageJ analysis, Figure 3b and c respectively. The extDNA at a length of

1000 bp contains 40 more repeat sequences than the oligo seed and hence more target binding sites per probe molecule.
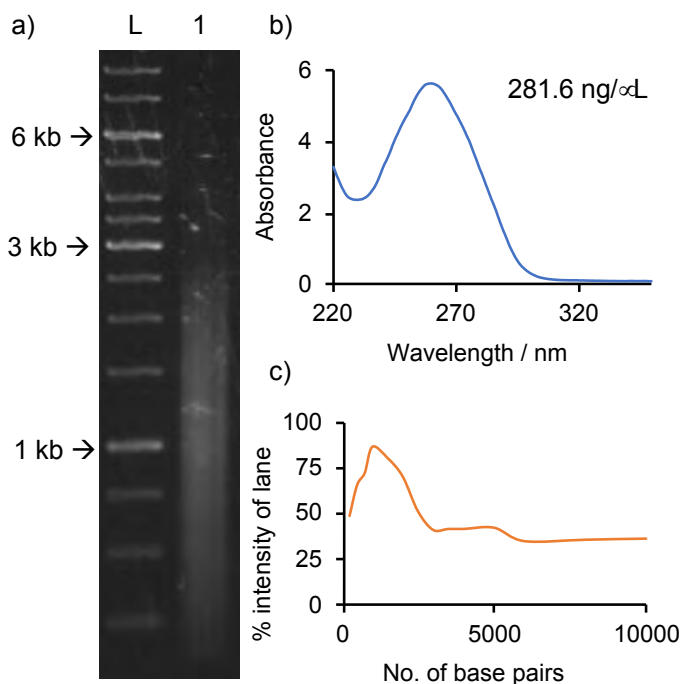

Figure 3. *Heat-cool cycle extension with Tgo-Pol Z3 exo- and [GATC]₅/[GATC]₅ for 20 cycles. a) agarose gel: lane 1 extension product after 20 cycles. b) UV-Vis plot c) Image J analysis of extension product. Analysis shows the intensity of the band as a percentage of the highest intensity compared to the ladder, L = DNA ladder.*

4.2.2 Extension of GATC off the surface

The extension of the 5'-amino modified GATC repeat sequence produces long, sequence defined DNA in solution, beyond the limits of automated DNA synthesis, therefore the procedure was trialled off a surface. The same surface modification, with APEGDMES and the amino modified probe-DNA, as used in Chapter 3 was employed to tether the dsDNA oligo seed onto the surface. A glass surface, cut to 0.5 cm^2, was cleaned with acetone, IPA and water followed by treatment with O_2 plasma to remove any remaining organic contaminants and to activate the surface with OH groups.[13] The oxide layer reacted with a PEG_4 linker (APEGDMES) by heating at 80 °C in toluene overnight. The surface was treated with 10% acetic solution containing the amino-modified GATC probe strand to reveal the aldehyde functionality at the terminus of the linker. Addition of sodium cyanoborohydride facilitated the reductive amination reaction between the aldehyde of the linker molecule and the amino functionality on the DNA strand. The surface was rinsed with nanopure water and placed in 0.5x PBS buffer for 30 min to remove any physisorbed DNA strands. The short ssDNA, now

covalently attached to the surface, was then hybridised with the complementary target DNA strand affording the 20 base dsDNA oligo seed required for the PCR-based enzymatic extension protocol. The surface was again rinsed with 0.5x PBS buffer. The PCR heat cool cycles were performed as they were in solution, however, the DNA-modified glass chip was cut to fit inside a standard PCR Eppendorf tube (0.2 mL) which is suitable for the PCR heat-cool block, see Scheme 3. The total volume of reagents for the extension was 180 μL to ensure the entire surface was covered during the full extension protocol. As in solution, 20 heat-cool extension cycles were performed which extends the oligo seed in the z-direction away from the surface resulting in long repeat sequence DNA brushes.
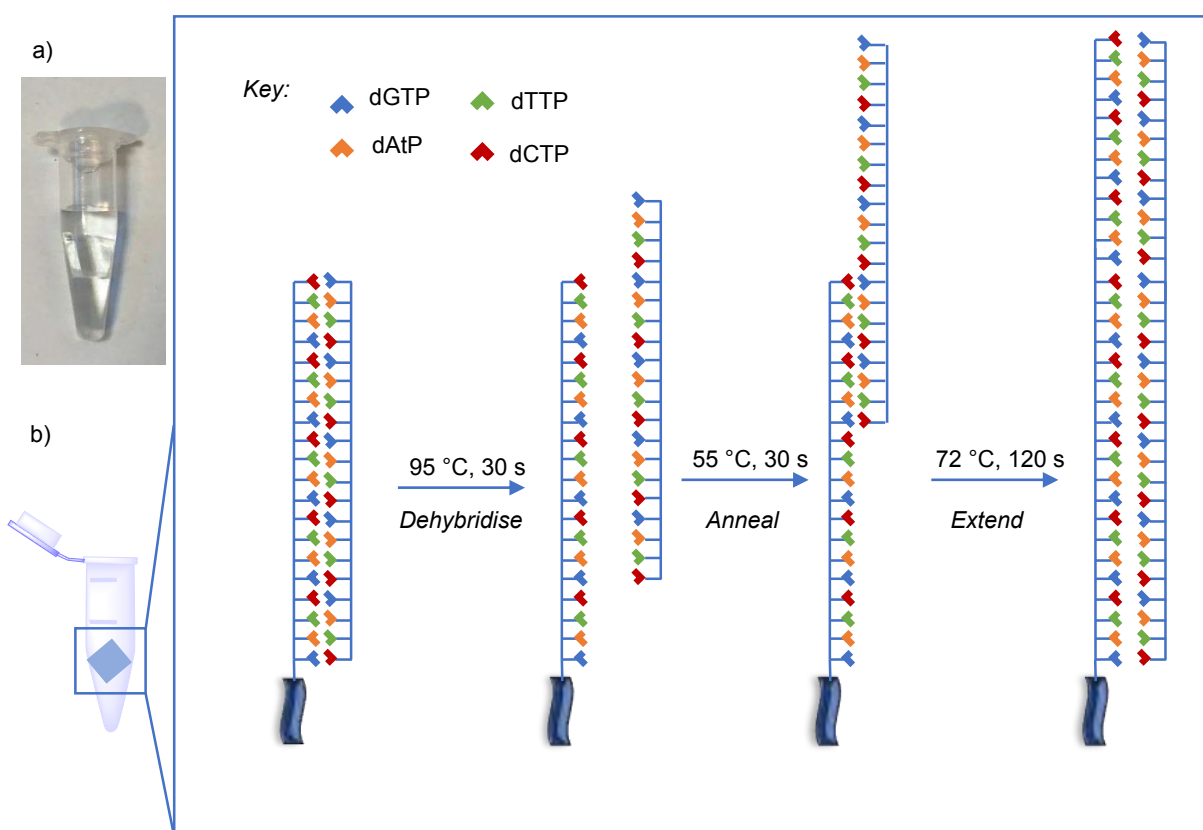
Scheme 3. *a) Oligo seed functionalised glass surface cut to fit in a standard PCR Eppendorf tube. b) Schematic of the mechanism of surface immobilised oligo seed enzymatic extension.*

In order to visualise the increase in number of DNA bases between the oligo seed surface and the extDNA surface, the fluorescent dye Picogreen (PG) was added to the surface. PG exhibits a >1000 fold increase in fluorescence upon binding to dsDNA.[14] PG intercalates into dsDNA via intercalation of the quinolinium group between base pairs stabilised by van der Waals, electrostatic interactions of the benzo-thiazol group with the phosphate backbone and the dimethylaminopropyl chains interact with the minor groove.[14] The surfaces were incubated with a 200-fold dilution stock solution of

114

PG for 30 min. The extDNA surface exhibited an increase in fluorescence intensity compared to the untreated oligo seed strands attached to the surface as shown in Figure 4b. PG is usually not strong enough to determine between short DNA surfaces, as seen in the comparable fluorescence intensities of ssDNA and dsDNA, however, with the increased number of base pairs, the extDNA and short DNA surfaces are distinguishable. The increase in fluorescence is slightly noticeable by eye however is clearly observed through the integrated density analysis performed using ImageJ software, Figure 4a. There is an obvious distinction between the short oligo seed and the extDNA surface attributed to the increase in number of PG binding sites per probe molecule.
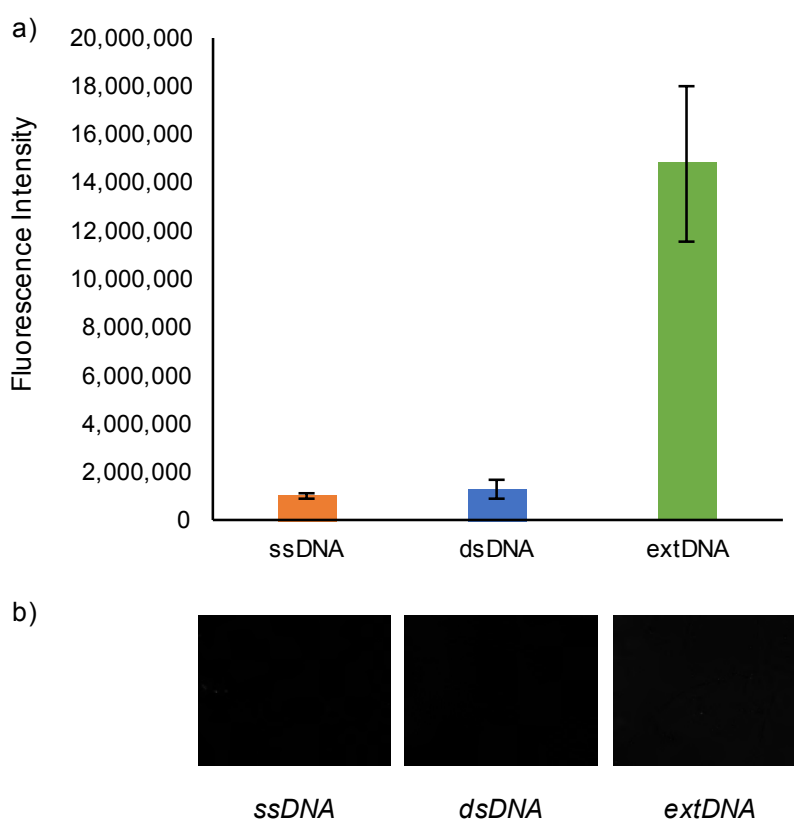
Figure 4. *a) Bar chart of the fluorescence intensity highlighting the difference between a surface modified with short oligomers compared to long extDNA. b) fluorescence images of each different surfaces.*

The increase in fluorescence intensity is an excellent indicator that the DNA has extended off the surface. In order to further confirm the increase in DNA length, the extDNA on the surface was dehybridised and the long complementary strand which is not covalently attached to the surface was removed from the surface and collected. The extDNA surface was immersed twice in nanopure water heated to 95 °C for

dehybridisation. AFM was used to visualise the long DNA by taking 5 μL of sample and placing it on freshly cleaved mica via molecular combing which is known to extend the flexible DNA strand.[15] The AFM image for the ssDNA is displayed in Figure 5. Many of the ssDNA strands are aggregating on the surface which is typical for ssDNA,[16] however some single strands are visible with an average height of 0.5 nm, see Figure 5b, comparable to previously reported dimensions for ssDNA.[17] Analysis of the average length of the ssDNA strands gave a range from 160-300 bp confirming the successful extension of the oligo seed off the surface. The length of the strands obtained from the surface is shorter than observed in the agarose gel from the solution-based extension. This observation is expected due to the steric hindrance of the surface restricting full movement of the enzyme hence reducing the reaction rate.
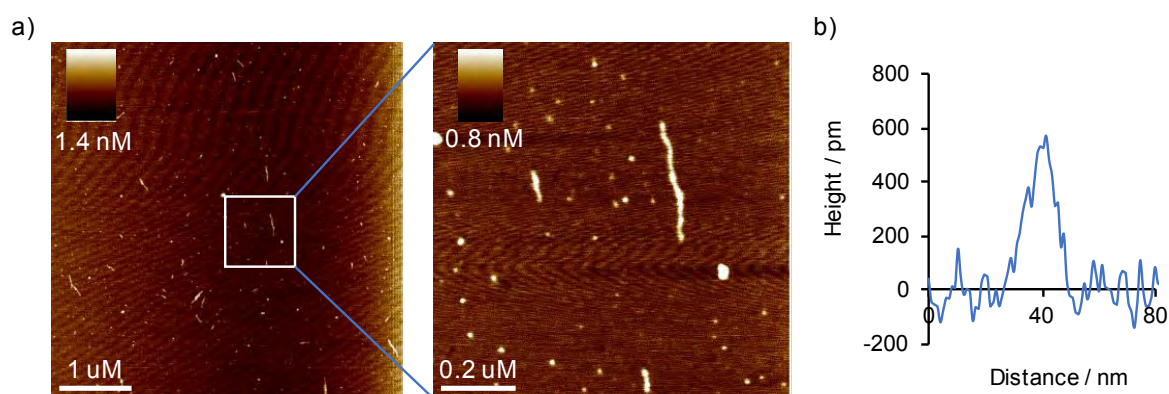

Figure 5. a) AFM image of long single stranded extDNA dehybridised from the surface. b) height profile of a single DNA strand confirming the dimensions expected for ssDNA

Another method to visualise the DNA and determine the height of the DNA brush is to use total internal reflection fluorescence, TIRF. TIRF is generally used for the visualisation of events in the plasma membrane of cells.[18] The TIRF signal is generated by an evanescent wave used to illuminate fluorophores directly neighbouring the glass surface. The wave is only visualised if the incident light is totally internally reflected at the glass-sample interface. The signal produced decays exponentially, therefore the height from the surface capable of visualising is 100 nm. The extension protocol employed in this work produces a range of DNA lengths on the surface as described earlier. TIRF could be used to determine an accurate height of the DNA lengths similar to the reported height gradient obtained for DNA brushes by Bracha *et al.*[7] As the number of cycles is increased, the length of the DNA extends and the range expands.[12] Using TIRF, surfaces which have different length DNA ranges can be compared, controlled by the number of cycles undertaken. In order for the DNA surfaces to be

active for TIRF, a fluorescent probe, Alexa 488, was attached to the 5'-end of the complementary strand during synthesis of the DNA-modified surface. The DNA oligo seed was extended for either 2 or 20 cycles with the fluorescent probe always located at the terminus of the DNA brush. Surfaces which have 20 cycles producing DNA on average of 1000 bp corresponding to 340 nm would not be visible by TIRF as this is out of the viewing range. However, surfaces that have undergone a 2-cycle extension could have a maximum DNA brush length of 16.3 nm which is within the height range applicable for TIRF measurements.
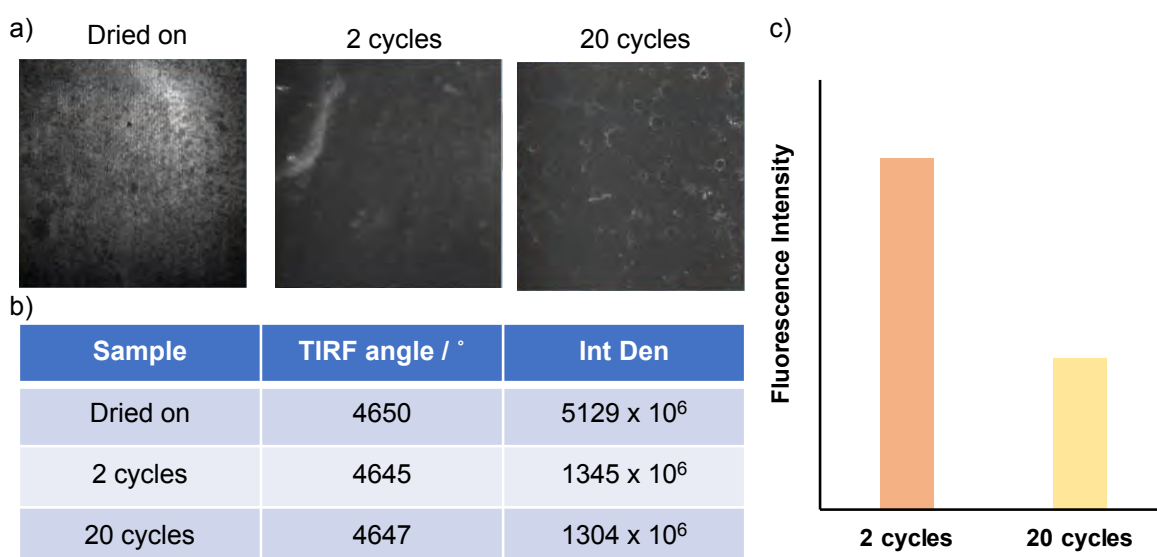
Due to the depth sensitivity of the TIRF measurements, the extension method had to be carried out on glass coverslips 170 µm thick rather than the previously used glass microscope slides. Since the DNA-modified coverslips need to be 0.5 cm^2 in order to fit into the Eppendorf tube for the extension, the placement of the coverslip in the microscope for TIRF measurements had to be altered to account for the small sample size. Usually the microscope slide is mounted in a specially designed holder to ensure the flatness of the surface which is necessary for TIRF. However, as the coverslip is too small to fit into the holder, the coverslip had to be attached to a glass slide by vacuum grease around the perimeter of the surface to hold it in place, Scheme 4. Although this method successfully holds the surface in place, the flatness of the surface is not known, and it is possible that this could hinder measurements.
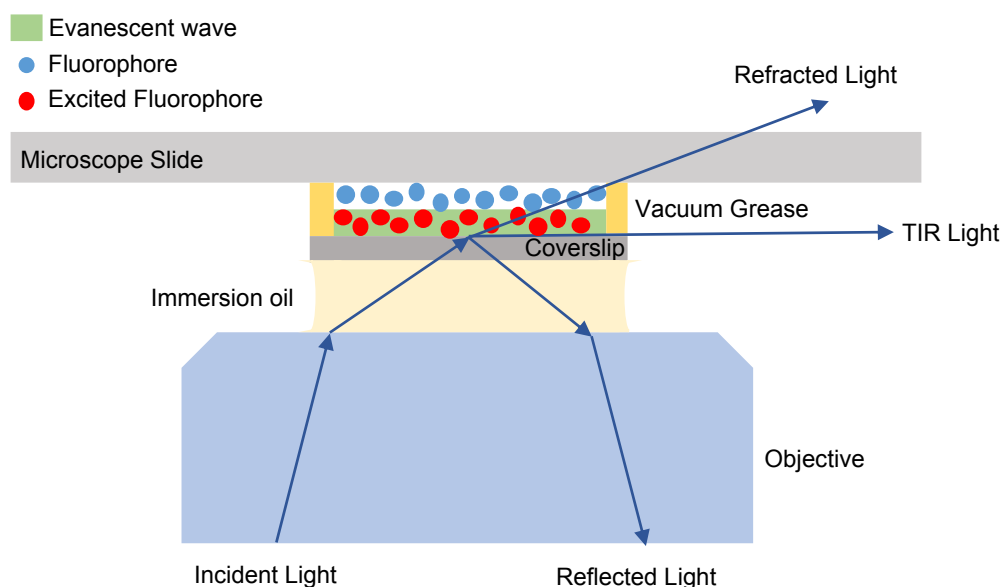
Scheme 4. *The mounting of the small coverslip to the microscope slide for TIRF measurements.*

Initially, the fluorescently tagged complementary DNA strand was dried onto the coverslip so the Alexa 488 was in direct contact with the coverslip, Figure 6a. This

allows the TIRF angle to be found easily as the tag is in close range to where the measurement takes place. The found TIRF angle can then be used as a baseline for the other samples so the TIRF can be observed more easily. Analysis of the image, by ImageJ software, calculated a high integrated density of 5129×10^6. The angle was set to 4650, corresponding to the angle calculated for the control dried on sample, to find the TIRF fluorescence for the 2-cycle sample. As seen in the drop of integrated density to 1345×10^9, there is a much lower amount of TIRF present. This is expected as the fluorescent tag is now further from the surface and therefore giving off a lower TIRF signal even though the whole DNA brush layer is still within the limit of TIRF. In comparison with the 20 cycle sample, the integrated density does reduce to 1304×10^6 compared to the 2 cycle surface, although not as much as expected. The height of the DNA brushes should be 340 nm, on average, and this should not be visible by TIRF as it exceeds the height limit, however; as mentioned previously, the DNA lengths for this sequence range from 160-300 bp. Therefore, the 160 bp DNA strand corresponds to 54.4 nm if fully stretched, which does fall within the limit of TIRF and hence, would be observed. In both the 2 cycle and 20 cycle surfaces, wave like patterns and holes are observed in the TIRF images. It is hypothesised that this is a result of slight cracks in the coverslip surface generated by the method of cutting the coverslips. Laser cutting of the coverslips to size could minimise these effects and result in a more even formation of the DNA monolayer.

| Sample	TIRF angle / °	Int Den
Dried on	4650	5129×10^6
2 cycles	4645	1345×10^6
20 cycles	4647	1304×10^6

Figure 6. a) TIRF images of the fluorescently tagged probe dried onto the coverslip, after a 2-cycle extension and after a 20 cycle extension. b) Table displaying the TIRF angle and Fluorescence Intensity for each surface and c) a bar chart highlighting the difference between the two extended surfaces.

Although a difference is observed between the samples, conclusive results could not be obtained. Additionally, as a range of lengths is present on the surface, some fluorescence will always be observed even for the longer lengths. However, the increase in fluorescence intensity and the AFM of cleaved ssextDNA is sufficient to confirm the successful extension of the oligo seed off the surface.

4.2.3 Extension of CFTR sequence

Long DNA brushes with repeat sequences have the potential to distinguish between single base mismatches in diseases, ideal for DNA biosensing. Many diseases are the result of mutations in the gene causing differences in the DNA sequence.[19] A platform to differentiate between the specific sequences would allow for early detection of disease or determination of the type of defect.

One possible disease where this type of device would be beneficial is the cystic fibrosis transmembrane conductance regulator known as the CFTR gene. The CFTR gene codes for a protein and this acts as a channel to control the transport of chloride ions in and out of cells to manage water content for mucus production. The protein is also necessary for sodium regulation in the lungs and pancreas. The most common frameshift mutation seen in CFTR is a 3-base deletion of the bases CTT, known as delta F508, resulting in a change in gene coding by the removal of the amino acid phenylalanine, Figure 7. The deletion of amino acid results in the complete distortion of the gene shape which causes the break-down of the ion channel. Without a functioning ion channel, cells which line the pancreas, lungs and other organs generate a thick mucus resulting in the blockage of airways and glands. Detecting this change early would allow immediate treatment, reducing the effects of the disease to improve the quality of life. Therefore, the DNA sequence for the CFTR delta F508 mutation was chosen as the next sequence to trial with the extension method off the surface.
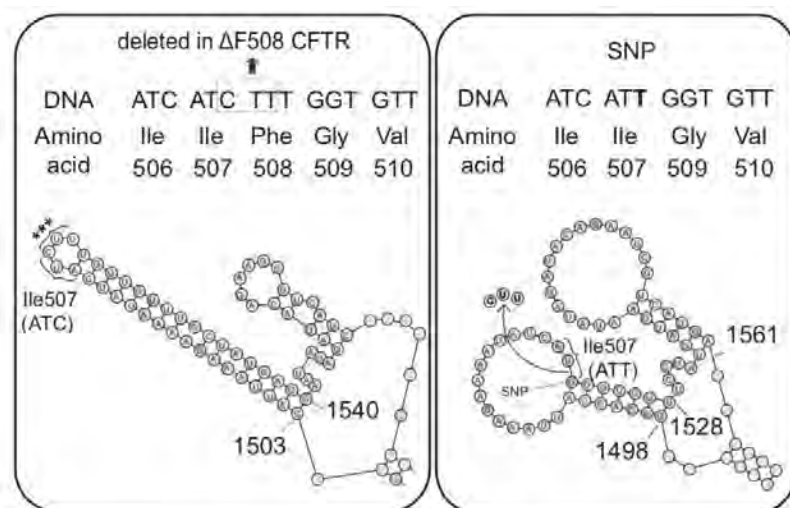
Figure 7. *The change in gene shape caused by the deletion of the phenylalanine amino acid during the CFTR mutation*[19]

The CFTR sequence was initially extended in solution as described in section 4.2.1 to ensure the specific sequence is extendable using this method. The duplex was made from the amino-modified probe and target DNA sequences described in Table 2.

Table 2. *The amino-modified DNA sequences used for the CFTR extension.*

Name	Sequence (X = amino-c6)
CFTR-probe	5'- X –GCATCTTTCGGCATCTTTCG-3'
CFTR-target	5' – CGAAAGATGCCGAAAGATGC -3'

DNA products were analysed by agarose gel electrophoresis, Figure 8a, and the modal length of 300 bp was determined using ImageJ analysis software. The length of this DNA sequence is much lower than for the GATC sequence and also exhibits a lower concentration. However, it is still extending to a length which gives 30 repeat sequences per probe strand and so, the extension off the surface was still undertaken.
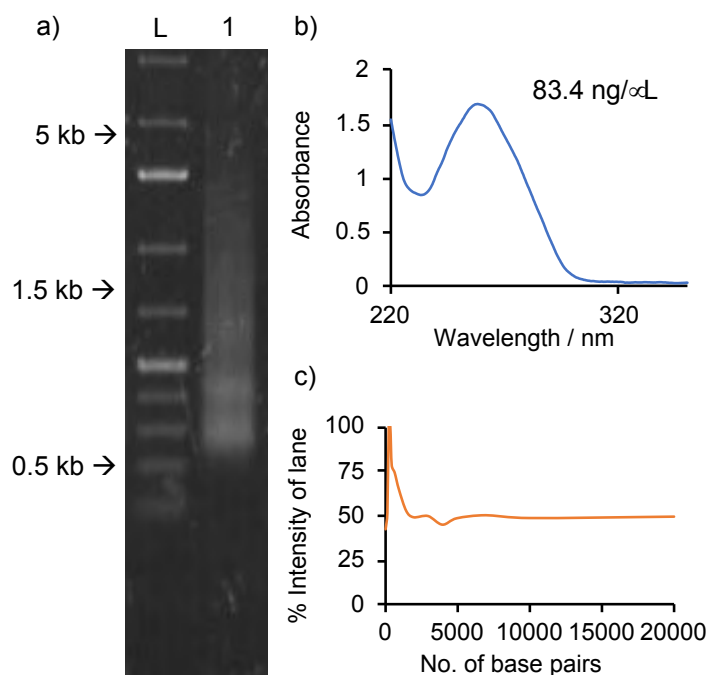
Figure 8. Heat-cool cycle extension with Tgo-Pol Z3 exo- and [GCATCTTTCG]$_2$/[CGTAGAAAGC]$_2$ for 20 cycles. a) agarose gel: lane 1 extension product after 20 cycles. b) UV-Vis plot c) Image J analysis of extension product. Analysis shows the intensity of the band as a percentage of the highest intensity compared to the ladder, L = DNA ladder.

The CFTR oligo-seed sequence was immobilised on a glass surface and subjected to the reaction conditions for enzymatic extension for 20 cycles. After addition of PG to the surfaces, fluorescence images were obtained to observe the increase in fluorescence intensity for the extDNA sample, Figure 9. The extDNA exhibits increased fluorescence intensity compared to the short oligo seeds however, the difference is not as considerable as for the GATC sequence. This is expected as the CFTR sequence in solution did not extend as well as the GATC sequence, meaning there is less DNA base pairs for the PG to bind to, resulting in a decreased fluorescence intensity compared to the GATC surface.
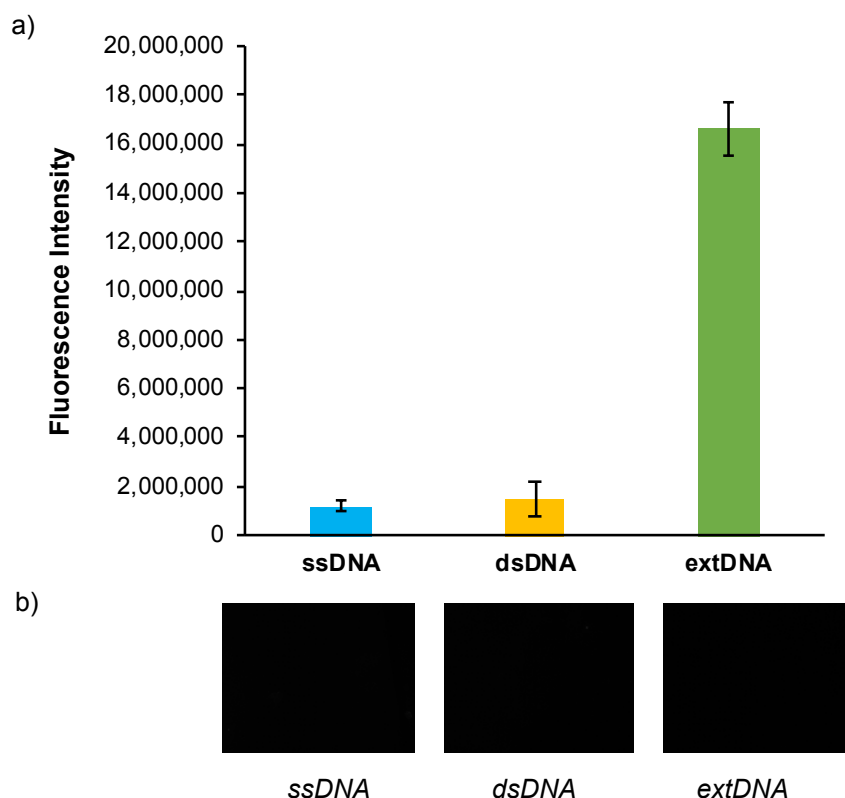
Figure 9. *a) Bar chart of the fluorescence intensity highlighting the difference between a surface modified with short oligomers compared to long extDNA for the CFTR sequence. b) Fluorescence images of the different DNA surfaces.*

The contact angle of the each of the surfaces, ssDNA, dsDNA and extDNA, was determined in order to examine the hydrophobicity of the different surface modifications, Table 3. The contact angle for dsDNA, 32.33°, is lower than the ssDNA surface, 37.10°, as seen in chapter 3 due to the increased hydrophilicity of dsDNA for water. After the extension from the surface, the contact angle increases dramatically to 73.11°. The extensive increase in hydrophobicity is attributed to the hydrophobic nature of the DNA bases. In the duplex conformation of short oligomers the bases are sheltered from any water molecules, on the other hand, with long DNA the structure is less rigid and more bases could be in contact with the water droplet resulting in a hydrophobic terminal monolayer and an increase contact angle.[20] The contact angle after each cycle of DNA extension, from oligo seed to the 20 cycle extension, would document the change from a hydrophilic surface to a hydrophobic surface with increasing DNA brush length.

Table 3. *Contact angles of a water droplet on the ssDNA, dsDNA and extDNA surface for the CFTR sequence.*

Surface	Contact angle / ˚
ssDNA	37.10
dsDNA	32.33
extDNA	73.11

Although the CFTR extDNA surface exhibits enhanced fluorescence intensity compared to the short oligo seed surfaces, the extent of enhancement is not adequate for further investigations into the sensing properties of these surfaces. Therefore, an AT rich DNA sequence was explored for surface extension as AT rich sequences are known to extend easier than GC rich sequences.

4.2.1 Extension of BAT25 sequence

Microsatellite instabilities, MSI, are known markers for genetic instability found in the majority of tumours in patients with hereditary colorectal cancer and in several sporadic colorectal cancers.[21] MSI's are noncoding mononucleotide repeat sequences which display differences in allele length in tumour cells compared to normal DNA alleles from the same patient, either due to deletions or insertions. One of the most commonly used mononucleotide repeat marker used for MSI identification is the BAT25 sequence, a polyT repeat unit. The BAT25 sequence can be used without comparison to normal DNA and involves significant base deletions in virtually all tumours displaying MSI.[21] Understanding the type of MSI allows for identification of tumour type and can conceivably anticipate the patient's chemotherapeutic response. It is crucial for a quick, sensitive and reproducible identification of the MSI to enable rapid diagnosis and treatment.

Current methods for MSI recognition involves using a specially designed panel, the Bethesda panel, in which 5 microsatellite markers are screened; the mononucleotide repeat markers, BAT25 and BAT26, and dinucleotide repeat markers, D2S123, D5S346 and D17S250. If 2-5 of the markers are mutated, the patient is deemed to have high microsatellite instabilities, MSI-H. However, there are discrepancies in the consistent specificity and sensitivity of the panel throwing doubt upon the reliability of the test.[22]

Therefore, the identification of the MSI by our extension method would decrease the time of diagnosis and increase sensitivity. Once the device is taken forward to an array

type pattern the screening of multiple MSI markers from one DNA sample simultaneously would be achievable.

The BAT25 mononucleotide repeat sequence was used to test the efficiency of this method for microsatellite instability detection. The probe and target strands used to form the BAT25 oligo seed are displayed in Table 4. The amino-modified duplex extension was trialled in solution before attempting the extension off the surface.

*Table 4.* The amino-modified DNA sequences used for the BAT25 extension.

Name	Sequence (X = amino-c6)
BAT25-probe	5'- X - GAAAAAAAAAAACGAAAAAAAAAAC-3'
BAT25-target	5' - GTTTTTTTTTTCGTTTTTTTTTTTC-3'

The BAT25 extension products were analysed by gel electrophoresis, Figure 10a, and possess a modal length of 2000 bp. DNA Sanger sequencing was carried out by GATC-biotech on a 5 cycle extension product for BAT25 sequence, Figure 10d. The sequencing results confirm the accurate incorporation of each base by the DNA polymerase. DNA sequencing was not attainable for the GATC and CFTR sequence, presumably due to the challenges associated with GC-rich DNA sequences. Both the GATC and CFTR sequences contain 50 % GC content.
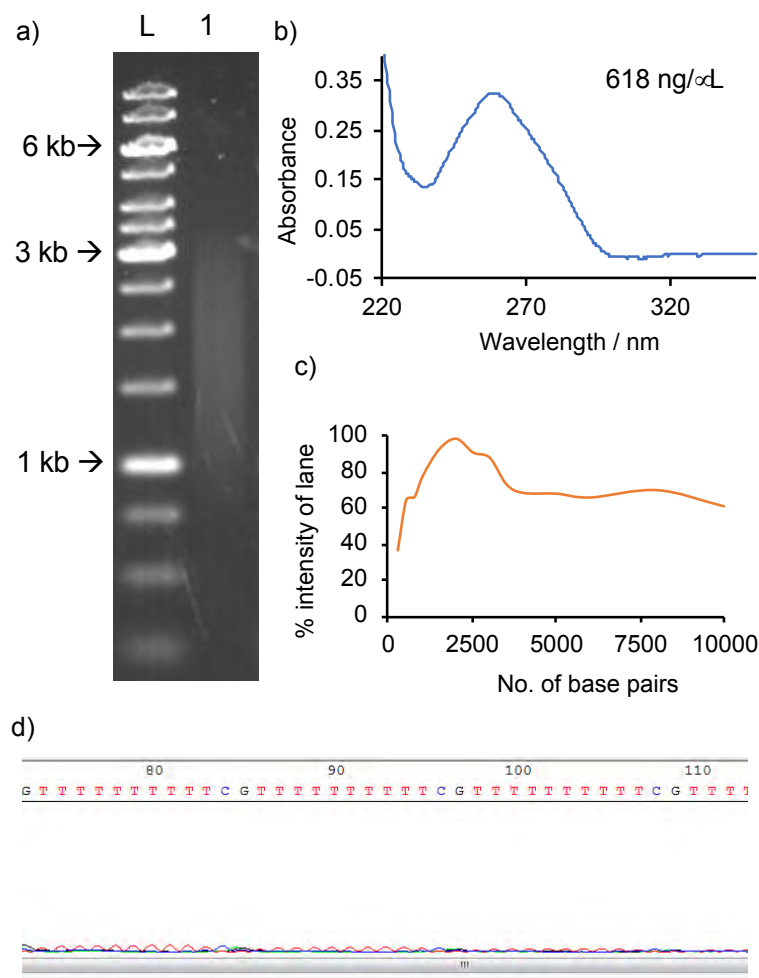
Figure 10. *Heat-cool cycle extension with Tgo-Pol Z3 exo- and [GAAAAAAAAAAC]₂/[CTTTTTTTTTTG]₂ for 20 cycles. a) agarose gel: lane 1 extension product after 20 cycles. b) UV-Vis plot c) Image J analysis of extension product. Analysis shows the intensity of the band as a percentage of the highest intensity compared to the ladder, L = DNA ladder. d) Sanger sequencing of the DNA sequence.*

The DNA length for the BAT25 sequence is much longer compared to the GATC and CFTR sequences with a much higher concentration of 618 ng/μL indicating improved extension. The bp length ranges from approximately 750 bp to 3000 bp also confirmed by AFM analysis of the dsDNA extension products, Figure 11. The average height of the dsDNA was calculated to be 0.87 nm with the DNA length ranging from 130 bp to 1500 bp, consistent with the gel analysis. The BAT25 sequence was extended off the surface after attachment of the amino-modified oligo seed. Addition of PG revealed increased fluorescence for the extDNA compared to the short-immobilised oligo seeds, Table 5.
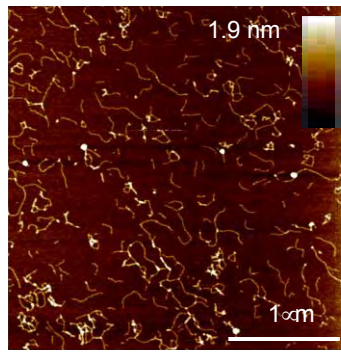
Average Height	0.872 nm ±0.27
Average Length	222 nm ±109
Length range in bp	130-1500

Figure 11. *AFM image of solution extended DNA and the average height and length of the DNA strands confirming the dimensions expected for dsDNA.*
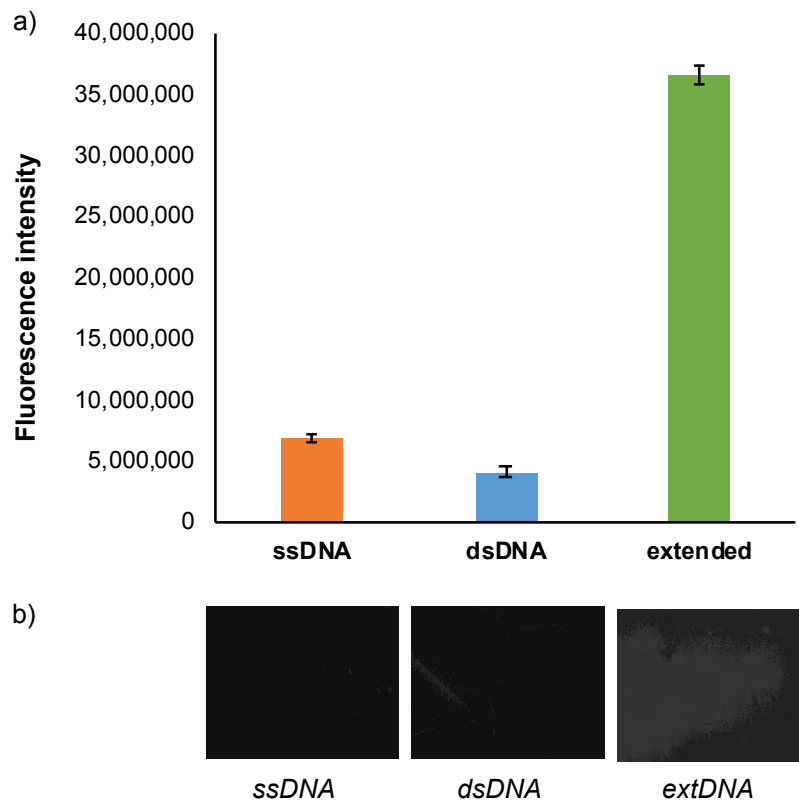

Figure 12. *a) Bar chart of the fluorescence intensity highlighting the difference between a surface modified with short oligo-seeds compared to long extDNA for the BAT25 sequence. b) fluorescence images of each different surfaces.*

The same increase in contact angle measurement was observed for the BAT25 extDNA sequence as for the CFTR sequence, Figure 12.

Table 5. *Contact angles of a water droplet on the ssDNA, dsDNA and extDNA surface for the BAT25 sequence.*

Sample	Contact Angle / °
ssDNA	29.64
dsDNA	25.58
extDNA	74.84

The dsextDNA strands were dehybridised as described in section 4.2.2 and combed onto freshly cleaved mica for AFM analysis, Figure 13. Due to the susceptibility of single stranded AT rich DNA to fold and stack,[23,24] an abundance of the strands appear aggregated, however, several strands are elongated and available for height and length analysis. The height of the single strands on average was 0.5 nm with lengths ranging from 51 nm to 85 nm corresponding to 150-250 bp. The length of the ssDNA is lower than expected however, confirms the increase in length from the oligo seed. The reduced length is attributed to the folding of the ssDNA and the reduced extension for surface bound oligo seeds compared to those extended in solution.
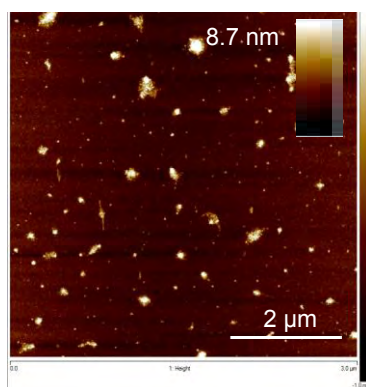
Figure 13. *AFM image of long single stranded extDNA dehybridised from the surface for the BAT25 sequence and the average height and length of a single DNA strand confirming the dimensions expected for ssDNA.*
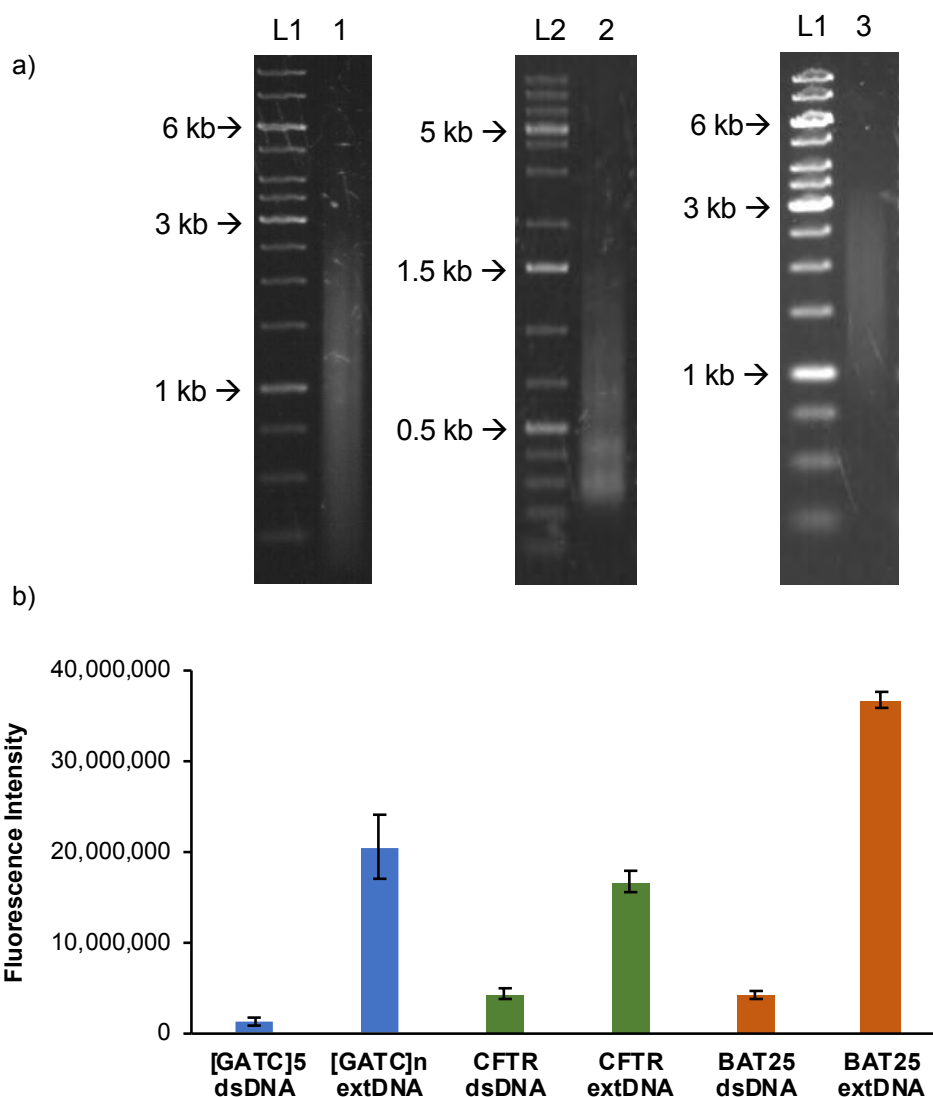
Figure 14. *a) Agarose gel length comparison for 1) [GATC], 2) CFTR and 3) BAT25 b) Comparison of the fluorescence intensities for the surfaces modified with each sequence highlighting the difference between short oligo-seed and extDNA.*

The enhanced fluorescence intensity for the BAT25 sequence is greater than observed in both the GATC and the CFTR sequences. A comparison of the gel electrophoresis and fluorescence intensity for the GATC, CFTR and BAT25 sequences are shown in Figure 14, confirming the longer extension both in solution and off the surface.

The extension of the BAT25 sequence exhibits the greatest increase in fluorescence intensity compared to the other sequences studied and has medical importance, therefore the BAT25 sequences were used for further investigations into the sensing applications of the device.

4.2.3 Optimisation of parameters

Despite the distinguished difference in fluorescence intensity for the extDNA compared to the short oligo seed, several parameters to improve the sensitivity and reliability were carried out to maximise the potential of the device.

PG is established as a dsDNA intercalator irrespective of the base pairs. Other potential fluorescent dyes which are sequence specific could conceivably further enhance the fluorescence intensity change for extDNA samples. The BAT25 sequence is AT-rich and so, the fluorescent stain DAPI was analysed for suitability. DAPI is a popular stain due to the 20x increase in fluorescence upon binding to AT regions in dsDNA.[25] DAPI solution was placed on the surface for 20 min and fluorescent images were obtained using filter 02 with excitation at 360 nm. The difference in fluorescence intensity is displayed in Figure 15. The FI for the extDNA sample is lower than for the short dsDNA so is not ideal. The standard deviation is extremely high suggesting that this DAPI does not give a reliable or reproducible FI. The difference between dsDNA and extDNA using PG is consistently observed to a greater degree, so PG continued to be used.
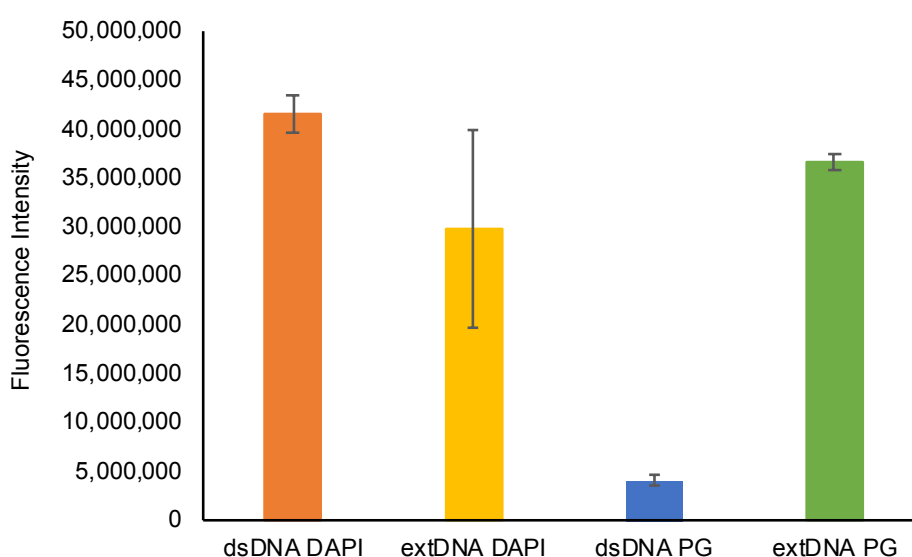
Figure 15. *Fluorescence intensity comparison of surfaces stained with DAPI and with PG.*

PG is traditionally used in a Tris-EDTA buffer, TE,[26] however when placing the PG-TE solution onto the surface, several salt spots are visible which are not seen if PG is deposited in nanopure H_2O, Figure 16b. The FI for PG in H_2O is also significantly higher than when PG is in TE therefore for future studies PG was dissolved in H_2O.
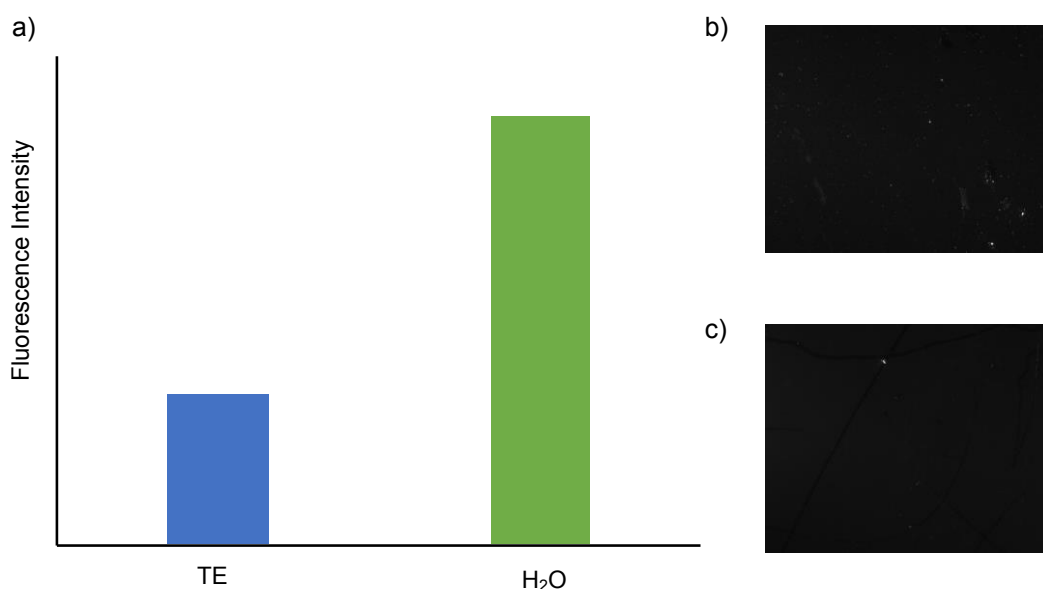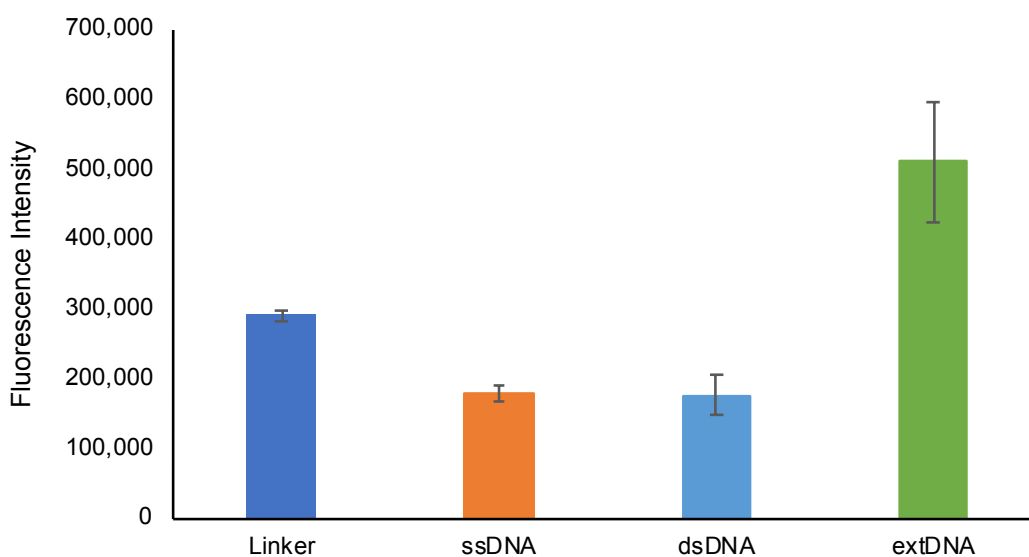
Figure 16. *a) Fluorescence intensity of extDNA and PG in TE buffer and H_2O. b) Fluorescence image of extDNA in PG/TE solution and c) Fluorescence image of extDNA in PG/ H_2O solution.*

The binding time of PG is thought to be almost instantaneous upon interaction with DNA,[26] however with the DNA localised onto the surface, it could take longer for the intercalation of PG into the DNA to take place due to steric hindrance of the surface. PG was placed on extDNA surfaces for varying times and the fluorescence intensities compared, Figure 17. After consecutive increases in FI with 5 min time increments, the FI decreases after 20 min. Therefore, for subsequent investigations the PG was placed on the surface for 20 min before washing.
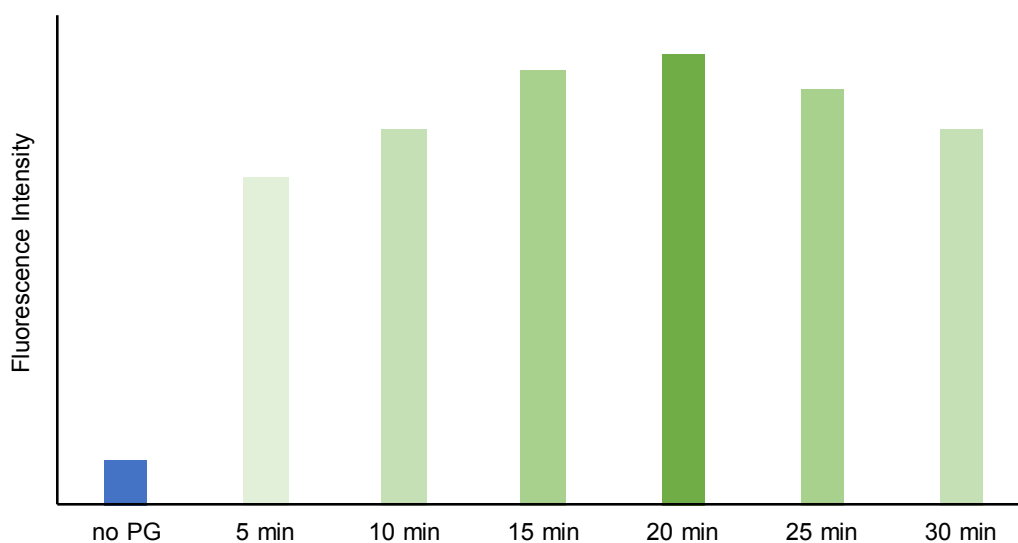
**Figure 17.** *Fluorescence intensity for various PG binding times.*

All extensions from the surface have so far been carried out on cut glass microscope slides. In order to see if the same phenomenon is observed on a different surface the extension protocol was performed on a silicon wafer. The extension method was carried out on silicon wafers, p-type (100) cut to 0.5 cm^2 and PG was applied to the surface for fluorescence imaging, Figure 18. An increase in fluorescence is observed from short dsDNA to extDNA but the difference is not as significant as seen on a glass surface. Nevertheless, there is still a clear enhancement for the extDNA highlighting the versatility of the extension method. Not only the sequence but the surface can be tailored to the desired application.

Figure 18. *Fluorescence intensity of extDNA grown on silicon dioxide surfaces.*

4.2.4 Dehybridisation of long DNA

In order for the device to be usable in the real world as a sensor, the long extended strand must be dehybridised to generate a long ssDNA on the surface capable of hybridising with target strands. Several dehybridisation methods are described in the literature mainly using heat or urea for several iterations.[27,28] Dehybridisation of our extDNA was tested using both the heat method and urea, with the FI calculated for each, Figure 19. Heat dehybridisation was carried out by immersion of the surface in 1 ml of nanopure H$_2$O for 10 min at 95 °C. Urea dehybridisation involved the immersion of the surface in 5 M urea for 15 min. As shown in Figure 19, the heat dehybridisation removes more of the fluorescence intensity, therefore denatures more of the DNA compared to the urea dehybridisation method. Residue was also left over after submerging, which lead to the heat dehybridisation process being chosen.
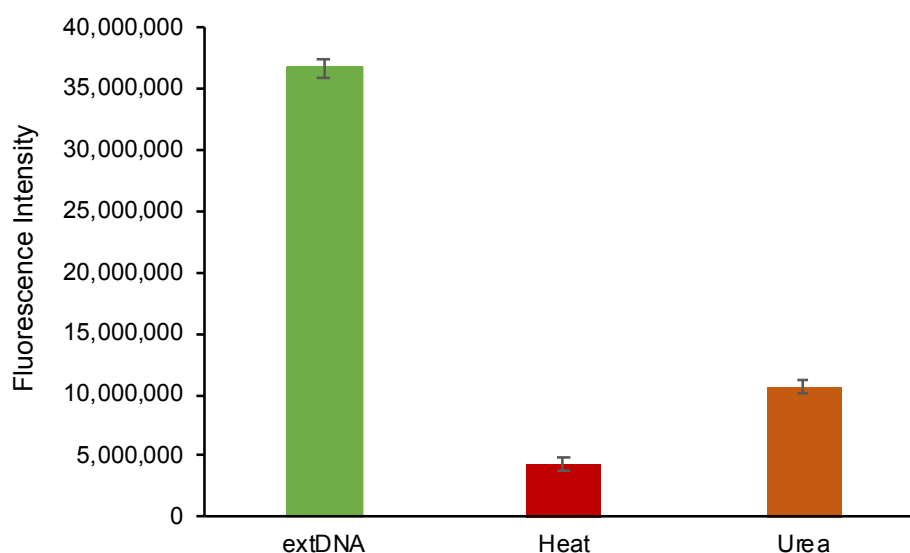
Figure 19. *Fluorescence intensity of extDNA surfaces dehybridised with heat and urea.*

In order to ensure as much of the long ssDNA is removed from the surface, the heat dehybridisation procedure was carried out multiple times and monitored by FI, Figure 20. The FI dramatically decreases after the first dehybridisation, and again slightly after the second. After 2 dehybridisation steps, the FI remains relatively consistent. To keep the time of the whole process to a minimum, 2 dehybridisations was decided to be sufficient to remove the long DNA.
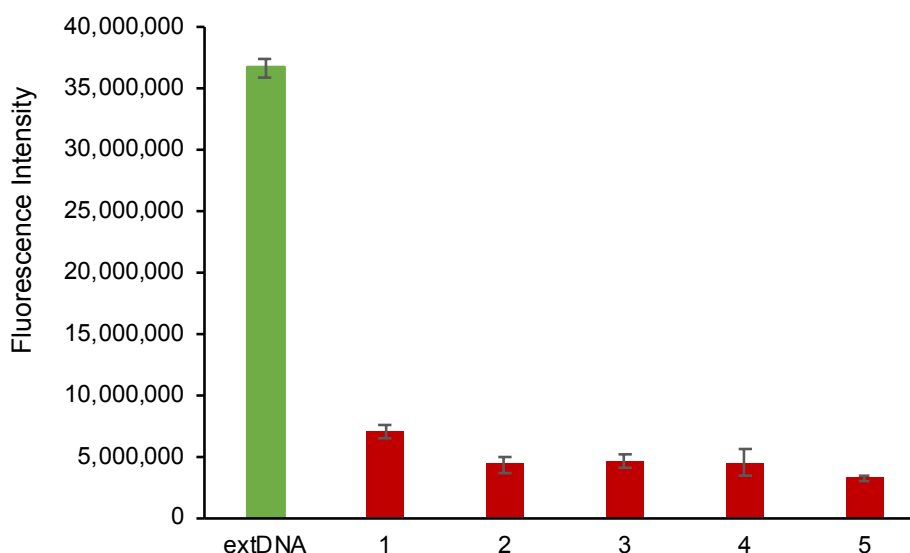
Figure 20. *Fluorescence intensity of 5 successive dehybridisations of extDNA surfaces.*

4.2.5 Re-addition of short target strands

The main application of the extension of DNA off the surface is to form a DNA biosensor capable of distinguishing between DNA sequences. The hybridisation of the long ssDNA on the surface with target complementary strands was investigated. It is

132

expected that with successful hybridisation, an increase in FI will be observed compared to the dehybridised surface. The fluorescence intensity will most likely not reach the same intensity as for the fully complementary (comp) dsDNA strand as not all bases will be paired, therefore there will be less regions for the PG to bind to. A successful DNA biosensor is able to distinguish between comp and non-complementary (noncomp) DNA sequences. In the ideal situation, the device would be able to discriminate between fully complementary and a single base mismatch (1BM), in which only one base differs from the target. With this in mind, three short oligomers were designed mimicking each situation, Table 6. Each of the strands contains flanking regions at each end which are not complementary to resemble the rest of the DNA strand in a real patient's DNA sample as only short base regions are the target of the sensor and in a real DNA sample there will be many other regions of untargeted sequences.

Table 6. Table of short oligomers used for rehybridisation with ssextDNA on the surface.

| Name	Sequence
Comp	5' - AAGTTTTTTTTTTCAA -3'
1BM	5' - AAGTTTTTTTTTTTCAA -3'
Noncomp	5' - CTAGCTAGCTAGCTAGCTAG -3'

Hybridisation with the short strands was achieved by immersion 10 nM target oligomer solution for 10 min at 75 °C. The samples were cooled slowly to room temperature to allow hybridisation. PG was added to each surface and the fluorescence intensities compared, Figure 21.
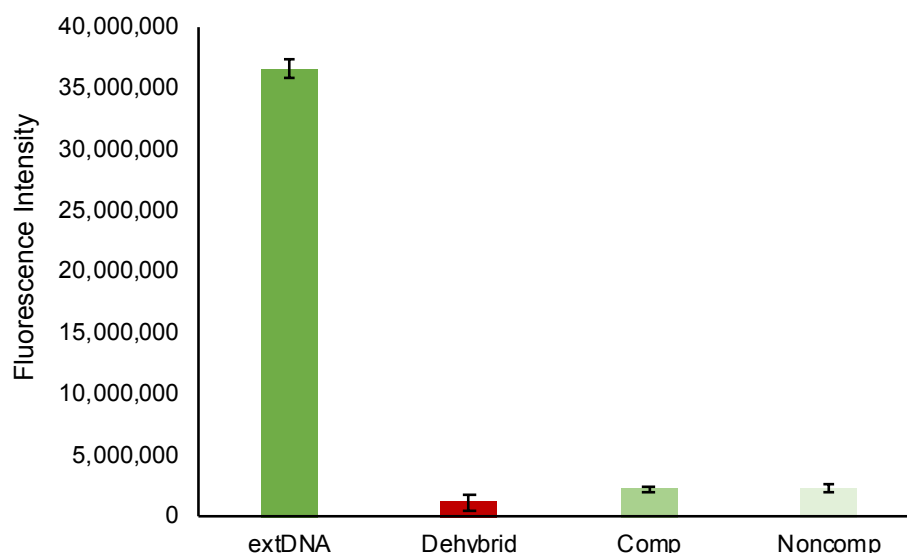
Figure 21. *Fluorescence intensity of extDNA surfaces after hybridisation with comp and noncomp strands.*

A negligible difference between oligomer rehybridisations was observed. The highest FI was detected for the comp oligomer however is still very similar to the noncomp oligomer. With a view to increase the hybridisation and balance any repulsion between the negatively charged phosphate backbones, the hybridisation procedure was performed in a $MgCl_2$ buffer and the FI monitored, Figure 22. The difference between comp, 1BM and noncomp is now more significant and identifiable with a good separation between comp and 1BM.
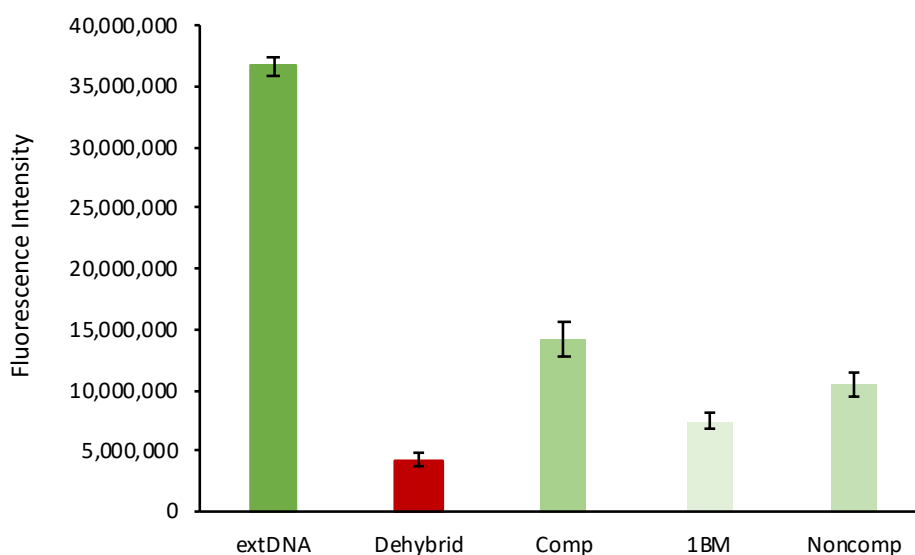
Figure 22. *Fluorescence intensity of extDNA surfaces after hybridisation with comp, 1BM and noncomp strands in $MgCl_2$ buffer.*

4.2.6 Target concentration test

In order to deduce the sensitivity limits of the device, several concentrations of target complementary DNA ranging from 5 µM to 0.1 nM were tested. The readout was monitored by fluorescence intensity, Figure 23.
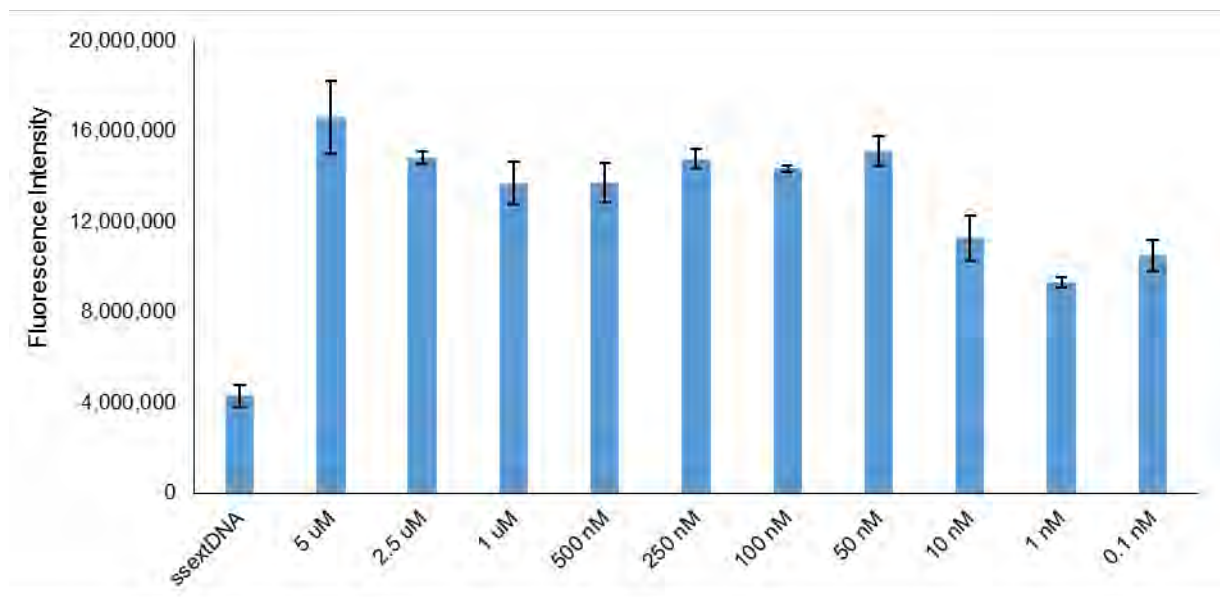
Figure 23. *Fluorescence intensity of extDNA surfaces with varying concentrations of target DNA.*

Below 50 nM, the FI decreases slightly but it is still larger than the dsDNA sample and so, is distinguishable. This proves that the device is capable of detecting target DNA sequences down to 0.1 nM.

4.2.7 Hybridisation/dehybridisation stability

To explore the stability of the extDNA surfaces, the dsextDNA was denatured and subsequently rehybridised with target complementary strands. The denaturation and hybridisation steps were executed as previously described with a target concentration of 50 nM. The fluorescence intensity during six successive denaturation/hybridisation cycles is displayed in Figure 24. Over the six cycles, the decrease in fluorescence intensity was 31 %, with only a 15 % decrease after four cycles, highlighting the reproducibility and stability of the extDNA surface.
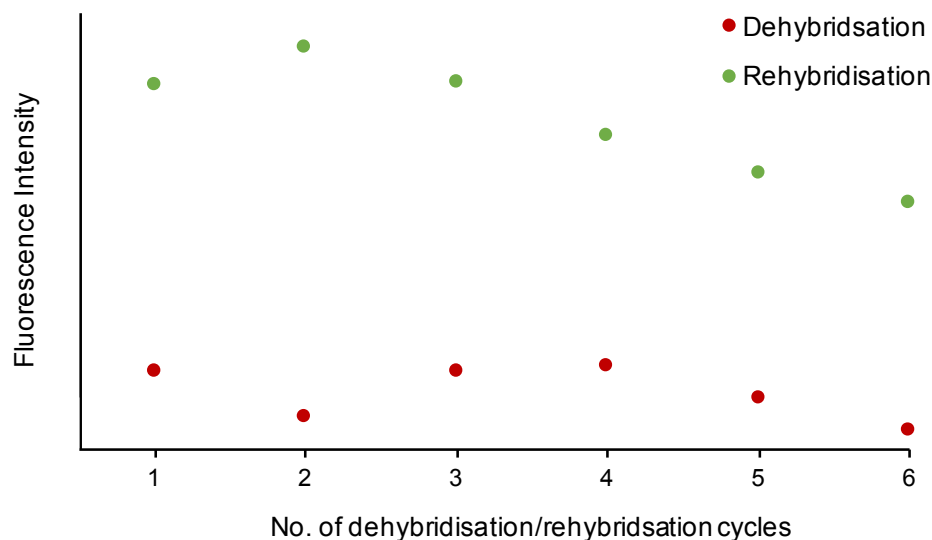
Figure 24. *Fluorescence intensity of extDNA surfaces toward 50 nM target DNA during six denaturation/hybridisation cycles.*

4.2.8 Extension using patterned surfaces

Although the extension method has been proven to work for one sequence per surface, an array-type patterning of the surface would allow multiple DNA target sequences to be screened simultaneously from one DNA sample. Each different DNA sequence would be confined to localised regions on the surface and therefore be able to detect distinct target sequences.

Another method of restricting the binding of the DNA molecules is to print the linker molecule so selected regions of the surface are available for DNA binding and extension. With the linker printed in certain areas, DNA extension will only occur at the selected regions creating an array type pattern on the surface. Different DNA sequences can then be attached to each linker spot allowing for one surface to include many different probe DNA strands for extension. The linker was printed onto the glass surface by an inkjet printer in a dot pattern, Figure 25a and b, and a track, Figure 25c and d, in collaboration with Tom Bamford (PGR, Newcastle University).

However, after DNA extension no fluorescence intensity was observed. This is attributed to requirement of a high temperature for 16h for the attachment of the linker to the surface. The surface was placed on a heat block in a toluene chamber to try and induce the silanisation reaction, however the linker deposits did not remain where they were printed.

136
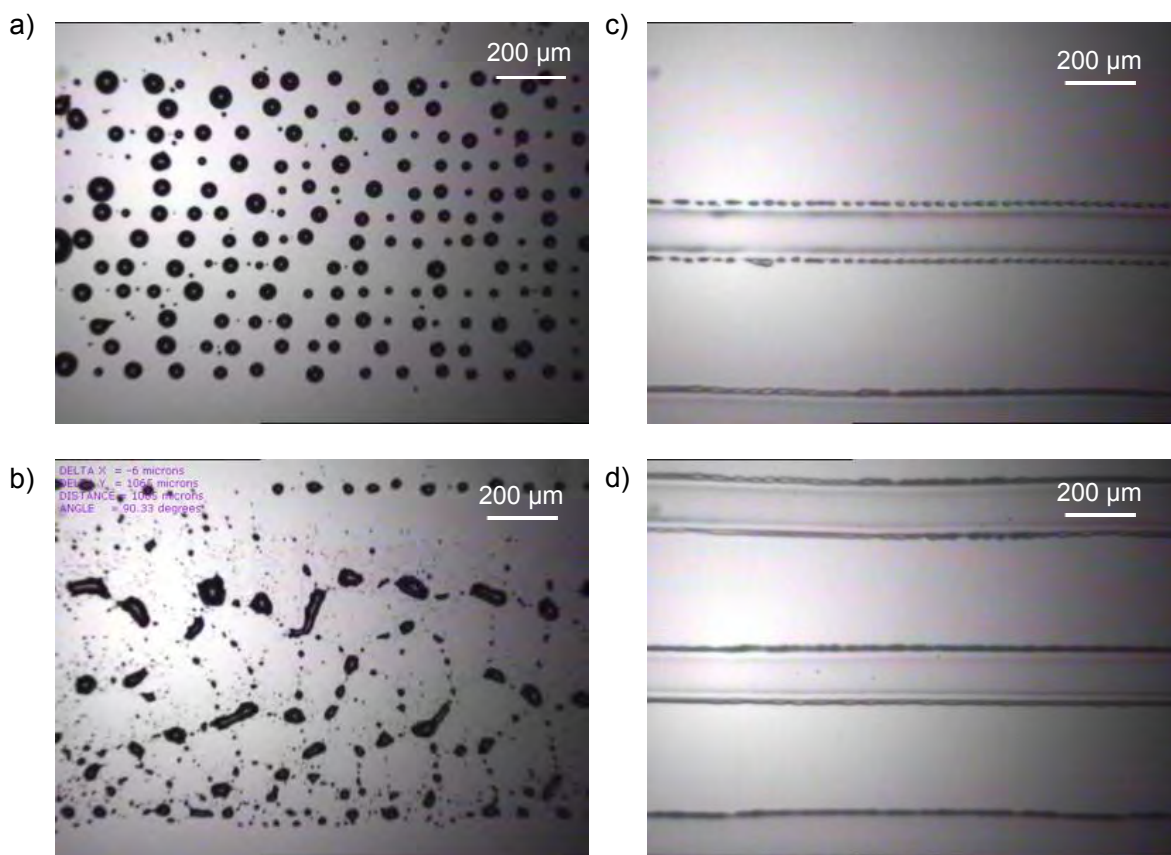
Figure 25. *Printing of linker onto a pre-cleaned glass surface. a-b) Dot pattern and c-d) a track.*

Due to the fact that the printed linker did not appear to remain in the localised regions in which it was placed on the surface and another method for patterning the surface was explored. The printing of graphene oxide films has attracted interest due to the potential utilization in semi-conductor devices,[29] electrode arrays for micro super-capictors,[30] and sensors.[31] A graphene oxide ink was printed onto the cleaned glass surface in a dot design. The printed surface was baked in a vacuum oven at 150 °C to attempt to fuse the graphene oxide with the surface to increase the stability, but not oxidise it. In order to attach the oligo-seed to the surface, the amino-modified DNA probe was dissolved in a 1 mg/ml solution of HATU to facilitate the coupling between the aldehyde group on the graphene oxide and the amine on the DNA.[32] The DNA was hybridised with the target strand and subjected to the heat-cool extension protocol described earlier. After addition of PG, fluorescence images of the surface were obtained, Figure 26. It is expected that each spot will reveal an increased fluorescence compared to the glass surface however each spot appears as dark as the spots with no extension treatment. The marks observed on the spots in Figure 26b are thought to be due to the several hours of submersion with the various solutions and are the result of the graphene oxide being scraped off the surface.
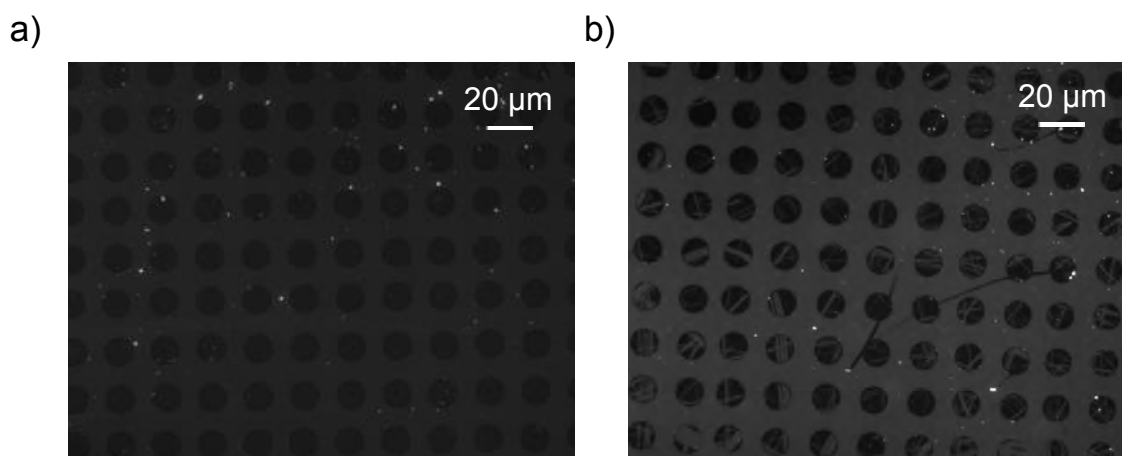
Figure 26. *Fluorescence images of the extDNA localised onto printed graphene oxide spots.*

It was then found that graphene oxide is known to inhibit fluorescence,[33] therefore using a fluorescence method of detection is not realistically viable coupled with the graphene oxide tracks. Although the DNA is not observable by fluorescence, successful attachment of the DNA probe was confirmed by XPS analysis, Figure 27. P2p peaks associated with the phosphate in the DNA are observed from a dsDNA-modified GO printed sample. Other readout measurements such as conductance could be used to detect the extension, however, as discovered in chapter 3, although a difference is visualised, measurements can take a very long time to obtain and are therefore not ideal for the rapid disease detection required.
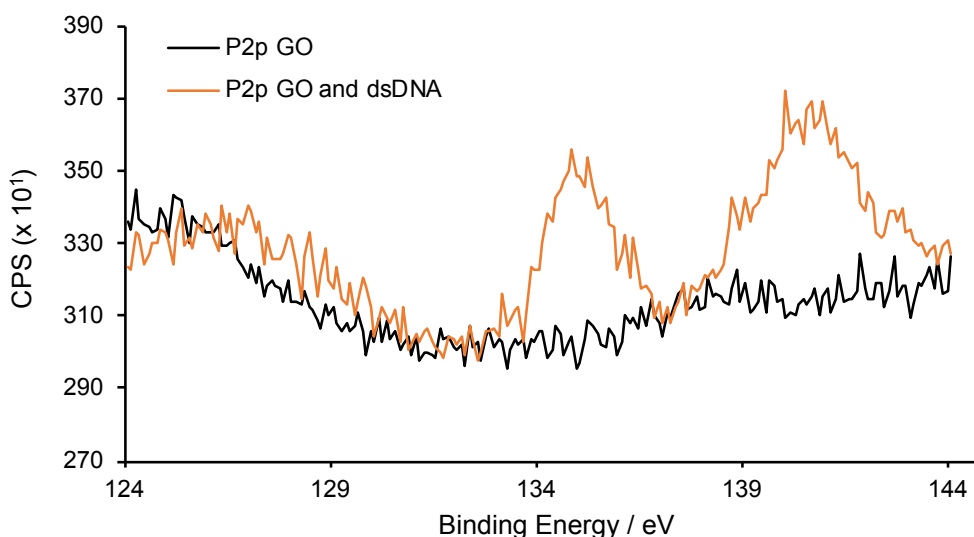
Figure 27. *XPS binding energy profiles highlighting the appearance of the P2p phosphate peak attributed to the phosphate backbone in the DNA.*

Although attempts to pattern the surface and observe the increased fluorescence for extDNA were unsuccessful, further investigation is required to find a suitable,

reproducible method for patterning the surface to attain the necessary multiple DNA sequence surface.

4.3 Conclusion

The extension of DNA off a surface to construct long DNA brushes provides an increased number of binding sites, multiplexed in the z direction, for the binding of target DNA strands in biosensing.

Initially a random repeat sequence DNA oligo-seed, [GATC]$_5$/[GATC]$_5$, was successfully attached to a glass surface, cut to 0.5 cm^2, via the same linker chemistry employed in Chapter 2. The oligo-seed modified chip was then subjected to enzymatic PCR heat-cool cycles to allow the extension of the DNA strand using Z3 polymerase. After addition of the DNA intercalator PG, an increase in fluorescence intensity was observed for extDNA surfaces compared to the oligo-seed surfaces. The successful extension was further confirmed by AFM analysis of the ssextDNA strands denatured from the surface which indicated DNA lengths up to 300 bp confirming the increase in length of the oligo-seed tethered to the surface.

The extension method was then performed on a medically important DNA sequence, the CFTR gene, to highlight the potential of the method for real-world applications. The same increase in fluorescence intensity was observed, however the enhancement was not as significant as for the GATC sequence. Therefore, another well-studied DNA mutation was explored, BAT25. The extension of the BAT25 sequences resulted in longer lengths of DNA both in solution, as confirmed by agarose gel electrophoresis, and off the surface, observed by a larger increase in fluorescence intensity. As a result, the BAT25 sequence was chosen to continue optimisation of the method in the direction of sensing applications. Re-addition of short sequences to the ssextDNA strand exhibited a greater fluorescence intensity, and hence binding, towards the complementary target compared to a one base mismatch and a non-complementary strand.

To increase the capabilities of the method, patterning of the surface was attempted in order to allow the attachment of multiple DNA sequences on one surface for simultaneous screening of numerous DNA mutations. Attempts to extend the DNA off the patterned surface were unsuccessful and so, further investigations are required.

4.4 Experimental

Chemical reagents

All chemical reagents were purchased from Sigma Aldrich and used as received without further purification. Tgo-Pol Z3 exo- variant was prepared and purified in house.[11] Glass slides were purchased from Henso Labware Manufacturing Co., Ltd (Hangzhou, China). APEGDMES was purchased from NewChem Technologies Limited (Newcastle-Upon-Tyne, UK). DNA was purchased from Eurofins Genomics (Ebersberg, Germany).

Primer template annealing

Primer duplexes for extension were prepared: DNA annealing buffer (10 mM Hepes pH 7.5, 100 mM NaCl and 1 mM EDTA) was added to the oligomers and heated to 95 °C for 10 min. Duplex solutions were slowly cooled to room temperature and stored at -20 °C.

DNA polymerase

Tgo-Pol Z3 exo- DNA polymerase was used for the extension. The enzyme belongs to the Archael family B polymerase low fidelity variant with the 3'$\rightarrow$5' exonuclease activity removed and alterations to the fingers domain.

DNA extension in solution

0.5 μM DNA duplex, 200 nM Tgo-Pol Z3 exo- DNA polymerase, DNA polymerase reaction buffer (200 mM Tris-HCl (pH 8.8, 25 °C), 100 mM $(NH_4)_2SO_4$, 100 mM KCl, 1 % Triton X-100, 1 mg/mL Bovine Serum Albumin (BSA) and 20 mM $MgSO_4$), and 0.5 mM deoxynucleotide triphosphates (dNTPs) (dCTP, dATP, dTTP and dGTTP) were mixed together. Heat-cool thermocycles were performed on an Applied Bioscience Veritt 96 well Thermal Cycler for the following cycles:

> Number of cycles (20) x 30 seconds at 95 °C, 30 seconds at 55 °C and 2 min at 72 °C.

The solution was cooled to 4 °C after the reaction. The DNA extension product was purified using QIAquick PCR purification kit (250) (QIAGEN, Manchester, UK) following the manufacturers protocol.

Agarose Gel Electrophoresis

DNA extension products were analysed by gel electrophoresis in TBE buffer (Tris, Boric acid and $Na_2EDTA.2H_2O$). 1% Agarose (Melford, Ipswich, UK) was added to 1x TBE buffer and heated until fully dissolved. The gel mixture was cooled to 50 °C and poured into a gel cassette to set. The DNA ladders, GeneRuler 1 kb and 1 kb+, (Thermo Scientific) were provided with a Loading dye (2.5 % Ficoll-400, 11 mM EDTA, 3.3 mM Tris-HCl (pH 8.0, 25 °C), 0.017 % SDS and 0.015 % bromophenol blue). 2 μL gel loading dye was added to DNA samples (20 ng/μL) and loaded into the gel wells. The gels were run at 100 V, 100 mA 10 W for approximately 1 hr. The gel was post-stained with 5 μg/mL solution of ethidium bromide and visualised using an UV transilluminator.

UV-Visible Spectroscopy

UV-Vis spectroscopy was performed using a NanoDropONE Spectrometer (Thermo Scientific). The spectrometer was blanked using nanopure H_2O.

Pre-treatment of glass surface

Glass slides were diced into 0.5 cm^2 chips. The chips were wiped with acetone, IPA and NP-H_2O and sonicated in acetone, IPA and NP-H_2O for 15 mins sequentially and dried with N_2. The chips were placed under O_2 plasma treatment for 15 min.

Linker attachment to surface

The pre-cleaned chips were immersed in APEGDMES/toluene solution (233 μM, 3 mL) preheated to 65 °C for 16 h. The chips were washed with toluene, ethanol and NP-H_2O 3 times sequentially before being placed under vacuum in a vacuum oven at 120 °C for 40 min.

DNA attachment to linker

Amino-tagged DNA probe solution (40 μL, 100 μM) in 10% acetic acid solution was drop cast onto the chips for 1 h in a humid environment. $NaCNBH_3$ (40 μL, 16 μM) in 50% MeOH solution was deposited on top of the probe solution for a further 2 h in a humid environment. The chips were washed with phosphate buffered saline (0.5x) and excess water to remove any excess DNA molecules. Chips were dried with a stream of nitrogen.

DNA hybridisation

Complementary DNA target solution (40 μL, 200 nM) in PBS buffer (0.5x) was drop cast onto the silicon chips for 15 min in a humid environment. Chips were washed with PBS buffer (0.5x) for 30 min and NP-H$_2$O for 30 min then dried under a stream of nitrogen.

DNA extension off the surface

The chips were placed in an Eppendorf along with the required solution for heat-cool cycles: 200 nM DNA polymerase, DNA polymerase reaction buffer (200 mM Tris-HCl (pH 8.8, 25 °C), 100 mM (NH$_4$)$_2$SO$_4$, 100 mM KCl, 1% Triton X-100, 1 mg/mL Bovine Serum Albumin (BSA) and 20 mM MgSO$_4$), and 0.5 mM deoxynucleotide triphosphates (dNTPs) (dCTP, dATP, dTTP and dGTTP). Heat-cool thermocycles were performed on an Applied Bioscience Veritt 96 well Thermal Cycler for the following cycles:

> Number of cycles (20) x 30 seconds at 95 °C, 30 seconds at 55 °C and 2 min at 72 °C.

The solution was cooled to 4 °C after the reaction. The chips were removed from the solution and washed in NP-H$_2$O for 30 min and dried under a stream of nitrogen.

Fluorescence microscope imaging

Samples were placed on an Axioshop 2 plus (Zeiss, Germany) image platform, set to filter 44, with a Plan-NEOFLUAR 10 x/ 0.3 objective lens (Zeiss). The sample was excited at 490 nm from a ebq100 mercury lamp (LEJ, Germany) and images were taken using an AxioCam HRm (Zeiss).

TIRF

TIRF measurements were carried out using a Nikon TiE microscope with a Nikon PlanApo, TIRF, 100x, 1.49NA lens. The camera used to obtain images was the Andor iXON 885 EM CCD (1024 x 1024) and the images were analysed using Nikon Elements software.

AFM

The top layer of the mica surface was cleaved using sticky tape. 5 μL of DNA sample (either 2 ng/μL or 4 ng/μL) dissolved 1 mM MgCl$_2$ was placed onto the mica surface

held at a 25° angle to allow the DNA to flow across the mica surface. After 5 min, 5 μL nanopure H_2O was dropped on top of the DNA sample, again at 25° angle. A gentle stream of N_2 was passed over the surface and then further dried under laminar flow for 1 hr. AFM images were obtained using a Dimension V with a nanoscope controller (Veeco Instruments Inc., Metrology Group, Santa Barbara, CA) on an isolation table (Veeco Inc., Metrology Group) to reduce interference. The software NanoScope Analysis 1.8 was used to obtain data.

Contact angle

Contact angle measurements were performed on a KSV Cam 101 (KSV Instruments Ltd., Finland) using built-in CAM 2008 software. A 1 μL drop of NP-H_2O was dropped onto the surface. The software was used to estimate the angle of the water droplet on the surface. 10 measurements for each sample were obtained. Measurements collected where there was more than a 2° difference in the left and right angle of the droplet were discarded. Measurements which were more than 2 standard deviations away from the average value were also discarded.

DNA heat dehybridisation

extDNA surfaces were placed in 1 mL nanopure H_2O at 95 °C for 10 min. Surfaces were transferred to a fresh 1 mL nanopure H_2O at 95 °C for 10 min and dried with N_2.

DNA urea dehybridisation

extDNA surfaces were placed in 1 mL 5 M urea for 10 min. Surfaces were rinsed with 1 mL nanopure H_2O and dried with N_2.

DNA rehybridisation

ssextDNA surfaces were immersed in 400 μL 100 μM target oligomer at 75 °C for 10 min and cooled slowly to room temperature. Samples rinsed with 1 mL nanopure H_2O and dried with N_2. For the target concentration test, the concentration of target oligomer was altered as described in section 4.2.6.

Printed toluene linker

APEGDMES/toluene linker solution was loaded into a printing cartridge (Dimatix Materials Cartridges, Model DMC-11610/PN2100201146, FujiFilm, 10pl) and inserted into the printer (Dimatix Materials Printer, DMP-2800). A silicon wafer cut to 1 cm^2 was placed under O_2 plasma treatment for 15 min. Linker solution was printed, in a dot

array and a track formation, onto the silicon wafer by Tom Bamford. The printed wafer was placed in a toluene chamber (the chip was elevated from the toluene to avoid immersion and removal of the printed spots) and heated to 80 °C for 3 hours.

Printed graphene tracks and DNA immobilisation

The graphene oxide was formulated into an ink by dispersion in water and diluted with glycol to improve wettability (carried out by Tom Bamford). The graphene oxide was printed onto a pre-cleaned glass chip, cut to 0.5 cm^2. The printed chip was placed in a vacuum oven for 2 hr at 150 °C. Amino-modified DNA (GATC sequence) was dissolved in 1 mg/mL HATU solution. 4 μL of DNA/HATU solution was placed on the printed glass chip and left in a humidity chamber for 8 hr. 4 μL of complementary DNA placed on printed glass chip and left for 2 hr for hybridisation. Enzymatic extension was carried out off the surface as described earlier.

4.5 References

1   Hays, J. B. Persistence length of DNA. *Biopolym.* **8**, 531-536 (1969).
2   Nimse, S. B., Song, K., Sonawane, M. D., Sayyed, D. R. & Kim, T. Immobilization Techniques for Microarray: Challenges and Applications. *Sensors (Basel, Switzerland)* **14**, 22208-22229 (2014).
3   Drummond, T. G., Hill, M. G. & Barton, J. K. Electrochemical DNA sensors. *Nature Biotechnology* **21**, 1192 (2003).
4   Gong, P. & Levicky, R. DNA surface hybridization regimes. *Proceedings of the National Academy of Sciences* **105**, 5301-5306 (2008).
5   Metzker, M. L. Sequencing technologies — the next generation. *Nature Reviews Genetics* **11**, 31 (2009).
6   Valignat, M.-P., Theodoly, O., Crocker, J. C., Russel, W. B. & Chaikin, P. M. Reversible self-assembly and directed assembly of DNA-linked micrometer-sized colloids. *Proceedings of the National Academy of Sciences of the United States of America* **102**, 4225-4229 (2005).
7   Bracha, D., Karzbrun, E., Shemer, G., Pincus, P. A. & Bar-Ziv, R. H. Entropy-driven collective interactions in DNA brushes on a biochip. *Proceedings of the National Academy of Sciences* **110**, 4534-4538 (2013).
8   Nakamura, S. *et al.* DNA Brush-Directed Vertical Alignment of Extensive Gold Nanorod Arrays with Controlled Density. *ACS Omega* **2**, 2208-2213, doi:10.1021/acsomega.7b00303 (2017).
9   Sun, L., Svedhem, S. & Åkerman, B. Construction and Modeling of Concatemeric DNA Multilayers on a Planar Surface as Monitored by QCM-D and SPR. *Langmuir* **30**, 8432-8441 (2014).
10   Wang, C. *et al.* DNA microarray fabricated on poly(acrylic acid) brushes-coated porous silicon by in situ rolling circle amplification. *Analyst* **137**, 4539-4545 (2012).
11   Jozwiakowski, S. K. & Connolly, B. A. A Modified Family-B Archaeal DNA Polymerase with Reverse Transcriptase Activity. *ChemBioChem* **12**, 35-37 (2011).
12   Whitfield, C. J., Turley, A. T., Tuite, E. M., Connolly, B. A. & Pike, A. R. Enzymatic Method for the Synthesis of Long DNA Sequences with Multiple Repeat Units. *Angewandte Chemie International Edition* **54**, 8971-8974, doi:10.1002/anie.201502971 (2015).
13   Terpilowski, K. & Rymuszka, D. Surface properties of glass plates activated by air, oxygen, nitrogen and argon plasma. *Glass Physics and Chemistry* **42**, 535-541 (2016).
14   Dragan, A. I. *et al.* Characterization of PicoGreen Interaction with dsDNA and the Origin of Its Fluorescence Enhancement upon Binding. *Biophysical Journal* **99**, 3010-3019 (2010).
15   Li, J. *et al.* A convenient method of aligning large DNA molecules on bare mica surfaces for atomic force microscopy. *Nucleic Acids Research* **26**, 4785-4786 (1998).
16   Hansma, H. G., Sinsheimer, R. L., Li, M.-Q. & Hansma, P. K. Atomic force microscopy of single-and double-stranded DNA. *Nucleic Acids Research* **20**, 3585-3590 (1992).
17   Hansma, H. G., Revenko, I., Kim, K. & Laney, D. E. Atomic Force Microscopy of Long and Short Double-Stranded, Single-Stranded and Triple-Stranded Nucleic Acids. *Nucleic Acids Research* **24**, 713-720 (1996).

18   Mattheyses, A. L., Simon, S. M. & Rappoport, J. Z. Imaging with total internal reflection fluorescence microscopy for the cell biologist. *Journal of Cell Science* **123**, 3621-3628 (2010).

19   R. A. Bartoszewski *et al.* A Synonymous Single Nucleotide Polymorphism in ΔF508 CFTR alters the Secondary Structure of the mRNA and the Expression of the Mutant Protein. *J. Bio. Chem* **285**, 28741-28748 (2010).

20   Costa, D., Miguel, M. G. & Lindman, B. Responsive Polymer Gels: Double-Stranded versus Single-Stranded DNA. *The Journal of Physical Chemistry B* **111**, 10886-10896 (2007).

21   Zhou, X.-P. *et al.* Determination of the replication error phenotype in human tumors without the requirement for matching normal DNA by analysis of mononucleotide repeat microsatellites. *Genes, Chromosomes and Cancer* **21**, 101-107 (1998).

22   Umar, A. *et al.* Revised Bethesda Guidelines for Hereditary Nonpolyposis Colorectal Cancer (Lynch Syndrome) and Microsatellite Instability. *Journal of the National Cancer Institute* **96**, 261-268 (2004).

23   Luzzati, V., Mathis, A., Masson, F. & Witz, J. Structure transitions observed in DNA and poly A in solution as a function of temperature and pH. *Journal of Molecular Biology* **10**, 28-41 (1964).

24   Mills, J. B., Vacano, E. & Hagerman, P. J. Flexibility of single-stranded DNA: use of gapped duplex helices to determine the persistence lengths of Poly(dT) and Poly(dA)11Edited by B. Honig. *Journal of Molecular Biology* **285**, 245-257 (1999).

25   Kapuscinski, J. DAPI: a DNA-Specific Fluorescent Probe. *Biotechnic & Histochemistry* **70**, 220-233 (1995).

26   Singer, V. L., Jones, L. J., Yue, S. T. & Haugland, R. P. Characterization of PicoGreen Reagent and Development of a Fluorescence-Based Solution Assay for Double-Stranded DNA Quantitation. *Analytical Biochemistry* **249**, 228-238 (1997).

27   Dodge, A., Turcatti, G., Lawrence, I., de Rooij, N. F. & Verpoorte, E. A Microfluidic Platform Using Molecular Beacon-Based Temperature Calibration for Thermal Dehybridization of Surface-Bound DNA. *Analytical Chemistry* **76**, 1778-1787 (2004).

28   Lockett, M. R. & Smith, L. M. Fabrication and Characterization of DNA Arrays Prepared on Carbon-on-Metal Substrates. *Analytical Chemistry* **81**, 6429-6437 (2009).

29   Eda, G., Fanchini, G. & Chhowalla, M. Large-area ultrathin films of reduced graphene oxide as a transparent and flexible electronic material. *Nature Nanotechnology* **3**, 270 (2008).

30   Le, L. T., Ervin, M. H., Qiu, H., Fuchs, B. E. & Lee, W. Y. Graphene supercapacitor electrodes fabricated by inkjet printing and thermal reduction of graphene oxide. *Electrochemistry Communications* **13**, 355-358 (2011).

31   He, Q. *et al.* Centimeter-Long and Large-Scale Micropatterns of Reduced Graphene Oxide Films: Fabrication and Sensing Applications. *ACS Nano* **4**, 3201-3208 (2010).

32   Mohanty, N. & Berry, V. Graphene-Based Single-Bacterium Resolution Biodevice and DNA Transistor: Interfacing Graphene Derivatives with Nanoscale and Microscale Biocomponents. *Nano Letters* **8**, 4469-4476 (2008).

33   Liu, F., Choi, J. Y. & Seo, T. S. Graphene oxide arrays for detecting specific DNA hybridization by fluorescence resonance energy transfer. *Biosensors and Bioelectronics* **25**, 2361-2365 (2010).

Outlook

The method of DNA integration with surfaces outlined in this thesis provide routes to the synthesis of modified DNA bases for directed assembly of metal ions and the use of DNA surfaces for sensing applications using both electrical and optical readout systems.

The silica controlled pore glass (CPG) bead was utilised to facilitate the selective conversion of guanosine (G) to thio-guanosine (tG) in the oligomer, 5'-$A_6G_4T_6$-3' (**oligo-3**). Performing the synthesis whilst the oligomer is still bound to the solid support allows for easy purification and isolation. The modified oligomer was cleaved from the CPG bead and characterised by HPLC, UV-Vis and IR. The conversion was found to be selective for guanosine, leaving the other three natural bases unmodified as shown by HPLC, IR, UV-vis and MALDI-TOF analysis. Oligo-3 was self-annealed to form **duplex-3** to observe the effect of the modified base on the duplex stability. The tG base caused significant destabilisation to the whole duplex determined by the decrease in melting temperature compared to the fully complementary duplex. Exiton splitting was not observed in the CD spectra in the 340 nm region attributed to the thiol group. Upon addition of cadmium ions, the stability of the duplex was restored to that of the fully complementary duplex indicating metal-mediated duplex healing. Molecular modelling calculations indicated an increase in flexibility for each base in duplex-3, which then exhibited a ten-fold reduction base flexibility in the presence of the cadmium ions. The straightforward conversion of G to tG on column provides a route for thiol modified oligomers, capable of directed metal assembly for duplex healing.

The electron transport mechanism of a redox-tagged oligomer integrated with a semi-conductor silicon surface was investigated. A silane linker molecule was utilised to attach ssDNA and dsDNA to the silicon surface. The large-area molecular junction EGaIn technique was used to explore the charge transport mechanism through DNA monolayers. The current density for the ssDNA surface was compared to the current density for linker molecule which indicated the ssDNA was coiled and not perpendicular to the surface discernible by the similar curve profiles. Upon hybridisation to dsDNA, the curve profile changed as the current density decreased and an increase in rectification was observed. This observation signifies that the dsDNA monolayer is now perpendicular to the surface and available to take part in charge transport. The room temperature junctions indicate that the charge transport mechanism in ssDNA monolayers is electron tunneling, whereas the mechanism in dsDNA monolayers is both charge hopping and electron tunneling. Temperature

dependence measurements were carried out to clarify the charge transport mechanism in both DNA monolayers which confirmed the electron tunneling mechanism for ssDNA. The charge transport for dsDNA is still not confirmed therefore further measurements are required. The difference in current density profiles and charge transport mechanisms between ssDNA and dsDNA could potentially be used in DNA sensors based upon hybridisation events.

Short probe DNA strands (referred to as oligo seeds) immobilised on glass surfaces were extended using a heat-cool enzymatic extension method resulting in the formation of repeat sequence DNA brushes. This method increases the number of binding sites per probe molecule in the z-direction to the surface allowing for increased DNA loading. The sequence $[GATC]_5/[CATG]_5$ was initially extended to prove the extension method resulted in long DNA off the surface. Fluorescence images of the extDNA surfaces, after the addition of fluorescent intercalator PicoGreen, displayed increased fluorescence compared to the short oligo seed immobilised surfaces. The extension protocol was expanded to study medically important gene sequences, CFTR mutation and the BAT25 mutation. The extension for the CFTR gene was not as successful as for the BAT25 sequence therefore the BAT25 sequence was selected to optimise parameters for sensing device applications. Dehybridisation of the extDNA and subsequent re-addition of short target strands demonstrated the potential of the device for sensing applications.

The successful conversion of G to tG enabled the duplex stability of a modified duplex to be determined. A continuation of the project could involve the on-column conversion to alternative base modifications facilitating the straightforward modification of DNA bases for additional applications. The immobilisation of the thio-modified DNA onto surfaces for the study by the EGaIn technique would allow investigations into the charge transport mechanisms of modified bases in the absence and presence of metal ions.

The difference in charge transport mechanism between ssDNA and dsDNA monolayers provides a method for electrical DNA sensing. Further investigations into the density of the DNA monolayers is required to determine surface coverage and establish if any defects in the surface are affecting the charge transport measurements. The temperature dependence measurements and current density measurements of different length DNA monolayers must be repeated to gather reliable data, not affected by silicon oxide growth or melting temperatures. The immobilisation of the DNA

monolayers on gold would be an interesting alternative to the silicon surface used in this thesis due to the extensive studies of gold-immobilised monolayers.

The enzymatic extension of DNA monolayers off a surface to afford long repeat sequence DNA brushes demonstrates the potential of the method for DNA-biosensing applications. Further optimisation of the method is required to improve sensitivity and reproducibility of the device. The printing of the DNA probes into localised regions on the surface would allow for the immobilisation and detection of many different gene target sequences using one surface in a microarray arrangement.

Duplex Healing of Selectively Thiolated Guanosine Mismatches through a Cd^{2+} Chemical Stimulus

Samantha M. L. Lunn,[a] Samira Hribesh,[b] Colette J. Whitfield,[a] Michael J. Hall,[a] Andrew Houlton,[a] Agnieszka K. Bronowska,[a] Eimer M. Tuite,*[a] and Andrew R. Pike*[a]

The on-column selective conversion of guanosine to thioguanosine (tG) yields modified oligomers that exhibit destabilisation over the fully complementary duplex. Restoration to a stabilised duplex is induced through thio-directed Cd^{2+} coordination; a route for healing DNA damage. Short oligomers are G-specifically thiolated through a modified on-column protocol without the need for costly thioguanosine phosphoramidites. Addition of Cd^{2+} ions to a duplex containing a highly disrupted tG central mismatch sequence, 3'-A$_6$tG$_4$T$_6$-5', suggests a (tG)$_8$Cd$_2$ central coordination regime, resulting in increased base stacking and duplex stability. Equilibrium molecular dynamic calculations support the hypothesis of metal-induced healing of the thiolated duplex. The 2 nm displacement of the central tG mismatched region is dramatically reduced after the addition of a chemical stimuli, Cd^{2+} ions, returning to a minimized fluctuational state comparable to the unmodified fully complementary oligomer.

DNA has moved beyond its biological function into the arena of nanotechnology, for which it has been re-purposed as a building material for the construction of functional nano-architectures.[1] Artificial oligonucleotides incorporating modified nucleosides at predetermined sites are of increasing interest due to their potential applications in conducting nanowires,[2] functional DNA origami structures[3] and drug-delivery systems.[4] Of particular interest is the modified purine 6-thio-2-deoxyguanosine (tG), due to potential applications in therapeutics[5] and the ability to coordinate metal ions to form coordination polymers.[6] Thiol-containing artificial nucleobases are typically exploited as soft ligands to bind soft transition metals, for example, gold nanoparticles[7] and silver ions.[8] Herein, we firstly report a facile and cost-effective synthetic route for incorporating tG into oligonucleotides. Secondly, duplexes containing multiple mismatched tG sites show considerable de-stabilisation of the helix. Finally, dramatic re-stabilisation is achieved through metal-mediated healing of the tG:tG

[a] S. M. L. Lunn, C. J. Whitfield, Dr. M. J. Hall, Prof. A. Houlton, Dr. A. K. Bronowska, Dr. E. M. Tuite, Dr. A. R. Pike
School of Chemistry, Newcastle University
Newcastle-upon-Tyne, NE1 7RU (UK)
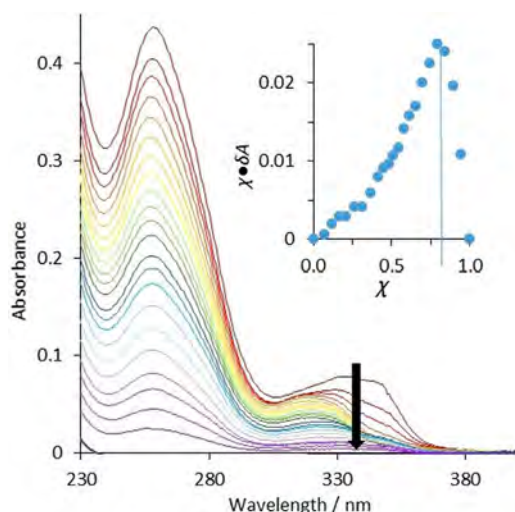E-mail: andrew.pike@ncl.ac.uk
      eimer.tuite@ncl.ac.uk

[b] Dr. S. Hribesh
Department of Chemistry, Faculty of Arts and Sciences
Al-Mergeb University, Al-Khums (Libya)

Supporting information and the ORCID identification numbers for the authors of this article can be found under https://dx.doi.org/10.1002/cbic.201800100.

mismatches through the addition of Cd^{2+} ions. Scheme 1 summarises these three concepts. Understanding the stabilising effects of metal ions on tG bearing duplexes would be of benefit in the directed assembly of DNA nanomaterials through a chemical stimulus.
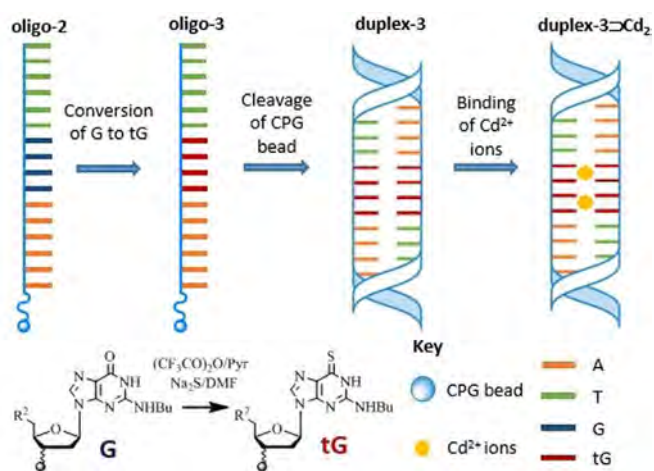
Scheme 1. Schematic overview highlighting the on-column conversion of G to tG, the formation of a tG:tG mismatched duplex, and the subsequent binding of Cd^{2+} to the tG region to re-stabilise the helix.

Reported syntheses of DNA containing tG include incorporation by chemical[9] or enzymatic[10] approaches. Enzymatic approaches can prove problematic due to limitations of structural tolerance of polymerases.[11] Chemically, the incorporation of protected tG bases can be achieved;[12] however, the synthesis can involve complex organic chemistry and is often prohibitively expensive. A synthetic route for the facile conversion of guanosine (G) into tG that is compatible with standard phosphoramidite protecting chemistries is therefore attractive. Herein, simple homobasic oligonucleotides (consisting of only guanine bases), G$_n$ (n = 2, 3, 4 and 5), were synthesized on controlled porous glass (CPG) beads. The surface-immobilised oligomers were subjected to thiolation conditions by using a procedure developed by Jones and Jung,[13] and were then cleaved from the solid support;[14] see the Supporting Information for full details on synthesis and characterisation. Thus, we demonstrate that G$_n$ oligonucleotides can be converted into tG$_n$ oligonucleotides whilst still bound to the standard CPG column; this greatly aids purification and isolation without the need to purchase costly pre-thiolated phosphoramidite reagents.

To study the effect of the replacement of G with tG on the overall stability of duplex formation, the oligomer $T_6G_4A_6$ (oligo-1) and its complement $T_6C_4A_6$ (oligo-2) were synthesized (Scheme 1). Oligo-1, upon thiolation, yielded oligo-3 ($T_6tG_4A_6$); for full synthetic details, see the Supporting Information. The sequence details of these three 16-base oligomers and the perfectly matched G–C (duplex-1), mismatched G–G (duplex-2), mismatched tG–tG (duplex-3) and partially matched tG–C (duplex-4) duplexes formed from them are given in Table 1.

Table 1. Base sequences of the oligomers and duplexes formed to study the effect of the central four-base sequence on thermal stability.

oligo-1	5′-TTT TTT GGGG AAA AAA-3′
oligo-2	5′-TTT TTT CCCC AAA AAA-3′
oligo-3	5′-TTT TTT tGtGtGtG AAA AAA-3′
duplex-1	5′-TTT TTT GGGG AAA AAA-3′
	3′-AAA AAA CCCC TTT TTT-5′
duplex-2	5′-TTT TTT GGGG AAA AAA-3′
	3′-AAA AAA GGGG TTT TTT-5′
duplex-3	5′-TTT TTT tGtGtGtG AAA AAA-3′
	3′-AAA AAA tGtGtGtG TTT TTT-5′
duplex-4	5′-TTT TTT tGtGtGtG AAA AAA-3′
	3′-AAA AAA C C C C TTT TTT-5′

It is proposed that duplex-3 could direct metal-ion coordination to the central tG_4 region, similar to the artificial bases employed by Shionoya et al.[15] Cd^{2+} has a well-known binding affinity for tG,[16] and we hypothesise it could induce metal-ion-mediated duplex stabilisation. Upon addition of an increasing concentration of Cd^{2+} to duplex-3, the absorbance at $\lambda = 341$ nm gradually decreased and exhibited a blueshift to $\lambda = 319$ nm (Figure 1). We attribute this change in absorbance to the complexation of Cd^{2+} ions through the metal-coordinating thione C6=S, which undergoes binding-induced deprotonation to yield the deprotonated thiol; see the Supporting Informa-
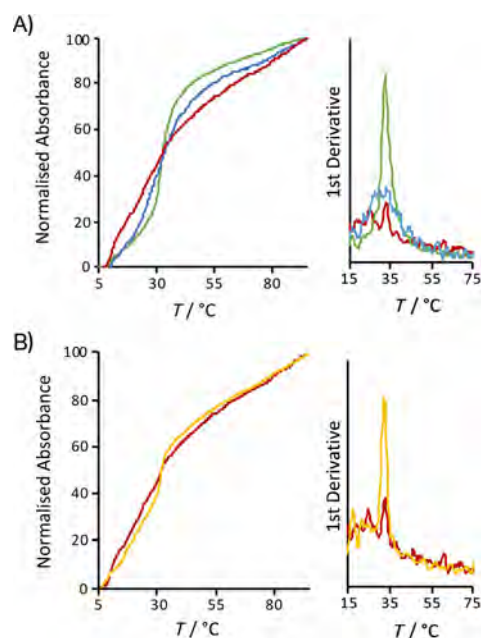
tion for full UV studies into the mode of deprotonation.[17] The Job plot of this titration indicates a clear 1:4, Cd^{2+} to tG binding ratio (Figure 1, inset), which suggests a total of two metal ions coordinated within the duplex to give duplex-3⊃Cd_2.

We hypothesise that each Cd^{2+} coordinates to the tG bases on both strands through a combination of the C6–sulfur and N7 donor groups to form the stabilized duplex-3⊃Cd_2. An analysis of crystal structures in the Cambridge Structural Database that contain sulfur and nitrogen ligands coordinated to Cd^{2+} indicates that the most commonly reported structures consist of Cd^{2+} coordinated to four sulfur atoms and two nitrogen atoms, which corresponds with the 1:4 Cd^{2+} to tG binding ratio; see Table S1 in the Supporting Information for full details.[5,16] This hypothesis is further supported by a low-temperature NMR spectroscopy study of tG, which, upon addition of Cd^{2+}, exhibits a downfield shift of the N1 proton from $\delta = 12.55$ to 14.19 ppm, as previously reported for mercaptopurine.[16]

The thermal stabilities of duplex-1, -2 and -3 were compared. Duplex-1 showed the expected UV absorption denaturation curve with a T_m of 32.2 °C, whereas duplex-3 did not (Figure 2A). The steady increase in absorption with increasing temperature for duplex-3 indicates extensive unwinding of the duplex due to increased destabilisation caused by the thiol groups on both strands. We estimated the T_m to be 22.5 °C, which indicated a destabilisation of about 10 °C, comparable to a previous report by Somerville et al.[18] We hypothesise that the 12 (2×6) complementary terminal A:T base pairs do not fully overcome the destabilising central tG_4:tG_4 region.[19] Duplex-2 shows an intermediate denaturation curve, which indicates partial destabilisation of the duplex through the four

Figure 1. UV/Vis plot showing the change in absorbance of duplex-3 at increasing concentrations of $CdNO_3$ (from red to purple). Inset: the Job plot of the molar fraction (χ) of thiobase multiplied by the change in absorbance at $\lambda = 341$ nm versus the molar fraction.

Figure 2. Thermal denaturation curves for A) duplex-1 (green), -2 (blue) and -3 (red) in the absence of metal ions, and B) duplex-3 (red) and duplex-3 ⊃Cd_2 (yellow). Inset: the first derivative for each melting curve; this highlights that T_m is only pronounced for duplex-1 and duplex-3⊃Cd_2.

G:G mismatches. Duplex-**3**, upon complexation of Cd^{2+}, duplex-**3**⊃Cd_2, exhibits a more typical denaturation curve with a T_m of 30.0 °C, which indicates about 7.5 °C stabilisation over duplex-**3** (Figure 2 B).

Equilibrium molecular dynamics (MD) simulations were performed to assess the stability of the duplexes at the atomistic level. All duplexes were subjected to 50 ns of unrestrained MD simulations (see the Supporting Information), and obtained trajectories were analysed by monitoring system energetics, stability in terms of deviations from the native DNA geometry (duplex-**1**), and flexibility in terms of per-residue root-mean-square fluctuations (RMSF; Figure 3). Relative to fully comple-
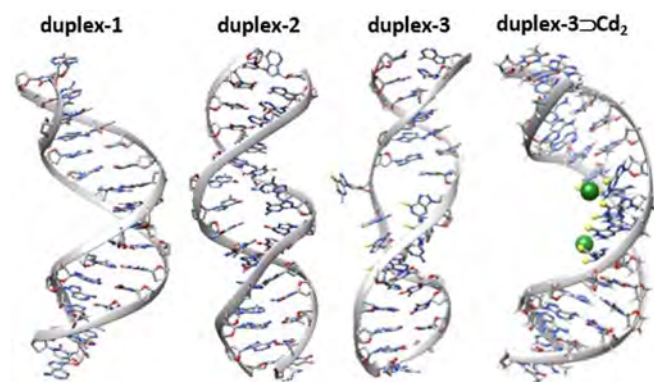
Figure 3. Snapshots representative of the highest populated clusters in conformational ensembles of the DNA duplexes under investigation. Cadmium ions (green spheres) found interacting with the sulfur atoms of the four central tG bases (small yellow spheres) induced stabilisation on flexible duplex-**3**.

mentary duplex-**1**, and to duplex-**2**, duplex-**3** retains a B-type helix, despite the introduction of the four tG residues into each strand; see the MD simulation videos in the Supporting Information for full details. The modelling images show that, upon incorporation of the tG bases within the duplex, the stacking of the nucleobases in the central region becomes distorted, but the duplex maintains a right-handed helical structure.[20] Hydrogen-bond base pairing between two tG bases is not expected, and hence, the tG bases are directed outwards from the centre of the helix (Figure 3, duplex-**3**).[18] This lack of complementary hydrogen bonding between the two sets of four tG bases in the central region results in increased fluctuational movement of all bases along the duplex. The individual mobility of each of the 16-nucleobase residues within both strands of duplex-**3** was quantified in terms of per-residue RMSF (red markers in Figure 4). In fully complementary duplex-**1** (green markers in Figure 4), the RMSF of the central four base pairs is about 0.2 nm, whereas for duplex-**3**, it is up to 2 nm; a tenfold increase in movement, corresponding to a partial unwinding of the double helix.

Addition of Cd^{2+} ions stabilised duplex-**3** through direct interactions between the Cd^{2+} ions and the sulfur atoms of the central tG residues (Cd–S distances of 2.60–2.75 Å); this resulted in increased stacking of the tG bases that previously protruded from the duplex. The restorative effect of Cd^{2+} on the
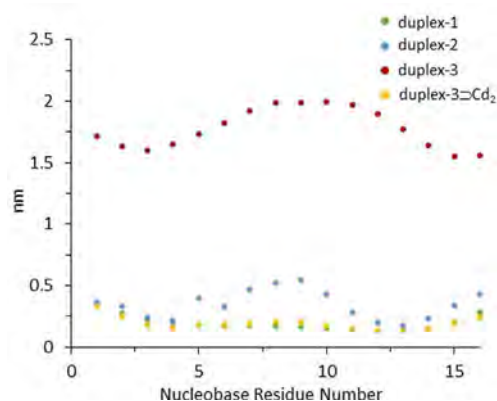
Figure 4. Graphical representation of the RMSFs of each of the 16-nucleobase residues within a single strand of duplex-**1**, duplex-**2**, duplex-**3** and duplex-**3**⊃Cd_2. Data for the second strand of each duplex is provided in the Supporting Information.

distorted duplex-**3** is considerable, resulting in reduced residue fluctuations from end-to-end of duplex-**3**⊃Cd_2 (yellow markers in Figure 4). The induced local ordering of the structure and decreased overall flexibility of the system support the observed Cd^{2+}-mediated stabilisation of the T_m for duplex-**3**⊃Cd_2.

It is conceivable that oligo-**3** could form an intrastrand hairpin structure due to terminal self-complementary A:T sequences. In this structure, the four tG bases would lie within a loop section that could coordinate a single Cd^{2+}; thus giving a 1:4 Cd^{2+}/nucleobase ratio. To test this possibility, oligo-**3** was annealed with oligo-**2** to form duplex-**4**, in which the central section contained four tG bases on one single strand opposite four "complementary" C bases. The T_m measurement of duplex-**4** indicated an intermediate thermal stability between those of duplex-**1** and -**3**, as expected. However, the binding titration of duplex-**4** with Cd^{2+}, to yield duplex-**4**⊃Cd_2, indicated a 1:2 Cd^{2+} to tG binding ratio (Figure S20), which suggested that Cd was associated between two adjacent bases in the linear duplex. In addition, there was no noticeable difference in the thermal stability between duplex-**4** and duplex-**4**⊃Cd_2 (Figure S23), which supported the proposal that the Cd^{2+} ions were critical in the stabilisation of the mismatched tG:tG region only in duplex-**3**. Furthermore, MD simulations of the possible intrastrand hairpin structures formed from oligo-**1** and -**3** indicated that the overall structures were flexible and had minimum energy values of −4240 and −927 kJ mol^{-1} for hairpin-**1** and -**2**, respectively; see the Supporting Information for full details. This suggests that hairpin formation within tG-modified oligo-**3** is unlikely due to its higher energy conformation. Energy calculations after the inclusion of Cd^{2+} ions showed some stabilisation of the hairpin-**2** structure, but the MD simulations showed no intimate interactions of Cd^{2+} with the tG nucleobases (Figure S17). We therefore conclude that the predominant structure of tG-modified oligo-**3** after the addition of Cd^{2+} is duplex-**3**⊃Cd_2, rather than the formation of a hairpin.

To investigate further the structures of duplexes-**1**, -**2** and -**3** predicted from the MD simulations, circular dichroism (CD) spectra of each duplex were recorded (Figure 5). In all cases,
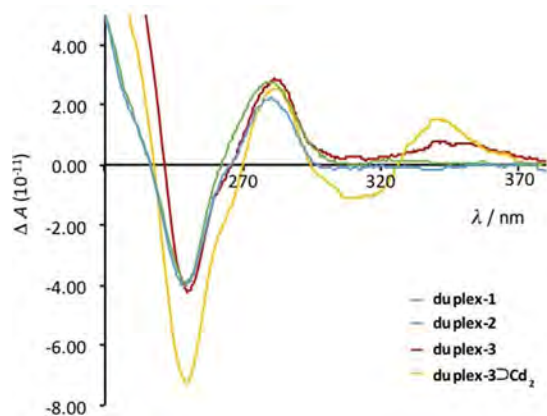
Figure 5. CD spectra of duplex-**1**, -**2**, -**3** and duplex-**3**⊃Cd$_2$

exciton splitting centred at $\lambda \approx 260$ nm is consistent with the spectrum of B-form DNA.[21] Duplex-**3** now exhibits an exciton splitting centred at $\lambda = 320$ nm, which is indicative of Cd^{2+} binding to the DNA through the tG sites. Therefore, Cd^{2+} induces some stacking of G to tG, as observed by the additional absorption band at $\lambda = 344$ nm. However, because no band splitting is observed, the tG bases are not stacked concertedly. Upon addition of Cd^{2+}, the tG CD band now exhibits exciton splitting, which is attributed to the stacking of the previously displaced tG bases, and hence increases the overall stability of the duplex.

We have shown that G can be selectively converted into tG within oligonucleotides that are still immobilised on a CPG solid support. The tG bases are shown to destabilise the duplex, as seen by increased nucleobase fluctuations in the central region and evidenced by the loss of base-stacking order in the CD spectrum. Upon coordination of Cd^{2+} ions to the sulfur atoms of tG, induced base stacking and a reduction of base fluctuations re-stabilises the DNA duplex. Herein, the Cd^{2+}-induced stabilisation of multiple single-atom base mutations within a DNA duplex illustrates the potential for the metal-mediated healing of DNA damage. Future work could exploit this approach to develop a route for the design of functional DNA hybrid nanomaterials from highly artificial and potentially unstable oligomeric building blocks, which, in response to chemical stimuli, can be re-assembled.

Acknowledgements

Conflict of Interest

The authors declare no conflict of interest.

[1] A. V. Pinheiro, D. Han, W. M. Shih, H. Yan, *Nat. Nanotechnol.* **2011**, *6*, 763–772.
[2] T. J. Morrow, M. Li, J. Kim, T. S. Mayer, C. D. Keating, *Science* **2009**, *323*, 352.
[3] J. S. Choi, C. W. Kang, K. Jung, Y. W. Yang, Y. Kim, H. Han, *J. Am. Chem. Soc.* **2004**, *126*, 8606–8607.
[4] S. M. Douglas, I. Bachelet, G. M. Church, *Science* **2012**, *335*, 831–834.
[5] P. Amo-Ochoa, S. S. Alexandre, S. Hribesh, M. A. Galindo, O. Castillo, C. J. Gomez-Garcia, A. R. Pike, J. M. Soler, A. Houlton, F. Zamora, R. W. Harrington, W. Clegg, *Inorg. Chem.* **2013**, *52*, 5290–5299.
[6] C. A. Mirkin, R. L. Letsinger, R. C. Mucic, J. J. Storhoff, *Nature* **1996**, *382*, 607–609.
[7] N. Zimmermann, E. Meggers, P. G. Schultz, *J. Am. Chem. Soc.* **2002**, *124*, 13684–13685.
[8] Y. Takezawa, K. Tanaka, M. Yori, S. Tashiro, M. Shiro, M. Shionoya, *J. Org. Chem.* **2008**, *73*, 6092–6098.
[9] S. Yoshida, M. Yamada, S. Masaki, M. Saneyoshi, *Cancer Res.* **1979**, *39*, 3955–3958.
[10] Y. H. Ling, J. A. Nelson, Y. C. Cheng, R. S. Anderson, K. L. Beattie, *Mol. Pharmacol.* **1991**, *40*, 508–514.
[11] a) Y. H. Ling, J. Y. Chan, K. L. Beattie, J. A. Nelson, *Mol. Pharmacol.* **1992**, *42*, 802–807; b) M. Kuwahara, J. Nagashima, M. Hasegawa, T. Tamura, R. Kitagata, K. Hanawa, S. Hososhima, T. Kasamatsu, H. Ozaki, H. Sawai, *Nucleic Acids Res.* **2006**, *34*, 5383–5394.
[12] a) M. S. Christopherson, A. D. Broom, *Nucleic Acids Res.* **1991**, *19*, 5719–5724; b) Y. Z. Xu, Q. Zheng, P. F. Swann, *Tetrahedron* **1992**, *48*, 1729–1740; c) Q. Zheng, Y. Wang, E. Lattmann, *Tetrahedron* **2003**, *59*, 1925–1932.
[13] P. P. Kung, R. A. Jones, *Tetrahedron Lett.* **1991**, *32*, 3919–3917.
[14] M. P. Reddy, N. B. Hanna, F. Farooqui, *Nucleosides Nucleotides* **1997**, *16*, 1589–1598.
[15] K. Tanaka, A. Tengeiji, T. Kato, N. Toyama, M. Shionoya, *Science* **2003**, *299*, 1212–1213.
[16] P. Amo-Ochoa, O. Castillo, S. S. Alexandre, L. Wette, P. J. de Pablo, M. I. Rodriquez-Tapiador, J. Gomez-Herrero, F. Zamora, *Inorg. Chem.* **2006**, *45*, 7642–7650.
[17] C. Santhosh, P. C. Mishra, *Spectrochim. Acta* **1993**, *49a*, 985–993.
[18] L. Somerville, E. Y. Krynetski, N. F. Krynetskaia, R. D. Beger, W. Zhang, C. A. Marhefka, W. E. Evans, R. W. Kriwacki, *J. Biol. Chem.* **2003**, *278*, 1005–1011.
[19] V. M. Marathias, M. J. Sawicki, P. H. Bolton, *Nucleic Acids Res.* **1999**, *27*, 2860–2867.
[20] S. Johannsen, N. Megger, D. Bohme, R. K. Sigel, J. Muller, *Nat. Chem.* **2010**, *2*, 229–234.
[21] L. M. Nielsen, S. V. Hoffmann, S. B. Nielsen, *Photochem. Photobiol. Sci.* **2013**, *12*, 1273–1285.